Stents for Transcatheter Aortic Valve Replacement

by

Kenneth Stuart Park

PRKKEN002

SUBMITTED TO THE UNIVERSITY OF CAPE TOWN

In fulfilment of the requirements for the degree

Master of Science in Biomedical Engineering

September 2017

Division of Biomedical Engineering, Department of Human Biology

University of Cape Town

Supervisors:

Assoc. Prof. D. Bezuidenhout

Dr. H. Appa

Dr J. Scherman

Declaration

I, Kenneth Stuart Park, hereby declare that the work on which this dissertation/thesis is based is my original work (except where acknowledgements indicate otherwise) and that neither the whole work nor any part of it has been, is being, or is to be submitted for another degree in this or any other university.

I empower the university to reproduce for the purpose of research either the whole or any portion of the contents in any manner whatsoever.

Signature: Signed by candidate ……………………………… Signature removed

Date: 09/10/2017 …………………………………….

Abstract

Rheumatic heart disease (RHD) is the leading cause of aortic valve disease in the world. Surgery to repair or replace the diseased valves is the only means to save a patient's life once the disease becomes symptomatic. Transcatheter aortic valve replacement (TAVR) has revolutionised the treatment of age-related degenerative aortic valve disease, but is currently not suitable for the majority of RHD sufferers due to the rapid degeneration of flexible leaflet valves in younger patients, contraindications of commercial devices to regurgitant or non-calcific aortic valve disease, and also due to resource or funding limitations. The current research project aimed to develop and test novel compressible balloon-expandable stents suitable for patients with symptomatic rheumatic aortic valve disease, and which would allow for a percutaneous polymeric valve to be manufactured, be crimped onto balloon-based devices, and be expanded into a compliant or non-calcific native aortic valve.

Several stent concepts were developed and evaluated using Finite Element Analysis (FEA) and two favoured concepts were selected for more complex FEA, in which the balloon was simulated using an Ogden material model, and rigorous testing. The stent material, a nickel-cobalt-chromium alloy, was modelled as an isotropic elasto-plastic material with isotropic hardening. The novel stent designs incorporated a native leaflet-mimicking crown shape for continuous leaflet attachment and mechanisms to anchor the stented valve within compliant aortic roots. The first of the favoured designs provided tactile location during delivery and anchored using self-expanding arms on a balloon-expandable frame of the same material ("self-locating stents"). The second design anchored using arms that protruded during deployment as a consequence of plastic deformation incurred during crimping ("expanding arm stents"). Prototypes were successfully manufactured through laser cutting and electropolishing and showed good surface quality. *In vitro* testing included determination of crimping and expansion behaviour and measurement of mechanical properties such as resistance to migration in the anatomy. Valve performance was evaluated through *in vitro* haemodynamics in a pulse duplicator and durability was tested in a high-cycle fatigue tester. Simulated use testing was performed using cadaveric animal hearts. Finally, valves were also implanted into the aortic valve position of pigs (in acute termination experiments) through a transapical approach in order to verify valve deployment behaviour and function *in vivo*, and determine the stent's ability to anchor in the native anatomy.

Stents could be crimped to diameters below 6mm and deployed using commercial balloons and proprietary non-occlusive deployment devices. FEA simulations of stent crimping and deployment matched experimental behaviour well and provide a tool to optimise stent performance. Peak Von

Mises stresses during deployment (1437 MPa and 1633 MPa for self-locating and expanding arm stents, respectively) were comparable to a “zig-zag” stent simulated for control purposes (1650 MPa). Radial strength, evaluated for expanding arm stents, was lower than the Control stent (116 N vs. 347 N). This design, although predicted to be safe under fatigue loading, had a lower fatigue safety factor than the Control stent. Stents resisted migration to forces of at least 22 N, which is four times greater than physiological loading on the valves. Polymeric valves incorporating the stents were constructed and demonstrated good *in vitro* haemodynamic performance (Effective Orifice Areas $\geq 2.0\text{cm}^2$, $\Delta P<9$ mmHg, regurgitation <6%) and durability of over 400 million cycles. Designs functioned as intended in simulated use tests. Valves constructed using self-locating stents could be successfully deployed without rapid pacing in eight of nine pigs, and valve position was correct in seven of these. Valves of expanding arm stents remained anchored in six of eight attempted implants in pigs. This study has demonstrated proof of concept for a novel balloon-expandable stent for a polymeric transcatheter heart valve that is capable of anchoring in a compliant native aortic valve.

Acknowledgements

I am greatly indebted to my supervisor, Prof Deon Bezuidenhout, for his guidance, advice and encouragement throughout my thesis, and for suggesting design alternatives.

I would like to thank my co-supervisors, Dr Harish Appa and Dr Jacques Scherman for their support. Dr Appa patiently helped me with FEA and provided a sounding board for stent design. In addition, Dr Appa is responsible, following on from the work of Claude Visagie, for the design of the leaflets used in the valves described in this thesis. Dr Scherman provided valuable input on stent requirements and on the preclinical testing of the devices.

This thesis would not have been possible without the vision of Prof Peter Zilla, who gave me the opportunity to do this thesis, and provided many stimulating ideas and comments on design.

I am thankful for funding provided by Strait Access Technologies Holdings (SATH).

I am grateful to my fellow MSc students Johan Coetzee and David Conradie, who helped to manufacture the polymeric valves and to Ursula Saralina who helped to manufacture the bioprosthetic valves used in the preclinical trials.

I am also grateful for the help and support of all colleagues and friends in UCT’s Cardiovascular Research Unit and SATH, including Braden van Breda, Alan Sutherland, Robin Smith, Jeremy Jarmin, Bruce de Jongh, Aminah Rujub, Wian van den Bergh and Remy Roux dit Buisson.

Several people helped with preclinical planning and/or testing of valves, particularly Giuseppe Geldenhuys, Dr Chima Ofoegbu, Rose Boltman, Johanna Klopper and Raymond Michaels. I am grateful for the help of these individuals and the veterinary staff at the Faculty of Health Sciences Animal Unit and to the anaesthetists who participated. Deployment devices for stent crimping and deployment were manufactured by SATH.

I would also like to thank Mr Hellmut Bowles and Dr Greg Mitchell of Finite Element Analysis Services (Pty) Ltd, who provided support and advice for stent modelling in Abaqus. Mr Bowles developed the method for calculating and plotting the inverse fatigue safety factor for fatigue life prediction. Graham Inggs, Engineering Faculty Unix Systems Administrator, helped me to run Abaqus on the UCT cluster.

Contents

Declaration i
Abstract ii
Acknowledgements iv
Contents v
List of Figures viii
List of Tables xi
List of Equations xii
Nomenclature/Abbreviations xiii
1 Introduction 1
  1.1 Background and Motivation 1
  1.2 Aim 2
  1.3 Thesis Outline 2
2 Literature Review 4
  2.1 Anatomy and Physiology of the Heart 4
  2.2 Functional Anatomy of the Aortic Root 5
  2.3 Rheumatic Heart Disease 12
  2.4 The Aortic Valve in Disease 13
  2.5 Heart Valve Replacement 15
    2.5.1 Surgical Valve Replacement 15
    2.5.2 Transcatheter Aortic Valve Replacement (TAVR) 16
    2.5.3 Sutureless and Hybrid Valves 20
    2.5.4 Valve Longevity 21
  2.6 Design and Simulation of Stents 23
    2.6.1 Structural Design of a Stent 23
    2.6.2 Leaflet Design 25
    2.6.3 Computational Simulation of Stent Performance 26
  2.7 Concluding Remarks from Literature Review and Statement of Objective 28
3 Design Inputs and Methods 31
  3.1 Design Requirements 31
    3.1.1 Valve Requirements 31
    3.1.2 Stent Requirements 31
  3.2 Stent Design, Drafting and Material Selection 35
    3.2.1 Development Methodology 35
    3.2.2 Drafting 36
    3.2.3 Material Selection 37
4 Numerical methods 39
  4.1 Theoretical framework 39
  4.2 Modelling overview 41
    4.2.1 Stent model creation 41
    4.2.2 Balloon model creation 43
    4.2.3 Crimping and relaxation 45
    4.2.4 Expansion and relaxation 45
    4.2.5 Valve loading 45
    4.2.6 Radial crushing 46
  4.3 Model validation 46
  4.4 Parameters for evaluation 46
    4.4.1 Stent static behaviour 46
    4.4.2 Stent radial strength 47
    4.4.3 Stent fatigue 47
5 Experimental Methods 48

5.1 Stent Manufacture 48
  5.1.1 Stent Cutting 48
  5.1.2 Descaling 48
  5.1.3 Electropolishing 49
  5.1.4 Additional manufacturing steps 51
  5.1.5 Valve Manufacturing 51
5.2 Materials Testing 52
5.3 In Vitro Stent Testing 53
  5.3.1 Testing overview 53
  5.3.2 Inspection and Measurement 53
  5.3.3 Stent Mechanical Testing 54
5.4 In Vitro and Ex Vivo Valve Testing 56
  5.4.1 Valve deployment 56
  5.4.2 Explanted heart tester 56
  5.4.3 Pulse duplicator 57
  5.4.4 Valve Fatigue 58
5.5 In Vivo Experimental Methods 59
  5.5.1 Study Design 60
  5.5.2 Procedure 61
6 Concept development 63
6.1 Basic Structure – Native Valve Mimicking Shape 63
6.2 Ideation and Concept Generation 68
6.3 Concept Development 70
  6.3.1 Crown support Concept 1: Support at top and bottom 71
  6.3.2 Crown support Concept 2: Intermediate support 71
  6.3.3 Anchorage Concept A: Friction 71
  6.3.4 Anchorage Concept B: “Paper lantern” 71
  6.3.5 Anchorage Concept C: Arms attached to the outside of the stent 72
  6.3.6 Anchorage Concept D: Integrated expanding arms 72
6.4 Concept Evaluation 72
  6.4.1 Concept 1A 73
  6.4.2 Concept 1B 74
  6.4.3 Concept 1C 76
  6.4.4 Concept 1D 76
  6.4.5 Concept 2A 77
  6.4.6 Concept 2B 78
  6.4.7 Concept 2C 79
  6.4.8 Concept 2D 80
6.5 Concept Selection 81
7 Results 84
7.1 Modelling Results 84
  7.1.1 Balloon Modelling Results 84
  7.1.2 Model structural validation – Radial crush 85
  7.1.3 Crimping and Deployment 86
  7.1.4 Foreshortening and recoil 94
  7.1.5 Radial strength and fatigue analysis 94
7.2 In Vitro and Ex Vivo Results 97
  7.2.1 Material properties 97
  7.2.2 Stent inspection and measurement 98
  7.2.3 Stent mechanical performance 102
  7.2.4 Valve performance 105
7.3 In Vivo Results 112

7.3.1 Design 1: Self-locating valve 114
7.3.2 Design 2: Expanding arm valve 117
8 Discussion 120
8.1 Stent Design 120
8.2 Stent and Valve Manufacture 123
8.3 Experimental Testing 125
8.4 Finite Element Modelling 129
9 Conclusions and Recommendations 133
9.1 Limitations 134
9.2 Recommendations 134
9.3 List of Outputs 136
9.3.1 Patents 136
9.3.2 Congresses and Presentations 136
9.3.3 Proposed Publications 136
10 References 137
Appendix A. Comprehensive list of transcatheter valves A-1
Appendix B. Characterisation of stents B-1
Appendix C. Mesh refinement C-1
Appendix D. Additional manufacturing information D-1
Appendix E. Stent measurements – additional information E-1
Appendix F. Dogbone for materials testing F-1
Appendix G. Stent origins, concepts and structures: the fuzzy front end G-1
Appendix H. FEA results of stent crimping and deployment H-1
Appendix I. Additional stent images I-1
Appendix J. Detailed predictions and measurements of stent recoil and foreshortening J-4
Appendix K. Hollomon material model K-1

List of Figures

Figure 1-1. Non-occlusive deployment device, rendering and sketch of deployment 2
Figure 1-2. Flowchart of thesis 3
Figure 2-1. Sectional anatomy of the heart 4
Figure 2-2. Schematic of aortic root, adapted from Sutton, Ho, and Anderson (1995) 6
Figure 2-3. Image of the aortic root opened from the left ventricle (left) showing fibrous continuities between interleaflet triangles, the fibrous trigones, and the membranous septum, and a schematic (right) showing the relations of the atrioventricular conduction system with respect to the aortic valve leaflets, from Piazza et al. (2008) 6
Figure 2-4. Opened-out mitral and aortic valves, from Du Plessis and Marchand (1964). 7
Figure 2-5. View of an aortic root opened longitudinally, showing the basal ring (white line) and the VAJ (black dashed line), from De Kerchove et al. (2015). (L – Left coronary cusp; R – Right coronary cusp; N – Non-coronary cusp) 7
Figure 2-6. Histology of the aortic valvar complex (Piazza et al., 2008) 8
Figure 2-7. Relative cross-sectional schematic of the aortic root: (A) End diastole; (B) During ejection, at maximum dilation. Adapted from Lansac et al. (2002) 11
Figure 2-8. A) Normal trileaflet aortic valve, B) Stenotic calcified bicuspid aortic valve, C) Calcified (degenerative) trileaflet aortic valve, D) Thickened leaflets and commissural fusion associated with Rheumatic aortic valve disease, from Anderson, Becker, et al. (2009) 14
Figure 2-9. Excised diseased valves. A) Calcified (degenerative) trileaflet aortic valve, B) Calcified bileaflet aortic valve and C) Rheumatic aortic valve, from http://www.cthsurgery.com/aetiology-of-aortic-valve-stenosis.html. 14
Figure 2-10. Medtronic Hall™ Tilting disc valve, Edwards MIRA™ bileaflet valve (Abu-Omar & Ratnatunga, 2007), and TTK Chitra™ valve (Walters, 2015) (left to right) 16
Figure 2-11. Carpentier-Edwards Perimount™ pericardial valve and Edwards Prima Plus™ stentless bioprosthesis (Abu-Omar & Ratnatunga, 2007) 16
Figure 2-12. Edwards Lifesciences Sapien THV™, deployed on balloon and illustrated antegrade implantation through the left ventricular apex (Chiam & Chao, 2013) 18
Figure 2-13. Fifteen-year freedom from structural valve dysfunction versus age at implant (Banbury et al., 2001) 22
Figure 2-14. Age distribution for patients receiving replacement heart valves in a developing country and in the developed world (Zilla et al., 2008) 22
Figure 2-15. Examples of stent structures proposed in the literature 24
Figure 2-16. Schematic showing leaflet design as per Labrosse et al. (2006) 26
Figure 3-1. Project design and development model 35
Figure 3-2. Computer-aided drawing of 3D stent model. 36
Figure 3-3. Full stent geometry completed using "mirror" and "combine" features 37
Figure 3-4. Computer-aided drawing of stents for manufacture 37
Figure 4-1. Stress-strain curves for balloon material 44
Figure 4-2. Comparison between test data and Ogden material model 44
Figure 4-3. Balloon sketch profile and meshed geometry 44
Figure 5-1. Electropolishing apparatus 49
Figure 5-2. Tensile grips 52
Figure 5-3. Photographs of explanted heart rig, showing A) rig placed on table in operating theatre with fluoroscopy and endoscopy available, and B) cannulated heart. 57
Figure 5-4. ViVitro pulse duplicator 59
Figure 5-5. BDC Labs durability tester 59
Figure 5-6. Operating theatre 60
Figure 6-1. Images from explanted heart tester showing the left ventricular aspect of a first generation zig-zag valve A) immediately after deployment and B) following embolization of the valve into the ventricle after several seconds 63
Figure 6-2. Example cubic Bézier function from Scilab used to construct crowns 65
Figure 6-3. Diagram showing eight different Bézier curves generated in the x-z plane, and as crown structures 65
Figure 6-4. A) Crown-shape generated from Bézier curves, with simple leaflet attached. B) Simplified Leaflet .. 66

Figure 6-5. Finite element model geometric representation for Bézier analysis 66
Figure 6-6. Bézier Crown Version 1 geometry (left) and FEA Von Mises Stress after crimping (Right)................ 67
Figure 6-7. Bézier Crown Version 8 geometry (left) and FEA Von Mises Stress after crimping (Right)................ 67
Figure 6-8. Von Mises Stress for leaflet from Bézier Crown Version 2 under closing pressure (left) and for leaflet from Version 1 (right) under opening pressure.. 67
Figure 6-9. Graph showing maximum Von Mises stress in crown structure and leaflets for different Bezier functions. Stresses for the chosen crown shape, Version 4, are shown in the rectangle..................................... 68
Figure 6-10. Potential anatomical positions considered for stent anchoring 69
Figure 6-11. Concept 1A FEA results following simple modelling, showing deployed stent geometry (A, B and D) and crimped geometry (C) 74
Figure 6-12. Concept 1A prototype 74
Figure 6-13. Concept 1B FEA results following simple modelling, showing deployed stent geometry (A, B and D) and crimped geometry (C) 75
Figure 6-14. Concept 1B prototype after crimping and deployment 75
Figure 6-15. Concept 1C FEA results following simple modelling, showing deployed stent geometry (A, B and D), crimped geometry (C) and relaxed geometry after crimping (E) 76
Figure 6-16. Concept 1D FEA results following simple modelling, showing deployed stent geometry (A, B and D) and crimped geometry (C) 77
Figure 6-17. Concept 1D prototype before crimping (left), and after crimping and deployment (right) 77
Figure 6-18. Concept 2A FEA results following simple modelling, showing deployed stent geometry (A, B and D) and crimped geometry (C) 78
Figure 6-19. Concept 2B FEA results following simple modelling, showing deployed stent geometry (A, B and D) and crimped geometry (C) 79
Figure 6-20. Concept 2C FEA results following simple modelling, showing deployed stent geometry (A, B and D), crimped geometry (C) and relaxed geometry after crimping (E) 80
Figure 6-21. Concept 2D FEA results following simple modelling, showing deployed stent geometry (A, B and D) and crimped geometry (C) 81
Figure 7-1. Comparison between experimental and predicted balloon diameters... 84
Figure 7-2. Balloon deployment simulation showing initial unfolding, and subsequent stretching, from 0 atm to 4 atm.. 85
Figure 7-3. Von Mises Stress distribution in the balloon at 4 atm. 85
Figure 7-4. Comparison between radial crush force predicted from FEA and determined experimentally 85
Figure 7-5. Von Mises stress distribution for Control stent in crimped (A&B) and deployed (C&D) conditions. Stents are shown with and without balloons... 87
Figure 7-6. Location of maximum Von Mises Stress after deployment of Control stent...................................... 87
Figure 7-7. Maximum Principal Stress of Control stent at integration point of element 53426, which is the element with the highest maximum principal stress at the end of relaxation after deployment........................ 89
Figure 7-8. Mesh used for Design 1 89
Figure 7-9. Von Mises stress distribution for Design 1 stent in crimped (A&B) and deployed (C&D) conditions. Stents are shown with and without balloons... 90
Figure 7-10. Deformed geometry and Von Mises stress distribution associated with Design 1 stent irregularities. A) Distorted crown, showing area of greatest Von Mises stress in the model, B) Preferential stretching of long elements (*), C) Raised top row of diamonds elements (arrow), D) Trapped hairpin junction (++) 91
Figure 7-11. Mesh used for Design 2 92
Figure 7-12. Von Mises stress distribution for Design 2 stent in crimped (A&B) and deployed (C&D) conditions. Stents are shown with (B&D) and without (A&C) balloons.. 93
Figure 7-13. Deformed geometry and Von Mises stress distribution associated with Design 2 stent irregularities. A) Area of greatest Von Mises stress in the model, B) Distorted crown element near commissure posts 93
Figure 7-14. Radial strength 95
Figure 7-15. Fatigue diagram of inverse fatigue safety factors for Control stent 96
Figure 7-16. Contour plots of nodal inverse fatigue safety factors for Control stent 96
Figure 7-17. Fatigue diagram of inverse fatigue safety factors for Design 2 at the integration points 96
Figure 7-18. Contour plots of inverse fatigue safety factors for Design 2 97
Figure 7-19. Stress-strain curves from uniaxial tensile testing of MP35N dogbones: A) Engineering stress-strain for three samples; B) True stress-strain and extracted plastic stress-strain data for FEA for Sample 1.............. 98
Figure 7-20. Macro photographs of stents. A) Design 1, B) Design 2 99
Figure 7-21. Micro photographs of stents. A) Design 1, B) Design 2 99

Figure 7-22. SEM images of stents. A) Design 1, B) Design 2 99
Figure 7-23. Measurement locations for Design 1 100
Figure 7-24. Measurement locations for Design 2 101
Figure 7-25. Crimped stents on commercial balloon. A) Control stent, B) Design 1, C) Design 2 102
Figure 7-26. Deployed stents on commercial balloon. A) Control stent, B) Design 1, C) Design 2 103
Figure 7-27. Undeformed and deformed stents. A) Control Stent, B) Design 1, C) Design 2. Clockwise from top left for each cluster: photograph of as-manufactured stent, FEA model of original geometry, FEA model of deformed geometry after deployment and recoil, photograph of deformed stent. 104
Figure 7-28. Migration test. A) Design 2 valve deployed into Freestyle xenograft. B) Test setup for migration test, including a force gauge and sutures connecting the base of the stent to the gauge. 105
Figure 7-29. Polymeric valve constructed from Design 1 stent (left) and Design 2 (right). Design 1 incorporates a polyurethane film skirt and shows marker lines used to indicate free edge of leaflet for cutting. Design 2 incorporates an electrospun polyurethane skirt 106
Figure 7-30. Free deployment of Design 2 valve on SATH Mechanical expander and annular balloon. The long black line indicates the location of the nadir of the crown shape in the crimp condition and the short line indicates the location of the nadir in the deployed condition 107
Figure 7-31. Endoscopic images of location and deployment of Design 1 valves, from the aortic view. Asterisk shows area of potential leakage. 111
Figure 7-32. Fluoroscopic images of location and deployment of Design 1 valves, deployed using SATH non-occlusive balloon catheter 111
Figure 7-33. Endoscopic images of deployed Design 2 valves, from the ventricular (left) and aortic (right) views 112
Figure 7-34. Fluoroscopic images of location and deployment of Design 2 valves, deployed using SATH mechanical expander and annular balloon 112
Figure 7-35. Exemplary crimped valves used in the preclinical evaluation of Design 1. A) Bioprosthetic valve on SATH mechanical expander; B) Polymeric valve on SATH self-sustaining balloon catheter 113
Figure 7-36. Exemplary crimped valves used in the preclinical evaluation of Design 2. A) Bioprosthetic valve on SATH mechanical expander; B) Polymeric valve on SATH self-sustaining balloon catheter 113
Figure 7-37. Typical fluoroscopic image of an implanted Design 1 valve, from Pig 1-10; the valve is circled 116
Figure 7-38. Post-mortem images of Design 1 valve in position in a porcine aortic root. A) Typical valve shown with most of the SoV excised; note location of arm behind cusps and proximity of native leaflets to replacement leaflets. B) Ventricular view of valve from Pig 1-3 showing arm pierced through leaflet. 116
Figure 7-39. Typical fluoroscopic image of an implanted Design 2 valve, from Pig 2-7; the valve is encircled. 119
Figure 7-40. Post-mortem images of Design 2 valve in position in a porcine aortic root. A) Valve from Pig 2-7 shown with ascending aorta excised; arms are located behind cusps. B) Ventricular aspect of valve from Pig 2-6 showing arm below the basal plane (arrow); the arm behind the leaflet indicated by the asterisk is on the muscle shelf, while the third arm (not visible) is behind the leaflet 119
Figure 8-1. Comparison between In Vitro test geometry and FEA geometry for Control (A,B), Design 1 (C,D) and Design 2 (E,F). The images on the left (A,C,E) show FEA original geometry superimposed over photograph of as-manufactured stent. The images on the right (B,D,F) show FEA deformed geometry superimposed over photograph of deployed stent 131

List of Tables

Table 2-1. Aortic root measurements of normal patients from 3D TOE, from Calleja et al. (2013), in mm 9
Table 2-2. History of significant developments leading up to percutaneous aortic valve implantation.............. 17
Table 2-3. CE Marked TAVR devices (Bourantas & Serruys, 2014; Rozeik, Wheatley, & Gourlay, 2014; Taramasso et al., 2014; Weiss et al., 2015; Wiegerinck, Van Kesteren, Van Mourik, Vis, & Baan, 2016) 19
Table 2-4. Non-CE-marked balloon-expandable TAVR (Ismail, Hon, Chan, & Leo, 2012; Jamieson, Zhang, & Quijano, 2006; Jilaihawi et al., 2010; Kemp et al., 2013; Leon, 2013; Pontes et al., 2013) 20
Table 2-5. Polymer TAVR (historical and active) (Bezuidenhout, Williams, & Zilla, 2015)................................... 20
Table 3-1. Key current design requirements 32
Table 4-1. Comparison of simple and complex FEA methods used for stent modelling 41
Table 4-2. Ogden material parameters 43
Table 5-1. Electropolishing parameters 50
Table 6-1. Main stent concepts.. 70
Table 6-2. Summary of results of different concepts 73*
Table 6-3. Concept selection matrix for comparing design concepts (score 0-5) 82
Table 7-1. Comparison between experimental and model results of balloon diameter...................................... 84
Table 7-2. Maximum Stress and Strain in Control stent at the end of each step (based on integration points) .. 86
Table 7-3. Summary of results of complex modelling.. 88
Table 7-4. Maximum Stress and Strain in self-locating stent at the end of each step... 90
Table 7-5. Maximum Stress and Strain in expanding arm stent at the end of each step 92
Table 7-6. Summary of recoil values from FEA and physical measurements... 94
Table 7-7. Summary of foreshortening values from FEA and physical measurements.. 94
Table 7-8 Material Properties for MP35N 97
Table 7-9. Stent dimensions for Design 1.. 100
Table 7-10. Stent dimensions for Design 2 101
Table 7-11. Frames from high speed photography at different parts of the cardiac cycle................................ 108
Table 7-12. Haemodynamic results 109
Table 7-13. Durability test results... 109
Table 7-14. Summary of animal data, deployment device and pre-implant conditions for pig study............... 114
Table 7-15. Device performance and complications for Design 1 (self-locating) valve 114
Table 7-16. Device performance and complications for Design 2 (expanding arm) valve................................. 117

List of Equations

Equation 4-1 Principle of Virtual Work 39
Equation 4-2 Governing equation 39
Equation 4-3 Dynamic equilibrium 40
Equation 4-4 Simplified dynamic equilibrium 40
Equation 4-5 Central difference method 40
Equation 4-6 Acceleration 40
Equation 4-7 Stability limit 40
Equation 4-8 Ogden 43
Equation 4-9 Fatigue safety factor 47
Equations 5-1 True Stress and Strain 52
Equation 5-2 Hollomon's Law 52
Equations 5-3 Hollomon parameters 53
Equation 5-4 Radial force 55
Equations 5-5 Foreshortening and recoil 55
Equation 5-6 Effective Orifice Area 57
Equation 5-7 Root mean square of flow 58
Equation 6-1 General Bézier Curve 64
Equation 6-2 Cubic Bézier Curve 64

Nomenclature/Abbreviations

Activated Clotting Time (ACT)	Standardised test of blood clotting time
Acute Rheumatic Fever (ARF)	Inflammatory disease caused by auto-immune response to streptococcal throat infection
American College of Cardiology (ACC)	
American Heart Association (AHA)	
Antigen mimicry	Auto-immune responses based on similarity between the body and a foreign microorganism
Aortic annulus/ virtual annulus/ virtual ring/ basal ring/ surgical annulus	Fibrous area at the base of the aortic valve, defined by various terms; Surgical annulus is crown-shaped while others are used to describe a ring at base of the leaflets
Aortic Stenosis (AS)	Aortic valve narrowing
Aortic Regurgitation (AR)	Aortic valve disease causing leakage
Atrium (pl. atria)	Thin-walled upper chamber of the heart
Atrioventricular (AV) node	Specialised group of heart muscle cells in centre of heart that help regulate conduction of electricity in the heart
Bézier curve	Parametric curves used to generate smooth shapes based on a finite number of parameters
Biological heart valve (BHV)	Heart valve constructed using animal (including human) tissue
Bundle of His	Part of the heart's electrical conduction system that conducts electrical signals from the AV node to the tip (apex) of the heart
Calcification	Deposition of calcium in body tissue, causing hardening
Central fibrous body	Strongest fibrous area of the heart at areas where valves meet
Central Venous Pressure (CVP)	Blood pressure in the venae cavae, just before blood returns to the heart
Coaptation	Area of contact between surfaces of valve leaflets
Commissure	Area where leaflets join
Commissurotomy	Surgical separation of joined leaflets
Compliance	Amount by which a dimension (esp. valve diameter) changes with load (esp. pressure)
Computed Tomography (CT)	X-ray imaging system capable of producing cross-sectional images
Computer-aided Design (CAD)	Use of computers to design
Computer Numerical Control (CNC)	Automated computer control of manufacturing
Contrast angiography	Medical imaging technique that uses a radiopaque substance to visualise body cavities, particularly in the heart
Coronary arteries	Arteries that supply the blood to the heart
Cusp/ Leaflet/Lunula	Flexible flaps that open and close in a heart valve
Diastole	Part of the heart cycle where chambers fill with blood and the muscle relaxes
Echocardiography/ Transoesophageal / Transthoracic echocardiography (TOE/TTE)	The use of ultrasound waves to study the heart, with probes either on the chest (transthoracic) or down the gullet (transoesophageal)
Effective Orifice Area (EOA)	Area of the blood stream where diameter is the smallest, after passing through a narrowing such the aortic valve.
Elastic limit	The stress beyond which permanent deformation occurs
Elastic modulus	Measure of stiffness of a material defined as the slope of the stress-strain curve in the elastic region (recoverable deformation)
Electrospinning	Technique that uses electricity to draw polymer fibres into a fabric
Embolus/ Embolisation	An object carried in the blood stream to block a cavity/ the process by which the object detaches

Endothelial cells	Thin layer of cells lining the inside of a blood vessel
Endurance limit	The cyclic stress at which a material can resist fatigue failre indefinitely
Engineering stress/strain	Stress calculated as applied load divided by the original cross-sectional area/ strain calculated as deformation divided by the original length of the material
Fatigue strength	See endurance limit
Fatigue safety factor	Ratio of a particular stress state at a point and the point of intersection with the “Goodman” line (see Goodman diagram below).
Fibrosa	Fibrous layer on the aortic side of the aortic valve leaflets
Fibrosis	Excessive fibrous tissue formation
Fibrous trigones	Thickened ends of fibrous continuity between aortic and mitral valves
Finite Element Analysis (FEA)	Numerical technique to solve physical problems based on dividing the problem into simpler parts
Fluid Structure Interaction (FSI)	In modelling, a method of coupling computational fluid modelling to solid structural modelling
Fluoroscopy	Continuous X-ray imaging
Food and Drug Administration (FDA)	United States federal agency governing food and healthcare, including medical devices
Foreshortening	Percentage change in length (esp. a stent) from compressed to final conditions
Goodman diagram	Graph of mean versus alternating stress; infinite life is assumed if stress state (mean and alternating) are below a line constructed from the UTS and endurance limits of the material (the Goodman line).
Hollomon Power Law	Stress/strain relationship such that stress is a power function of strain
Hoop force	Force in circumferential direction
Hourglassing	An error in numerical analysis caused by zero energy degrees of freedom.
Intellectual Property (IP)	Creations (typically inventions) frequently legally protected through patents.
Inter-commissural distance (ICD)	Distance between the commissures of a valve
International Standards Organisation (ISO)	International non-governmental organisation that creates standards
Ischaemia	Lack of oxygen supply to tissues due to insufficient blood flow
Isotropic	Having the same properties in all directions
Left bundle branch (LBB)	Branch of the Bundle of His that travels down the left side of the intraventricular septum, the wall separating the two ventricles
Left Ventricular Outflow Tract (LVOT)	Part of the left ventricle through which blood passes out the ventricle
Lumen	The space inside a tube-like structure such as an artery
Mechanical heart valves (MHV)	Synthetic replacement valve with rigid parts; the majority have a tilting disc or two hinged rigid leaflets
Membranous septum	Thin part of the ventricular septum close to the aortic valve
Mesh	In FEA, the subdivision of a structure or problem into smaller regions known as elements, for which equations may be solved
Multi-detector row Computed Tomography (MDCT)/ Multi-slice CT (MSCT)	CT system equipped with multiple rows of detectors to create images of multiple sections.
Nadir	Lowest point of a structure such as a crown or leaflet
Nodulus of Arantius	Thickening in the middle of the free edge of a leaflet
Ogden material model	Non-linear hyper-elastic model to describe the behaviour of materials like rubber
Percutaneous coronary intervention (PCI)	Catheter-based method of opening a blocked coronary artery
Radial force	Force directed towards or away from the centre of a curve such as a stent
Rayleigh damping	Viscous damping of a material proportional to mass and/or stiffness
Recoil	The percentage that a stent moves backwards once a force or displacement is removed; used particularly to refer to the spring back following expansion
Rheumatic Heart Disease (RHD)	Damage to the heart valves as a complication of rheumatic fever
Shear locking	An error in FEA that makes elements appear to be stiffer than they are in bending

Sinotubular Junction (STJ)	Area between the Sinus of Valsalva and the ascending aorta
Sinus of Valsalva (SoV)	Widenings of the wall of the aorta at the level of the aortic valve
Spongiosa	Gel-like central layer of a heart valve leaflet
ST elevation	Raised portion of the electrocardiogram (ECG) known as the ST segment, which corresponds to the depolarisation phase of the heart cycle; an indicator of ischaemia.
Stent/ Stent graft	A support frame or structure/ a covered stent
Strain / Peak Plastic Equivalent Strain (PEEQ)	Deformation associated with a stress / amount of permanent strain in a material
Stress (Von Mises, Maximum Principle)	Forces acting on a particular area in a material. Von Mises stress (based on distortion energy) is considered to be the best stress value to describe yielding (onset of permanent plastic deformation) in ductile (malleable) materials. Maximum Principle Stress is the highest value of tensile (pulling) stress (or the least compressive stress) in the material; although best for brittle materials, it is used in the study of fatigue of ductile materials
Structural valve dysfunction (SVD)	Inability of a heart valve to function due to changes in its physical structure, such as through calcification of leaflets
Surgical Aortic Valve Replacement (SAVR)	Removal and replacement of a heart valve through direct surgery
Systole	Part of the heart cycle where the muscle contracts and blood is ejected
Total Regurgitant Fraction	Total percentage of blood that flows backwards during systole, including closing flow and leakage through the valve
Transcatheter Aortic Valve Implantation/ Replacement (TAVI/TAVR)	Catheter-based method of implanting/replacing a diseased heart valve; the terms are typically used interchangeably
Triangle of Koch	A triangle (used as a landmark for the AV node) on the inside surface of the right atrium defined by three anatomical structures
True stress/ strain	Stress calculated as the applied load divided by the instantaneous cross-sectional area/ strain calculated as the instantaneous change in the instantaneous length
Ultimate Tensile Strength (UTS)	Highest stress determined in a tensile test
Valvuloplasty	Widening of a narrowed valve, typically using a balloon
Ventricle/ Ventricular Septum	Main muscular chambers of the heart/ wall separating the two ventricles
Ventricularis	Elastic layer on the ventricular side of the aortic valve leaflets
Ventriculo-aortic junction (VAJ)	Region between the left ventricular muscle (myocardium) and the fibrous aortic wall
Yield Stress	See elastic limit
Young's Modulus	See elastic modulus

1 Introduction

1.1 Background and Motivation

Rheumatic heart disease (RHD) is the leading cause of aortic valve disease in the world and is responsible for over 1 million deaths per year. It is estimated that up to 78 million people are living with RHD, the majority of whom live in the developing world (Paar et al., 2010; Sliwa & Zilla, 2012; Zühlke et al., 2015). Surgery to repair or replace the diseased valves is frequently the only means to save a patient's life once the disease becomes symptomatic (Cannon, Roberts, Milne, & Carapetis, 2017; Carapetis, 2007; Sliwa & Zilla, 2012; Zühlke, Engel, Remenyi, Wyber, & Carapetis, 2013; Zühlke, Mirabel, & Marijon, 2013).

Transcatheter aortic valve replacement (TAVR) is a minimally-invasive procedure that has revolutionised the treatment of aortic heart valve disease over the last decade (Taramasso et al., 2014). Most of these procedures are carried out within developed countries, on elderly patients who suffer from age-related calcific degenerative aortic stenosis (AS). A comparatively recent intervention, TAVR (with commercially available replacement devices such as the Edwards Sapien™) was originally used to treat patients who have unacceptable or high risk for open-heart surgical valve replacement. It is increasingly being used to treat patients at moderate risk (Reardon et al., 2017) but there is currently insufficient clinical evidence to support the use of the devices in low risk patients (Panayiotides & Nikolaides, 2014; Rosato et al., 2016). Although surgical valve replacement for low-to-moderate risk patients, and TAVR for high risk and inoperable patients are considered the standard-of-care in the developed world, these devices are unsuitable for the majority of the developing world, where there are relatively few cardiac surgery centres, catheterisation laboratories or the sophisticated hybrid laboratories (with associated advanced X-ray imaging equipment) required for transcatheter delivery of commercial TAVR devices. Furthermore, TAVR devices are too expensive to be affordable in developing economies (Neyt, Van Brabandt, Devriese, & Van De Sande, 2012). There is therefore a great need for lower cost TAVR devices and procedures suitable for developing countries (Remenyi, ElGuindy, Smith, Yacoub, & Holmes, 2016; Zilla, Brink, Human, & Bezuidenhout, 2008).

Researchers within the Cardiovascular Research Unit (CVRU) at the University of Cape Town have recognised the need for a TAVR procedure that can be simplified to make it possible to perform heart valve replacements and repairs at regional hospitals. Transcatheter valve deployment devices are therefore being developed that do not occlude blood flow during deployment, and allow valves to be placed using tactile information about location within the heart instead of relying on advanced imaging. The devices incorporate balloons that can deploy a replacement valve in the affected anatomy. An example of a device currently in development is shown in Figure 1-1. In parallel with the development of the deployment devices, replacement aortic valves are also being developed. While commercial TAVR valves are hand-sewn using animal tissue leaflets, the ability to mass-produce valves with polymer leaflets would make these valves far more accessible to hospitals in developing countries.

The current thesis project aims to develop and test a novel balloon-expandable stent for a polymeric TAVR. It forms part of the broader programme to develop a low cost and durable balloon-expandable replacement heart valve suitable for patients with symptomatic rheumatic aortic valve disease. The valve is intended to be delivered to the site of implantation and deployed by the devices discussed above.

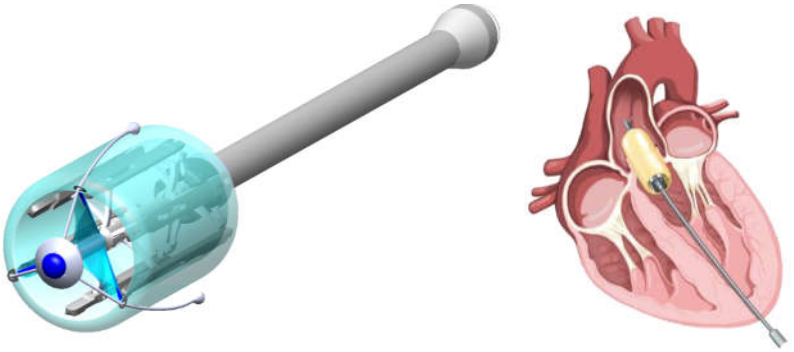

Figure 1-1. Non-occlusive deployment device, rendering and sketch of deployment

1.2 Aim

This thesis project involves the development of a new technology. Specifically it aims to develop and test a balloon-expandable stent suitable for use in RHD, suitable for the manufacture of polymer valves and able to be crimped onto deployment devices.

1.3 Thesis Outline

Chapter 2 provides a literature review of heart and aortic valve anatomy, as well as presenting details of the effect of rheumatic heart disease on the aortic valve. It also presents a summary of commercially available transcatheter aortic valves or valves in development, and describes published work on stent and valve design and simulation. Finally it presents concluding comments on the literature review and defines the specific objectives of the thesis.

Chapter 3 presents the user needs and design requirements identified for the valve (and describes how this is translated to the engineering requirements for the stent) and presents methodology related to design and material selection.

Chapters 4 and 5 describe the numerical and experimental methods. Specifically Chapter 4 presents the theory and methods related to computational modelling of stent performance; Chapter 5 presents the methods used to manufacture stents, and the methods used to test stent and valve performance using *in vitro* bench tests and *in vivo* studies in large animals.

The results of design and testing are presented in Chapters 6 and 7. Specifically Chapter 6 describes the generation and selection of stent concepts to satisfy user needs; Chapter 7 presents the results of simulation, prototyping and test activities performed on favoured design concepts selected from Chapter 6.

Chapter 8 provides a discussion of the results in the context of prior work in the field and compares the solution to the engineering requirements.

Chapter 9 concludes the report, discusses limitations and provides recommendations for further research and development, including recommendations for design alternatives.

The thesis layout is presented as a flowchart in Figure 1-2.

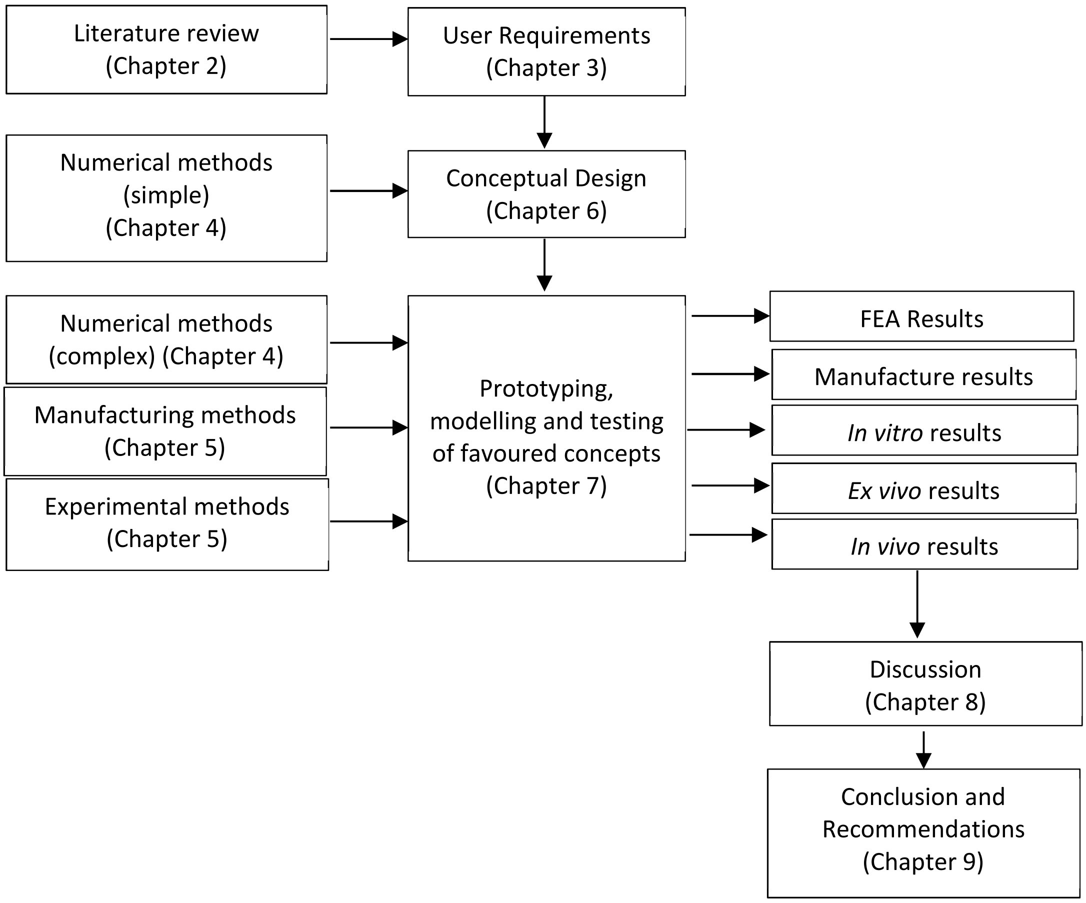

Figure 1-2. Flowchart of thesis

2 Literature Review

2.1 Anatomy and Physiology of the Heart

The human heart is a four-chambered muscular pump that circulates blood around the body (Fuster, O'Rourke, & Walsh, 2007). Referring to Figure 2-1, deoxygenated blood (blue arrows) from the venous system returns to the right atrium of the heart, where it is pumped through the tricuspid valve into the right ventricle. The blood is then ejected by the right ventricle through the pulmonary valve and then through the lungs, where oxygen is absorbed and carbon dioxide is released. The newly oxygenated blood (red arrows) travels to the left atrium, where it is pumped into the left ventricle through the mitral valve. The blood is then ejected, by the contraction of the left ventricle, through the aortic valve to provide the body with oxygenated blood. The purpose of the four heart valves is to control the direction of blood flow, allowing forward flow and preventing backward flow (Yoganathan, Lemmon, & Ellis, 2000).

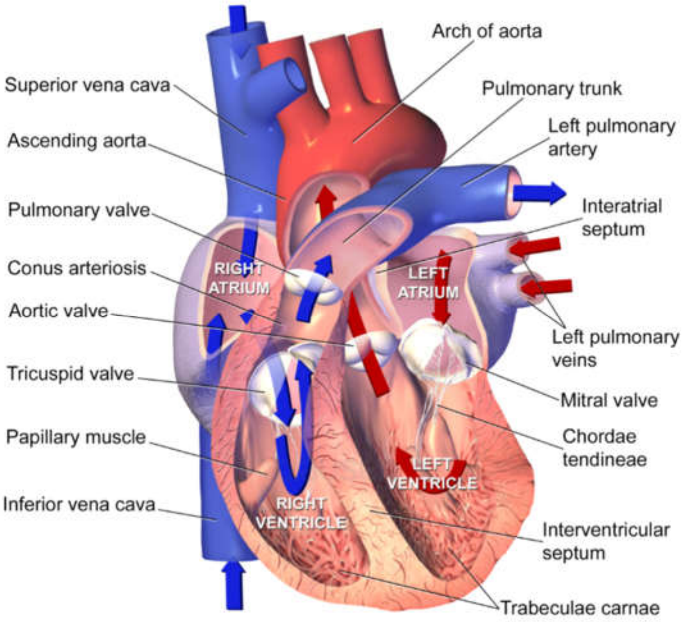

Figure 2-1. Sectional anatomy of the heart[1]

Immediately prior to contraction of the left ventricle, the mitral valve is open and the aortic valve is closed; the blood pressure in the left atrium and the left ventricle are therefore similar. As the left ventricle begins to contract, the pressure in the left ventricle rises rapidly and the mitral valve begins

---

[1] "Blausen 0457 Heart Sectional Anatomy" by Blausen Medical Communications, Inc. - Donated via OTRS, see ticket for details. Licensed under CC BY 3.0 via Wikimedia Commons - http://commons.wikimedia.org/wiki/ File:Blausen_0457_Heart_ Sectional Anatomy.png

to close. When the pressure in the left ventricle reaches the aortic pressure, the aortic valve opens. The aortic and ventricular pressures continue to rise together as the rate at which blood is ejected from the ventricle is greater than the rate at which the blood is delivered to the arterial branches. Towards the end of the ventricular contraction phase, aortic and ventricular pressures drop gradually, and the aortic valve leaflets begin to close just before ventricular relaxation. After the aortic valve closes, the ventricular pressure drops rapidly until the pressure in the ventricle is lower than the pressure in the left atrium and the mitral valve opens, allowing the ventricle to fill with oxygenated blood from the atrium. Near the end of ventricular systole, the pressure in the atrium and ventricle rise briefly due to atrial contraction, and the cardiac cycle repeats (Katz, 2010).

2.2 Functional Anatomy of the Aortic Root

The anatomy of aortic valve and associated structures has been described for centuries, originating during the Renaissance, with sketches and descriptions by Leonardo da Vinci, and interest was renewed during the development of surgical aortic valve replacement (SAVR). Recently, interest in the anatomy of the aortic valve has been stimulated by the development of TAVR and the required understanding of anatomic factors relevant to the performance of these devices (Anderson, Becker, & Piazza, 2009; Piazza et al., 2008; Schubert & Ghanta, 2016). Knowledge of the anatomy is important in the development of replacement valves that must be positioned within the anatomy.

The aortic root, illustrated in Figure 2-2, starts as a continuation of the left ventricular outflow tract (LVOT), at the base of the leaflets, ends at the sinotubular junction (STJ), and incorporates the three aortic valve leaflets and the sinus of Valsalva (SoV) (Piazza et al., 2008). The bulbous SoV creates vortices to aid in valve closure, prevents the valve leaflets from contacting the aortic wall and reduces leaflet stresses by allowing smooth leaflet closure (Katayama, Umetani, Sugiura, & Hisada, 2008). The coronary arteries usually arise from the two anterior SoV. The plane through the base of each leaflet attachment site (the basal ring) is typically referred to as the aortic annulus. The aortic annulus, however, rather than being a circular ring, is crown-shaped (Anderson, 1991), as can be seen in Figure 2-2. Similarly, the intersection of the tubular aorta and the bulbous SoV means that the STJ is also scallop-shaped rather than circular. Significantly for TAVR design, at the level of the basal ring, two-thirds of the circumference of the aortic root is muscular (part of the ventricular septum) while the remaining third is the fibrous continuity between the aortic valve and the mitral valve, as shown in Figure 2-4.

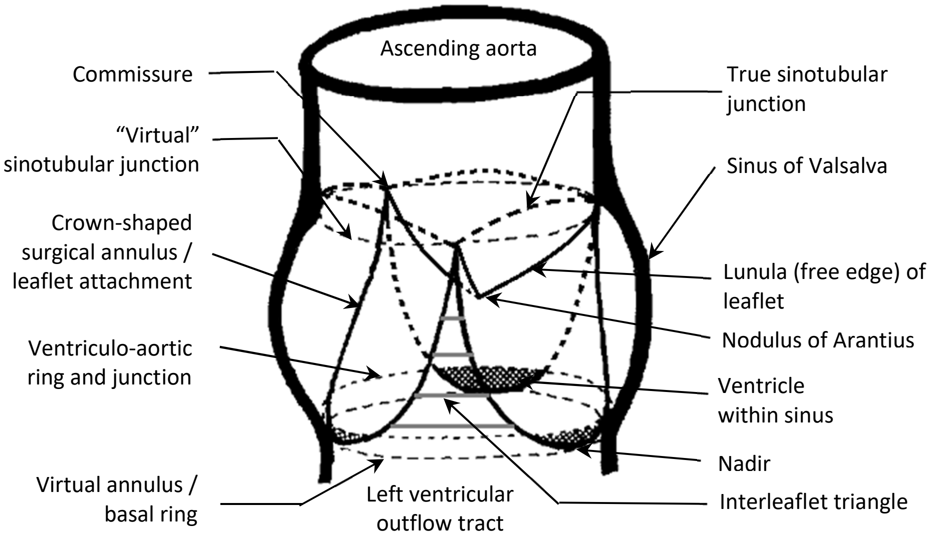

Figure 2-2. Schematic of aortic root, adapted from Sutton, Ho, and Anderson (1995)

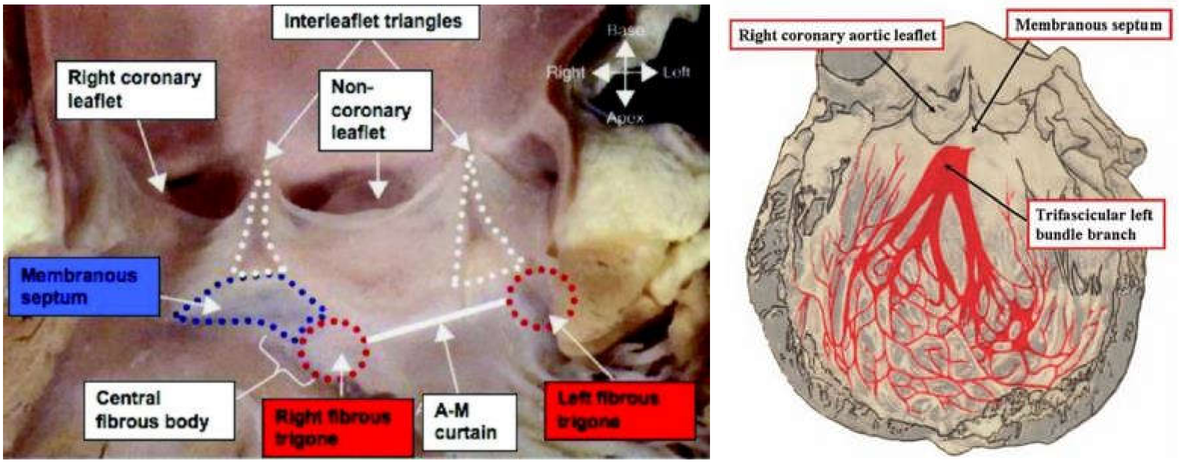

Figure 2-3. Image of the aortic root opened from the left ventricle (left) showing fibrous continuities between interleaflet triangles, the fibrous trigones, and the membranous septum, and a schematic (right) showing the relations of the atrioventricular conduction system with respect to the aortic valve leaflets, from Piazza et al. (2008)

The basal attachment sites of the leaflets to the wall are below the level of the ventriculo-aortic junction (VAJ), the termination of the ventricular myocardium and the start of the aorta (Anderson, 2000; Piazza et al., 2008) . De Kerchove et al. (2015) examined the anatomy of 58 fresh human aortic roots and identified that the VAJ is above the basal ring in the area around the right coronary cusp, from the nadir of the left coronary cusp to the nadir of the non-coronary cusp. Specifically the VAJ was 4.6 ± 1.4 mm above the basal ring at the left coronary/right coronary commissure and 2.5 ± 1.6 mm above the basal ring at the right coronary/non-coronary commissure, as shown in Figure 2-5.

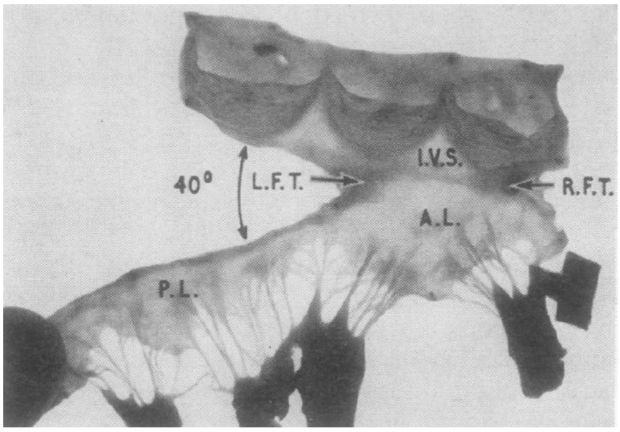

Figure 2-4. Opened-out mitral and aortic valves, from Du Plessis and Marchand (1964). (A.L. – Anterior Mitral Leaflet; I.V.S – Intervalvular Space; L.F.T. – Left Fibrous Trigone; R.F.T. – Right Fibrous Trigone; P.L. – Posterior Mitral Leaflet).

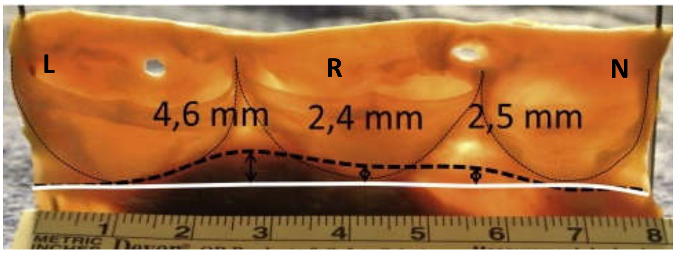

Figure 2-5. View of an aortic root opened longitudinally, showing the basal ring (white line) and the VAJ (black dashed line), from De Kerchove et al. (2015). (L – Left coronary cusp; R – Right coronary cusp; N – Non-coronary cusp)

Aortic root thickness was measured at the level of the basal ring and found to vary from 1 ± 0 mm at the left coronary/non-coronary commissure to 6.2 ± 1.2 mm at the right coronary cusp. The fact that the bases of the leaflets lie below the level of the VAJ is also demonstrated clearly in histological sections through the aortic valvar complex, as shown in Figure 2-6 (Piazza et al., 2008). The leaflets have a three-layered fibrous core (the layers are the collagenous Fibrosa, the gel-like Spongiosa and the elastic Ventricularis) and are lined with endothelial cells. The aortic valve therefore does not have a true structural annulus. It is useful at various times to refer the basal ring or virtual ring/annulus (the plane through the nadirs of the leaflet hinges), surgical annulus (the leaflet attachment margin) and the VAJ. The functional anatomy of the aortic valve cannot be understood in isolation, as the aortic valve is the centrepiece of a fibrous scaffold known as the cardiac skeleton, and is positioned between the mitral, tricuspid and pulmonary valves (Bateman, Quill, Hill, & Iaizzo, 2013).

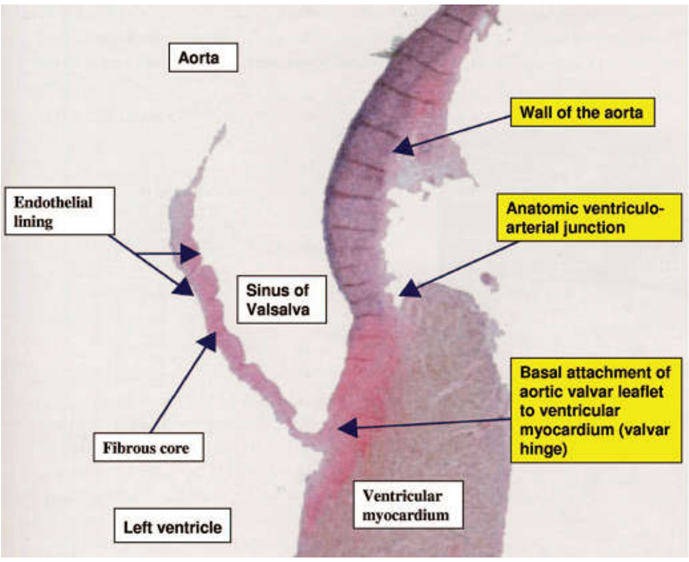

Figure 2-6. Histology of the aortic valvar complex (Piazza et al., 2008)

.

Unlike the right ventricle, which has a tubular muscular outflow tract (infundibulum) and therefore has a muscular boundary between the pulmonary and tricuspid valves known as the ventriculo-infundibular fold (S. Y. Ho & Nihoyannopoulos, 2006), the aortic valve and mitral valve are intimately involved and are both essentially part of a single aorto-mitral orifice. Fibrous tissue extends between the aortic and mitral valves to form the aorto-mitral curtain (see Figure 2-4). The extremities of the fibrous curtain are thickened to form the left and right fibrous trigones, which support the curtain within the base of the left ventricle. The right fibrous trigone is continuous with the membranous septum and together they form part of the central fibrous body, the strongest part of the cardiac skeleton.

Various authors have tried to quantify aortic valve compliance. Swanson and Clark (1974) determined the response of the aortic root to pressure by filling cadaveric human aortic roots with silicone rubber and allowing to cure while under pressure. They found that the valve diameter increased by a mean of approximately 10% over a pressure change of 100 mmHg, but there was very large variation between specimens. One of the specimens had 18% compliance over a 60 mmHg pressure change. Such cadaveric studies are limited by the fact that samples are not tested fresh, and the aortic root is excised from the heart, meaning that the influence of other structures in the heart is not considered. A better determination of valve diameter may be obtained using modern imaging techniques, as true *in situ* measurements can be made. Multi-detector Computed Tomography (MDCT) has the best agreement with surgical measurements compared to echocardiography and contrast angiography (Litmanovich et al., 2014; Tsuneyoshi, Komiya, & Shimamoto, 2016; Yano et al., 2012), and is considered the gold standard.

Changes in diameter between systole and diastole (i.e. compliance) were evaluated using MDCT by de Heer et al. (2011), who found that the mean diameter of the basal ring was 27.1mm and 27.4mm in diastole and systole, respectively (1% increase, not statistically significant), with a mean difference between the maximum and minimum diameters of 6.0 ± 2.6 mm in diastole and 4.6 ± 2.5 mm in systole. This demonstrates that the basal ring is oval over the entire heart cycle but becomes more circular during systole. The mean diameter of the STJ changed from 30.5mm in diastole to 31.2mm in systole. It is worth noting that the unpressurised “surgical” STJ has a diameter approximately 90% of the virtual annulus (Kunzelman, Grande, David, Cochran, & Verrier, 1994). Hamdan et al. (2012) also found using MDCT that perimeter increased by the small but significant ($p=0.01$) amount of 2.2% in normal patients despite a cross-sectional area increase of 11.2 ± 5.4%. They conclude that the increase in aortic valve area is almost entirely due to changes in annular shape rather than stretch. This finding is in sharp contrast to the reports of Blanke et al. (2012), who measured a change in perimeter-derived diameter of 7.3 ± 2.1% even though all patients had severe aortic stenosis. The authors speculate that the differences in measurement are a result of a two-fold improvement in both temporal resolution and sampling rate of the CT protocol, and the fact that the maximum perimeter does not necessarily occur at the same instant as maximum area. Differences between diameter measurements across CT studies may also be due to poor standardisation and different smoothing functions across MDCT systems (Tsuneyoshi et al., 2016). Due to the changing shape of the aortic annulus, traditional 2D echocardiography using a standard long-axis parasternal view does not lead to accurate annulus sizing.

Table 2-1. Aortic root measurements of normal patients from 3D TOE, from Calleja et al. (2013), in mm

Leaflet

	Left	**Non**	**Right**
Leaflet ICD	21.3±1.7	22.8±1.7	21.8±2.1
Leaflet Free Edge Length	30.6±2.4	32.2±2.3	31.6±2.7
Leaflet height	14.9±1.2	15.8±1.3	14.4±1.6

Annulus-leaflet-ostia

	Left	**Right**
Annulus-commissure	17.2±1.5	18.6±1.5
Annulus-ostia	13.3±1.8	14.8±1.9
Leaflet-ostia	11.3±2.1	11.6±2.4

Annulus-STJ-SoV

	Annulus	**STJ**	**SoV**
Diameters	24.2±1.9	25.3±2.0	30.2±2.7

The normal aortic root is slightly asymmetrical, with the left cusp being the smallest. Some discrepancies exist between measurements from surgery and from imaging. Berdajs, Lajos, and Turina (2002) found using surgical measurements that inter-commissural distance (ICD) was largest for the right coronary cusp, intermediate for the non-coronary cusp and smallest for the left coronary cusp (ratio of 1.08:1:0.87). Similarly the right sinus height was the largest, followed by the non- and left coronary sinus (ratio: 1.10:1:0.99). Calleja et al. (2013) however measured ICD from 3D Transoesophageal Echocardiography (TOE) to be largest for the non-coronary cusp (relative ratio 0.96:1.0:0.93 for right:non:left). The dynamic behaviour of the valve is also asymmetric, and this asymmetry is considered to have an important haemodynamic role by decreasing the tilt angle of the aortic root during ventricular ejection (Loukas et al., 2014). Several key measurements of the aortic root from Calleja et al. (2013) are shown in Table 2-1.

The conduction system of the heart is also closely associated with the aortic valve (Anderson, Yanni, Boyett, Chandler, & Dobrzynski, 2009). The atrioventricular (AV) node is situated in the triangle of Koch within the right atrium and is positioned close to the membranous septum on the ventricular part of the interleaflet triangle between the right coronary and the non-coronary leaflets, as shown in Figure 2-3. The bundle of His conducts electrical impulses from the AV node to the apex of the heart through left and right bundle branches, which run within the ventricular septum. The left bundle branch (LBB) runs superficially along the left ventricular septum from just below the membranous septum. The His bundle is positioned approximately 6 mm below the basal plane, while the LBB may be found 12mm below the valve (Atkinson, Kharche, Bateman, Iaizzo, & Dobrzynski, 2016). This has important implications for TAVR valves that have ventricular components because the lower the replacement valve is implanted in the LVOT the more likely damage will occur to the conductive tissues, which may cause heart block or rhythm abnormalities.

The mean heights of the coronary arteries above the basal plane are approximately 13-15mm and 15-17mm for the left and right coronary arteries, respectively (Calleja et al., 2013; Knight et al., 2009; Tops et al., 2008). Coronary height can vary dramatically; Knight et al. (2009) measured a range of 9.8mm to 29.3mm for the left coronary ostium and 10.4mm to 28.5mm for the right coronary ostium. The behaviour of the aortic root is complex, with parts of the root dilating and tilting over the cardiac cycle (Loukas et al., 2014). Functionally, healthy aortic valve leaflets open rapidly during ventricular ejection, and are viewed as thin parallel lines in a long-axis transthoracic echocardiography (TTE) view, close to the wall of the aorta (Tilea et al., 2013). As the aortic root dilates during the ventricular filling part of systole, the commissures are pulled outwards, straightening the free edges of the leaflets and creating an orifice that is triangular rather than circular, as illustrated in Figure 2-7. The leaflets begin to close at the end of systole due to vortices created behind the leaflets within the SoV, and close fully during diastole (completion of ventricular filling). When the valve is closed, the leaflets are concave and the free edges of the leaflets, or lunulae, overlap to form a region of coaptation that prevents aortic regurgitation. A fibrous thickening of the free edge at the midpoint, known as the Nodulus of Arantius aids in the prevention of regurgitation.

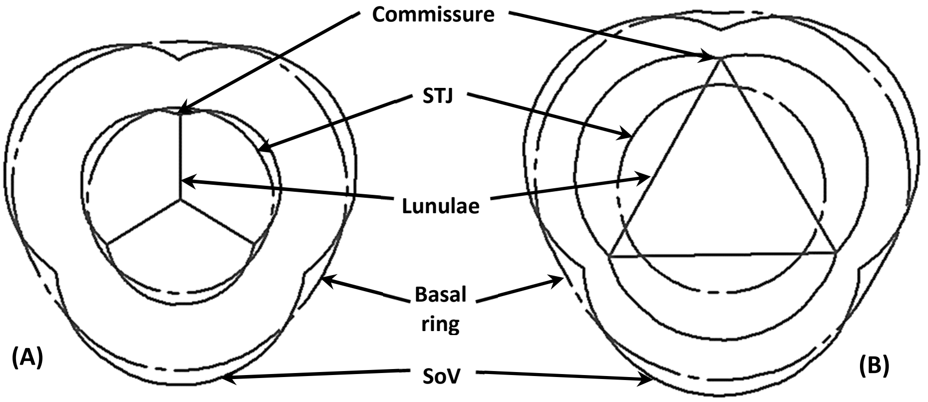

Figure 2-7. Relative cross-sectional schematic of the aortic root: (A) End diastole; (B) During ejection, at maximum dilation. Adapted from Lansac et al. (2002)

The ascending aorta is tilted with respect to the left ventricle. Buzzatti et al. (2013) found using MDCT that the long axes of the aortic root and the LVOT are at an angle of 22.3 ± 10.3° to each other. The plane of the STJ lies at an angle of 5 to 11° to the aortic valve basal plane due to the different sizes of the sinuses (of Valsalva) (Berdajs et al., 2002; Siew Yen Ho, 2009; Labrosse, Beller, Robicsek, & Thubrikar, 2006).

Aortic valve diameter increases steadily with age. In combined autopsy studies involving 965 normal hearts, Kitzman, Scholz, Hagen, Ilstrup, and Edwards (1988) and Scholz, Kitzman, Hagen, Ilstrup, and Edwards (1988) found that mean aortic valve circumference increases from birth until death. Aortic valve circumference increases exponentially from 24 mm at 1 year of age to 52 mm at age 20 (corresponds to equivalent circle diameters of 8 mm and 17 mm, respectively), and from 57/60mm (women/men) in the third decade of life to 79/85mm (women/men) in the tenth decade (equivalent diameters of 18/19mm and 25/27mm, respectively). In contrast the three other heart valves increase initially and decrease in the fifth to seventh decades of life, but this apparent decrease in size disappears when valve circumference is indexed for body surface area. During valve closure, the aortic valve experiences a transvalvular pressure gradient of 80mmHg to 120mmHg, which acts normal to the leaflet surface and results in leaflet stretch and a large area of coaptation. During valve opening the valve experiences fluid shear stresses, and over the complete heart cycle the leaflets experience a complete curvature reversal, resulting in the development of bending stresses (Balachandran, Sucosky, & Yoganathan, 2011).

2.3 Rheumatic Heart Disease

RHD is a valvular heart disease caused by one or more attacks of acute rheumatic fever (ARF). The bacterium responsible for the infection is *Streptococcus pyogenes*. The pathophysiology of ARF involves a combination of three factors, namely a rheumatogenic streptococcal strain, an individual with a genetic predisposition to the disorder and an abnormal immune response to the infection (Marijon, Mirabel, Celermajer, & Jouven, 2012). Central to the abnormal immune response is similarity between proteins on the surface of the bacterium and various cardiac proteins (antigen mimicry). An autoimmune reaction ensues in the heart, where antibodies generated as part of the immunological response to the pathogen cross-react with the cardiac proteins (Root-Bernstein, 2014). ARF typically occurs approximately three weeks after infection, which is usually pharyngitis, and can affect the skin, the large joints, the heart and the brain. When ARF leads to persistent heart valve damage, it is known as RHD. Serious complications of RHD include atrial fibrillation, infective endocarditis, stroke, pregnancy-related problems and heart failure (Remenyi et al., 2016). The first attack of ARF usually occurs in children between the ages of 5 and 15, while RHD is most prevalent amongst 25-45 year olds. RHD is firstly a disease of the mitral valve, and the occurrence of clinically isolated rheumatic aortic valve disease is rare (Nkoke et al., 2016). It has been reported that the aortic valve is never affected *anatomically* in RHD without also affecting the mitral valve *anatomically* (William C. Roberts, 1970; William Clifford Roberts & Ko, 2008).[2] The first two to three decades of life are primarily associated with mitral disease (first pure regurgitation, then mixed mitral disease and subsequently mitral stenosis). The involvement of other valves (in particular the aortic valve) increases with age (Remenyi et al., 2016).

A recent global study of RHD, the REMEDY study (Zühlke et al., 2015), has demonstrated that RHD is a seriously neglected disorder in the developing world. Although a thorough prevention program requires education and surveillance programs, primary medical prevention of RHD involves preventing the first attack of ARF, and is achieved through treatment of suspected streptococcal sore throat using penicillin or other appropriate antibiotics (Gerber et al., 2009). Secondary prevention (which aims to prevent recurrent bouts of ARF in patients who have documented RHD or who have had a previous attack of ARF) is achieved through continuous administration of prophylactic antibiotics (WHO, 2004). There is however no proven medical therapy that can alter the course of severe rheumatic aortic valve disease, and cardiac surgery is a life-saving intervention (Remenyi et al., 2016).

---

[2] The mitral valve may however function normally or the disease may not be clinically significant while the aortic valve is significantly affected. In this way a patient may present with aortic stenosis in the absence of mitral valve problems.

2.4 The Aortic Valve in Disease

Aortic valve disease falls into three major categories: degenerative, congenital or rheumatic. Congenital heart valve disease is usually related to the presence of a bicuspid valve. Figure 2-8 shows images of normal, bicuspid AS, tricuspid AS and rheumatic aortic valves. Although bicuspid valves are present in only 1-2% of the population, it is the most frequent indication for aortic valve replacement in individuals under 70 years of age in the developed world (Anderson, Becker, et al., 2009).

Calcific degenerative aortic valve disease is associated with age and risk factor-related calcification of the heart valve leaflets and the annulus. In contrast, rheumatic valves are characterised by fibrosis, fusion of the leaflets at the commissures and along the zone of coaptation, and leaflet thickening. A loss of height of the cusps and commissures occurs in the early phases of the disease, but as the disease progresses scarring occurs together with cusp retraction (Matsumura et al., 2002; Waller et al., 1991).

In the case of rheumatic aortic regurgitation (AR), the leaflet retraction and stiffening associated with leaflet thickening causes central regurgitation because leaflets are prevented from closing fully during diastole. Although calcification is frequently present in the leaflets of patients with rheumatic AR, calcification may be absent (Myers et al., 2010). Figure 2-9 shows an image of excised calcific tricuspid and bicuspid aortic valves and a tricuspid rheumatic aortic valve, which clearly show the penetration of calcium deposits through leaflet thickness, while in rheumatic valves the commissural fusion can be pronounced with much less calcium deposition.

In rheumatic AS, commissural fusion and calcification cause a central triangular or “fish-mouth” narrowing. Since commissural fusion and leaflet thickening can affect valve area during systole and prevent tight valve closure during diastole, mixed AS and AR are common in RHD. For degenerative calcific AS, calcification starts at the regions of maximum flexion, the base of the leaflets, and progresses into the Sinus of Valsalva (Anderson, Becker, et al., 2009). In rheumatic AS, however, calcium localisation tends to be more diffuse (Wallby, Steffensen, Jonasson, & Broqvist, 2013).

The aortic root remodels longitudinally in patients with calcific aortic stenosis. Akhtar et al. (2009) showed that the heights of the left and right coronary arteries were 2.2mm and 1.6mm lower, respectively, in patients with calcific aortic stenosis compared to age-matched controls, and similarly the height of the sinotubular junction above the virtual annulus was lower in calcific stenosis than in controls (16.7 ± 2.0mm vs. 21.0 ± 2.3 mm). Free edge length of the leaflets was reduced by approximately 4mm in AS, while the effective height of the leaflets, defined as the distance from the annulus to the leaflet tip, was increased in AS patients by approximately 2mm. Annulus diameter did not differ significantly between AS and normal groups. These findings are in agreement with a more recent study by Calleja et al. (2013), who also found that the distance from the annulus to the commissures was 1.5 to 1.8 mm smaller in AS than controls. STJ and SoV diameters were not statistically different between AS and normal patients.

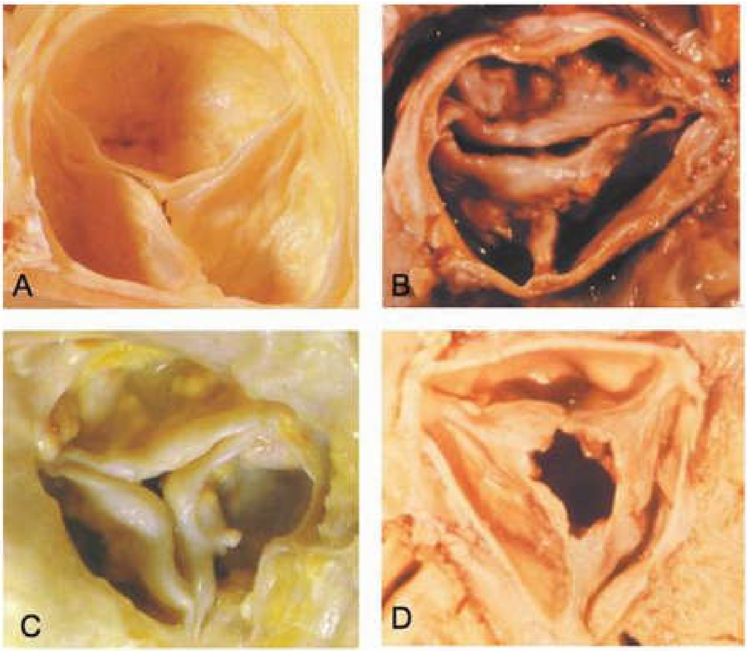

Figure 2-8. A) Normal trileaflet aortic valve, B) Stenotic calcified bicuspid aortic valve, C) Calcified (degenerative) trileaflet aortic valve, D) Thickened leaflets and commissural fusion associated with Rheumatic aortic valve disease, from Anderson, Becker, et al. (2009)

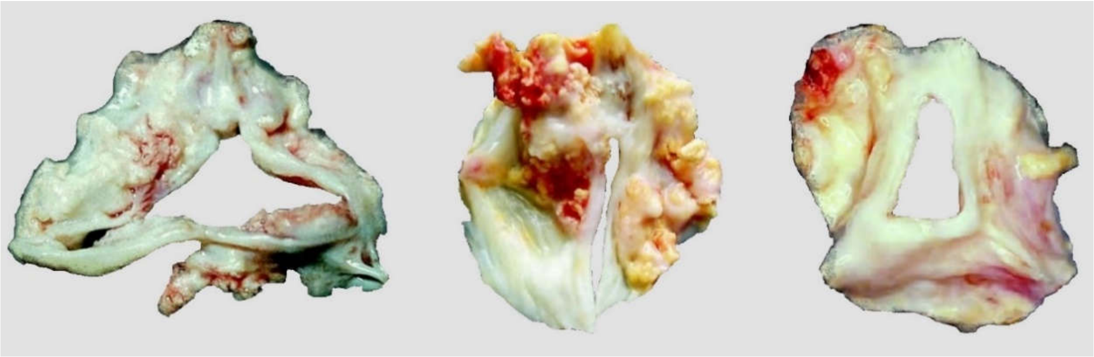

Figure 2-9. Excised diseased valves. A) Calcified (degenerative) trileaflet aortic valve, B) Calcified bileaflet aortic valve and C) Rheumatic aortic valve, from http://www.cthsurgery.com/aetiology-of-aortic-valve-stenosis.html.

As with normal patients, patients with AS have oval annuli (Tops et al., 2008). Buellesfeld et al. (2013) also found that the ovality was significantly more pronounced in the LVOT than in the annulus. They also showed that perimeter-derived diameters of the annulus, LVOT and SoV, as well as coronary ostia heights, were greater in men than in women, while ascending aorta diameter was similar between the sexes. In contrast to patients with AS, Calleja et al. (2013) found a significant increase in annulus diameter for patients with dilated aortic roots (for those with AR the average annulus diameter was

31.3 ± 3.8 mm vs. 24.2 ± 1.9 mm for controls). In the patients, ICD, leaflet length and leaflet height were higher in all leaflets compared to controls.

Compliance is reduced in calcified valves. Hamdan et al. (2012) found that calcified valves experience a change in cross-sectional area of 6.2 ± 4.8% from diastole to systole, but in these patients there was a negligible change in perimeter (0.56 ± 0.85%). Several authors have evaluated valve compliance from pre-TAVR CT scans. Jilaihawi et al. (2012) found that perimeter-derived diameter increased from 23.8 ± 2.4 mm to 24.7 ± 2.5 mm (3.8%, $p<0.001$) and mean diameter increased from 23.3 ± 2.3 mm to 24.2 ± 2.6 mm over the heart cycle (3.9%, $p<0.001$). Figini et al. (2015) similarly reported an increase in perimeter-derived diameter of 2.7%, from 23.9 ± 1.83 mm to 24.5 ± 1.85 mm, $p<0.001$. Shibayama et al. (2014) reported comparable compliance of 1.9% for tricuspid aortic valves using TOE. Blanke et al. (2012) found an increase in perimeter of 7.3 ± 2.1% from CT scans, and they attribute these higher values to a higher resolution and sampling rate of their scans. von Aspern et al. (2015), however, reported only 0.9% change in perimeter-derived diameter (24.5 ± 3 to 24.7 ± 3) in pre-TAVR CT scans despite also using dual-source 128-row MSCT; in fact all patients showed less than 2mm difference between diastolic and systolic measurements.

No published literature could be found relating to the compliance behaviour of aortic valves in patients with non-calcific aortic valve disease or RHD. Since rheumatic aortic disease is not associated with focal calcium in the annulus or sinus of Valsalva, the rheumatic aortic root may be more compliant than the degenerative calcific aortic root, although no literature has yet been found to verify this. Furthermore, as rheumatic aortic valves are associated with cusp fusion, they may be more suited to balloon-expandable valve implantation due to the ability for the balloon to perform a commissurotomy during implantation (Remenyi et al., 2016), as mitral valves with commissural fusion have been shown to benefit from balloon commissurotomy (Bouleti et al., 2012)

2.5 Heart Valve Replacement

2.5.1 Surgical Valve Replacement

Since the first successful mitral valve replacement was performed in 1960, surgical heart valve replacement has become a routine procedure, with more than 300 000 procedures performed globally every year (Mohammadi & Mequanint, 2011). Two different types of surgical heart valves are currently implanted, namely mechanical heart valves (MHVs) and biological heart valves (BHVs), examples of which are shown in Figure 2-10 and Figure 2-11, respectively. MHVs are constructed entirely from synthetic materials, and although many different designs have been attempted, the most frequently implanted types are tilting-disc and bileaflet valves. MHVs are very robust and durable, but require lifelong anti-coagulation (Abu-Omar & Ratnatunga, 2007). An inexpensive tilting-disc valve called the Chitra valve has been produced and is widely implanted in India (P. Kumar et al., 2004). BHVs incorporate material of biological origin and are either stentless or stented. Stented valves, usually constructed from porcine roots or bovine pericardium, incorporate a support frame and sewing ring, and animal tissues that are chemically treated to reduce antigenicity and calcification. Stentless valves do not have a rigid sewing ring or support frame and include hetero-grafts (from non-human animal), homografts (from another human) or autografts (from the same patient). BHVs have a limited lifespan but do not require lifelong anticoagulation (G. Hoffmann, Lutter, & Cremer, 2008); BHVs are therefore typically chosen if anticoagulation is contraindicated in the patient, if anticoagulation is unavailable, if the patient is unlikely to be compliant on anticoagulation or in patients with life expectancy shorter than the expected durability of the valve (Abu-Omar & Ratnatunga, 2007).

Figure 2-10. Medtronic Hall™ Tilting disc valve, Edwards MIRA™ bileaflet valve (Abu-Omar & Ratnatunga, 2007), and TTK Chitra™ valve (Walters, 2015) (left to right)

Figure 2-11. Carpentier-Edwards Perimount™ pericardial valve and Edwards Prima Plus™ stentless bioprosthesis (Abu-Omar & Ratnatunga, 2007)

2.5.2 Transcatheter Aortic Valve Replacement (TAVR)

TAVR represents the culmination of many developments in cardiac surgery, catheter-based intervention techniques and equipment design from the first surgical aortic valve dilation in 1912 to the first human TAVR in 2002. The history of significant events leading to the first human TAVR is presented in Table 2-2. Andersen, Knudsen, and Hasenkam (1992) were the first to describe the percutaneous implantation of an aortic valve as a closed-chest minimally-invasive alternative to surgical valve replacement. The first percutaneous implantation of a replacement valve in humans was performed by Bonhoeffer et al. (2000), who implanted pulmonary valves in children. The first human TAVR was performed by Alain Cribier et al. (2002) in an inoperable patient with severe AS. TAVR valves are compressed to a low profile for catheter-based insertion into the patient's native aortic valve position using antegrade or retrograde approaches, and are deployed (or allowed to deploy) to their operating shape within the diseased native valve, forcing the diseased native cusps (leaflets) against the aortic wall. Figure 2-12 shows an image of a transcatheter aortic heart valve inflated on a balloon and an illustration of the same valve being deployed inside the native aortic valve using an antegrade transapical technique.

Table 2-2. History of significant developments leading up to percutaneous aortic valve implantation

Year	Event
1912	Tuffier performs first aortic valve dilation by invaginating the aortic wall using his forefinger and pushing the wall through the diseased valve (Dhaval, 2010).
1923	Cutler performs first successful surgical mitral valve repair (Bland, 1952)
1941	Cournand and Richards perform the first diagnostic cardiac catheterisation (Mueller & Sanborn, 1995).
1948	Bailey performs the first mitral commissurotomy, using a knife with a curved blade (C. P. Bailey, 1949)
1950	First aortic commissurotomy, with a dilator instrument (C. P. Bailey, Bolton, Jamison, & Nichols, 1954)
1952	Gibbon performs first successful open heart surgery using a cardiopulmonary bypass machine (Cohn, 2003)
1952	Hufnagel implants first mechanical valve in the descending aorta (Butany et al., 2002)
1953	First transaortic approach to commissurotomy (C. P. Bailey et al., 1954).
1953	Seldinger technique developed for percutaneous interventional procedures (Seldinger, 1953)
1960	Braunwald performs first mitral valve replacement, using a polyurethane valve with Teflon chordae tendinae (Braunwald, 1989)
1960	Harken et al. (1960) perform the first successful surgical aortic valve replacement, with a mechanical valve.
1960	Rohman, Goetz and team perform the first successful coronary artery bypass surgery (Dee, 2003)
1962	Ross (1962) performs first aortic homograft valve replacement
1964	Duran performs first porcine aortic valve replacement (Shumacker, 1992)
1965	Davies (1965) describes the first use of a catheter-mounted, polymeric, valve
1967	First transfemoral coronary angiography performed using special catheters (Judkins, 1967)
1971	Ionescu performs the first implantation of a stented chemically treated bovine pericardial valve (Ionescu, Pakrashi, Holden, Mary, & Wooler, 1972)
1985	Cribier performs the first adult balloon aortic valvuloplasty in adults (Alain Cribier, 2012)
1989	First balloon-expandable aortic valve implanted into pigs by Andersen et al. (1992)
2000	First percutaneous implantation of replacement valves in humans by Bonhoeffer et al. (2000); a bovine jugular vein was attached to a platinum-iridium stent and implanted into the right ventricle to pulmonary artery conduits of children
2002	First human implantation of a percutaneous aortic valve by Alain Cribier et al. (2002)

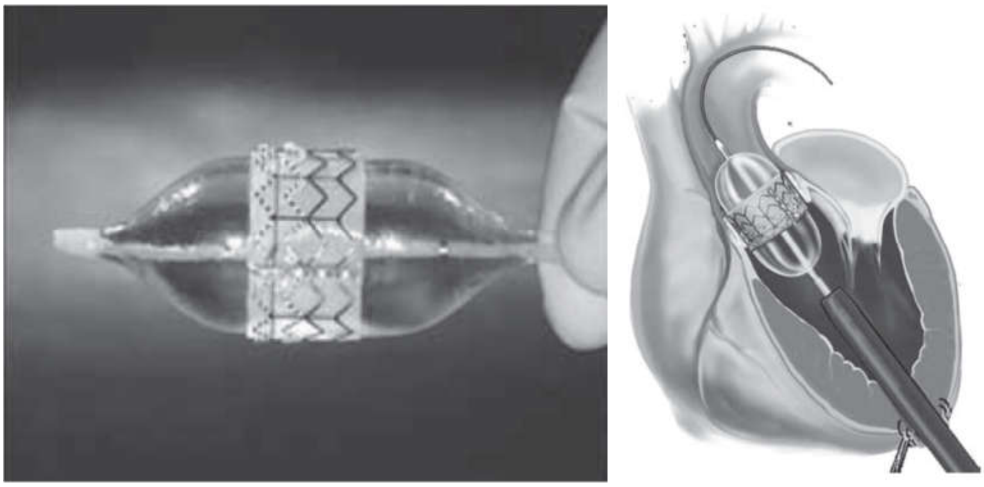

Figure 2-12. Edwards Lifesciences Sapien THV™, deployed on balloon and illustrated antegrade implantation through the left ventricular apex (Chiam & Chao, 2013)

The first commercially available TAVR devices, both of which received European certification in 2007, were the Edwards Sapien THV™, consisting of a tri-leaflet bovine pericardial valve mounted on a balloon-expandable stainless steel stent, and the Medtronic CoreValve™, consisting of a tri-leaflet porcine pericardial valve mounted on a self-expanding Nitinol frame. Today many devices have received the CE mark and many more are in development (Weiss et al., 2015). A list of CE-marked valves is shown in Table 2-3. Non-CE marked balloon-expandable valves are listed in Table 2-4. A list of polymeric transcatheter valves (historical and in development) is provided in Table 2-5. A comprehensive list of all valves known to the author is provided in Appendix A.

There are also isolated reports of devices being used to treat aortic insufficiency (Cholteesupachai, Franzen, & Sondergaard, 2014; Dumonteil, Marcheix, Lairez, & Laborde, 2013; Franzone et al., 2016; Hildebrandt, Erbel, & Kahlert, 2013; Wei et al., 2015), including rheumatic aortic insufficiency (Ducrocq, Himbert, Hvass, & Vahanian, 2010), and the devices have been used for rheumatic AS (Akujuo, Dellis, Britton, & Bennett, 2015; Bilge, Saatci Yasar, Alemdar, & Ali, 2014; Daly et al., 2015), but these are off-label uses for most devices. It is interesting to note that during early animal trials of the Cribier-Edwards™ valve that more than 30% of valves migrated in the non-calcific aortic annulus (Dewey et al., 2006). Subsequent animal models required a modified Cosgrove™ annuloplasty ring to be stitched into the aortic root to eliminate stent migration (Edwards, 2015).

Table 2-3. CE Marked TAVR devices (Bourantas & Serruys, 2014; Rozeik, Wheatley, & Gourlay, 2014; Taramasso et al., 2014; Weiss et al., 2015; Wiegerinck, Van Kesteren, Van Mourik, Vis, & Baan, 2016)

	Device name	**Stent**	**Leaflet/(skirt) material**
	Edwards SAPIEN THV™ (Edwards Lifesciences)	Stainless steel	Bovine pericardium/(PET)
	Edwards SAPIEN XT™ (Edwards Lifesciences)	Co-Cr (MP35N)	Bovine pericardium/(PET)
	Edwards SAPIEN 3™ (Edwards Lifesciences)	Co-Cr (MP35N)	Bovine pericardium/(PET)
	CoreValve™ (Medtronic)	Nitinol	Porcine pericardium/ (porcine pericardium)
	CoreValve Evolut™ (Medtronic)	Nitinol	Porcine pericardium/ (porcine pericardium)
	Direct Flow™ (Direct Flow Medical, Santa Rosa)	PET, inflatable	Bovine pericardium/ (Polyester)
	Edwards Centera™ (Edwards Lifesciences)	Nitinol	Bovine pericardium/ (Polyester)
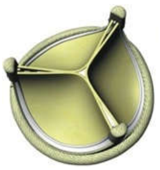	Vanguard II (ValveX change)	Nitinol	Bovine pericardium
	Inovare (Braille Biomedica)	Co-Cr	Bovine pericardium/(Polyester)

	Device name	**Stent**	**Leaflet/(skirt) material**
	Portico™ (St Jude)	Nitinol	Bovine pericardium/ (porcine pericardium)
	Lotus™ (Boston Scientific)	Nitinol	Bovine pericardium/ (poly urethane)
	Acurate TA™ (Symetis)	Nitinol	Porcine root/ (porcine pericardium)
	Acurate NEO TF™ (Symetis)	Nitinol	Porcine pericardium/ (porcine pericardium)
	JenaValve™ (JenaValve Technologies)	Nitinol	Porcine root/(porcine pericardium)
	Engager™ (Medtronic)	Nitinol	Bovine, Pericardial/ (polyester)
	Colibri™ (Colibri Heart Valve)	Stainless steel	Porcine pericardium
	Trinity Flexx™ (Transcatheter Technologies)	Nitinol	Bovine pericardium
	Aortx (Hansen Medical Inc)	Nitinol	Pericardial

Table 2-4. Non-CE-marked balloon-expandable TAVR (Ismail, Hon, Chan, & Leo, 2012; Jamieson, Zhang, & Quijano, 2006; Jilaihawi et al., 2010; Kemp et al., 2013; Leon, 2013; Pontes et al., 2013)

	Device name	**Stent**	**Leaflet/ (skirt) material**		**Device name**	**Stent**	**Leaflet/ (skirt) material**
	MyVal (Meril Cardio-vascular)	Co-Cr	Bovine pericardium (Pericardial/ PET)		Entrata ATS 3F (ATS Medical)	Stainless steel	Equine (Pericardial)
	Stellenbosch University	Co-Cr, BE	Kangaroo	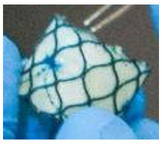	Dura LowPro Valve (Dura Biotech)	Co-Cr	Pericardium

Table 2-5. Polymer TAVR (historical and active) (Bezuidenhout, Williams, & Zilla, 2015)

	Device name	**Stent**	**Leaflet/ (skirt) material**		**Device name**	**Stent**	**Leaflet/ (skirt) material**
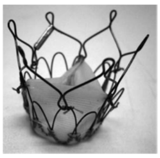	PHV (Stony Brook, Claiborne)	Nitinol	Dacron-reinforced SIBS		Sochman et al.	Nitinol	Poly-urethane tilting disc
	Triskele UCL	Nitinol	POSS-PCU, (POSS-PCU)	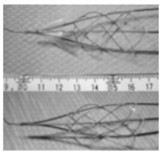	Hashimoto et al. (Tottori University)	Nitinol	Desmorac 4125 (Poly-urethane)
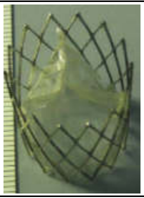	Lutter	Nitinol	Poly-urethane		Zhang et al. (Changhai Hospital)	Co-Cr	PC-coated ePTFE
	University of Iowa	Nitinol	Cellulose and cellulose-silicone composite		Colorado State University	Nitinol	HA/LLDPE

2.5.3 Sutureless and Hybrid Valves

A number of different technologies have been developed to make surgical valve replacement easier and faster, and improve clinical outcomes. Sutureless valves such as the Perceval™ S (Sorin Group, Saluggia) eliminate the need for sutures and therefore reduce the duration of cardiopulmonary bypass and cross-clamping of the aorta. The valves simplify minimally invasive surgical procedures and are particularly appreciated in complex procedures (Phan et al., 2015).

Two-part valves have been developed (by ValveXchange, Inc., Colorado) that comprise a permanent docking station and a replaceable set of leaflets that may be placed and exchanged using minimally invasive techniques (Vesely, 2010). Initially the docking stations were designed to be surgically implantable, but subsequent designs include transapical and transfemoral versions.

2.5.4 Valve Longevity

Mechanical valves are more durable than bioprosthetic valves, with mechanical valves lasting 20-30 years compared to 10-15 years for bioprosthetic valves (Vongpatanasin, Hillis, & Lange, 1996). Bioprosthetic valves are susceptible to calcification, pannus formation or leaflet tearing, and bioprosthetic valve design can dramatically affect long-term valve performance (Vesely, 2003). A landmark randomised trial by Hammermeister et al. (2000) found that all-cause mortality after surgical aortic valve replacement was significantly lower for mechanical valves than bioprosthetic valves (66% versus 79%). This was primarily due to the fact that primary valve failure rates were much higher for bioprosthetic valves; in patients younger than 65 years, 26% of bioprosthetic valves failed while in mechanical valves valve failure was completely absent.

Age is a well-known predictor of bioprosthetic valve failure. As shown in Figure 2-13, freedom from explant for structural valve dysfunction (SVD) is almost 100% in 85 year-old patients, but is only 30% for 25 year old patients (Banbury et al., 2001). Current AHA/ACC guidelines (Nishimura et al., 2014) recommend that bioprosthetic valves should be considered in patients >70 years of age, mechanical valves should be considered in patients <60 years of age, and either valve may be considered in patients between 60 and 70 years of age (Class IIa recommendation). A recent propensity-matched multicentre cohort analysis showed, however, that there was no difference in 15 year mortality for patients between 50 and 69 years receiving mechanical and bioprosthetic valves, although re-operation was more likely in the bioprosthetic device group and major bleeding was more likely in the mechanical device group (Chiang et al., 2014). The choice of valves for middle-aged patients remains controversial.

Some investigators have noted that the valve guidelines are inappropriate for developing countries, where lower life expectancy, device and resource availability, the younger age of patients receiving valve replacements (see Figure 2-14), socio-economic status and other factors influence device selection (Choudhary, Talwar, & Airan, 2016; Zilla et al., 2008). Long-term durability of TAVR valves is not yet known since the devices have been CE marked for fewer than 10 years, and little attention was given to the issue as the first patients receiving the valves were elderly patients with limited life expectancy.

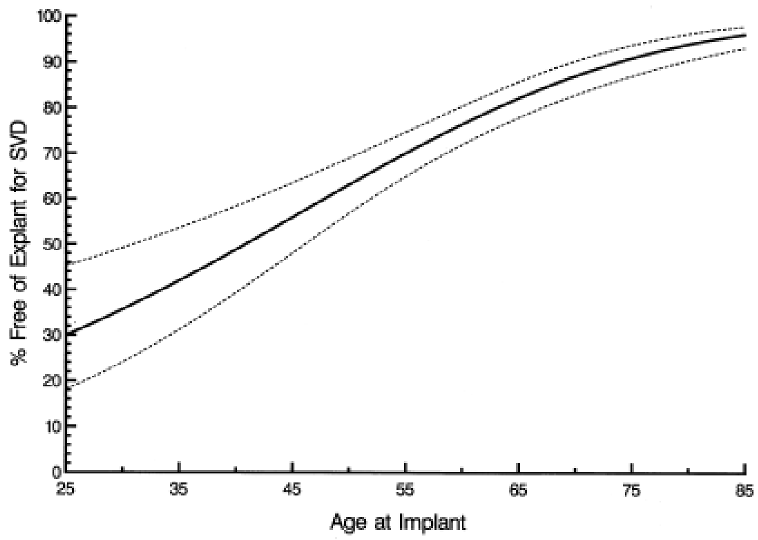

Figure 2-13. Fifteen-year freedom from structural valve dysfunction versus age at implant (Banbury et al., 2001)

TAVR durability is becoming more important as valves are increasingly being used in intermediate risk and low-risk patients. Although the current data available beyond 5 years suggest that durability is similar for transcatheter and surgical valves, there are differences that may result in reduced reliability in the longer term. These include: the increased risks of worsening paravalvular leak; increased leaflet stresses due to potentially non-circular expansion, less flexible frames and the presence of the calcified native leaflets; the potential for leaflet weakening from crimping; and the risk of late dislocation (Arsalan & Walther, 2016).

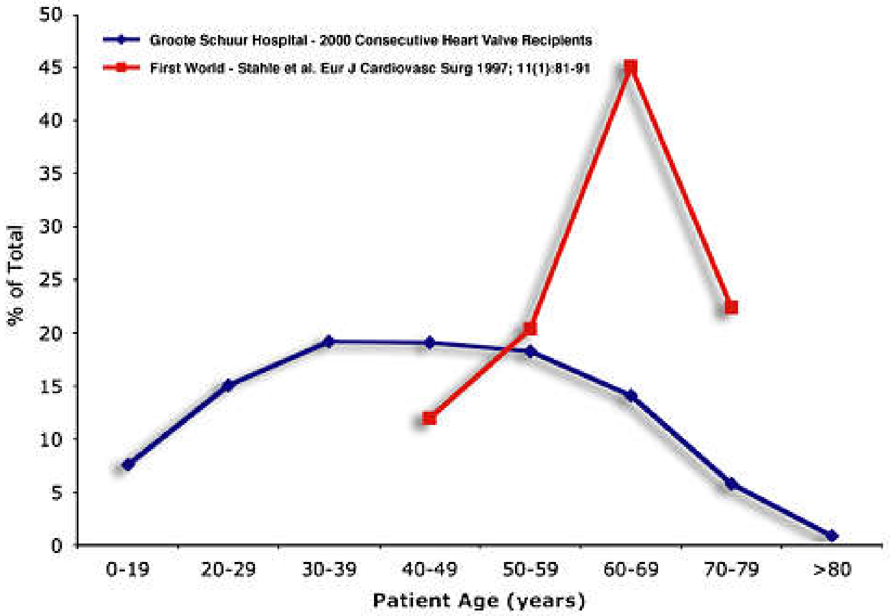

Figure 2-14. Age distribution for patients receiving replacement heart valves in a developing country and in the developed world (Zilla et al., 2008)

In the event of transcatheter valve failure, repeat TAVR (valve-in-valve procedure) is possible and has been shown to be safe, with good acute and medium term clinical outcomes (Barbanti et al., 2016). Although polymer valves have demonstrated *in vitro* durability of up to one billion cycles (equivalent of 25 years), no polymer aortic valve has ever demonstrated durability in humans beyond five years (Bezuidenhout et al., 2015). Despite the fact that bioprosthetic valves may be expected to last up to 15 years (approximately 600 million heart cycles) in appropriately selected patients, international standards only require that valves be shown to remain functional for 200 million cycles *in vitro* and that the stent frame itself should remain functional for twice this duration (ISO-5840-3, 2013).

2.6 Design and Simulation of Stents

Over the last two decades a large body of literature has been generated regarding the design and simulation of stents for percutaneous coronary intervention (PCI), peripheral vascular interventions and for vascular stent grafts, particularly with regards to understanding mechanical properties such as radial strength, compliance, resistance to embolization and fatigue life (Harewood, Thornton, & Sharp, 2011; Keevy, 2004; Marrey, Burgermeister, Grishaber, & Ritchie, 2006; Van der Merwe, Reddy, Zilla, Bezuidenhout, & Franz, 2008). This experience has provided a base for investigators to design and model stents for TAVR. The sections below present literature relating to stent design and modelling, respectively, with a focus on the modelling of stents used for transcatheter valves.

2.6.1 Structural Design of a Stent

Several groups have proposed and compared structural members for use in stents (for coronary and peripheral arteries and for structural heart applications). Examples of typical and novel structural members are shown in Figure 2-15.

The vast majority of stents are constructed of variations of zig-zag, “chicken-mesh” or diamond geometry (Sangiorgi et al., 2007; Stoeckel, Bonsignore, & Duda, 2002; Vaizasatya, 2013), and several authors have presented strategies for optimisation of such stents (Amirjani, Yousefi, & Cheshmaroo, 2014; Hsiao, Wu, Yin, Lin, & Chen, 2014). Stent designs are frequently proposed to compare or improve particular mechanical properties, such as with Douglas, Phani, and Gagnon (2014), who compared the effect of different idealised stent geometries (chevrons, diamonds, auxetics and hybrid designs) on stent foreshortening, and Kumar et al. (G. V. P. Kumar & Mathew, 2008; Perme et al., 2009), who have proposed several stent designs to improve anchorage and paravalvular leak in transcatheter valves. Auxetic structures exhibit a “negative Poisson’s ratio” effect and are therefore useful for minimisation of stent foreshortening (Ali, Amin, Ansari, Minhas, & Shahid, 2015).

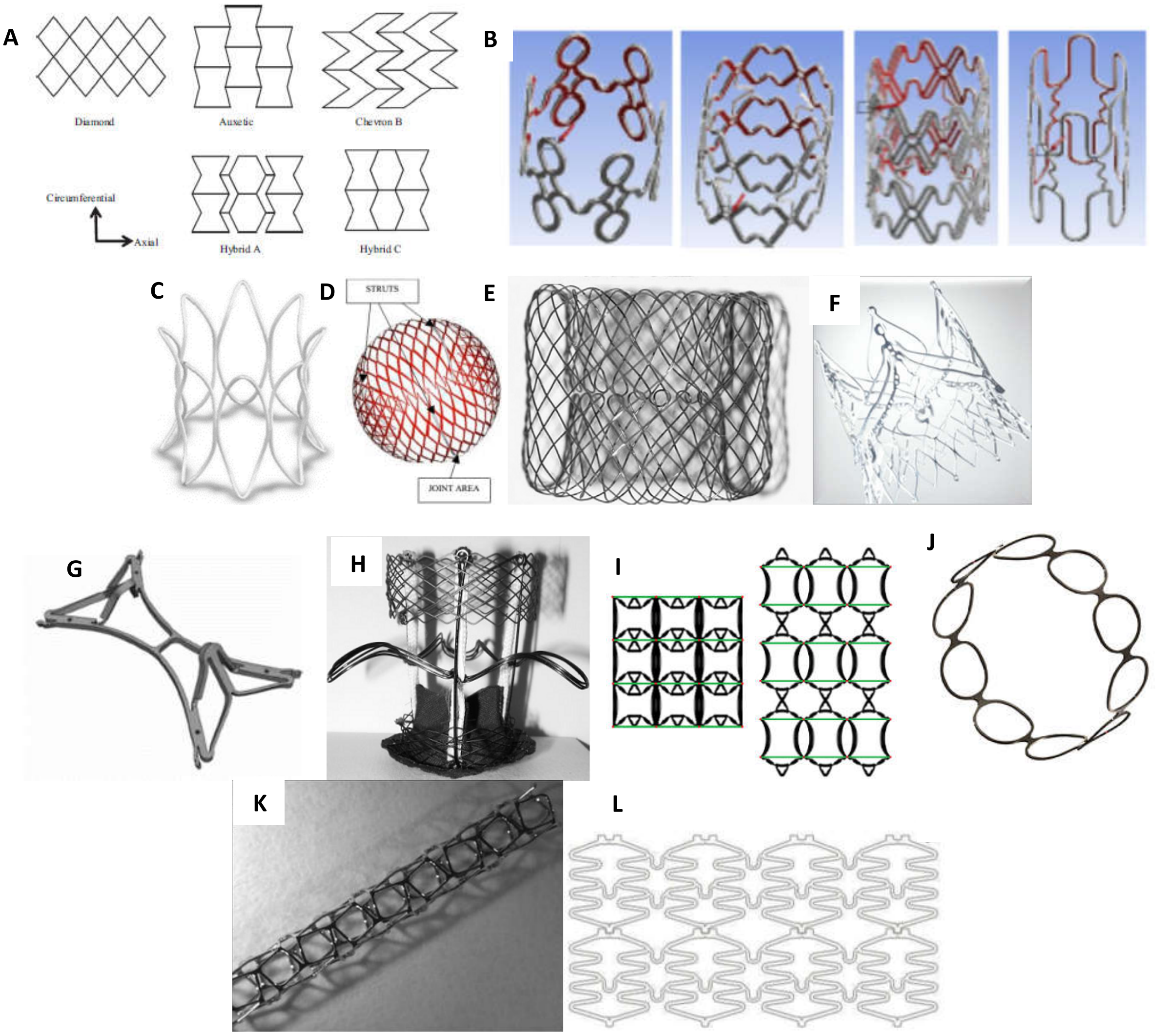

Figure 2-15. Examples of stent structures proposed in the literature.

A) Diamond, auxetic and hybrid structures (Douglas et al., 2014; Karnessis & Burriesci, 2013), B) Several shapes to optimise stent performance (Vaizasatya, 2013), C) Flared designs for reduced leakage and improved anchoring, one of many alternatives by the authors, including barbs (G. V. P. Kumar et al., 2013; G. V. P. Kumar & Mathew, 2009), D) Barrel-shaped stent (Atwood, Bougie, Carneiro, Pico, & Wnek, 2007), E) Double-layer (Basquin et al., 2010), F) Stent with locating members for behind cusps (Rudolph & Baldus, 2013), G) protruding members for anchorage (M. Young et al., 2012), H) Stent with multiple anchoring strategies (Marchand, Heim, & Durand, 2010a), I) a bi-stable stent structure (James & Waisman, 2016), J) Lattice shapes to reduce fatigue (Abad, Pasini, & Cecere, 2012) K) Negative Poisson's ratio stent (Ali et al., 2015), L) Detaching "growth" stent (Ewert et al., 2004).

Stents constructed from nitinol can be formed into a shape desired by the designer using heat treatment processes, including flared (G. V. P. Kumar et al., 2013), bulbous (Atwood et al., 2007), double-layered (Basquin et al., 2010) and complex winged shapes (Marchand et al., 2010a; Rudolph & Baldus, 2013).

A particularly novel stent design has been described by M. Young et al. (2012). The authors developed an anti-migration nitinol valve stent that contains wing elements to anchor about the mitral valve annulus. When crimped, the wings are flush with the rest of the stent, but when the stent is expanded the wings protrude first, as a result of “recessed indentations” on the wings. This expansion occurs not because of plastic strain within the stent but because of the unique wing design. James and Waisman (2016) describe a novel design that overcomes a limitation of nitinol stent designs, namely that a sheath is required to maintain the stent in its crimped condition. The authors developed a “bi-stable” stent with stable configurations in both the crimped and expanded conditions, requiring only a small force to cause “snap-through” to the other stable condition. Ewert et al. (2004) describe a stent that overcomes another limitation of most stents, namely an inability to grow with the patient. The authors sutured two halves of a stent together with degradable sutures, which provides sufficient strength for the initial scaffolding of the vessel, after which the sutures eventually disappear and the vessel may grow.

Stoeckel et al. (2002) have categorised stent designs according to geometry, form, material and method of fabrication. This initial categorisation was amended based on the stent structures described here and the valves described in Section 2.5.2 and Appendix A, and is presented in Appendix Figure B-1.

2.6.2 Leaflet Design

The design of the leaflet belly and free edge of the leaflet fall beyond the scope of this thesis. The stent and leaflet, however, share the shape of the leaflet attachment site. Although bileaflet and quadri-leaflet replacement valves have been developed and tested successfully, the majority of aortic valves described in the literature have trileaflet designs. A number of different shapes and mathematical expressions for surfaces have been used to describe natural valve geometry or to design replacement valves, including spherical, cylindrical, conical, paraboloid, alpharabolic, hyperboloid, ellipto-hyperbolic, domed, semi-domed, triangular and flat; analytically optimised shapes, including those based on Bézier curves, have also been described (Bezuidenhout et al., 2015).

Several authors have observed that the leaflet attachment site is formed by the intersection of a flat plane with the conical or cylindrical aortic root (Labrosse et al., 2006; Mercer, Benedicty, & Bahnson, 1973; Swanson & Clark, 1974), which means that the attachment site is necessarily elliptical, parabolic or hyperbolic. Labrosse et al. (2006) established a functional model of leaflet behaviour, where the three leaflets are identical in size, and the nadirs and commissures of the leaflets lie on the base and frustum of a cone, respectively. The area below the coaptation zone, namely the “load-bearing surface”, is nearly cylindrical when fully closed or fully open, and the attachment zone is defined as the intersection between the cone and a plane such that the “load-bearing surface” of the closed and open leaflets are mirrored about the plane. The attachment zone is therefore a combination of a parabola for the load surface and straight lines for the coaptation area. This is illustrated in Figure 2-16.

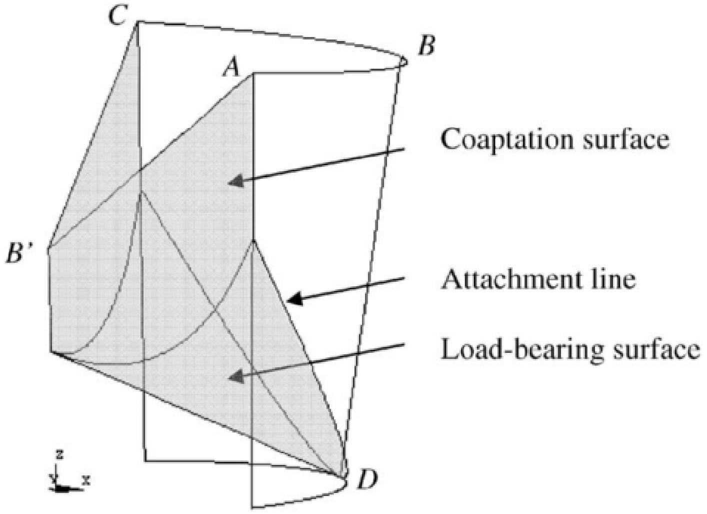

Figure 2-16. Schematic showing leaflet design as per Labrosse et al. (2006)

2.6.3 Computational Simulation of Stent Performance

The first FEA models of stents for percutaneous heart valves were performed by collaborating investigators at University College London (UCL) and the Politecnico di Milano in order to understand fatigue fracture in percutaneous pulmonary valves, firstly using free stent deployment (Schievano et al., 2007) and subsequently using post-intervention patient-specific models that included fatigue analysis based on a Goodman approach (Schievano et al., 2010).

Many articles have been published on patient-specific FEA, with the goal of improving surgical planning. The most active academic groups in this area have included UCL (Bosi, Capelli, Khambadkone, Taylor, & Schievano, 2015; Capelli, Biglino, et al., 2012; Capelli, Bosi, et al., 2012; Capelli, Taylor, Migliavacca, Bonhoeffer, & Schievano, 2010; Spranger, Capelli, Bosi, Schievano, & Ventikos, 2015), University of Pavia (Auricchio, Conti, & Morganti, 2014; Auricchio, Conti, Morganti, & Reali, 2014; Morganti et al., 2015; Morganti et al., 2014), and University of Leuven (Bosmans, Famaey, Verhoelst, Bosmans, & Vander Sloten, 2016; de Jaegere et al., 2016; Schultz et al., 2016), although others are active.

Wu et al. (2016) reported on the crimping, expansion and Fluid Structure Interaction (FSI) analysis of a valve constructed using a nitinol stent frame, meshed with reduced integration hexahedral elements. The valve was partially crimped with twelve plates, with leaflets already attached, before releasing into a patient-specific aortic root. Cyclic loading provided by FSI allowed strain-based fatigue analysis to be done. Most studies omit leaflets from crimping and deployment analyses; the inclusion of leaflets was shown by J. Bailey, Curzen, and Bressloff (2015) to have little effect on stent shape. In order to determine the effect of physiological loading on stent leaflets, leaflets may be positioned within the stent frame after deployment, and then pressure may be applied to the leaflet and stent surfaces (Auricchio, Conti, Morganti, et al., 2014; Gunning, Vaughan, & McNamara, 2014). The inclusion of the native leaflets and calcium deposits has however been shown to improve the accuracy of patient-specific models (Ovcharenko et al., 2016; Russ et al., 2013). Starting position has also been shown to affect stent shift and final implant position (Russ et al., 2014).

Imaging performed during and after valve implantation has been used to generate post-intervention patient-specific FEA models. Investigators at ETH Zurich have used linear-elastic beam elements to calculate interaction forces between the stent and aortic root based on the deformed stent state reconstructed from CT scans of patients who had received the CoreValve (Gessat et al., 2014; Hopf, Gessat, Falk, & Mazza, 2012; Hopf, Sundermann, et al., 2017). The use of linear elastic beam elements allows computation time to be dramatically reduced (Hopf, Gessat, et al., 2017). Schievano and colleagues reconstructed models of valve stents from biplane fluoroscopic images in three states (deployed condition, at systole and at diastole) as a tool to predict fatigue fracture. The measured displacements of the struts from the crimped condition to each of the three analysed conditions were used as boundary conditions for an FEA model. In particular, Cosentino et al. (2014) used logistical regression analysis to predict failure in Melody valves, and Schievano, Capelli, Cosentino, Bosi, and Taylor (2012) used Goodman and Sines-based fatigue analysis to predict fatigue failure in valves.

Several authors have modelled the deployment of stents in simple geometry or in idealised or generic aortic anatomy (Dimasi et al., 2015; Ovcharenko, Klyshnikov, Savrasov, Nyshtaev, & Kudryavtseva, 2015; Sturla et al., 2016; Tzamtzis, Viquerat, Yap, Mullen, & Burriesci, 2013). Ovcharenko et al. (2016) compared the use of patient-specific models to models based on simplified generic geometric data from multiple patients. Tzamtzis et al. (2013) calculated the hoop force of a 26mm Edwards Sapien™ valve implanted in 22mm tubes (of various stiffnesses) to be up to approximately 14N, which corresponds to a radial force of 88N.

Free stent crimping, deployment and/or crushing (i.e. in the absence of an aortic root) have been performed to compare or optimise stent designs (G. V. P. Kumar et al., 2014; Ovcharenko, Klyshnikov, Savrasov, Nyshtaev, & Glushkova, 2014; M. Young et al., 2012), evaluate alternative materials (G. V. P. Kumar, Jafary-Zadeh, Tavakoli, & Cui, 2016), and study fatigue behaviour (Esterhuyse et al., 2012; G. V. P. Kumar et al., 2013). Full patient-specific simulations (particularly those that incorporate the native leaflets and calcium deposits) clearly result in the most accurate predictions of stent stresses, strains and deployed shape, but the stent stresses vary from patient to patient, and a large sample of patients may be required to satisfactorily determine the likelihood of fatigue fracture in a general patient population. Free stent deformation is a useful and effective tool to compare stent designs in preparation for more comprehensive analyses.

Stents have been meshed with a variety of element types, including beam elements (Bosmans et al., 2016; Gessat et al., 2014), full integration hexahedral elements (Ovcharenko et al., 2016) , incompatible mode hexahedral elements (Wang, Sirois, & Sun, 2012), and reduced integration hexahedral elements, which are the most commonly used (Auricchio, Conti, Morganti, et al., 2014; Gunning et al., 2014; Wu et al., 2016). A comparison of several element types for stent modelling is provided by Hall and Kasper (2006).

Contact between the stent and crimping/expansion tools typically include friction (Auricchio, Conti, Morganti, et al., 2014; Gunning et al., 2014) but may also be frictionless if stent movement is constrained in the axial direction (Morganti et al., 2014). Although self-expanding stents do not require deployment, most balloon-expandable stent expansion is modelled using an expanding rigid cylinder (Vy et al., 2015). Realistic balloons are however being used more frequently to deploy stents (Auricchio, Conti, Morganti, et al., 2014; Bosi et al., 2015; Wang, Kodali, Primiano, & Sun, 2015) since stent deployment behaviour is more realistic when balloons are modelled (De Beule et al., 2008).

2.7 Concluding Remarks from Literature Review and Statement of Objective

The aortic valve is a nearly-symmetrical tricuspid valve situated at the centre of a fibrous skeleton and is in close proximity to all the other heart valves and to the conduction system of the heart. The literature review has highlighted a number of anatomical factors that are particularly relevant for TAVR design:

- No true anatomical aortic annulus exists. At the level of the basal plane, one third of the circumference is made up of the fibrous continuity between the aortic and mitral valves.
- The annulus is best thought of as a crown-shaped structure that follows the leaflet attachment lines. A cylindrical valve expanded into the root will contact the root along this crown shaped region. The VAJ, which represents the junction between the muscular myocardium and the fibrous aorta, extends above the basal plane, and is also not a true ring as frequently represented. Therefore some of this crown region is muscular above the virtual annulus.
- The virtual aortic annulus is elliptical in shape, and valve area increases from diastole to systole primarily due to changes in eccentricity, rather than to tissue stretch. Valve sizing is therefore most appropriately performed using diameters derived from perimeters. Compliance (change is diameter over the heart cycle) is typically reported to be less than 4%.

- The aortic root dilates such that during ventricular ejection the leaflets form a triangular rather than circular orifice.
- The height of the coronary ostia above the basal plane varies greatly among patients, with mean heights between 13 and 17mm.
- The LBB is approximately 12mm below the virtual annulus
- The aortic root is slightly asymmetric (typically approximately 10% difference from mean measurements for ICD and SoV height) and tilts slightly with respect to the left ventricle.
- The diameter of the aortic valve increases with age
- In contrast to degenerative bicuspid and tricuspid aortic valve disease, where calcium is deposited extensively in the leaflets and annulus, rheumatic aortic valve disease is fibrotic and characterised by thickening of the leaflets and fusion of the leaflets along the zone of coaptation
- In calcific AS, the aortic root shortens, but annulus, STJ and SoV diameters are similar between AS and healthy aortic roots. Calcified valves are less compliant than healthy vessels.

In developing countries, valve replacements are implanted into younger patients, in whom the failure rates of bioprosthetic surgical valves are high. Many of these patients have RHD, which is recognised as a seriously neglected disease in the developing world.

A wide range of surgical, minimally invasive and transcatheter valves have been developed for the treatment of aortic valve disease. Several TAVR systems have CE Mark approval and are commercially available. Although the majority of TAVR are self-expanding, a number of balloon-expandable valves have been developed. All commercial transcatheter valves are bioprosthetic, but several groups have developed polymer valves. Medium term data suggests that transcatheter valves have similar durability to surgical bioprosthetic valves but long term data is not yet available. Four important points may be derived from examination of these transcatheter valves:

- The majority of valves are constructed from Nitinol because they may be made retrievable and/or repositionable, and because Nitinol valves also have the advantage of being able to be heat set for shape fixation in their deployed condition, allowing complex shapes to be formed;
- All commercial balloon-expandable valves have a uniformly cylindrical shape with repeating zigzag geometry around the circumference, related to the fact that the valves must be crimped and then deployed to their required size and shape using balloons; repeating patterns make this task simpler.
- The majority of valves rely on a crown-shaped leaflet attachment to a skirt material, rather than on a continuous attachment to the frame. A notable exception to this is the Triskele valve from UCL.

- None of the balloon-expandable valves and few of the self-expanding valves are indicated for use in non-calcific AR, with none specifically indicated for rheumatic aortic valve disease. Valves without dedicated anchoring mechanisms are at risk of migration in the absence of leaflet calcification. As Remenyi et al. (2016) have stated, “development of newer generations of transcutaneous aortic valves that do not need the presence of cusp calcification for proper anchorage might offer an alternative to future surgical valve replacement”.

Many stent designs have been proposed in the literature, and various simple and sophisticated approaches to the computationally modelling of their behaviour have been presented. No balloon-expandable stent design has been reported that facilitates attachment of a polymeric valve and is able to anchor within a non-calcific aortic valve. We have therefore recognised an opportunity to develop a novel balloon-expandable stent that allows for continuous leaflet attachment and anchors effectively in the native aorta, even in the absence of calcification.

This thesis therefore has the following specific research objectives:

- Objective 1: Design a novel compressible and balloon-expandable stent for a transcatheter aortic valve to which polymeric heart valve leaflets may be attached.
- Objective 2: Perform Finite Element Analysis (FEA) on stent designs to characterise deformed geometry, quantify stresses and estimate fatigue risk.
- Objective 3: Manufacture stent and valve prototypes and confirm adherence to dimensional specifications.
- Objective 4: Verify satisfactory performance of the stent against specifications using *in vitro* laboratory tests and acute termination experiments in a large animal model.

3 Design Inputs and Methods

3.1 Design Requirements

3.1.1 Valve Requirements

According to Pibarot and Dumesnil (2009) an ideal valve should be easy and practical to implant and should mimic the native valve, should not obstruct blood flow, should be non-thrombogenic, should have excellent haemodynamics and should be very durable. Vesely (2010) expands on this list from the surgical valve era, where the ideal valve was haemocompatible (did not create emboli, was inert chemically and did not damage blood elements), had excellent haemodynamics (offered no resistance to blood flow, closed rapidly, remained closed during the diastolic phase and was inserted at a physiological site), was practical to implant, durable and able to be fixed permanently, and did not annoy the patient. He observed, however, that some of these requirements are being re-evaluated or disregarded in the era of transcatheter valves. It is clear, however, that percutaneous valves need to strive for many of these same biocompatibility, haemodynamic, durability and implantability goals while being able to be compressed to a low profile and expanded to a functional size.

Specific user needs for the valve were determined through interpretation of the literature, interviews with several cardiac surgeons, experience gained on device manufacturability from early experience, examination of current devices and observation of TAVR procedures at Groote Schuur Hospital, Cape Town. Those needs were then examined with regards to their relevance to stent design and recorded. These are listed in the first column of Table 3-1.

3.1.2 Stent Requirements

The main purposes of a valve stent are to provide a frame onto which functioning leaflets may be attached and to support the leaflets within the anatomy.

The relevant valve needs, which are primarily described qualitatively, were then translated into engineering requirements, quantified where possible and reasonable, and divided into the following categories: *operational* requirements (relate to the stent's ability to satisfy its primary purpose); *safety* requirements (to ensure patient safety); *performance* requirements (to ensure good performance beyond the "standard" and to differentiate from other devices); *preferred* requirements (desirable but not mandatory); and *manufacturing* requirements (related to ease of manufacture and cost). A summary of the translation from user/customer needs to engineering requirements is presented in Table 3-1.

Table 3-1. Key current design requirements

User Needs Relevant to Stent Design	Translational Engineering Requirements for Stent Design	Method of verification
Operational Needs		
• The implant must be able to operate in a human heart and circulatory system at the full range of native aortic valves sizes, body temperatures, heart rates, cardiac outputs and blood pressures expected in patients affected by heart valve disease, including young adult patients affected by RHD.	• The stent must have an outer diameter when expanded of 23mm (valve sizes of 20mm, 23mm, 26mm and 29mm will be designed later to cover aortic annulus sizes of 18mm to 28mm). For this project, a 23mm valve will be designed to fit in a native aortic annulus size of 18 to 22mm. When fully expanded, the stent must have an inner diameter of 23mm to hold leaflets designed for this geometry.	Attribute
	• The design must be able to be scaled to other sizes.	Attribute
	• The stent shall be radially symmetric in order to receive a tri-leaflet valve design.	Attribute
• The valve must be compatible with and must be able to be deployed in the correct position using a balloon-based or mechanical non-occlusive deployment device	• The stent must be balloon-expandable	Attribute
	• The stent must not foreshorten in such a way as to interfere with good positioning (foreshortening may be ≤20%), and the sites of commissure attachments should not shorten at all.	In vitro testing, numerical modelling
	• Stent crimped length should be <35mm	In vitro testing, numerical modelling
• The valve must be able to be used in aortic valve stenosis, in pure regurgitant aortic valves and in mixed aortic valve disease, including fused commissures	• The stent should be able to hold the native leaflets away from the replacement leaflets	Ex vivo testing, In vivo testing
	• Stent radial strength must be similar to or greater than 88N at 15% diameter reduction (Tzamtzis et al., 2013).	Numerical modelling
	• The stent must limit metal to artery ratio below 25% where possible to limit foreign-body response.	Attribute
	• The stent must not suffer acute fracture even if over-deployed by 10% in diameter.	In vitro testing
• The implant must be able to function at physiological pressures and heart rates associated with the intended patients for the equivalent of 5 years at normal heart rates.	• Stent accommodate 14mm high leaflets (for 23mm valve)	Attribute
	• The stent should be constructed from a material with excellent strength and elongation properties.	Attribute
	• Stent function must not alter over 400 million cycles of loading from leaflet (haemodynamic) forces and from forces from the heart during extreme physiological conditions (*this will not be demonstrated in this project due to time limitations but will be included in design intent).* The role of the stiffness of the commissure posts should be considered.	N/A. Not verified in this thesis.
	• The stent must incorporate continuous attachment.	Attribute
	• The stent must not degrade over time	Attribute
• The implant shall be suitable for single use.	• The stent must be able to be crimped to its collapsed condition and expanded to its operating condition without acute fracture and achieve the intended leaflet attachment shape at the expanded diameter.	In vitro testing, numerical modelling
• The device must be compatible with all accessories involved in the procedures.	• When crimped the valve must not protrude in a manner that is traumatic or will interfere with standard sheaths	In vitro testing, numerical modelling
Safety Needs		
• All materials used in the valve should be biocompatible (in particular non-thrombogenic and non-haemolytic) for permanent implantation, and rapidly incorporated and tolerated by the patient's tissues.	• The stent shall be constructed from a material with a known history as a blood-compatible implant material.	Attribute
	• The stent must be electropolished to ensure that it presents a biocompatible surface with no burrs, rough edges or protrusions visible under X50 magnification. Breakdown potential and corrosion should be considered for manufacturing processes.	Surface inspected. Corrosion and breakdown potential are not tested in this thesis
	• The stent must resist damaging the replacement leaflets	Attribute

• The implant must remain in the deployed position and resist early and late embolization.	• The stent must be able to anchor in an aortic annulus with compliance of up to 10%, assuming that valve location can be established through the deployment device or from fluoroscopic positioning. Valve should not migrate under back pressures of 100mmHg; 23mm stent should therefore not migrate under 5.4N. In animals, valve must not embolise.	Ex vivo testing, in vivo testing
	• Stent recoil should be less than 5% to allow the 23mm stent to be implanted into a 22mm annulus (as measured during systole) without separation from the annulus, and also to reduce the risk of annular rupture and pressure on the mitral valve due to over-expansion.	In vitro testing, numerical modelling
• The implant shall not embolise during delivery and deployment	• The stent should resist forces that tend to shift the valve on the deployment devices of at least 2N.	N/A. Not tested in this thesis.
• The implant must have a low risk of atrioventricular block.	• The stent shall protrude no deeper into the left ventricle than 12mm, particularly at the position of the right coronary cusp and membranous septum.	Attribute
• The implant must not significantly disrupt mitral valve function.	• The stent shall not interfere with the function of the anterior mitral leaflet and shall have no sharp edges that may damage mitral leaflet.	Attribute, in vivo testing
• The device must not block blood flow to the coronary ostia significantly.	• Stent shall not block flow to the coronary arteries or jail with more than one strut or hairpin.	In vivo testing
Performance Needs		
• The valve should be novel	• The stent should have a novel design	Attribute, patent review
• The device and implant must be able to be delivered to the site of implantation through either an antegrade or retrograde approach.	• Stent must be able to be positioned for antegrade or retrograde implantation	Attribute
• The device must be compatible with an access port or sheath	• Stent should allow sheathing but should ideally not require sheathing	In vitro testing
• The implant must contain radiopaque or echogenic markers or signatures to allow precise positioning within the native anatomy.	• Stent should be visible under fluoroscopy, with identifiable features to facilitate precise positioning.	In vivo testing
• The device must have a large orifice area and present low resistance to forward blood flow.	• Without sacrificing radial strength, the wall thickness should be <0.5mm to maximise internal diameter, encourage endothelialisation and reduce metal volume.	Attribute
• Implant creates a minimal degree of flow separation and stasis and should not induce regions of high shear stress	• The angles of the struts should preferable not exceed 60 degrees from the axial direction on opening to reduce blood wall shear stress.	Attribute
• The device and implant shall have a shelf life of at least one year when first supplied.	• The stent properties must not alter over a period of 1 year in storage	N/A. Not verified in this thesis.
• The implant must minimize paravalvular leaks.	• The stent must allow a skirt to be attached for sealing.	In vitro testing
	• The stent shall have sufficient scaffolding (ideally a minimum of 18 struts around the circumference) to minimise paravalvular leaks.	Attribute
• The valve should have a low crimped profile	• The stent should be able to be crimped to an outer diameter of 6mm.	In vitro testing, numerical modelling
Preferred but Non-Essential Needs		
• The device should be visually appealing to clinicians.	• The stent should be attractive to surgeons	N/A. Not verified in this thesis
• The implant should be removable.	• The stent should be removable	N/A. Not verified in this thesis

Manufacturing Needs		
• The valve is required to be provided in a fully deployed condition, or in a condition that allows it to be opened to a fully deployed condition without fracture, and must be able to be crimped down to a suitable diameter for crimping onto a delivery and deployment device.	• Stent should ideally be manufactured close to operating diameter for precise manufacture. • The stent must be easily crimpable with standard techniques and equipment.	Attribute In vitro testing
• The valve must be able to be manufactured cost-effectively, including standard techniques where possible and using a spray-coating process on a mandrel.	• The stent must be able to be easily expandable to an internal diameter of 23mm for valve manufacture. • The stent shall be manufactured using established techniques for stents • The stent must have a relatively open structure for spray to travel between struts to valve leaflets. • Stents dimensional tolerance must be ± 20 µm (based on standard deviation).	In vitro testing Attribute Attribute In vitro testing

3.2 Stent Design, Drafting and Material Selection

3.2.1 Development Methodology

Stents were designed using a hybrid approach, combining design techniques favoured by the FDA in the United States and more current agile techniques. The FDA (through 21 CFR 820.30) and the International Standards Organisation (through ISO 13485 Clause 7.3) provide requirements relating to the control of medical device design processes as part of a quality management system. Both the FDA and ISO regulations describe, but do not strictly mandate, a traditional waterfall type development process (FDA, 1997). The process is iterative and subject to design reviews at the end of each phase. The waterfall model relies on the fact that the user needs are well understood at the beginning of the design, which is not always the case, and was not the case in this project. Furthermore, working devices are typically only ready late in the development. Another disadvantage is that it does not specifically allow for iterative design-test-redesign cycles in the design process. Recently the FDA launched its “Innovation Initiative” to facilitate innovation in medical devices (FDA, 2011). This pathway is similar to stage-gate or phase-based development processes considered best practices for medical device manufacturers (Pietzsch, Shluzas, Paté-Cornell, Yock, & Linehan, 2009). The process makes clear the design-test-redesign cycles frequently used in medical device development. Additional “Scoping” and “Business case” are sometimes added to phase-based development for more complex projects.

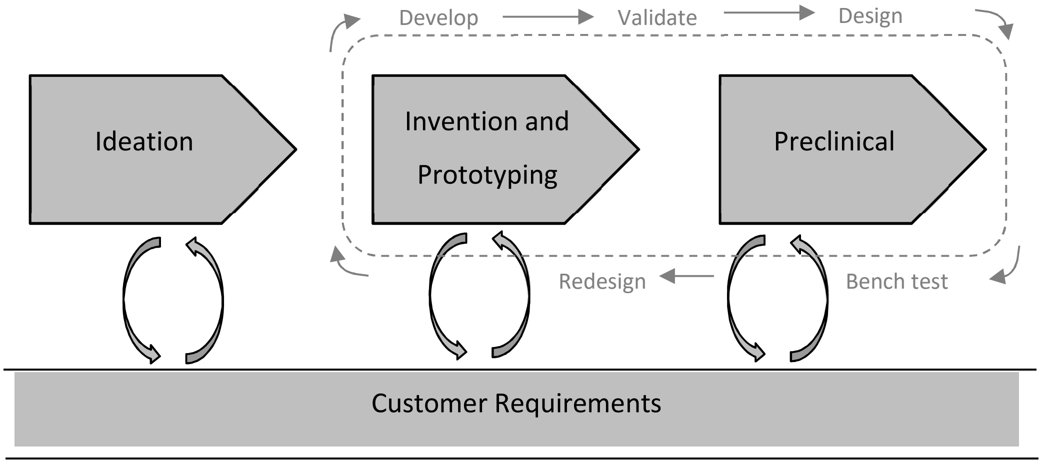

Figure 3-1. Project design and development model

The current project concerns itself with the first three phases, namely ideation, invention and prototyping, and preclinical testing; a schematic of the approach is shown in Figure 3-1. The figure shows that customer requirements are reviewed and refined throughout the design process as prototypes are tested, and illustrates the design-test-redesign loops that were used. This meant that concepts could be evaluated rapidly though simulation or bench testing, discarded early if unsuitable and tested further if promising. The methods for ideation and invention, including concept design and design refinement are discussed in Chapter 7. Prototyping and test methods are described in Chapter 6.

3.2.2 Drafting

Stent designs were rendered in computer-aided design (CAD) software (SolidWorks 2014, Dassault Systèmes SolidWorks Corp., Waltham, Massachusetts, USA) in one of two ways. For three-dimensional models and for the creation of Standard ACIS Text (.sat) files for detailed FEA, a wrap feature was used to emboss the stent onto the inside of a tube that was subsequently cut away. Angular symmetry allowed sketches to be drawn as a one-sixth sector of a cylindrical tube, and the stents were completed using “mirror” and “combine” features. These steps are illustrated in Figure 3-2 and Figure 3-3.

Figure 3-2. Computer-aided drawing of 3D stent model.
A) One-sixth geometry constructed as an embossed wrap on the inside of a tube of arbitrary wall thickness, B) The tube is cut away, leaving one-sixth geometry, C) One-third sector constructed using a merged mirror feature.

For stent manufacture (laser cutting), drawings were converted to Drawing Exchange Format (.dxf) files. Initially stents were drawn as single large sketches, but these became unwieldy due to large graphics memory requirements. Stents were subsequently modelled as short extrusions; as with the 3D models, stents were drawn as one-sixth portion of the stent circumference, mirrored and combined to form the full stent circumference. A new sketch was created from the extrusion using the “convert entities” feature, and finally the sketch was converted from a drawing of the stent geometry to the closed contours of the negative spaces that define the laser beam path. This geometry is illustrated in Figure 3-4.

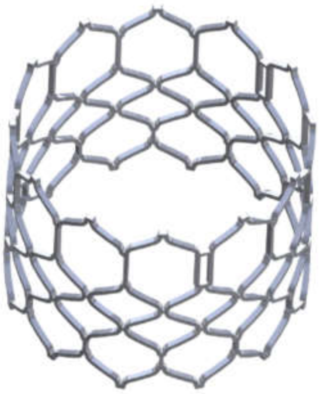

Figure 3-3. Full stent geometry completed using “mirror” and “combine” features

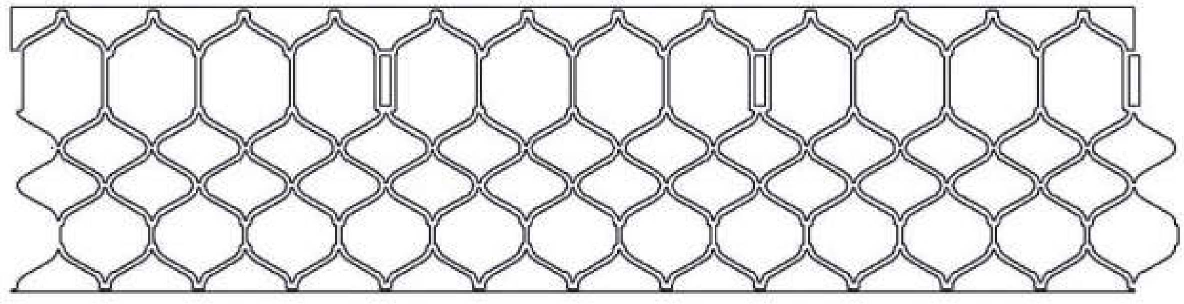

Figure 3-4. Computer-aided drawing of stents for manufacture

3.2.3 Material Selection

Based on the requirements set out in Section 3.1.2, the ideal material for a balloon-expandable stent will have the following characteristics (estimated quantitative limits are indicated in parentheses):

- High Ultimate Tensile Strength (UTS) for high radial strength; high strength in turn allows thinner struts to be used, which will allow for lower crimped profiles (>600MPa)
- High strain to failure, to withstand high strut opening angles (>25%)
- High elastic modulus to reduce recoil (>100GPa)
- Relatively low yield strength to allow for easy crimping and to limit spring-back off the balloon (Yield Stress < 600MPa)
- Excellent resistance to fatigue (Endurance limit > 100MPa, K_{Ic} > 10MPa.m$^{1/2}$)
- Biocompatible (use in implants, good biocompatibility or corrosion potential > 500mV)
- Radiopaque (Density > 5g.cm^{-3})

Using the materials selection charts provided by Ashby (2005), an analysis of fatigue strength (K_{Ic}) versus elastic limit (σ_f) based on the above criteria produced a subset of materials that included most metals, and some composites, but notably excluded all ceramics and polymers. The modulus (E) versus elastic limit (σ_f) chart further excluded traditional composites in general, and specifically excluded certain metal alloys, including the alloys of aluminium, magnesium and zinc, most of which also have low radiopacity and poor biocompatibility. Precious metals were also excluded for low strength. Alloys of iron were excluded due to their degradability. Most refractory metals and their alloys are unsuitable due to lower UTS (hafnium, tantalum and niobium), low elongation (rhenium) or high yield stress (tungsten, molybdenum). Copper alloys and carbon steels have poor biocompatibility. Although titanium alloys are popular in medical implants, commercially pure titanium has low UTS, and alloys of titanium have low elongation and relatively low modulus (Poncin & Proft, 2003).

It is recognised that tantalum, niobium, platinum-iridium and various polymers have been used in balloon-expandable stent applications before (O'Brien & Carroll, 2009; Stoeckel et al., 2002), but they are relatively weak and therefore do not provide optimum properties for a contemporary balloon-expandable valve stent. Based on good mechanical properties and biocompatibility, the list of potentially suitable materials was narrowed down to stainless steels (316LVM, ASTM F1586, ASTM F1314, nickel-free stainless steels, “platinum-chromium”), cobalt alloys (L605, MP35N, Elgiloy), nickel-chromium-molybdenum alloys (Inconel) and martensitic nitinol. Martensitic nitinol has been used in balloon-expandable stents (Sangiorgi et al., 2007), but the low modulus and high elastic range would result in large amounts of elastic recoil. In general the cobalt alloys had superior properties to the stainless steel alloys. Although no evidence could be found that stents have been manufactured from Inconel, it is believed the alloys would produce stents with good properties, but still inferior to the cobalt alloys.

MP35N was chosen as the desired stent material for the balloon-expandable valve due to its high Young’s modulus, large work hardening ability (stress difference between UTS and yield stress was large), high radiopacity and high elongation. L605 has greater strength and radiopacity, has proved effective in coronary stent design (Suttorp et al., 2015) and may be a superior stent material. MP35N was however more readily available commercially and has history as a valve stent material (it is used in the newer generation of Edwards Sapien™ valves (J. Bailey et al., 2015)), which is anticipated to have regulatory advantages.

4 Numerical methods

FEA was used to simulate crimping and expansion in order to determine deformed crimped and deployed geometries, to calculate maximum stresses and strains, and estimate stent fatigue resistance. FEA for stent modelling is also recommended by ASTM International ("Finite element analysis is a valuable method for evaluating the performance of metallic stents and in quantifying quantities such as internal stresses, internal strains, and deformation patterns due to applied external loads and boundary conditions") (ASTM, 2014). Stress analysis for fatigue life is recommended by the FDA ("We recommend that you identify the critical locations of stress or strain on the stent using finite element analysis"; "[We recommend] that you use the mean and alternating stresses/strains obtained from the stress/strain analysis as input for the fatigue life determination") (FDA, 2010). This chapter describes the pertinent FEA theory and details each step in the simulation procedure.

4.1 Theoretical framework

FEA is a numerical technique for the approximation of continuous systems. Solutions to finite element problems may be approximated by replacing equilibrium equations with an equivalent weaker form, which is expressed as an integral equation. Abaqus uses the principle of virtual work, which states that for any set of small virtual displacements imposed on a body in equilibrium, the total external virtual work is equal to the total internal virtual work. Given a domain volume V and domain boundary surface S, the virtual work principle may be expressed as follows (Dassault-Systèmes, 2014; Zienkiewicz & Taylor, 2000):

$$\int_V \delta\boldsymbol{\varepsilon}^{\mathrm{T}}\boldsymbol{\sigma}\, dV = \int_S \delta\mathbf{u}^{\mathrm{T}}\mathbf{t}\, dS + \int_V \delta\mathbf{u}^{\mathrm{T}}\mathbf{b}\, dV$$

Equation 4-1 Principle of Virtual Work

where $\delta\boldsymbol{\varepsilon}$, $\delta\mathbf{u}$, $\boldsymbol{\sigma}$ and $\mathbf{t}$ are the virtual strain rate, virtual displacement, stress and boundary traction, respectively.

Either implicit or explicit integration techniques may be used for the analysis of stents. Since the crimping and deployment of the stents in this thesis involves large displacements, large rotations, large strain, non-linear stress-strain data and non-linear boundary conditions (through complex contact), quasi-static Abaqus/Explicit analysis was considered the most appropriate method to model the stent behaviour.

The governing equation for nonlinear dynamic analysis may be expressed as follows:

$$\mathbf{F}_{\mathrm{I}}(t) + \mathbf{F}_D(t) + \mathbf{F}_E(t) = \mathbf{R}(t)$$

Equation 4-2 Governing equation

where $\mathbf{F}_I$ and $\mathbf{F}_D$ are the inertial and damping forces, respectively, $\mathbf{F}_E$ refers to the nodal point forces corresponding to the element stresses, and $\mathbf{R}$ is the external load vector; all loads are time dependent.

The governing equation may be expressed in terms of the element mass, damping and stiffness matrices, $\mathbf{M}$**,** $\mathbf{C}$ and $\mathbf{K}$, respectively as

$$\mathbf{Mu} + \mathbf{Cu} + \mathbf{Ku} = \boldsymbol{R}(t)$$

Equation 4-3 Dynamic equilibrium

where $\mathbf{u}$**,** $\mathbf{u}$ and $\mathbf{u}$ are the nodal acceleration, velocity and displacement vectors.

The dynamic equilibrium equation simplifies to

$$\mathbf{Mu} = \mathbf{R}(t) \quad \mathbf{I}(t)$$

Equation 4-4 Simplified dynamic equilibrium

where $\mathbf{I}$ is the internal force vector.

Explicit dynamic procedures are based upon the implementation of the central difference rule together with the use of diagonal element mass matrices. The central difference method may be stated as follows:

$$\mathbf{u}^{(i+\frac{1}{2})} = \mathbf{u}^{(i-\frac{1}{2})} + \frac{t^{(i+1)} + \quad t^{(i)}}{2}\mathbf{u}^{(i)}$$
$$\mathbf{u}^{(i+1)} = \mathbf{u}^{(i)} + \quad t^{(i+1)}\,\mathbf{u}^{(i+\frac{1}{2})}$$

Equation 4-5 Central difference method

where i and $i+1$ are the beginning and ends of increments, and $i+\frac{1}{2}$ and $i \quad \frac{1}{2}$ refer to the mid-increment values.

The diagonal nature of the element mass matrix allows the accelerations at the beginning of the increments to be calculated by inverting the mass matrix in Equation 4-4 as follows:

$$\mathbf{u}^{(i)} = \mathbf{M}^{-1} \quad (\mathbf{R}^{(i)} \quad \mathbf{I}^{(i)})$$

Equation 4-6 Acceleration

Unlike implicit integration procedures, which are unconditionally stable, the explicit central difference method is conditionally stable, and therefore the time increment t must be less than a stable time increment:

$$\mathrm{t} \leq \frac{2}{\omega_{max}}\left(\sqrt{1+\xi^2} \quad \xi\right)$$

Equation 4-7 Stability limit

where ω_{max} is the highest eigenvalue and ξ is the critical damping fraction in the highest mode.

4.2 Modelling overview

Since the stent simulation aims to model quasi-static processes, time steps of 1 to 10 seconds were used, mass scaling was employed and the application of loads and moving boundary conditions were smoothed. To verify that the model was truly quasi-static, the ratio of kinetic energy to internal energy was checked to ensure that it remained below 5%. Due to the large number of increments required for complex stent modelling, double-precision floating-point format was used for all analyses. Two different types of analyses were performed. In order to more rapidly compare concepts, such as those described in Chapter 6, stents were crimped using rigid plates and deployed using an expanding cylinder; this allowed stent symmetry to be exploited and led to fast modelling times. This method will be referred to as the "simple" FEA method. In order to accurately model stent performance on the balloon (for preferred concepts described in Chapter 7), a more sophisticated method was utilised. This "complex" method simulated crimping the full stent geometry onto a folded balloon. Stent deployment was then performed by inflating the balloon with an internal pressure, after which the balloon was deflated and loads were applied to the stent to simulate physiological conditions. A comparison between the simple and complex methods is shown in Table 4-1.

Table 4-1. Comparison of simple and complex FEA methods used for stent modelling

Step/Description	Simple	Complex
Stents	Concept selection – 8 stents	Favoured concepts – 2 stents
Initial	One-sixth stent	Full stent
Crimp	Flat plates 30° apart, no balloon inside stent	Flat plates 30° apart, folded balloon inside stent
Relaxation after crimp	Withdraw plates	Withdraw plates
Expansion	Cylindrical shell	Pressurised balloon
Relaxation after expansion	Withdraw cylinder	Deflate balloon
Loading	None	Radial pressure and leaflet loads
Fatigue analysis	None	Goodman analysis

4.2.1 Stent model creation

Three-dimensional stent geometry was exported from SolidWorks as a *.sat file as described before. A cylindrical coordinate system was calculated from the original Cartesian coordinates, with the origin of the system placed on the central axis of the stent. The stent was then manually partitioned and meshed using Abaqus version 6.14 (Simulia, Dassault Systems). The stent was modelled using an isotropic elasto-plastic material with isotropic hardening, a Young's Modulus of 236GPa (Altman, Meagher, Walsh, & Hoffmann, 1998) and a Poisson's Ratio of 0.40 (Matweb, 2016).

Engineering stress-strain data were determined from tensile testing, converted into True Stress and True Strain, and the plastic region of the curve was defined by discrete points along the True Stress-Strain curve from initial yield stress. A Hollomon power law was used to define stress-strain behaviour after necking (described in Section 5.2). In order to eliminate stent vibrations that occur in the quasi-static analysis during unloading (relaxation) steps, the material definition was edited to include Rayleigh damping with a mass-proportional damping constant α of 5, following confirmation that damping did not alter predicted peak stresses and strains.

Points on the outside surface of the stent were constrained in the axial direction to prevent free body motion of the stent through all steps (one point for simple analyses and three for complex). These points were placed in areas of the stent anticipated to be positioned at the basal plane of the aortic cusps, or at the commissure posts. Any erroneous stress concentrations at these constraint points were removed during post-processing. For comparison purposes, Control stents were created based on Edwards Sapien 3™ stents.

Since stents experience predominantly bending loads, stents were modelled using reduced integration 8-noded brick elements (C3D8R) with hourglass control (Hall & Kasper, 2006), and were monitored for instability.[3] Mesh sensitivity studies were performed to determine the effect of element selection and mesh density on maximum von Mises stress and maximum displacement and this was compared to computational cost. Although incompatible mode elements are frequently favoured for stent analysis, modelling of stents with relatively large changes in geometry and large strains showed the development of spurious modes that provided erroneous stress values even with a fine mesh. Similar spurious modes in incompatible elements have been identified by Sussman and Bathe (2014). As a result, the mesh refinement study describes only refinement using C3D8R elements. Details may be found in Appendix C.

Certain stent concepts incorporated the use of cold-drawn MP35N wire welded to the stent frame. In these cases, the cold-worked material was assigned a yield stress of 1600 MPa, UTS of 2000 MPa and

---

[3] Standard fully integrated first order elements are not suitable for bending dominated problems due to their susceptibility to shear locking. Reduced integration elements are computationally inexpensive but are susceptible to hourglassing because strains can't be detected at the central integration point. For this reason a minimum of four elements were used through the thickness. Even with four elements through the thickness, maximum stresses may be underestimated if they lie at the surface due to the fact that the central integration point is not near the surface. Incompatible mode elements are not susceptible to either shear locking (because of the incompatible deformation modes) or to hourglassing (because they are fully integrated elements). Despite being computationally more expensive than reduced integration elements, they can be used with a coarser mesh than with reduced integration elements because they model bending accurately. A major difficulty with incompatible mode elements is that they perform less accurately if they are not close to being perfectly cubic.

elongation to failure of 3.4% (Prasad, Reiterer, & Kumar, 2014; Sorensen, Li, Gerberich, & Mkhoyan, 2014). This data was converted to True Stress-True Strain as for the stent tubing.

4.2.2 Balloon model creation

The balloon was drawn as a surface in SolidWorks in a folded condition, with four folds, as shown in Figure 4-3, and exported as a *.sat file. Only the 40mm cylindrical barrel portion of the balloon was drawn, i.e. the cones on the ends of the balloons were neglected. The circumference of the balloon in the zero-pressure condition was obtained from the measurement of a used 23mm commercial valvuloplasty balloon catheter.

Balloon properties were obtained by cutting 10mm wide specimens from the balloon, in both longitudinal and circumferential directions, and performing uniaxial tensile tests on the samples in an Instron electromechanical tester, using a gauge length of 10mm. The stress-strain curves for the balloon material are shown in Figure 4-1. Two circumferential specimens and one longitudinal specimen provided usable data. The curves are similar for both directions over the first 10% strain, so the material was assumed to be isotropic. The specimen with the largest strain-to-failure, “Circumferential 1”, was used to generate material data for Abaqus.

A third-order hyper-elastic Ogden material model was used to model balloon performance, based on the experimental data. The Ogden model is frequently used to describe the non-linear behaviour of polymers and rubbers.

In Abaqus the strain energy potential is formulated as follows (Shahzad, Kamran, Siddiqui, & Farhan, 2015):

$$W = \sum_{i=1}^{N} \frac{2\,\mu_i}{\alpha_i^2}\left(\bar{\lambda}_1^{\alpha_i} + \bar{\lambda}_2^{\alpha_i} + \bar{\lambda}_3^{\alpha_i} \quad 3\right) + \sum_{i=1}^{N} \frac{1}{D_i}\left(J_{el} \quad 1\right)^{2i}$$

Equation 4-8 Ogden

where $\bar{\lambda}_i$ is the deviatoric principal stress, J_{el} is the elastic volume ratio, and α_i, μ_i and D_i are material properties shown in Table 4-2.

The Ogden model provided a reasonable approximation of the experimental data, as shown in Figure 4-2.

Table 4-2. Ogden material parameters

i	μ_i	α_i	D_i
1	-12910	2	9.935E-4
2	6914	4	0
3	6427	-2	0

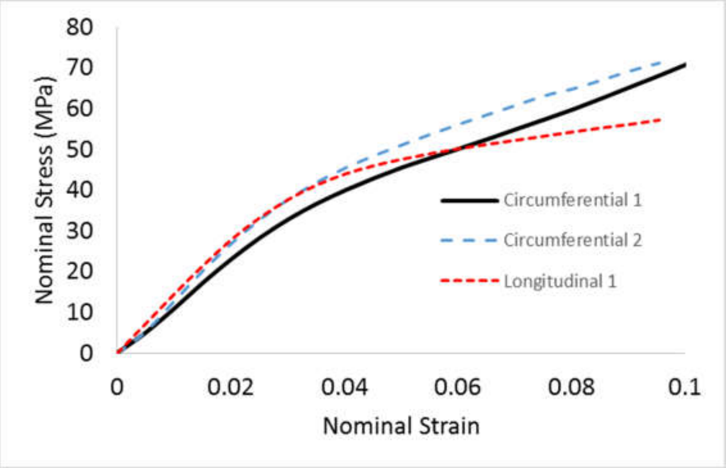

Figure 4-1. Stress-strain curves for balloon material

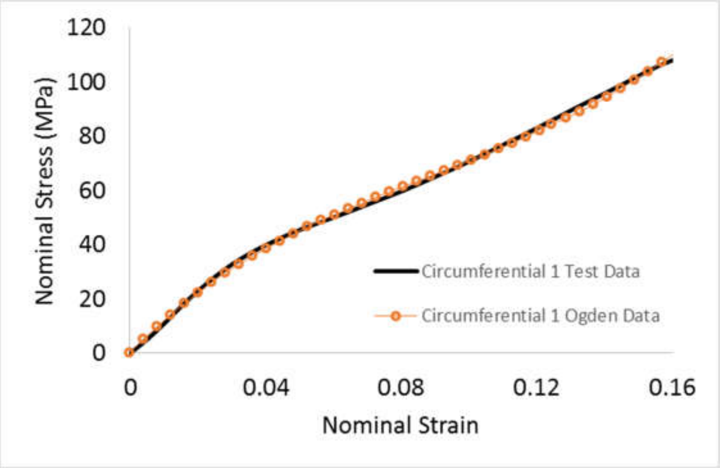

Figure 4-2. Comparison between test data and Ogden material model

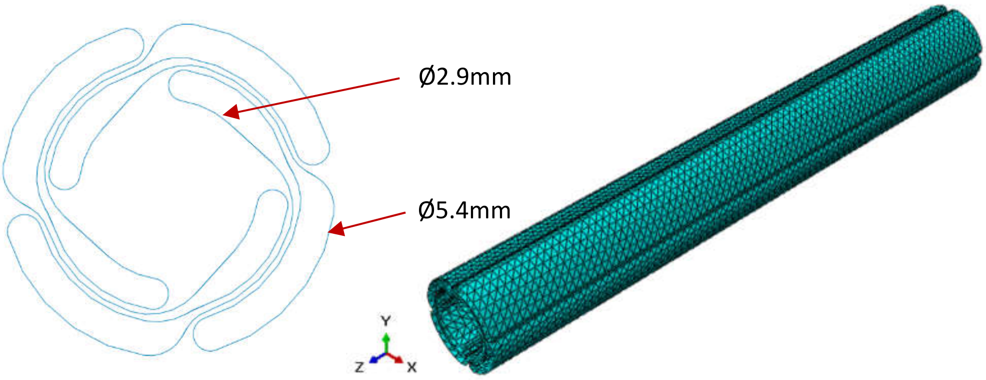

Figure 4-3. Balloon sketch profile and meshed geometry

A Poisson's ratio of 0.4 and a balloon wall thickness of 0.045mm were used. The circumference of the balloon was measured to be 66.29mm. The mass density of the balloon material was artificially increased by a factor of 1000 and set to 1.04 x 10^{-6} tonnes/mm^3 to decrease run times. Following partitioning, the balloon was meshed with 25,440 three-node triangular membrane elements (see Figure 4-3). The edges of the balloon at both ends were constrained in the axial direction.

4.2.3 Crimping and relaxation

The crimping simulation was designed to replicate the crimping action of a 12-plate crimping device such as those offered by Machine Solutions Inc., Flagstaff, AZ, USA and by Edwards Lifesciences, Irvine, CA, USA. As per the Edwards crimper, the model plates move radially inwards, with no twisting. The moving plates were modelled as discrete rigid geometry. Since self-contact was anticipated across the symmetry planes used in simple models, analytical rigid surfaces were placed at symmetry planes. "Hard" frictionless general contact is used to model contact between the stent and the crimping plates. Stent plates moved from a diameter beyond the stent outer diameter to an inscribed diameter of 6mm. For complex models, the balloon was placed inside the stent prior to crimping. Hard frictionless general contact was also used to model stent-balloon contact. After expansion, plates were withdrawn in a relaxation step to a position just past the point at which the plates leave the stent surface. This point was established through coarsely meshed models. This was done to ensure that the velocity of the moving plates was reduced using the smooth load function, to reduce stent vibrations.

4.2.4 Expansion and relaxation

Stent expansion for simple models was performed using a cylindrical tube that expanded to a final diameter of 23mm. Following stent expansion, the cylindrical tube was withdrawn to a position just past the point at which the cylinder leaves the stent surface, using a smooth step amplitude curve. Stent expansion for complex stent deployment was performed by applying a pressure of 4 atm to the inside surface of the balloon. The balloon was then deflated by applying a negative pressure to the inside surface of the balloon.

4.2.5 Valve loading

To simulate the physiological loads on the stent in complex models only, deformed stent geometry and final stress conditions were imported into a new model. Since Perlman et al. (2013) showed that many patients experience a rise in blood pressure following TAVR, with an associated increase in pulse pressure, a uniform pressure of 90 mmHg was applied to the outside surface of the cylindrical portions of stent. In addition, simple leaflets such as those described in section 6.1 were attached to the expanded stent using tie constraints and a conservative pressure of 100 mmHg was applied to the aortic surface of the leaflet to simulate the closing pressure during diastole.

4.2.6 Radial crushing

Radial crushing of stents was modelled by importing deformed geometry (following crimping, relaxation, deployment and recoil stages described above under complex modelling) into a new Abaqus/Explicit model and importing the final complex model stress state as a predefined field. As for the crimping step, 12 discrete rigid plates were moved radially inwards from beyond the stent to an inscribed diameter of 8mm, using hard frictionless contact. Step time was 5s and low mass scaling was used to ensure that kinetic energy was less than 1% of internal energy.

4.3 Model validation

Finite element models were validated for dimensional accuracy through comparison of recoil and foreshortening predictions and actual measurement of these parameters on physical prototypes. For validation of structural accuracy, the Control stent and each of the two favoured stent concepts underwent simulated crimping to 8 mm as for the simple model previously described, although the expansion cylinder was removed. The sum of radial reaction forces on the moving plates was then reported against diameter change. The simulated models were then compared to physical radial crushing tests performed as described in Section 5.3.3 A).

4.4 Parameters for evaluation

4.4.1 Stent static behaviour

Geometry before crimping and geometry after expansion and relaxation were compared to each other. The magnitudes and locations of peak Von Mises Stress, peak Maximum Principal Stress and Peak Plastic Equivalent Strain was reported at the end of each step. The amount of recoil and foreshortening (see definitions in Section 5.3.3 B) were calculated and reported.

4.4.2 Stent radial strength

Radial force was calculated as the sum of radial reaction forces on the twelve moving plates and reported against diameter change. Radial strength was defined as the force required to compress the 23mm stent by 15%, namely to 19.55mm.

4.4.3 Stent fatigue

Stent fatigue analysis was performed using a traditional Stress/Life (S-N) or "modified-Goodman" approach (Marrey et al., 2006). In this method the mean stress σ_m and stress amplitude σ_a are calculated based on the Maximum Principle Stresses at beginning and end of the pressure loading step. Reported endurance limits for MP35N vary widely in the literature from 340 MPa to 620 MPa (Altman et al., 1998; Piehler, 2005; Pilliar, 2009), depending on the cold work present in the material, but the endurance limit σ_{el} was conservatively taken to be 340 MPa (Pilliar, 2009). The true stress related to the UTS σ_u was calculated from experimental data (see Section 7.2.1). The fatigue safety factor n, which determines how close the mean stress and stress amplitude are to the modified Goodman line, may be determined as follows:

$$\frac{1}{n} = \frac{\sigma_m}{\sigma_u} + \frac{\sigma_a}{\sigma_{el}}$$

Equation 4-9 Fatigue safety factor

$$\sigma_m = \frac{\sigma_{max} + \sigma_{min}}{2}, \sigma_a = \frac{\sigma_{max} - \sigma_{min}}{2}$$

where σ_{max} and σ_{min} are the maximum and minimum values of the maximum principle stress over the cycle.

Calculation of the inverse of the fatigue safety factor allows the areas most at risk of fatigue fracture to be plotted as a contour plot.

5 Experimental Methods

5.1 Stent Manufacture

Stents were prototyped through laser cutting, acid descaling and electro-polishing. Following laser cutting, stents were descaled using corrosive acid solutions to remove oxides, and then stents were electropolished to achieve smooth surfaces and correct final dimensions. Certain prototypes required additional steps, including grinding and welding to achieve the desired functionality.

5.1.1 Stent Cutting

Drawings obtained from CAD were imported into Computer Numerical Control (CNC) programming software (CAGILA, CAM-Service GmbH, Hannover, Germany) and converted into machine code that could be used by the laser cutter. Stents were laser cut from 23 mm MP35N tubing (wall thickness 0.50mm), sourced in an annealed condition (Minitubes, Grenoble, France), using a StarCut Tube (Rofin-Baasel Lasertech, Starnberg, Germany) with a StarFiber FC fibre laser and 2-axis CNC motion control system. Stents were cut using oxygen as the assist gas and the following parameters: peak power was 200 W; pulse width was 35 µs; frequency was 4500 Hz; oxygen gas pressure was 10 bar. It was found that stents could be cut using a wide range of parameters, but the chosen parameters were determined empirically over several stent cutting attempts and produced reliable cutting, with relatively low reject rates and relatively low levels of oxide formation. Accurate cutting was achieved through rigorous optimisation of laser focus position and centrality and minimisation of tube rotation eccentricity (see Appendix D), and was verified through measurement of calibration disks.

Cut stent strut dimensions were made larger than targeted final dimensions by applying an offset in CAGILA that compensated for the kerf width. The kerf width was estimated to be approximately 50 µm based on discussions with the machine manufacturer (actual measurement of kerf width is described below). Since this means that the laser beam would cut 25 µm on either side of the laser path, an offset of 40 µm was applied to the cutting path. This was therefore expected to provide cut stent dimensions 30 µm larger than final desired geometry (for subsequent reduction during electropolishing).

5.1.2 Descaling

Since laser cutting uses oxygen as an assist gas, an adherent black oxide layer forms on the surface of the stent. In addition to this oxide layer, some or all of the waste tube material remains between the structural elements of the stent, and some dross and burrs remain where the assist gas has not blown the molten material out completely. Waste material and dross were removed mechanically from the laser cut stents, after which stents were immersed in an acidic solution in 50ml centrifuge vials placed in a heated ultrasonic cleaner (Labotec, 2.5L, 50W) for removal of oxides (known as pickling or descaling). A mixture of sulphuric acid, nitric acid, ammonium bifluoride and deionised water was used for pickling, following a period of research and experimentation described in Appendix D. This solution proved to be effective at removing oxides without aggressive base metal attack. Stents were soaked for up to three hours at 70±5°C and were sonicated for five minutes at 100% power every half hour during the soak, until no oxide material was visible on the stent surface. After pickling, stents were sonicated in deionised water for 10 minutes to clean stents and reduce carry-over of pickling solution to the electrolyte, and were then dried in air.

5.1.3 Electropolishing

Electropolishing is an electrochemical machining process routinely used in the production of stents. The process creates a smooth, rounded, low-injury and biocompatible surface. It removes surface imperfections that may result in fatigue crack initiation and growth. It further removes the outer layers of material, thereby removing the heat affected zone and residual surface thermal stresses caused by the heat generated during laser cutting. Electropolishing was performed using the apparatus shown in Figure 5-1.

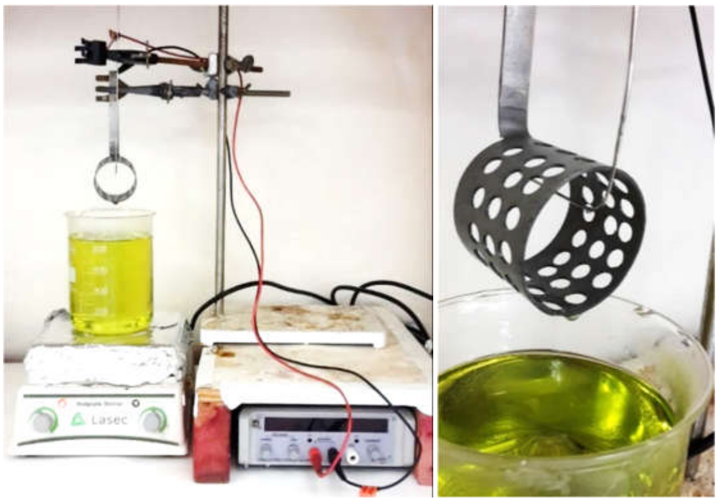

Figure 5-1. Electropolishing apparatus

Stents were electropolished in a glass beaker placed on a heated magnetic stirrer and the electrolyte was stirred using a PTFE-covered magnet stirrer bar. A stainless steel wire was connected as the anode (together with the stent). A cylinder with many holes was used as the cathode; the holes allowed the electrolyte to flow around the stent. Both anode and cathode were positioned horizontally to avoid bubble tracks on the stent surface. A power supply unit capable of providing 3 A was used. The electropolishing process is dependent on a number of factors, including the stent design and material, the stent's initial surface roughness, the chemical composition of the electrolyte, the applied voltage or current, temperature of the electrolyte, the amount of electrolyte agitation and the polishing time (Patil & Dulange, 2014). Stent design, material and surface roughness were taken as provided and therefore unalterable.

A small study was performed to identify a suitable electrolyte and electropolishing solution from the body of available literature (See Appendix D), based on experiments. The electrolyte used by Surmann and Huser (1998) gave the best surface appearance by visual estimation and was used for stent polishing; this electrolyte consisted of 10% Sulphuric Acid, 5% Hydrochloric acid and 85% Glycol by volume. Higher temperatures were used to increase polishing rate without sacrificing surface finish, as Surmann and Huser (1998) had selected a temperature of 48°C to avoid burning the operator, rather than because the best surface finish was obtained at this temperature. A summary of the electropolishing parameters is shown in Table 5-1.

Table 5-1. Electropolishing parameters

Fixed Inputs	Value/Setting
Stent design	Variable design slotted 23 mm outer diameter tube, 0.5 mm wall thickness
Stent material	MP35N (ASTM F562)
Surface roughness (of tubing)	Ra ≤ 0.6 µm
Electrolyte	
Electrolyte chemistry	10% H_2SO_4 (96% concentrated), 5% HCl (37% concentrated), 85% $C_2H_6O_2$
Variables	
Current	2A
Temperature	60 ± 5 °C
Agitation	ca. 240 rpm (mild)
Polishing time	Total ca. 6-9 min over two cycles. Stents were polished to desired weight. Stent was rotated approximately 120° three times during each cycle.
Stent-cathode distance	ca. 1cm at nearest point

Removal of stent material during electropolishing is inhibited at the area where electrical contact is made with the stent by the anode wire, so the stent was rotated three times during polishing to ensure that the stent polished evenly and that the contact point with the stainless steel anode wire was moved. Stents were polished to the weight calculated from the CAD software. To ensure correct weights were achieved, stents were subjected to approximately 4.5 minutes of electropolishing, followed by cleaning, drying and weighing. The weights of the partially polished stents were used to calculate polishing rates (the weight of the pickled stents had also been measured), and the times for the second polishing cycle were established from these rates. Polishing rate decreased as the electrolyte aged, but polishing quality was not noticeably affected.

5.1.4 Additional manufacturing steps

As described in subsequent chapters, some stent concepts were equipped with wire arms for anchorage. The arms were constructed by plastically deforming 0.44mm MP35N wire (sourced from Fort Wayne Metals, Fort Wayne, Indiana in a cold worked condition) and then spot welding the ends of the wire to the outside of the commissures of the stent using a Desktop Welding Laser (Rofin-Baasel Lasertech, GmbH & Co.KG., Starnberg, Germany). Certain stent concepts were required to have wall thickness reduced in regions designed to protrude outwards. In these cases material was removed from the inner surface by manually grinding with a rotary multi-tool equipped with a grinding disk.

5.1.5 Valve Manufacturing

Polymeric valves were manufactured through a proprietary spray coating process to produce flexible leaflets of thermoplastic silicone polycarbonate polyurethane (Carbosil, DSM Biomedical B.V., Geleen, The Netherlands) with a leaflet thickness of approximately 150µm. After drying overnight, valves were removed from the mould and the free edge of the leaflet was cut with miniature scissors or a scalpel. A sealing skirt was provided in one of two ways, either by creating a sprayed polyurethane film during the final spraying cycle, or using an electrospun fabric manufactured by SATH from the same polyurethane and heat bonding to the stent below the level of the leaflet attachment, to seal the valve to prevent paravalvular leak.

Bioprosthetic versions of valves were manufactured and implanted in certain animals. For these valves, stent designs were very similar to stents for polymeric valves, but valve attachment sites of stents incorporated holes for sutures. Valve leaflets were manufactured by sourcing porcine pericardium from a local abattoir. Following thorough cleaning of the pericardium and removal of fat layers, pericardium was either cross-linked in 0.7% glutaraldehyde solution or was decellularised (Tedder et al., 2009) and subsequently crosslinked. Leaflets were then cut out of the pericardial sheets using die cutters to produce leaflets that were approximately 0.25mm thick, with collagen aligned in the circumferential direction. Sealing skirts manufactured from either electrospun polyurethane (produced by SATH) or from polyester knitted fabric (Bard Peripheral Vascular OEM Products, Tempe, Arizona, USA) were stitched to the stents. Leaflets with similar thickness were then manually stitched onto the stents.

5.2 Materials Testing

Three miniature dogbone samples were laser cut from the 23mm MP35N tubing described above. The geometry of the dogbone specimens is shown in Appendix F. Samples were descaled to remove oxide and burrs. Cross-sectional area was measured by sectioning a dogbone specimen in half, grinding the resulting surface using 4000 grit abrasive paper (also shown in Appendix F) and using a calibrated stereo microscope with parallax adjustment to measure the dimensions of the gauge portion (a sector of the tube). Simple custom grips were designed and manufactured to hold the specimens. These are shown in Figure 5-2.

Figure 5-2. Tensile grips

Following a preload of 5N, specimens were subjected to tensile loading to break at a rate of 12.5mm/min. Three specimens chosen at different locations on the tube circumference were tested to determine UTS, 0.2% yield stress and strain to break. Engineering stress and strain were then converted to true stress and strain (before necking, where volumetric change during plastic deformation is assumed to be negligible) for use in FEA with the following equations:

$$\sigma_t = \sigma_e\,(1 + \varepsilon_e)$$

Equations 5-1 True Stress and Strain

$$\varepsilon_t = \ln\,(1 + \varepsilon_e)$$

where σ_t and σ_t are the true stress and strain, respectively, and σ_e and ε_e are the engineering stress and strain, respectively.

After necking, stress-strain data were extrapolated using Hollomon’s power law (Joun, Choi, Eom, & Lee, 2007):

$$\bar{\sigma} = K_{\mathrm{N}}\bar{\varepsilon}^{n_{\mathrm{N}}}$$

Equation 5-2 Hollomon’s Law

where $\bar{\sigma}$ and $\bar{\varepsilon}$ are the effective stress and strain, respectively, K_{N} is the reference strength coefficient and n_{N} is reference strain-hardening exponent, defined as the true strain at the necking point. K_{N} and n_{N} are calculated as follows:

$$K_{\mathrm{N}} = \sigma_e^{\mathrm{N}}\,(1+\varepsilon_e^{\mathrm{N}}) \Big/ \left[\ln(1+\varepsilon_e^{\mathrm{N}})\right]^{\ln(1+\varepsilon_e^{\mathrm{N}})}$$

Equations 5-3 Hollomon parameters

$$n_{\mathrm{N}} = \ln\left(1+\varepsilon_e^{\mathrm{N}}\right)$$

where $\varepsilon_e^{\mathrm{N}}$ is the nominal strain at the necking point and σ_e^{N} is the nominal stress at the necking point

5.3 *In Vitro* Stent Testing

This section describes laboratory testing performed on materials, stents and valves in order to characterise performance and compare design outputs to the customer requirements.

5.3.1 Testing overview

All stent concepts that were manufactured (see Chapter 6) were crimped onto either SATH deployment devices or onto used commercial balloon catheters and were deployed using manual disposable indeflators equipped with pressure gauges. Physical prototypes were subjectively compared to numerical simulations in terms of crimping and deployment behaviour. Two favoured concepts were then subjected to rigorous testing as outlined below, including inspection, measurement and a variety of mechanical tests of performance. A Control stent was also manufactured, inspected and tested in the same manner (see Section 4.2.1). Throughout testing, continuous variables were expressed as mean ± standard deviation and comparisons were performed using a two-tailed *t* test, with $p \leq 0.05$ considered statistically significant.

5.3.2 Inspection and Measurement

As described above, stents were drawn at the final desired dimensions, an offset was applied during the creation of programmes for laser cutting, and sufficient electropolishing was performed to return the stent to its desired weight and therefore dimensions. Kerf width was measured in the longitudinal and circumferential directions by cutting several slots in a short section of tubing, in both directions. After pickling, the width of the slots was measured near the end of the cut to eliminate the effects of initial piercing and to reduce any possible warping due to high cutting temperatures. In order to confirm that stent dimensions matched the designed dimensions and surface quality was acceptable, stents were inspected and measured after electropolishing.

A Nikon stereo microscope was used to inspect the quality of the stent surface at magnifications between X13 and X90. A stent manipulation frame was manufactured from acrylic and glass and was used to rotate the stent within the field of view, using top ring lighting. Additional high magnification inspection of stent surface quality was performed using a LEO S440 Scanning Electron Microscope (SEM). Stent dimensions were measured by photographing the stent struts at a magnification of 40X using a metallurgical microscope with lighting through the objective and back-lighting provided inside the stent using LED strip lighting. Struts were positioned orthogonal to the top light path, and the microscope was adjusted until the edges of the strut came into sharp focus, which occurs just below the outside surface of the stent and represents the widest dimension of the trapezoidal cross-section of struts.

Three stents of each favoured design and the Control stent were measured. Strut width and hairpin width were measured in duplicate at the top and bottom ends of the stents on one of the repeating stent “thirds” corresponding to leaflet locations. Strut width was then also measured in the same way for each of the other stent thirds (total of 12 strut width measurements per stent). Thickness was measured at a single region with direct line-of-sight from the outside. Commissure post width, crown-shaped member width, arm width, vertical member width, hinge width and link width, where appropriate, were measured on a single third on each stent. This led to a total of 20 to 22 measurements per stent. Measurement locations are further illustrated in Section 7.2.2.

5.3.3 Stent Mechanical Testing

To determine whether stents satisfy the requirements identified in Section 3.1.2, stents were tested for radial strength, recoil, crimping/expansion behaviour, foreshortening, migration resistance and manufacturability.

5.3.3 A) Radial Crush

The radial force required to crush stents were tested using a stand-alone RX650 segmented head radial strength testing machine (Machine Solutions Inc.). Stents were crushed from a diameter of 23 mm or 30 mm to a diameter of 8 mm. Tests were performed following encoder alignment and diameter and force calibration. Test speed was 1 mm/s. The temperature of the segmented head was maintained at 37 ± 1.2 °C.

The hoop force F_H was calculated from the transducer force using $F_H = 0.156 \quad F_T$. Radial force was in turn calculated from

$$F_R = 2\,\pi\,F_H$$

Equation 5-4 Radial force

5.3.3 B) Crimping, Deployment, Recoil and Foreshortening

Stents were crimped onto balloons using an Edwards Lifesciences disposable crimper following calibration of crimper diameter with respect to handle motion, to ensure that stents were crimped to a diameter of 6mm. The diameter of the stent was measured at three points along the length, namely the top, the bottom and in the annular area of the stent, using Vernier callipers, and total stent length was measured.

Stents were then inflated on balloons to 4 atm and stent diameter was measured at the three locations along the length of the stent. Balloons were deflated and the stent diameter was measured at the three positions again. The dimensions of any protruding members were also measured.

The shape of the stent, in particular the shape of the crown structure, was compared to the undeformed geometry to estimate the maximum deviation from the original shape; stents were photographed before crimping and after expansion.

Foreshortening was calculated as the percent change in stent length from a crimped to deployed condition. Recoil was calculated as the percentage change in stent diameter from its expanded condition on the balloon to its final relaxed state:

$$Foreshortening = \frac{(L_c \quad L_r)}{L_c} \quad 100$$

$$Recoil = \frac{(D_e \quad D_r)}{D_e} \quad 100$$

Equations 5-5 Foreshortening and recoil

where L_c is the relaxed stent length after crimping, L_r is the relaxed stent length after expansion, D_e is the expanded stent diameter while on the balloon, and D_r is the relaxed diameter following withdrawal of the balloon

The deformed shape of the stent determined experimentally was also compared to numerical predictions of the deformed shape. Stents were also over-expanded by 10% on a 25 mm valvuloplasty balloon and then further on a 29 mm balloon to determine failure point.

5.3.3 C) Migration Resistance

The ability to anchor in the aortic root was quantified by deploying stents inside a 25 mm Medtronic Freestyle xenograft and measuring the force required to dislodge the stents in the direction of the ventricle. A 23mm valve closing under a diastolic pressure of 100 mmHg will experience a downward force of 5.4N. Sutures were attached to the bottom row of struts and the sutures were pulled in an axial direction using a portable force gauge until the stent was extracted or the Freestyle valve appeared to show signs of damage (the test was halted at 22N, which corresponds to four times the anticipated force acting to dislodge valves in patients).

5.3.3 D) Manufacturability

As described above, polymeric valves were manufactured by placing stents onto machined forming mandrels. Stents were therefore evaluated for their ability to be expanded to 23mm inside diameter and placed over the mould for polymer valve manufacture, without fracture.

5.4 *In Vitro* and *Ex Vivo* Valve Testing

5.4.1 Valve deployment

A polymer valve was crimped onto an SATH deployment device (mechanical expander and annular balloon). The valve was then deployed to verify correct interaction between device and valve, and to determine whether the valve changed position over the deployment cycle. In this way compensation could be made to ensure the valve is deployed in the intended anatomical location. Valve deployment was filmed for subsequent still frame extraction to determine valve shape and position in the crimped condition, initial expansion using the mechanical expander and final expansion using the annular balloon. The displacement of the nadir of the valve from the initial crimped position to the final deployment position was measured digitally.

5.4.2 Explanted heart tester

Valve “simulated use” performance was evaluated by implanting valves into an *ex vivo* “explanted heart” model (using cadaveric pig or sheep hearts) and visualising using endoscopy. Hearts purchased from an abattoir were trimmed of excess tissue, and the heart was cannulated in the left ventricle, aortic arch and left atrium. A valved access port for device entry was also inserted through the apex of the heart, after the placement of purse-string sutures, into the left ventricle. Any leaks were sealed using cable ties or surgical clamps.

The test apparatus, provided by SATH, is shown in Figure 5-3. A lead screw-driven reciprocating pump was used to pump water through the apex, into the left ventricle, through the native aortic valve, to empty into a reservoir. The reservoir supplied a head of water into the left atrium, which allowed the ventricle to fill during reverse motion of the pump's piston. Systemic resistance and compliance were supplied by a flow restrictor and a Windkessel chamber, respectively. This allowed near-physiological cardiac output, aortic and ventricular pressures to be maintained at a heart rate of 60 beats per minute. A side port in the pipe entering the left ventricle provided an endovascular ventricular view of the aortic (and mitral) valve and a port in the right subclavian artery provided an aortic view of the aortic valve.

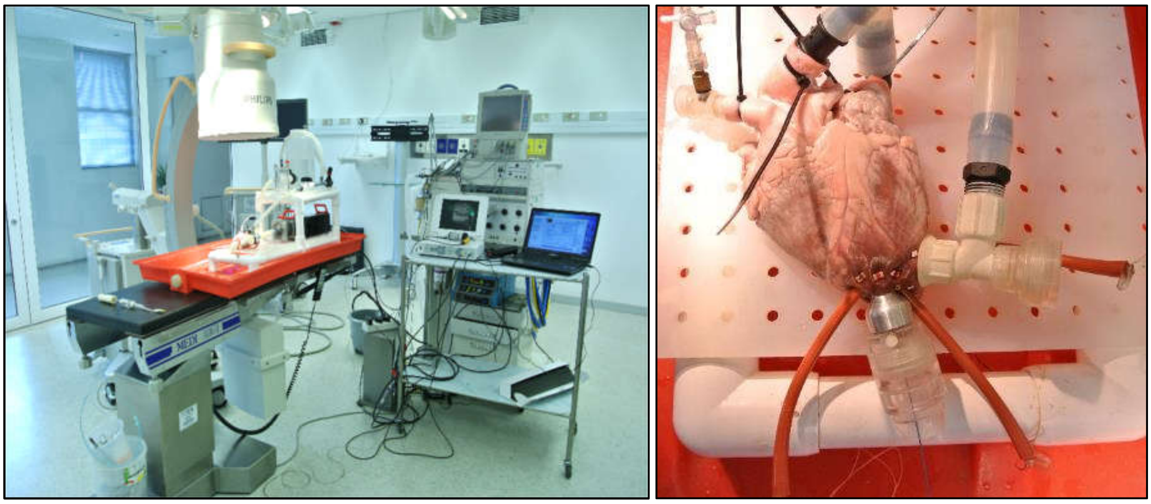

Figure 5-3. Photographs of explanted heart rig, showing A) rig placed on table in operating theatre with fluoroscopy and endoscopy available, and B) cannulated heart.

The explanted heart apparatus was placed on an operating table. Valve location and positioning was guided by fluoroscopy (using a portable C-arm), although videos were also captured using the endoscope by another operator.

5.4.3 Pulse duplicator

In order to evaluate stent performance as part of a valve, valve hydrodynamics were tested using a left heart simulator known as a pulse duplicator (ViVitro Labs Inc., Victoria, Canada), using water as the test medium. The pulse duplicator measured aortic flow, aortic and ventricular pressures over the heart cycle. Refer to Figure 5-4. From these measurements, the mean transvalvular pressure drop and effective orifice area (EOA) during systole, and the total regurgitant fraction during diastole were determined.

EOA was calculated (De Gaetano et al., 2015; ISO-5840-3, 2013) using Equation 5-6 below.

$$EOA = \frac{Q_{RMS}}{51.6\sqrt{\frac{p}{\rho}}}$$

Equation 5-6 Effective Orifice Area

where p is the mean pressure difference in mmHg, ρ is the density of the water in g.cm^{-3}, and Q_{RMS} is the root mean square of forward flow in mL/s and is given by

$$Q_{RMS} = \sqrt{\frac{\int_{t_1}^{t_2} Q(t)^2}{t_2 \quad t_1}}$$

Equation 5-7 Root mean square of flow

where $Q(t)$ is the instantaneous flow at time t, t_1 is the time at the start of forward flow and t_2 is the time at the end of the forward flow

Valves were tested at a heart rate of 70 beats per minute, cardiac output of 5 L/min and a mean arterial pressure of 100 mmHg. Systole was assumed to make up 35% of the cardiac cycle. Valves were filmed from the outflow end using a camera with a frame rate of 400 frames per second in order to qualitatively evaluate valve performance. Valve performance was compared to a 23mm surgical Hancock 2 tissue valve (Medtronic, Dublin, Ireland).

5.4.4 Valve Fatigue

Stent fatigue resistance was evaluated using a BDC Labs High Cycle durability tester, shown in Figure 5-5. Valves were mounted in appropriate silicone holders and tested under pulsatile loading at 15Hz until valves failed or were replaced. A stroboscope was used to verify that accelerated frequency leaflet function appeared to be similar to physiological heart rate leaflet function. Stroke length and resistance for each valve were adjusted individually to maintain a target peak differential pressure of 100 mmHg over the closed valve for over 95% of the test cycles and to maintain the pressure at 100 mmHg or greater for 5% or more of each cycle duration. The stroboscope was used to inspect valve functionality on week days, and valves were removed from the equipment for inspection for evidence of stent failure every 100 million cycles, upon visual evidence of leaflet failure, or when valves had to be removed to accommodate testing of other valves.

Figure 5-4. ViVitro pulse duplicator

Figure 5-5. BDC Labs durability tester

5.5 *In Vivo* Experimental Methods

Valves were tested in pigs in two study groups. The first study group involved implantation of *self-locating* (referred to in later chapters as Design 1) valves in 9 pigs. The second study group, performed after the first group, involved the implantation of valves that could *self-anchor* (referred to in later chapters as Design 2) but not self-locate (on second-generation deployment devices that incorporated location mechanisms) in 8 pigs. All experiments were performed in the operating theatre at UCT's Cardiovascular Research Unit, shown in Figure 5-6. All experiments were performed with the approval of the University of Cape Town Faculty Health Sciences Animal Ethics Committee (FHS AEC), with reference numbers 013/021 and 014/015. As for bench testing, continuous variables were expressed as mean ± standard deviation and comparisons were performed using a two-tailed *t* test, with $p \leq 0.05$ considered statistically significant.

5.5.1 Study Design

a) Pig Study Group 1

The aim of the first study group was to evaluate the ability to successfully deliver and place a replacement self-locating aortic heart valve within the native aortic valve, and to evaluate valve performance following implantation.[4]

Figure 5-6. Operating theatre

Twelve animals were included in the group, with a mean weight of 47.7 ± 3.2 kg (range 41.4 to 55.0 kg). Three animals died prior to any attempt to implant an aortic valve, due to procedural complications.[5] Valves were therefore implanted into nine animals, in four subgroups: Helical Balloon (HB) with Polyurethane (PU) valve (n=3); Mechanical Expander (ME) with Bioprosthetic (BP) valve (n=3); HB with BP (n=1); ME with PU (n=2).

b) Pig Study Group 2

The aim of the second pig study group was to evaluate the ability to deploy self-anchoring transcatheter heart valves (see Concept 2D of Section 6.3) using deployment devices that incorporated location members (for tactile feedback). These tests were intended to be used to verify the acceptable delivery, positioning, deployment and functioning of the stent *in vivo* without migration or

---

[4] The same animals were also used to evaluate aortic deployment and mitral repair devices designed by SATH but this will not be described in detail here.

[5] In two cases the animal could not be resuscitated following arrhythmias caused during port insertion; the third animal died due to arrhythmia that occurred in preparation for predilatation of the valve and blood loss that occurred following damage to the port back-up seal by the deployment device.

embolization. Following a pilot study of four animals to evaluate the location performance of deployment devices, eight animals were included in the group, with a mean weight of 47.7 ± 3.1 kg (range 45.0 to 54.9 kg).

5.5.2 Procedure

White landrace pigs sourced from a commercial farm were pre-medicated, intubated and restrained in a dorsal recumbent position. Animals were then placed on positive pressure ventilation and anaesthesia was maintained through inhalation of isoflurane and nitrous oxide.

The right femoral artery was accessed percutaneously, a 6F sheath was placed and a diagnostic pigtail catheter was advanced to the aortic valve cusps for contrast angiography. Injection of contrast medium allowed favourable positioning of the C-arm to be established. Lines were placed in the left femoral artery for monitoring of arterial blood pressure and in the left femoral vein for infusion of fluids and drugs and the measurement of central venous pressure (CVP). In certain animals a cannula was inserted into the left atrial appendage for left atrial pressure. Ventricular pressure was measured through the apical access port and aortic pressure was measured through the pigtail catheter. Transoesophageal echocardiography (TOE) and fluoroscopy were used during all procedures.

All procedures were performed using a transapical approach. Access to the heart was obtained by performing a full sternotomy, after which two concentric pursestring sutures were placed on the left ventricular apex with several pledgets. All animals were heparinised and adequate levels of heparinisation were maintained by measuring activated clotting time (ACT). The apex was punctured with a needle and a guidewire was advanced into the left ventricle, across the aortic valve into the ascending aorta. A customised dilator and sheath provided by SATH were then passed over the wire into the left ventricle.

In preparation for implant, valves were crimped onto deployment devices using a disposable valve crimper and were partially or completely covered with a thin-walled sleeve. Crimped valves were advanced through the sheath, after which the protective sleeve was removed. In the case of self-locating valves, the valves were advanced through the native aortic valve and withdrawn until correct location was established in a tactile manner. Position was then confirmed using fluoroscopy and/or echocardiography. In the case of self-anchoring valves, the crimped valve was placed across the native aortic valve and positioned using fluoroscopy, echocardiography, tactile feedback incorporated in the deployment device, or a combination of these techniques. Once the valve was judged to be in the correct position, the valve was deployed using a manual indeflator to inflate the device balloon.

Replacement valves were evaluated for their ability to access the aortic root, be positioned correctly, be deployed in the correct position and allow the delivery device to be withdrawn out of the valve. Delivery success was defined as successful insertion of the crimped valve through the access port and positioning of the valve across the aortic annulus. Location success was defined as the positioning of all three arms within the native cusps. Deployment success was defined as the ability to inflate the replacement valve across the aortic annulus. Withdrawal was judged to be successful when the deployment device could be removed from the implanted valve. Valves were judged to be anchored if they were in the correct position (if at least two of the valve arms were at or above the level of the basal ring and the bottom of the valve was within the annulus) and the valves did not embolise. Valve function was judged to be acceptable if replacement leaflets appeared to open and close. Sealing was judged to be successful if there was mild or negligible leak or regurgitation.

6 Concept development

6.1 Basic Structure – Native Valve Mimicking Shape

During the establishment of the current research project, a simple stent based on repeating zig-zag patterns (such as those described in Section 2.5.2) was designed, used to manufacture bioprosthetic valves and tested in the explanted heart tester. The same stents were used to manufacture polymeric valves. This experience confirmed two significant limitations of these designs. Firstly, the valves rapidly embolised into the ventricles of the compliant porcine hearts due to insufficient anchoring within the heart (refer to Figure 6-1).

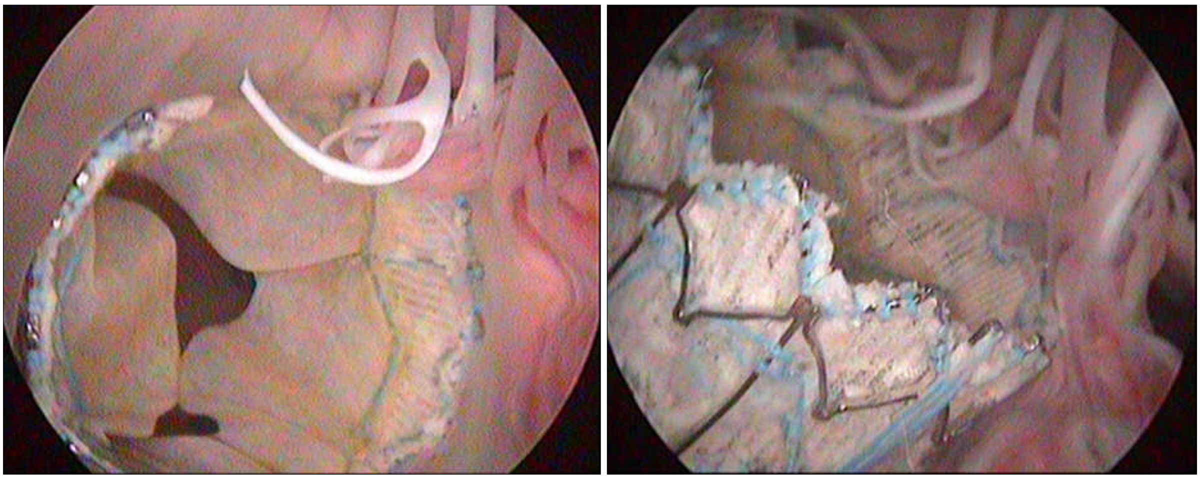

Figure 6-1. Images from explanted heart tester showing the left ventricular aspect of a first generation zig-zag valve A) immediately after deployment and B) following embolization of the valve into the ventricle after several seconds

Secondly, leaflets were attached to a polymer film formed around the stent during coating, rather than to the stent frame itself. This led to the deposition of large amounts of polymer (which caused a large crimping profile) and the delamination of polymer film and leaflets from the frame during expansion, due to large strains in the polymer "windows" incurred during crimping. Although it is possible to sew polymer film leaflets onto a fabric skirt such as Edwards Lifesciences had done during their early development of TAVR (Rowe & Bash, 2012), this negates one of the key advantages of a polymeric valve, namely low cost manufacture through automation.

It was therefore decided to use a crown (scallop) shaped stent that allows the leaflets to have a continuous contact zone along the metal of the stent, with the optimum shape of the leaflet attachment zone determined using FEA. As described in Chapter 2, many different leaflet shapes have been proposed, although most of this work was done on surgical valves. For a compressible valve with a continuous attachment zone, it was important to select a shape that minimises stresses in the leaflets (to improve longevity) and minimises stresses incurred in the stent structure during crimping and deployment (to reduce the risk of acute fracture and fatigue failure).

The height of the 23 mm Edwards Sapien™ valve was 14.5 mm (Padala et al., 2010), which means that the height of the cusps was approximately 12.5 mm. Recognising the need to increase valve height to reduce stresses at the commissures of a polymer valve (Vesely, 2003), but also to maintain valve height near mean normal coronary artery heights, a leaflet height for this thesis was chosen to be 14mm.

Bézier curves were used to define different shapes for the crown.[6] The explicit formulation of a Bézier curve of order n is as follow:

$$\mathbf{B}(t) = \sum_{i=0}^{n} \binom{n}{i} (1-t)^{n-i}\, t^{i} \mathbf{P}_i, \qquad 0 \le t \le 1$$

Equation 6-1 General Bézier Curve

> where $\binom{n}{i}$ are binomial coefficients and $\mathbf{P}_0$ through $\mathbf{P}_n$ are control points defining the curve. $\mathbf{P}_0$ and $\mathbf{P}_n$ are the ends of the curve but in general intermediate points do not lie on the curve.

By altering a few parameters an infinite number of curve shapes may be thereby be generated. For a third order (cubic) curve, with n = 3, the function may be expressed as follows:

$$\mathbf{B}(t) = (1-t)\mathbf{P}_0 + 3t(1-t)^2\mathbf{P}_1 + 3t^2(1-t)\mathbf{P}_2 + t^{\mathbf{3}}\mathbf{P}_3, \qquad 0 \le t \le 1$$

Equation 6-2 Cubic Bézier Curve

Bézier curves for crown construction were drawn on the $x-z$ plane before wrapping around a 23mm diameter cylinder. An example of the cubic curves used for crown construction is shown in Figure 6-2.

$\mathbf{P}_3$ was selected to be on the origin of the $x-z$ axis ($x = 0,\ z = 0$). $\mathbf{P}_0$ was positioned at a commissure, namely at a leaflet height, H, of 14mm and leaflet half-width equal to one-sixth of the circumference, πD ($x = -\pi D/6,\ z = 14$).

$\mathbf{P}_1$ could then be chosen from a range of values where $x = -\pi D/6,\ 0 < z < H$ and $\mathbf{P}_2$ could be chosen from a range of values where $-\pi D/6 < x < 0,\ z = 0$. In this way all crown shapes were generated by merely altering z_1, the z value of $\mathbf{P}_1$, and x_2, the x value of $\mathbf{P}_2$. Eight different curves were generated in this manner and are shown below in Figure 6-3.

---

[6] Bézier curves are parametric curves that may be used to generate smooth curves based on a finite number of parameters.

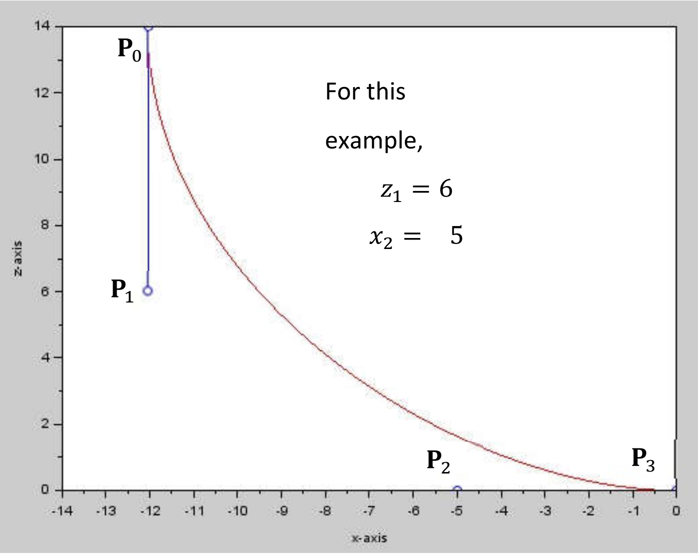

Figure 6-2. Example cubic Bézier function from Scilab used to construct crowns

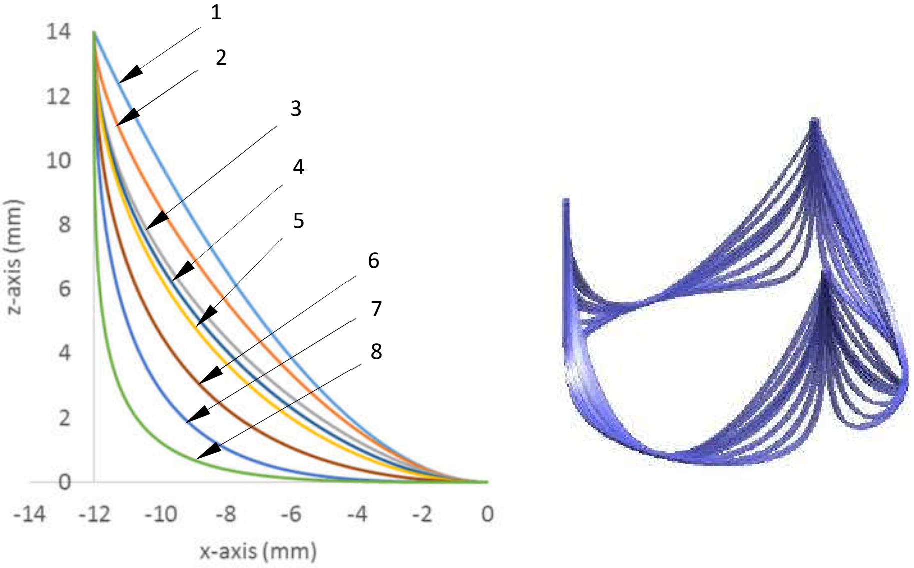

Figure 6-3. Diagram showing eight different Bézier curves generated in the x-z plane, and as crown structures

Curves were generated in Scilab and imported into SolidWorks as multiple points on a plane for subsequent joining by a spline, and the creation of a 0.4 mm wide by 0.5 mm thick three-dimensional crown shape with an outer diameter of 23 mm. For each crown shape a single simplified leaflet was drawn with a belly length equal to the valve height and a free edge of arc length 25.96 mm, as shown in Figure 6-4. A surface was then lofted from the crown-shaped base up to the free edge. This leaflet shape is not used in real valves but served to aid in the selection of appropriate crown shape.

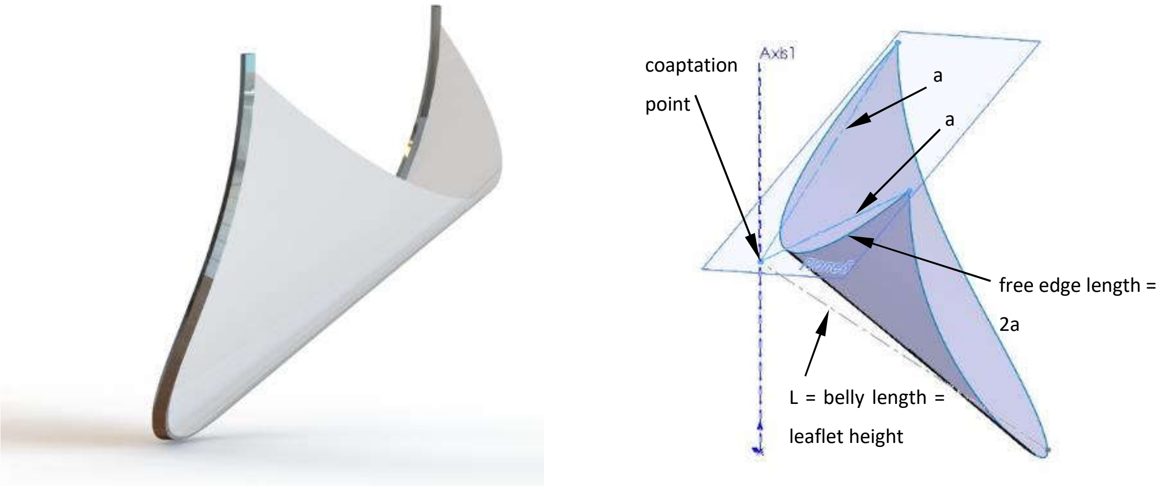

Figure 6-4. A) Crown-shape generated from Bézier curves, with simple leaflet attached. **B)** Simplified Leaflet

Each one-third crown structure was then subjected to simulated stent crimping using five crimping plates in a manner similar to that described in Chapter 4 and shown in Figure 6-5, and maximum Von Mises stresses were reported. In separate models, each leaflet was then fully constrained along the leaflet attachment line and a uniform pressure load of 40 mmHg was applied to the surface of the leaflets, firstly on the aortic side and secondly on the ventricular side. At this stage the leaflet was assumed to have a thickness of 0.15 mm and to be linearly elastic with a Young's modulus of 13 MPa. Maximum Von Mises stress was reported for each leaflet.

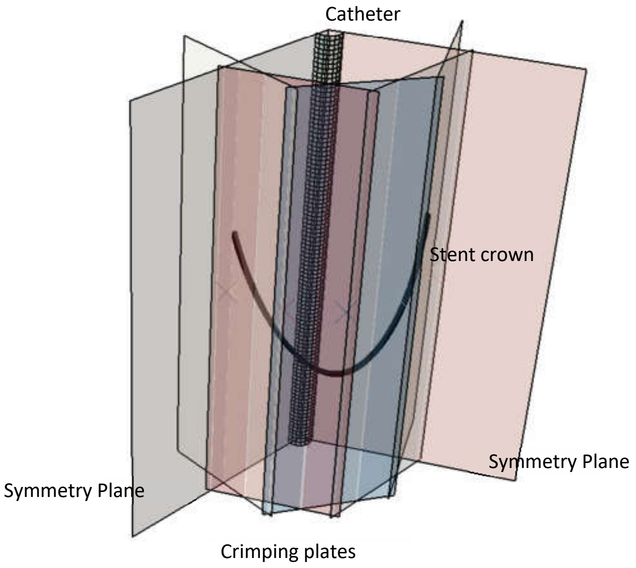

Figure 6-5. Finite element model geometric representation for Bézier analysis

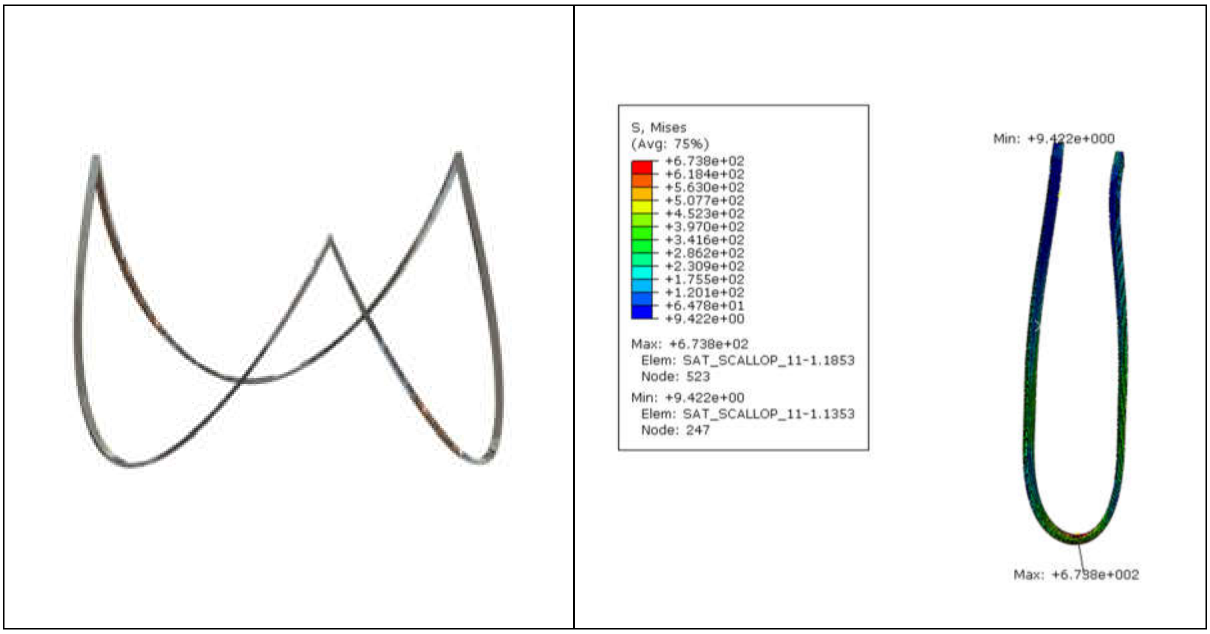

Figure 6-6. Bézier Crown Version 1 geometry (left) and FEA Von Mises Stress after crimping (Right)

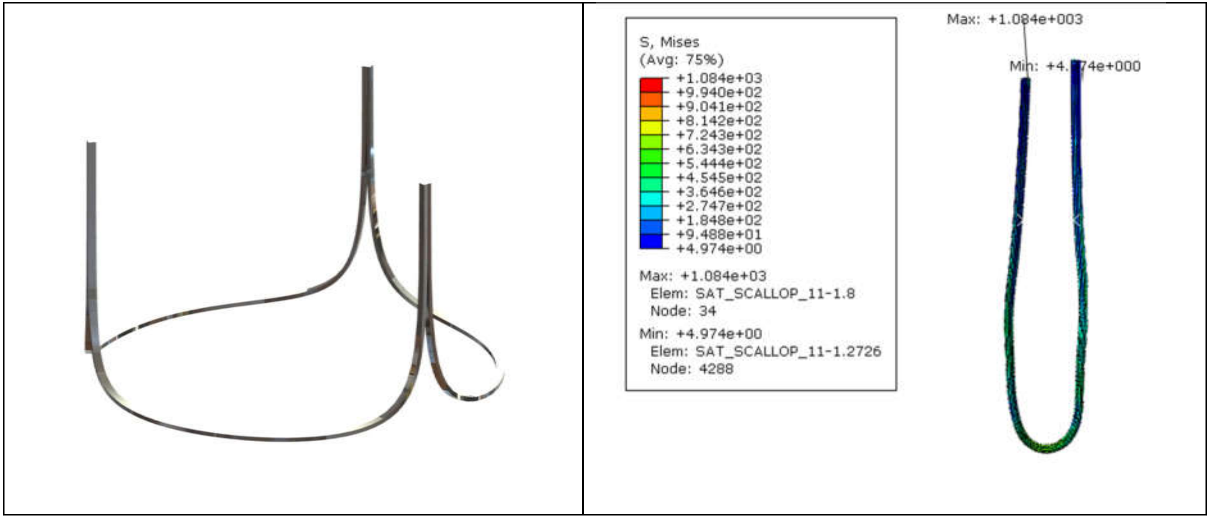

Figure 6-7. Bézier Crown Version 8 geometry (left) and FEA Von Mises Stress after crimping (Right)

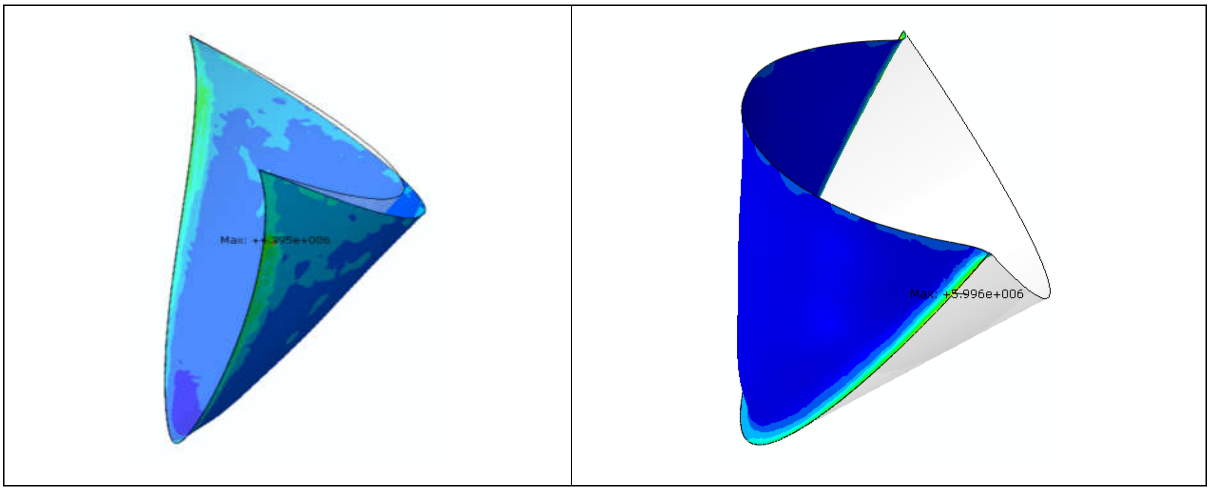

Figure 6-8. Von Mises Stress for leaflet from Bézier Crown Version 2 under closing pressure (left) and for leaflet from Version 1 (right) under opening pressure

The two extremes of the crown shapes with the respective Von Mises Stress results are shown in Figure 6-6 and Figure 6-7. Example Von Mises stress distributions for two of the leaflet shapes, one in each of closed and open configurations, are shown in Figure 6-8. The maximum Von Mises stress values for each of the eight geometries investigated are shown in Figure 6-9. Von Mises Stress values differed for each crown shape, for stents as well as leaflets. The lowest peak stent stress (674 MPa) occurred in Crown 1, which had the narrowest geometry at the nadir, while the highest stent stress occurred in Crowns 7 and 8 (1139 MPa and 1084 MPa, respectively), which had the widest geometry at the nadir. The location of the peak stress changed from near the nadir to near the commissures as the crown widened. Leaflet opening stress had the highest values for extremes of geometry, namely Crowns 1 and 8 (6.0 MPa and 6.5 MPa, respectively). Although Crown 1 also had high closing stress (4.4 MPa), Crown 8 did not have high closing stress (2.2 MPa).

Local stress minima occurred for an intermediate crown shape, Crown 4, which had a peak stent stress of 695 MPa, a peak opening leaflet stress of 4.7MPa and a peak closing leaflet stress of 2.3 MPa. This crown had the second lowest stent stress, the second lowest opening leaflet stress and the third lowest closing leaflet stress. This geometry was therefore chosen as the basic structure for further stent design.

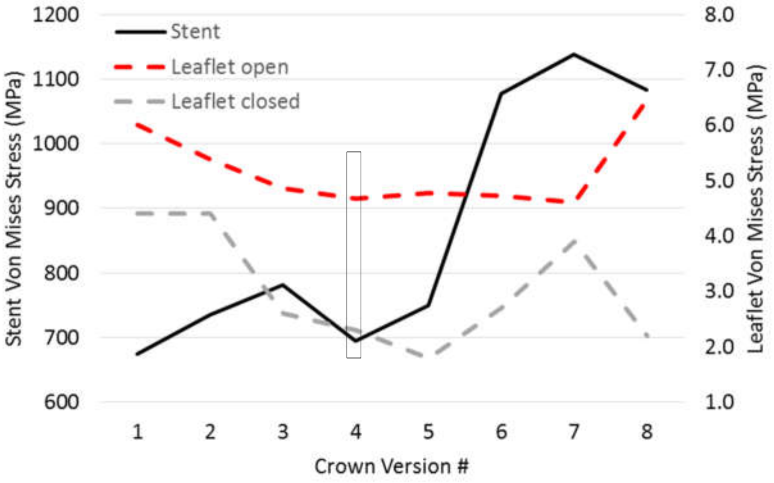

Figure 6-9. Graph showing maximum Von Mises stress in crown structure and leaflets for different Bezier functions. Stresses for the chosen crown shape, Version 4, are shown in the rectangle.

6.2 Ideation and Concept Generation

Since anchoring of the stent was identified to be one of the most critical and challenging components of the stent design, ideas for many different potential anchoring locations were generated. These included anchoring the stent behind the leaflet cusps, anchoring in the basal ring (virtual annulus) and anchoring by making use of the shape of the Sinus of Valsalva. Figure 6-10 shows all potential anchoring positions explored.

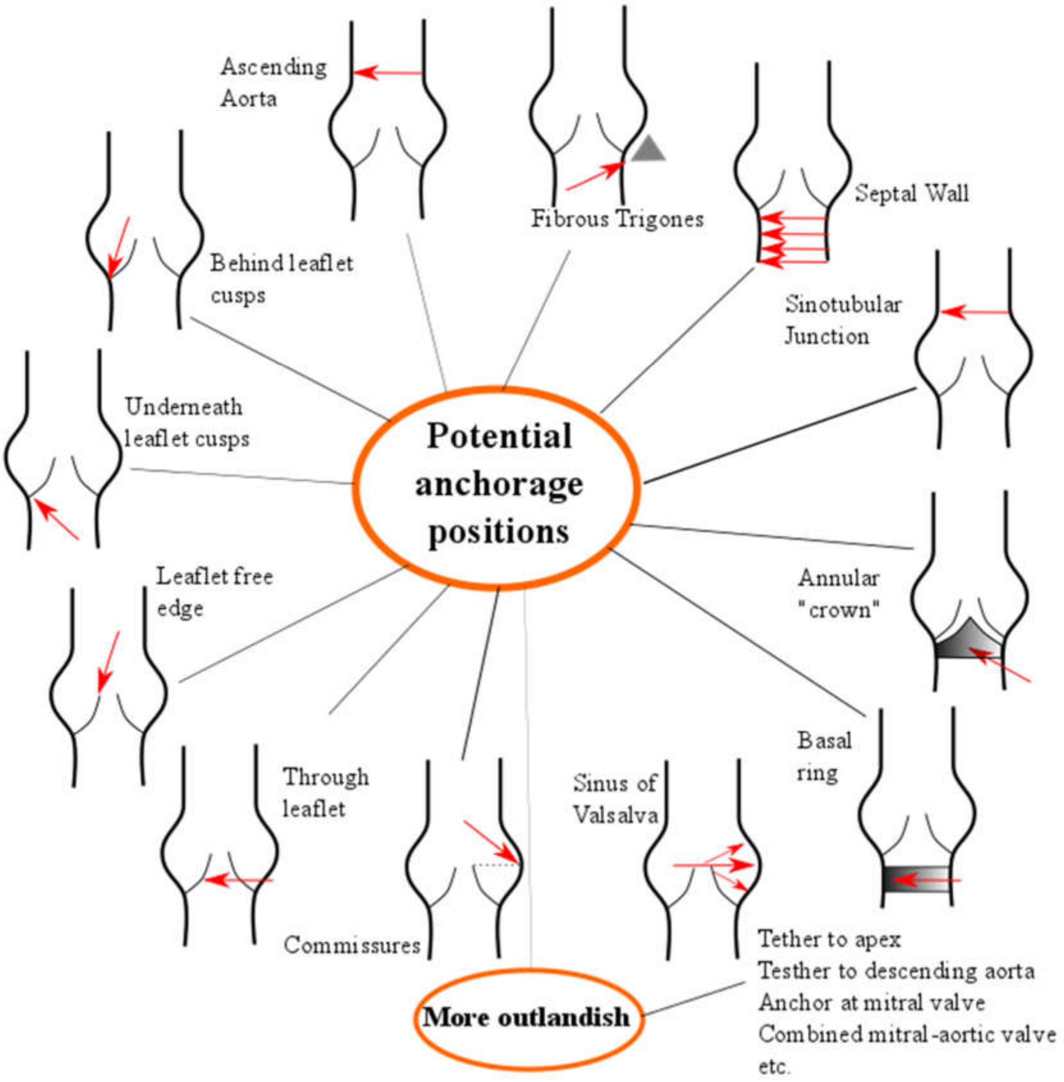

Figure 6-10. Potential anatomical positions considered for stent anchoring

Self-expanding stents, which to the author's knowledge are all constructed from Nitinol, have the advantage that they can be given any of a multitude of different shapes through a process known as shape setting. The stent is constrained in some way on a mould and a heat treatment is performed to set the desired shape and provide the stent with shape memory and/or super-elastic properties.

Designers of balloon-expandable valve stents face a number of relatively unique limitations and challenges relating to stent structure. Chief among these are 1) the requirement for the stent to be formed in such a way that it compresses to the crimped diameter in a predictable manner and remains in this crimped condition when the crimper is removed, and 2) the requirement that the deployed stent shape has to be achieved through mechanical expansion.

6.3 Concept Development

The conceptual design processes described above generated many different concepts for overall stent shape, key structural members and in particular mechanisms for stent anchoring and location.

Table 6-1. Main stent concepts

		Anchorage Mechanisms			
		Friction	**Sinus**	**External arms**	**Integrated arms**
Crown Support Structure	**Top/ Bottom Support**	CONCEPT 1A	CONCEPT 1B	CONCEPT 1C	CONCEPT 1D
		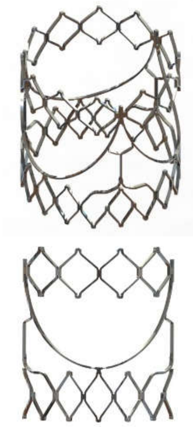		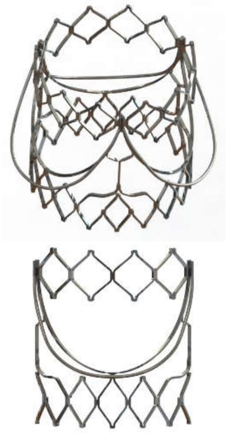	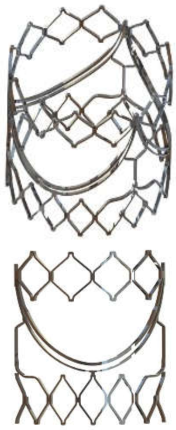
	Inter-mediate Support	CONCEPT 2A	CONCEPT 2B	CONCEPT 2C	CONCEPT 2D
				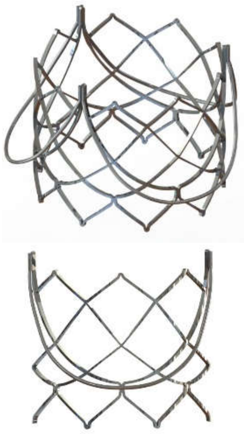	

Concepts were either sketched by hand or on computer and were evaluated qualitatively, taking into account anticipated function, simplicity of design, manufacturing feasibility, aesthetics, ability to be incorporated into the delivery and deployment methods of the non-occlusive deployment devices such as that shown in Figure 1-1. Combinations of various concepts were also considered. A history of concept generation, including early conceptualisation, is provided in Appendix G.

Based on all available ideas, a concept evaluation matrix was constructed by selecting two favoured concepts that incorporated the crown shape into the stent design, and four concepts for achieving anchorage in the aortic root. This matrix is shown in Table 6-1 and categories are described below.

6.3.1 Crown support Concept 1: Support at top and bottom

Concepts were generated that allowed the crown-shaped structure to be substantially isolated from the support structure on the inflow and outflow ends. Zig-zag structures were still present at both ends to allow the stent to remain firmly on the balloon when crimped and to prevent leaflet prolapse when operational. Attachment of support structures occurs only at the nadir of the replacement leaflets and near the commissure posts. Additionally, a linkage between the inflow and outflow supports is included to prevent longitudinal shortening during loading and to encourage the crown to return to its undeformed shape. This stent would have to be positioned with the nadir of the replacement valve at the same level as the native valve, as there is no annular support structure above this point.

6.3.2 Crown support Concept 2: Intermediate support

Concepts that incorporated the crown shape of the leaflet attachment zone into the stent structure itself were generated. These concepts started from a crown-shaped member, and various traditional stent structures, described in the stent design literature review, were incorporated. The result is an elegant, relatively short, strong stent. In a favoured concept the valve is intended to be deployed slightly sub-annularly. Since struts contact the crown struts at intermediate points, a structure is required above the crown to counter the excessive crown deformation that would occur in their absence. The radial strength is greatest in the area designed to fit within the annulus.

6.3.3 Anchorage Concept A: Friction

Concepts designed to anchor by friction have no additional protruding members of anchoring. The stent relies on an area of high radial strength over the area of the annulus. In some cases this effect is supplemented by the formation of a slightly hourglass shaped stent due to greater strength, and therefore greater resistance to expansion, of the waist area, which will resist embolization during systole and diastole.

6.3.4 Anchorage Concept B: "Paper lantern"

The "paper lantern" makes use of the bulbous shape of the Sinus of Valsalva for anchorage. It was recognised that the crown shape lengthens considerably during crushing, and has the corollary effect that it shortens in height during deployment. This concept uses the shortening that occurs during deployment to cause a member to protrude in the area inside the crown. It relies on plastic deformation of these central elements so that they do not merely return to the non-deployed shape upon deployment. Instead they take the lowest energy behaviour, which causes protrusion of the member in a different plane, i.e. outwards. These were tested on the bench but not tested in animals. The protruding members were designed to have thinner wall thickness than the rest of the stent to encourage them to bend radially outwards rather than circumferentially.

6.3.5 Anchorage Concept C: Arms attached to the outside of the stent

The “welded arm” concepts started with a crown-shaped member, then built support structures above and below the crown. The stent frame is constructed from annealed Co-Cr to take advantage of the low yield strength and extensive work hardening abilities. On the outside of the stent, however, were welded arms of the same material, but in a cold-worked wire form. This meant that the wires could be manufactured in a shape protruding outwards at the bottom. These arms are held down in the crimped condition by a sheath (in some earlier concepts the arms could be held down by portions of the stent itself). Upon removal of the sheath, or partial deployment of the stent, the arms protrude and allow themselves to be placed behind the native cusps. This concept makes use of balloon-expanding and self-expanding elements in the same stent.

6.3.6 Anchorage Concept D: Integrated expanding arms

The “expanding arm” concepts also used the fact that the crown lengthens during crimping and shortens again during deployment. This fact is exploited to cause arm members that are attached near the commissures to be plastically deformed during crimping, and instead of returning to the pre-crimped shape in the plane of the original cylinder, the extremities of the arms protrude beyond the diameter of the rest of the stent upon deployment. The protruding arms may then push the native leaflets into the Sinuses and support the stent on the muscular/fibrous shelf above the virtual annulus.

6.4 Concept Evaluation

The results of FEA on the concepts are summarised in Table 6-2. The results are discussed further in the sections to follow. Although all stents were analysed using FEA, only Concepts 1A, 1B, 1C and 1D and Concept 2D were physically prototyped.

Table 6-2. Summary of results of different concepts*

		Anchorage Mechanisms			
		Friction	**Sinus**	**External arms**	**Integrated arms**
Crown Support	**Top/ Bottom Support**	CONCEPT 1A	CONCEPT 1B	CONCEPT 1C	CONCEPT 1D
		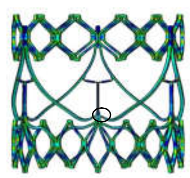 Crimped: 1387 MPa Deployed: 1422 MPa	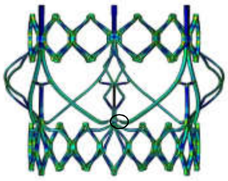 Crimped: 1416 MPa Deployed: 1455 MPa	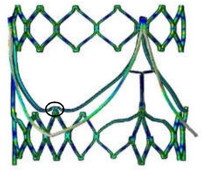 Crimped: 1402 MPa Deployed: 1542 MPa	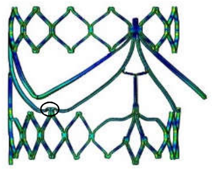 Crimped: 1324 MPa Deployed: 1518 MPa
	Inter-mediate Support	CONCEPT 2A	CONCEPT 2B	CONCEPT 2C	CONCEPT 2D
		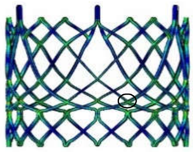 Crimped: 1312 MPa Deployed: 1893 MPa	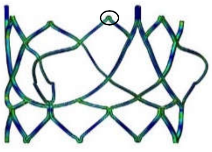 Crimped: 1360 MPa Deployed: 1794 MPa	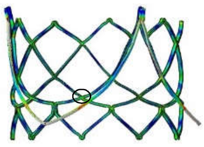 Crimped: 1090 MPa Deployed: 1631 MPa	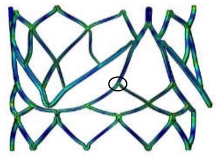 Crimped: 1480 MPa Deployed: 1846 MPa

* Peak Von Mises stresses at the end of crimping and deployment are provided, and the location of the peak deployment Von Mises stress is shown inside the oval.

6.4.1 Concept 1A

Concept 1A showed that a crown-shaped member supported both at the nadir and at points near the commissure posts could be crimped to a low profile. The member designed to facilitate full lengthening of the stent during crimping and proper opening of the crown shape during deployment was partially successful. Although it did lengthen during crimping, it caused the nadir of the crown to push upwards slightly. FEA results are shown in Figure 6-11. A physical prototype (shown in Figure 6-12) behaved similarly to the FEA results.

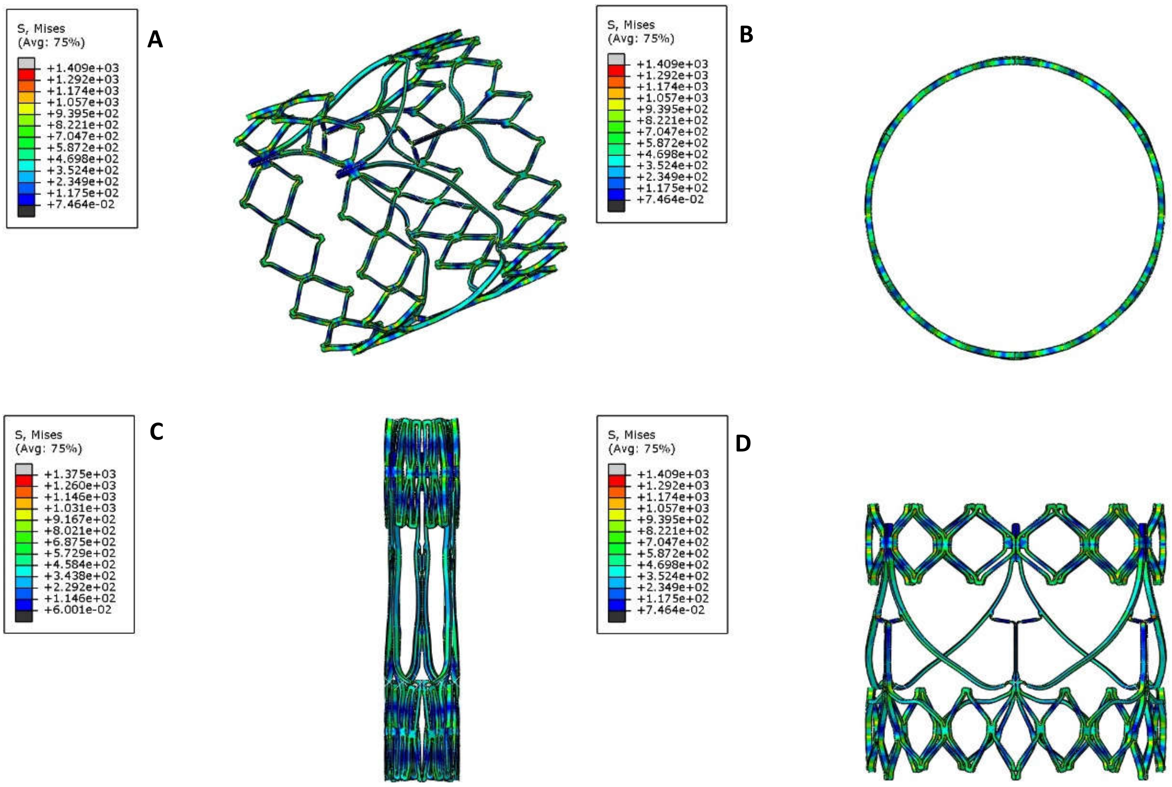

Figure 6-11. Concept 1A FEA results following simple modelling, showing deployed stent geometry (A, B and D) and crimped geometry (C)

Figure 6-12. Concept 1A prototype

6.4.2 Concept 1B

The crown member of Concept 1B had similar behaviour to that of Concept 1A. In the simple FEA model, the double-diamond members that stretch from the top row of struts to the nadir lengthened during crimping, and protruded outwards during deployment as intended (see Figure 6-13). When physical prototypes were manufactured, however, the double-diamond members were highly unstable and frequently buckled circumferentially. An example of this is shown is Figure 6-14.

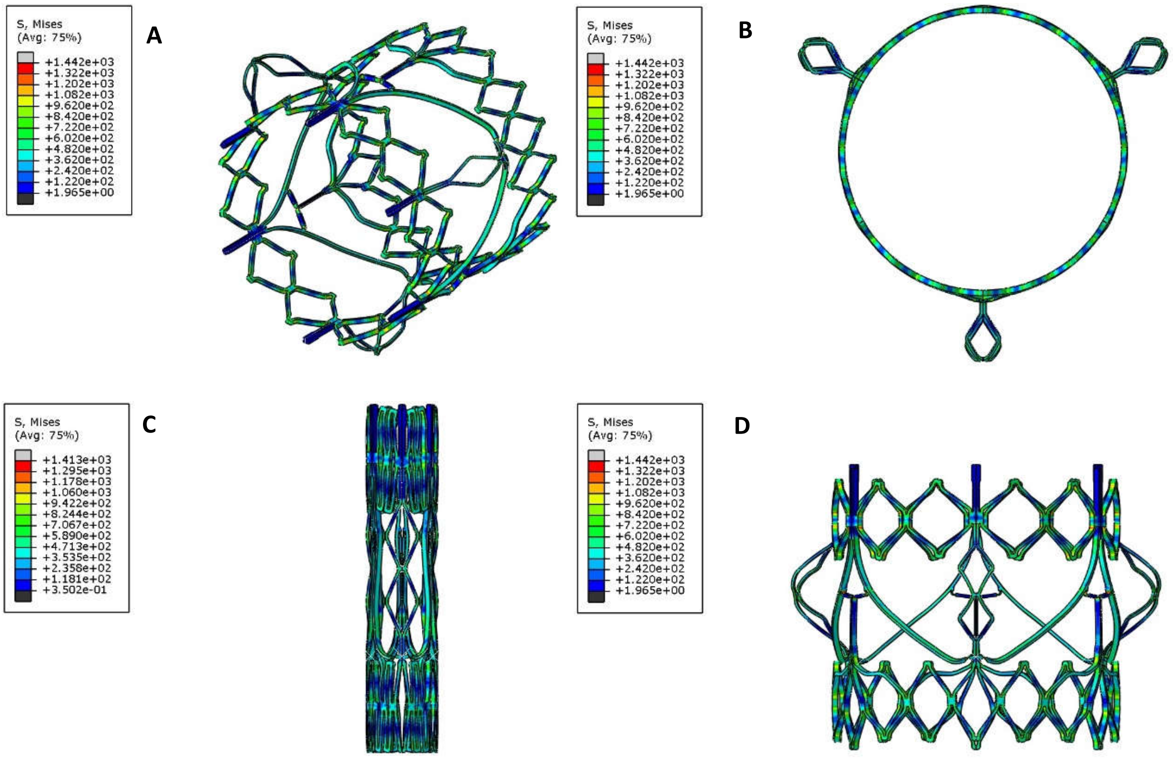

Figure 6-13. Concept 1B FEA results following simple modelling, showing deployed stent geometry (A, B and D) and crimped geometry (C)

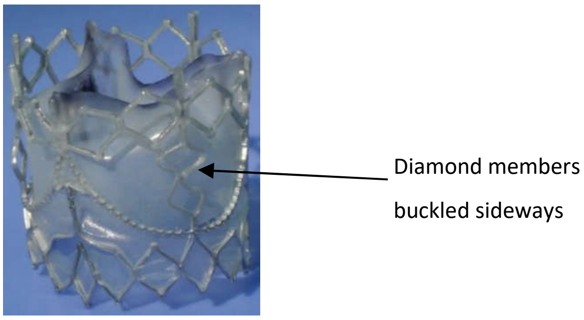

Figure 6-14. Concept 1B prototype after crimping and deployment

The difference between the FEA model and the physical prototypes was considered to be due to difficulty in thinning of the wall through micro-grinding and the symmetry boundary conditions in the FEA model, which artificially stabilise the model. In addition, the concept relied on the stent being crimped to a diameter of 6mm in order to undergo extensive plastic deformation, but early versions of the deployment device on which the stent was tested would not permit stents to be crimped below 9.5mm.

6.4.3 Concept 1C

The crown member of Concept 1C also had similar behaviour to that of Concept 1A. The welded arms, however, form a double layer that causes the stent frame to compress slightly more during crimping. The arms protrude following relaxation of the crimping plates, and remain slightly protruding after deployment (see Figure 6-15). These stents were prototyped physically, and this is described later.

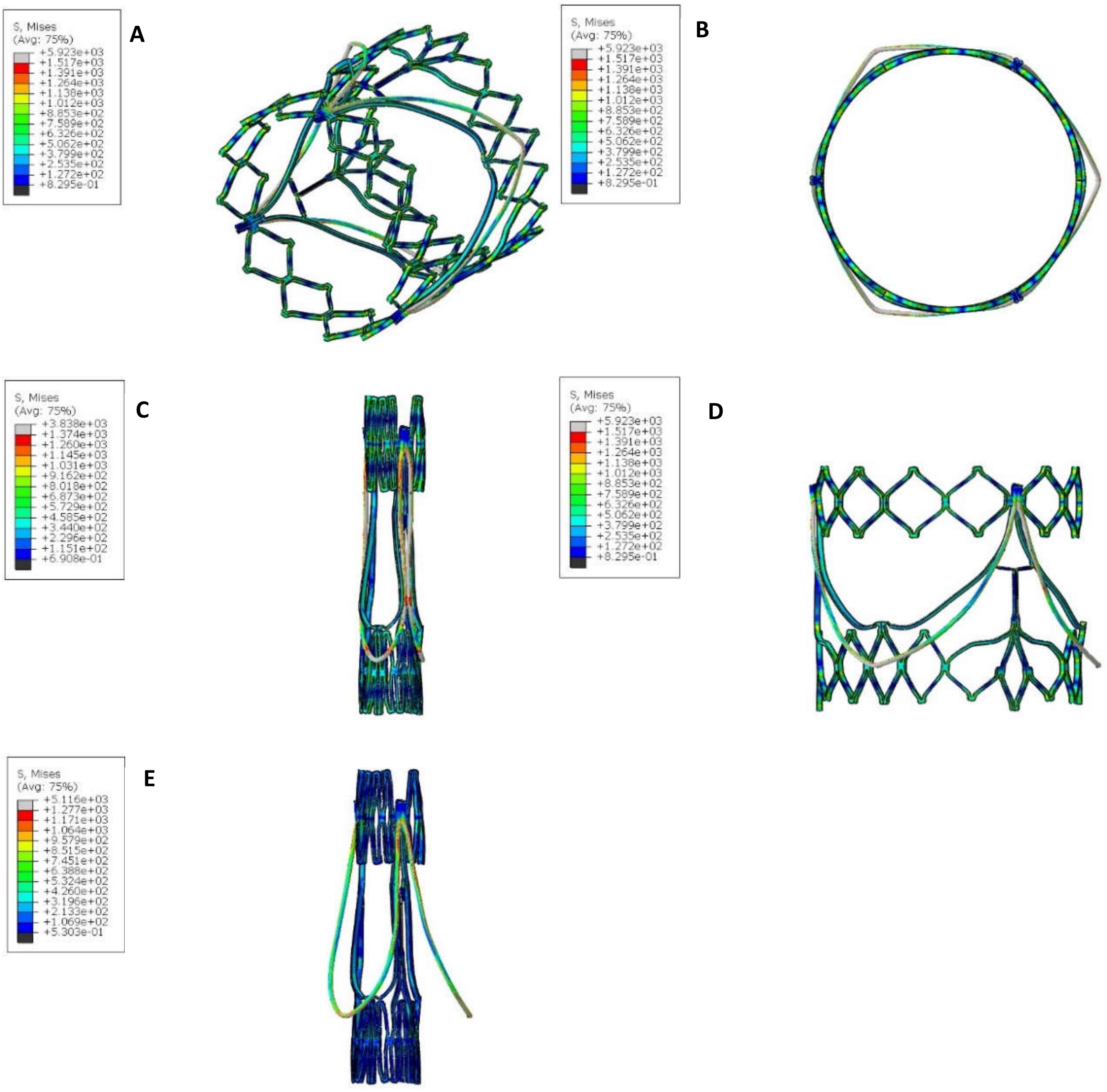

Figure 6-15. Concept 1C FEA results following simple modelling, showing deployed stent geometry (A, B and D), crimped geometry (C) and relaxed geometry after crimping (E)

6.4.4 Concept 1D

The crown member of Concept 1D had similar behaviour to other versions of crown support Concept 1, as shown in Figure 6-16. Physical prototypes behaved as calculated using FEA, as shown in Figure

6-17. The anchoring arms remained flush with the stent in the crimped condition, and protruded much further that the welded arms of Concept 1C at the end of deployment, but the arms were weak and could be deflected easily.

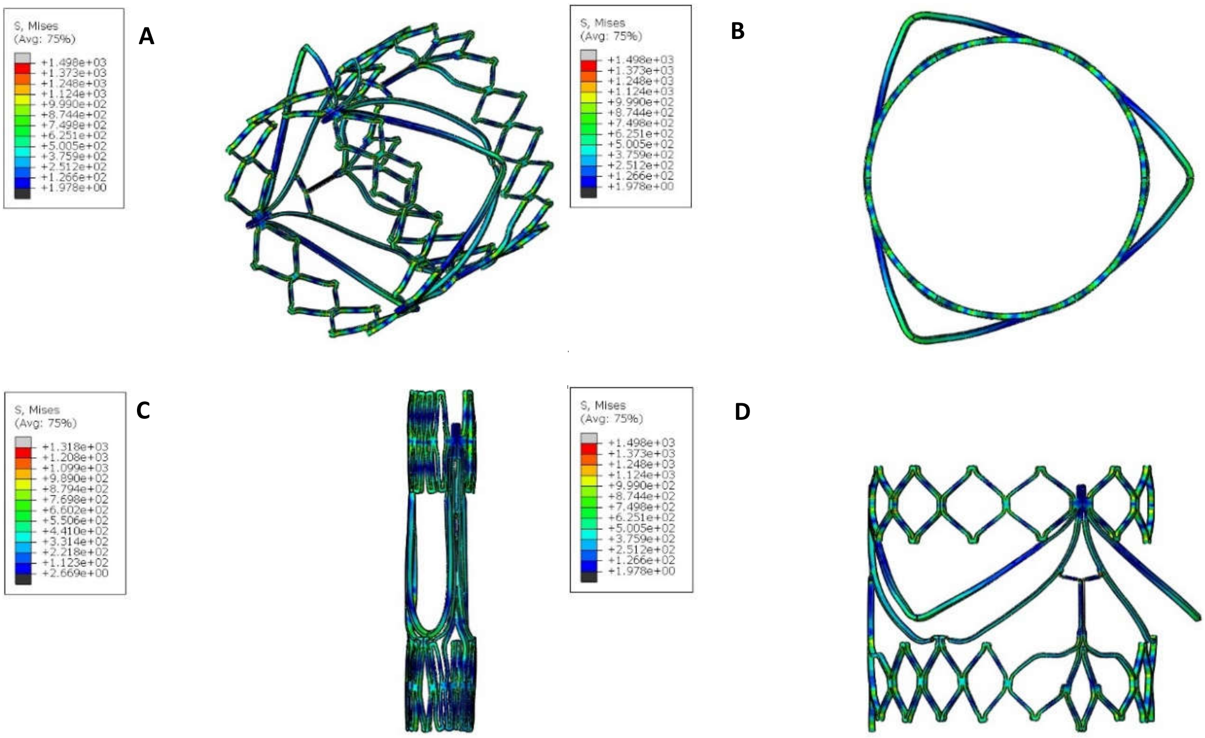

Figure 6-16. Concept 1D FEA results following simple modelling, showing deployed stent geometry (A, B and D) and crimped geometry (C)

Figure 6-17. Concept 1D prototype before crimping (left), and after crimping and deployment (right)

6.4.5 Concept 2A

Concept 2A features the crown shaped member integrated into the stent support structure. Although some struts became slightly bent during crimping, upon deployment the stent returns to a shape very close to the original undeformed geometry, as shown in Figure 6-18. This design was not physically prototyped after indications that Concept 1A would not satisfactorily anchor using friction alone.

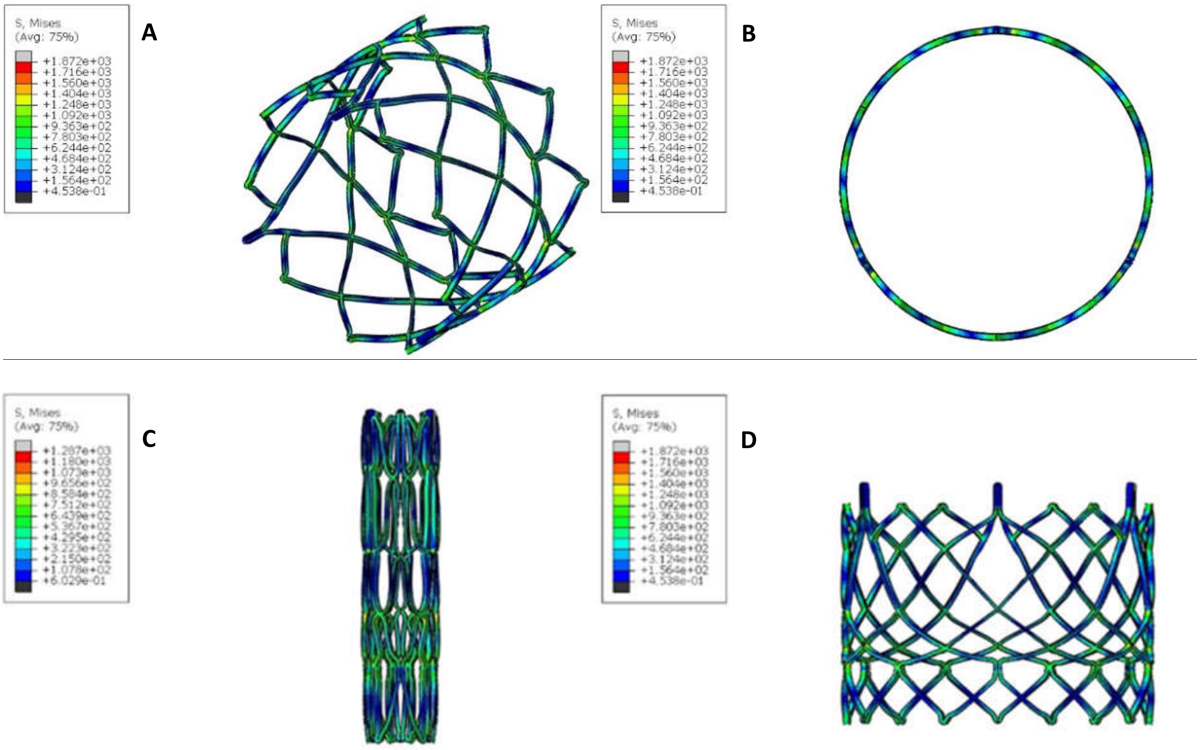

Figure 6-18. Concept 2A FEA results following simple modelling, showing deployed stent geometry (A, B and D) and crimped geometry (C)

6.4.6 Concept 2B

The crimped version of Concept 2B had a very similar appearance to Concept 2A, since they differ only in the structure of the area immediately above the nadir of the crown. The members above the nadir protruded as designed, as shown in Figure 6-19, although they did not protrude as far as the protrusions in Concept 1B. This design was not physically prototyped. The reduction of wall thickness in the protruding areas of the stent using micro-grinding while maintaining wall thickness in other areas was considered unreasonably difficult to achieve routinely.

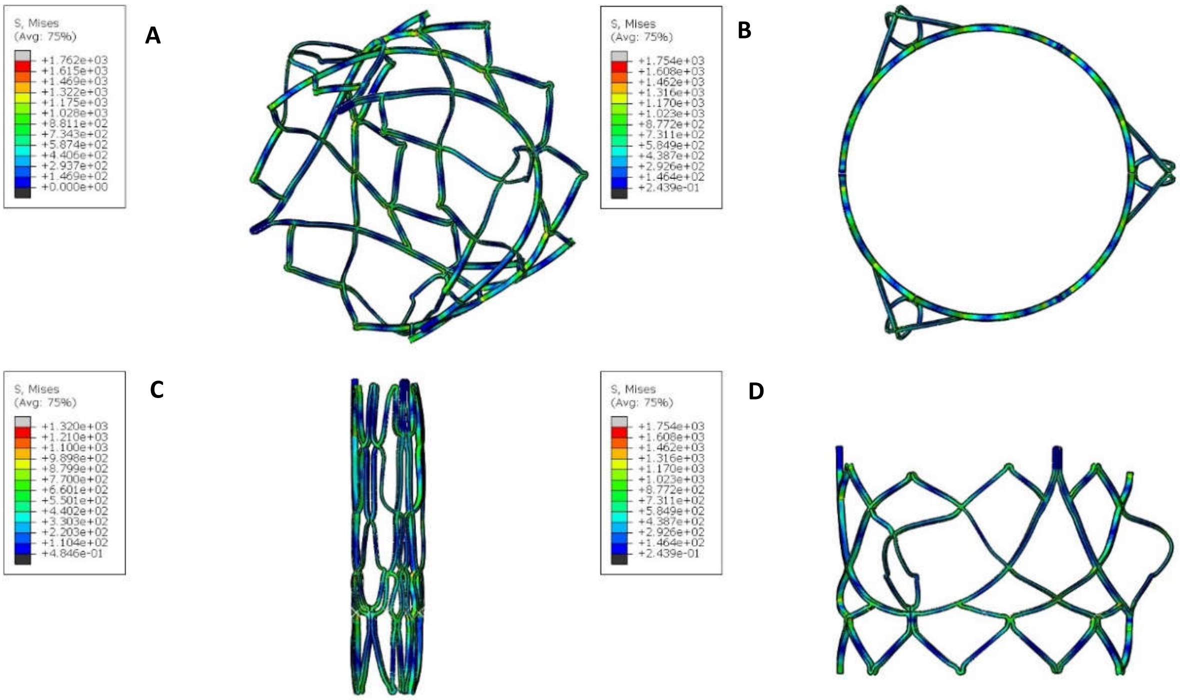

Figure 6-19. Concept 2B FEA results following simple modelling, showing deployed stent geometry (A, B and D) and crimped geometry (C)

6.4.7 Concept 2C

The crown member of Concept 2C also had similar behaviour to that of Concept 2A. The protruding arms behaved in the same way as they did for Concept 1C, protruding sufficiently following relaxation after crimping, and remaining slightly protruded after deployment (see Figure 6-20). These stents were also not prototyped physically, as the effectiveness of the arms could be determined by Concept 1C.

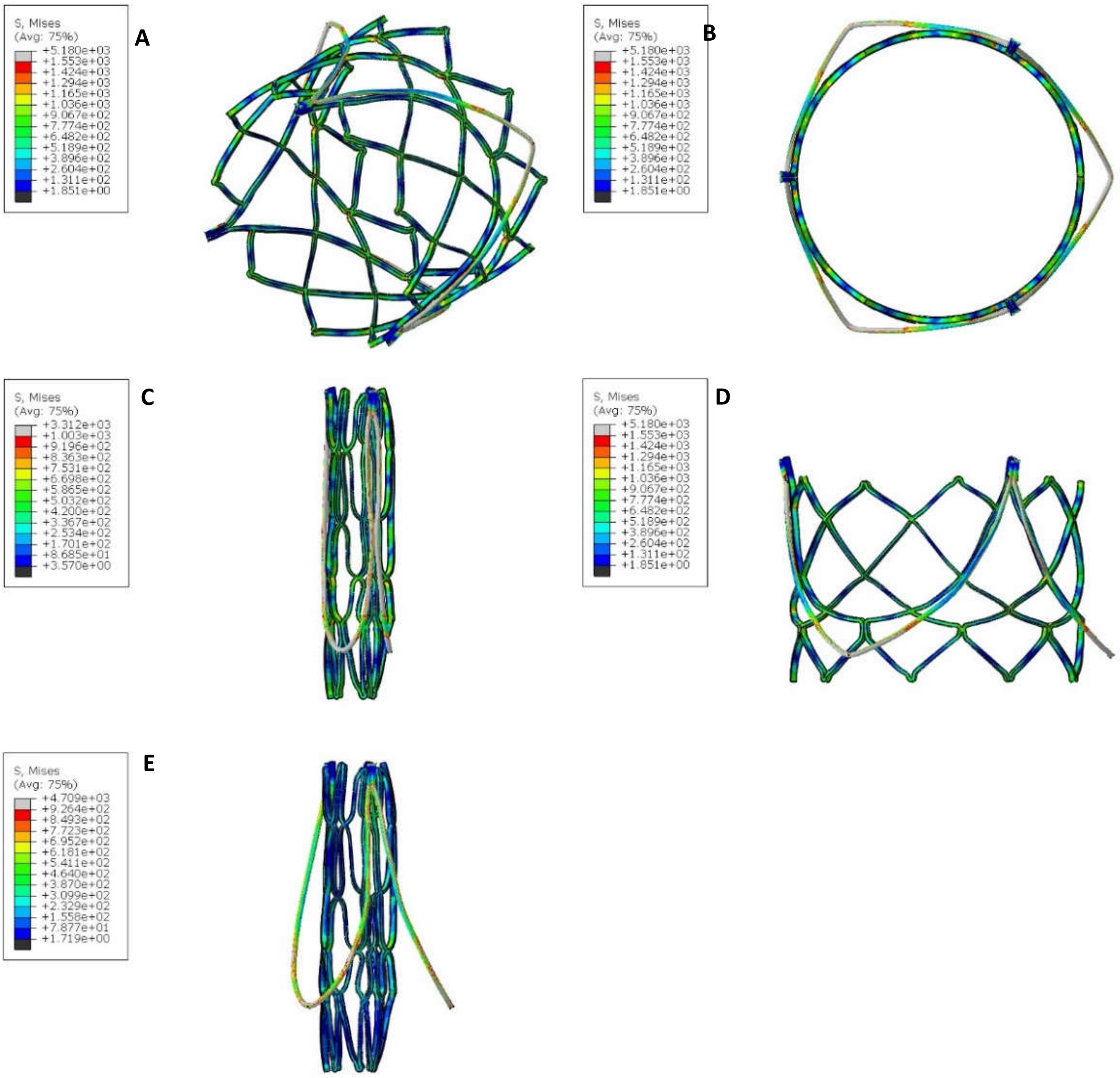

Figure 6-20. Concept 2C FEA results following simple modelling, showing deployed stent geometry (A, B and D), crimped geometry (C) and relaxed geometry after crimping (E)

6.4.8 Concept 2D

The crown member of Concept 2D had similar behaviour to Concept 2A despite the fact that the expanding arm members were not attached the crown member. The arm member prevented the two halves of the crown member from protruding towards each other too much during the crimp, as shown in Figure 6-21. Although the attachment points of the expanding arms with the crown member prevent full restoration of the crown to its original shape, the effect is relatively minor and concentrated near the commissures. These stents were prototyped physically, and this is described later.

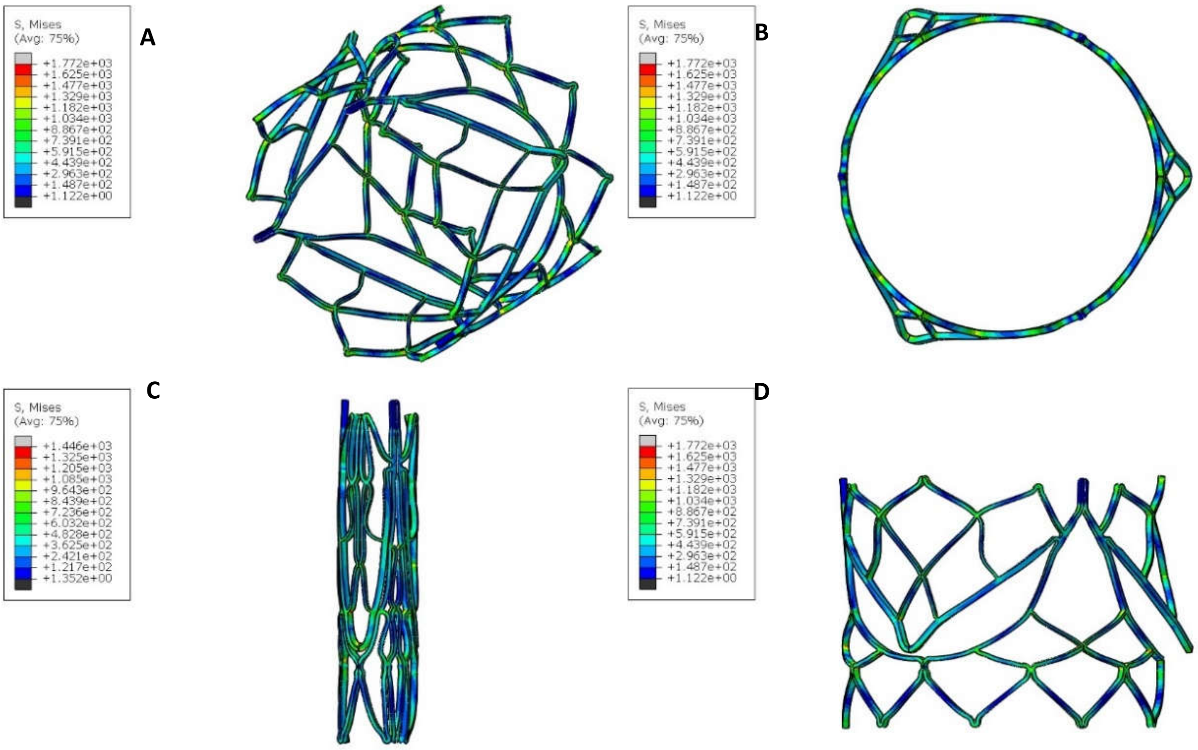

Figure 6-21. Concept 2D FEA results following simple modelling, showing deployed stent geometry (A, B and D) and crimped geometry (C)

6.5 Concept Selection

A concept selection matrix was constructed to help determine which concepts to proceed with for more complex analysis and experimentation. All concepts incorporated the required design attributes described in Chapter 3, including having a tri-leaflet design, a continuous attachment site, a balloon-expandable construction, the ability to be manufactured at deployed dimensions, and the ability to scale to other diameters. Therefore stents were evaluated based on the design criteria listed in Table 6-3. Each criterion was weighted based on judged importance, and each design was scored from 0-5, using an arbitrary score of 2 to correspond to the perceived score of the reference stent, the Edwards Sapien 3™. Values above and below 2 reflect better or worse performance than the reference, respectively.

In general Crown Support Concepts 1 and 2 were considered to be novel because both employed methods of incorporating a crown shaped member into balloon-expandable stent construction. The use of an annealed stent frame and cold-worked wires in stents with welded arms, thereby utilising balloon-expandable and self-expanding functions from the same material, also contributed towards novelty. Designs that utilised plastic deformation to cause elements to protrude were considered to contribute most to novelty.

Table 6-3. Concept selection matrix for comparing design concepts (score 0-5)

Design Criteria	**Weight**	**1A**	**1B**	**1C**	**1D**	**2A**	**2B**	**2C**	**2D**	**Sapien 3**
Novelty	3	3	5	4	5	3	5	4	5	2
Anchorage	3	1	3	5	3	2	3	5	4	2
Manufacturability	3	2	1	1	2	3	1	1	3	2
Correct shape	2	1	1	1	1	2	2	2	2	2
Foreshortening	2	3	3	3	3	2	2	2	2	2
Integrity/durability	2	1	1	1	1	2	2	2	2	2
Crimpability	1	3	2	2	2	2	2	1	2	2
Low leaflet damage	1	3	2	3	3	2	2	2	2	2
Push leaflets	1	1	2	2	1	2	2	2	2	2
Weighted total		35	43	47	46	42	45	47	54	36

Stents designed to anchor using friction offered the least secure anchoring. Crown support concept 1 relies on a narrow “landing zone”, but Crown support concept 2 anchorage was considered to be comparable to the Sapien 3 because greater radial strength is achieved in the waist area and a slight hourglass shape is formed at deployment, which may resist migration. The greatest anchoring security was offered by having members behind the native cusps, but members designed to push leaflets aside and to utilise the shape of the SoV still offered promising anchoring.

Manufacturability was evaluated based on the ease with which stents could be manufactured as well as the ease with which polymer leaflets could be sprayed onto the stents. In this regard, designs that required grinding techniques were ranked lower, as were designs that were challenging to place on spray coating mandrels or interfered with the ability to spray the mould directly.

The ability to return to the correct functional shape following crimping and deployment was better for designs using Crown Support Concept 2 than Crown Support Concept 1. Foreshortening was lower for concepts 1A to 1D than for Concepts 2A to 2D, which was comparable to the Sapien 3. Stents of Crown Support Concept 2 generally crimped and deployed more regularly, and Crown Support Concept 1 had high stresses at the hinge members near the nadir, so Crown Support Concept 2 stents were scored higher for integrity and durability.

The ability to be crimped to a low profile was influenced by the density of struts and strut width around the circumference, and whether the concept had another wire arm layer. In this respect, the lowest crimp profile would be achievable by Concept 1A while the largest profile would be Concept 2C. Most designs were able to push the native leaflets away, but Concept 1A did not have a mechanism to achieve this, and Concept 1D was considered too weak to perform this function reliably. No stents were considered to be a significant risk for leaflet damage, but the more open designs of Concepts 1A, C and D were considered less likely to cause damage.

The concept selection matrix was used as a guideline, recognising the fact that each design could be tweaked to improve score. The highest scoring stents were Concepts 2D, 1C and 2C. It was decided to proceed with two design concepts, namely Concept 1C and Concept 2D. This allowed stents with two different anchorage mechanisms and two different support concepts to be tested more thoroughly, including implantation in animals. Concept 1C had the ability to self-locate, which allowed fully functional valves to be tested in animals relatively early in the development phase for the deployment devices. Concept 2D had the ability to anchor, but not locate during delivery, and could be used with deployment devices that incorporated location mechanisms (or using guidance from medical imaging). Concept 2D stents were therefore manufactured and tested in animals chronologically after Concept 1C, as described in Section 5.5.

In the sections to follow, these two favoured stent concepts (1C and 2D) are referred to as the Design 1 stent (or self-locating stent) and Design 2 stent (or expanding arm stent), respectively. Stent height was 22.87 mm for Design 1 and 19.28 mm for Design 2, and Control stent height was 17.9 mm. Stent outside surface areas were 170 mm^2, 168 mm^2 and 189 mm^2, respectively.

7 Results

This chapter presents the results of complex FEA modelling, verification of manufacturing quality and dimensions, and the results of *in vitro*, *ex vivo* and *in vivo* testing performed on the two favoured design concepts.

7.1 Modelling Results

7.1.1 Balloon Modelling Results

The comparison between experimental and predicted diameters is shown in Table 7-1 and Figure 7-1. Predicted balloon diameter differed by a maximum of 0.1 mm at 2 atm and 4 atm. No balloon inflations beyond 4 atm were simulated. The stages of balloon inflation, starting with a four-pleat wrapped structure, through to a clover-leafed structure, to a fully unwrapped circular cross-section and finally a “stretched” circular cross-section at 4 atm are shown in Figure 7-2. When fully inflated to 4 atm, the median Von Mises stress in the balloon material was 95.1 MPa and the range of predicted stresses in the material was over the narrow range of 93.7 MPa to 96.5 MPa, as shown in Figure 7-3.

Table 7-1. Comparison between experimental and model results of balloon diameter

Pressure	Experimental (mm)	Model (mm)
0 atm	21.1	21.1
2 atm	21.6	21.7
4 atm	22.8	22.7

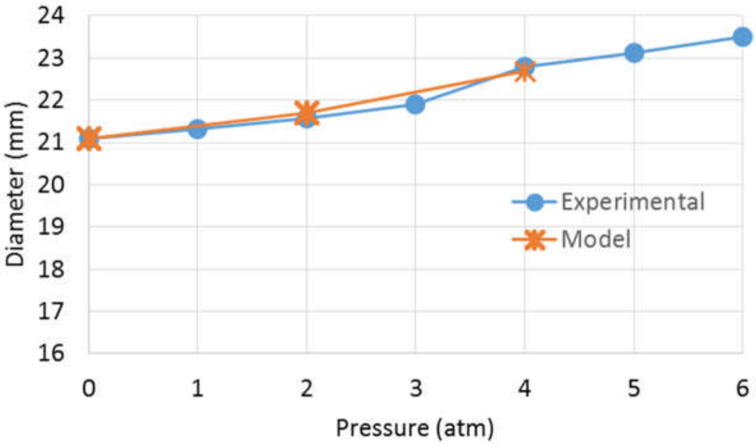

Figure 7-1. Comparison between experimental and predicted balloon diameters

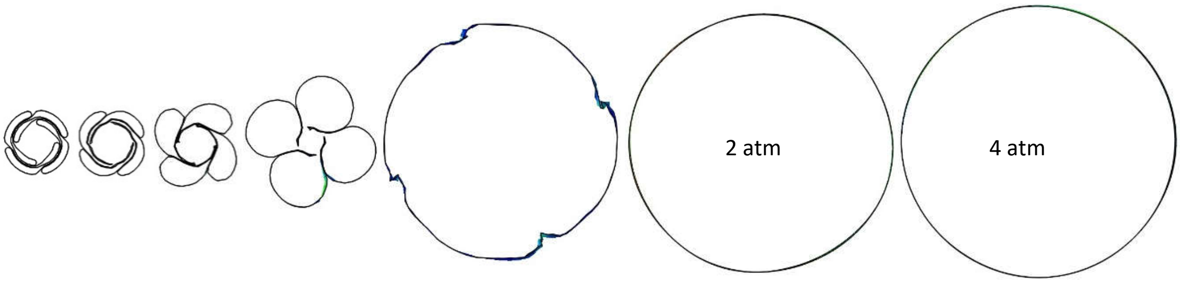

Figure 7-2. Balloon deployment simulation showing initial unfolding, and subsequent stretching, from 0 atm to 4 atm.

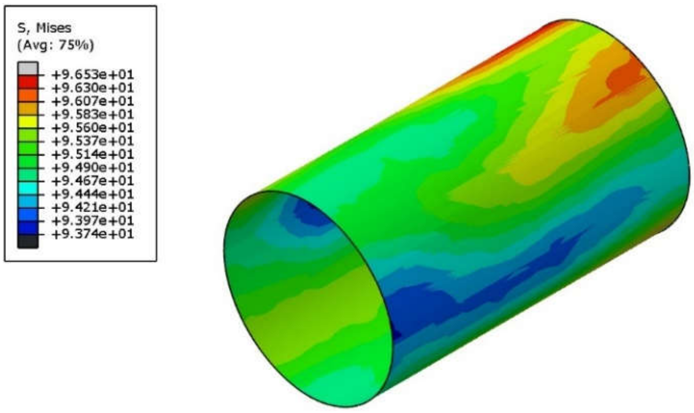

Figure 7-3. Von Mises Stress distribution in the balloon at 4 atm.

7.1.2 Model structural validation – Radial crush

Radial crush force predicted using FEA correlated well with the force measured experimentally, as shown in Figure 7-4. FEA under-predicted radial force for the Control stent, Design 1 and Design 2 stents by 6.2%, 7.0% and 9.6%, respectively at 15% diameter reduction, and only 1.3%, 3.1% and 8.3%, respectively at 50% diameter reduction.

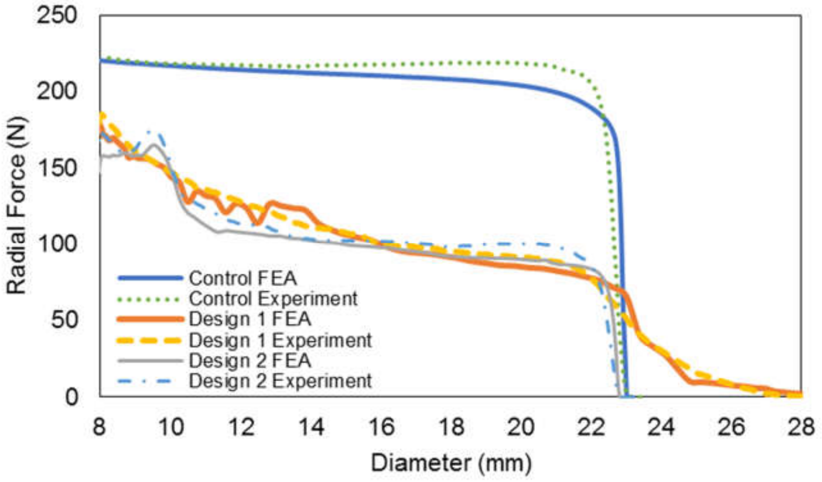

Figure 7-4. Comparison between radial crush force predicted from FEA and determined experimentally

7.1.3 Crimping and Deployment

A summary of FEA results for complex modelling on the Control stent, Design 1 and Design 2 is provided in Table 7-3, and more frames through the modelling stages are provided in Appendix H.

7.1.3a Control Stent

The Control stent was meshed using 99,200 hexahedral elements. The maximum Von Mises and Maximum Principal stresses in the stent at the end of each modelling step are shown in Table 7-2, as calculated at element integration points. Von Mises Stress reached 1650 MPa at the end of deployment.

Table 7-2. Maximum Stress and Strain in Control stent at the end of each step (based on integration points)

Step	Von Mises (MPa)	Maximum Principal Stress (MPa)	Equivalent Plastic Strain
Crimp	1223	1213	48%
Relax	778	607	48%
Deploy	1650	2591	95%
Recoil	754	853	96%

The Von Mises stress distributions at the end of crimping and deployment steps are shown in Figure 7-5. Crimped and deployed stents showed regular structured geometry, with the highest stresses concentrated near stent hairpin junctions and the lowest stresses near the strut midpoints. The deployed stent is slightly hourglass shaped, with a waist positioned just below the midline.

As shown in the stent shape progression in Table 7-3, the stent only reached full deployment at 4 atm. The greatest value of Von Mises Stress occurred at the inside radius of a hairpin junction, as shown in Figure 7-6. The greatest value of Maximum Principle Stress after recoil also occurred at the inside radius of a hairpin junction, on the bottom row of struts.

A stress history of the element with the greatest stress after recoil is plotted in Figure 7-7, showing that the stress at the inside radius is compressive during the crimp, reaches a tensile residual stress during relaxation, rises to peak at the end of deployment and drops to a final tensile residual stress of 853 MPa. A small amount of dynamic oscillation can be seen at the beginning of recoil but this resolves rapidly.

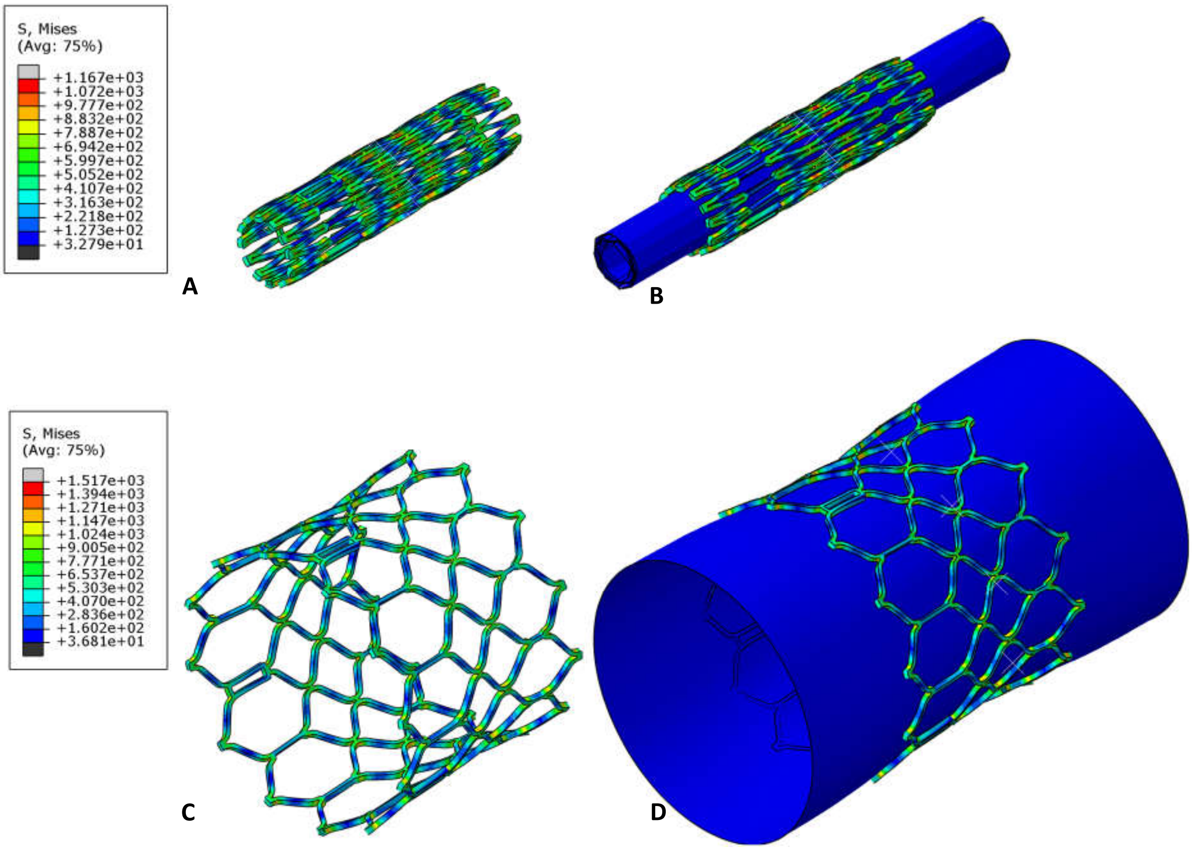

Figure 7-5. Von Mises stress distribution for Control stent in crimped (A&B) and deployed (C&D) conditions. Stents are shown with and without balloons.

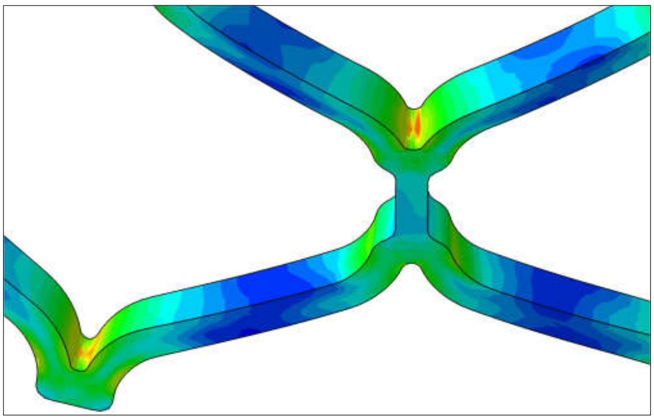

Figure 7-6. Location of maximum Von Mises Stress after deployment of Control stent

Table 7-3. Summary of results of complex modelling

Stage	**Control**	**Design 1**	**Design 2**
Crimped	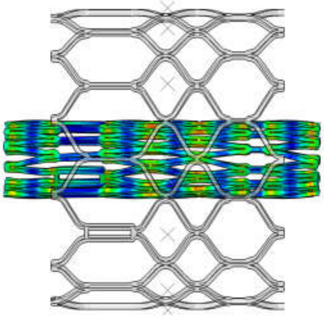	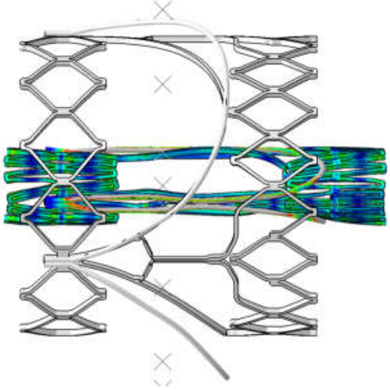	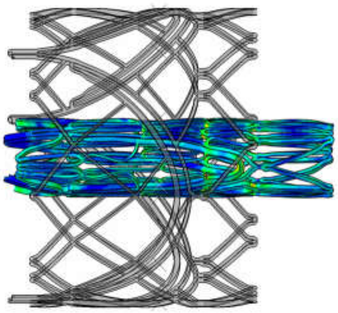
50% Deployment	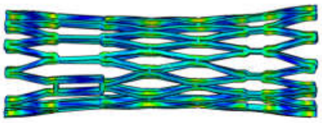	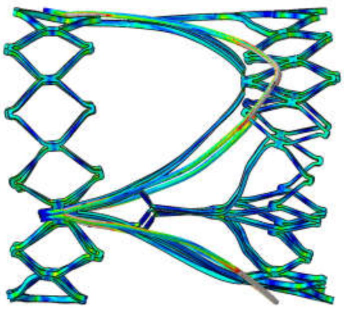	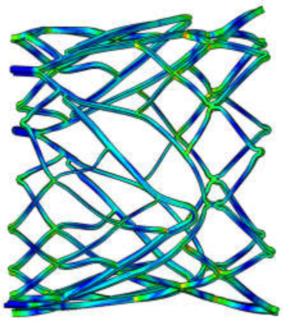
100% Deployment	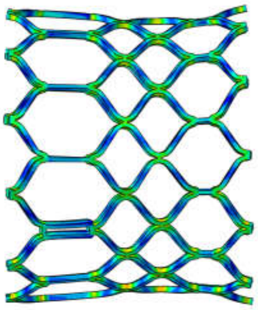	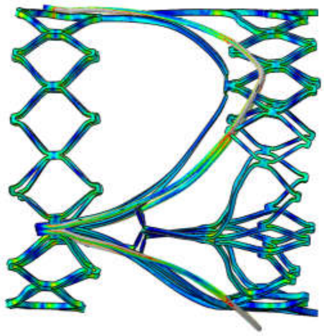	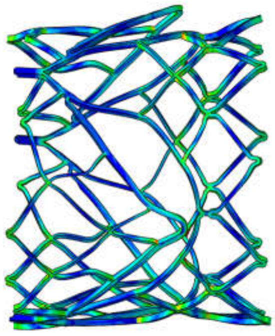
Recoil	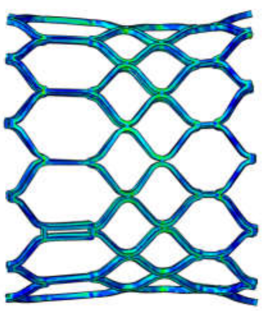	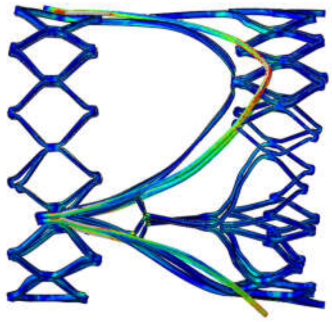	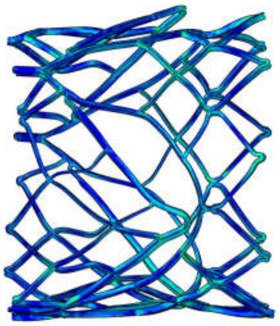

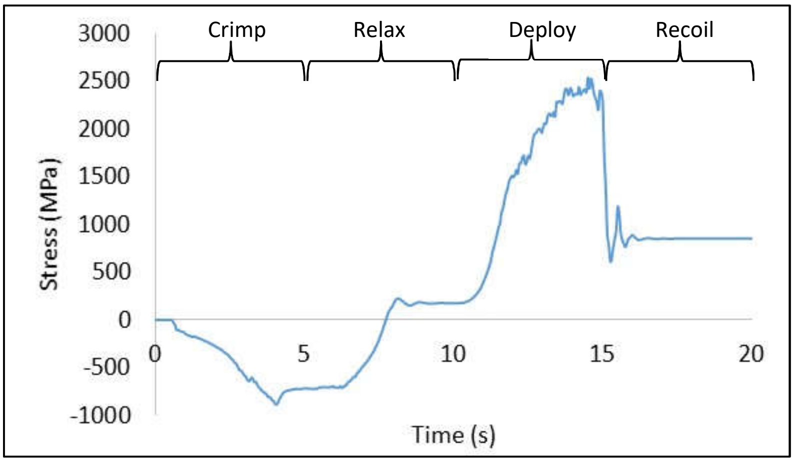

Figure 7-7. Maximum Principal Stress of Control stent at integration point of element 53426, which is the element with the highest maximum principal stress at the end of relaxation after deployment.

7.1.3b Self-locating Stent (Design 1)

The self-locating stent (Design 1) was meshed using 153,756 hexahedral elements for the stent and 30,993 tetrahedral elements for the wire arms. The mesh is shown in Figure 7-8. Although the greatest stresses in the model occurred at the extremities of the wire arms (peak Maximal Stress values were 2929 MPa during crimping and 2741 MPa during deployment), the focus of development in this project was the stent frame, so stresses in the welded arms are ignored in the analyses below. The maximum Von Mises and Maximum Principal stresses in the stent at the end of each modelling step are shown in Table 7-4 as calculated at element integration points. Von Mises Stress reached 1604 MPa at the end of recoil.

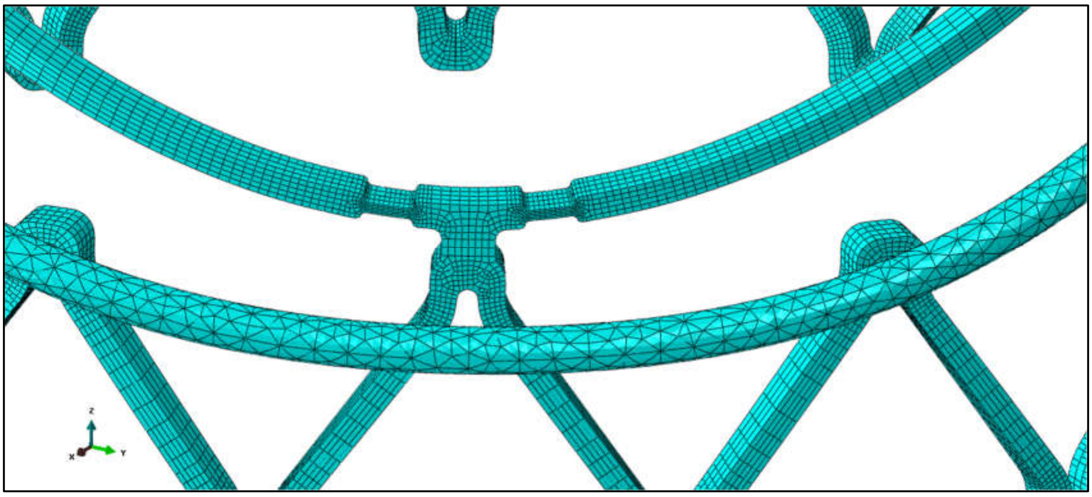

Figure 7-8. Mesh used for Design 1

The Von Mises stress distributions at the end of crimping and deployment steps are shown in Figure 7-9. As shown in the stent shape progression in Table 7-3, the stent achieved fully deployed shape at approximately 2 atm, although diameter continued to expand until 4 atm.

Table 7-4. Maximum Stress and Strain in self-locating stent at the end of each step

Step	Von Mises (MPa)	Maximum Principal Stress (MPa)	Equivalent Plastic Strain
Crimp	1418	1683	48%
Relax	1427	1651	49%
Deploy	1437	2175	82%
Recoil	1604	1626	82%

The greatest values of Von Mises Stress occurred at the hinge points on either side of the crown nadirs, as shown in Figure 7-10A. The greatest value of Maximum Principle Stress after recoil occurred at the hinge of the branch elements attached to the crown shape near the commissure posts, although high residual stress values were present at the hinges on either side of the crown nadir. This final residual Maximum Principle Stress exceeded the true stress value of UTS (1315 MPa) in several areas near such hinge points.

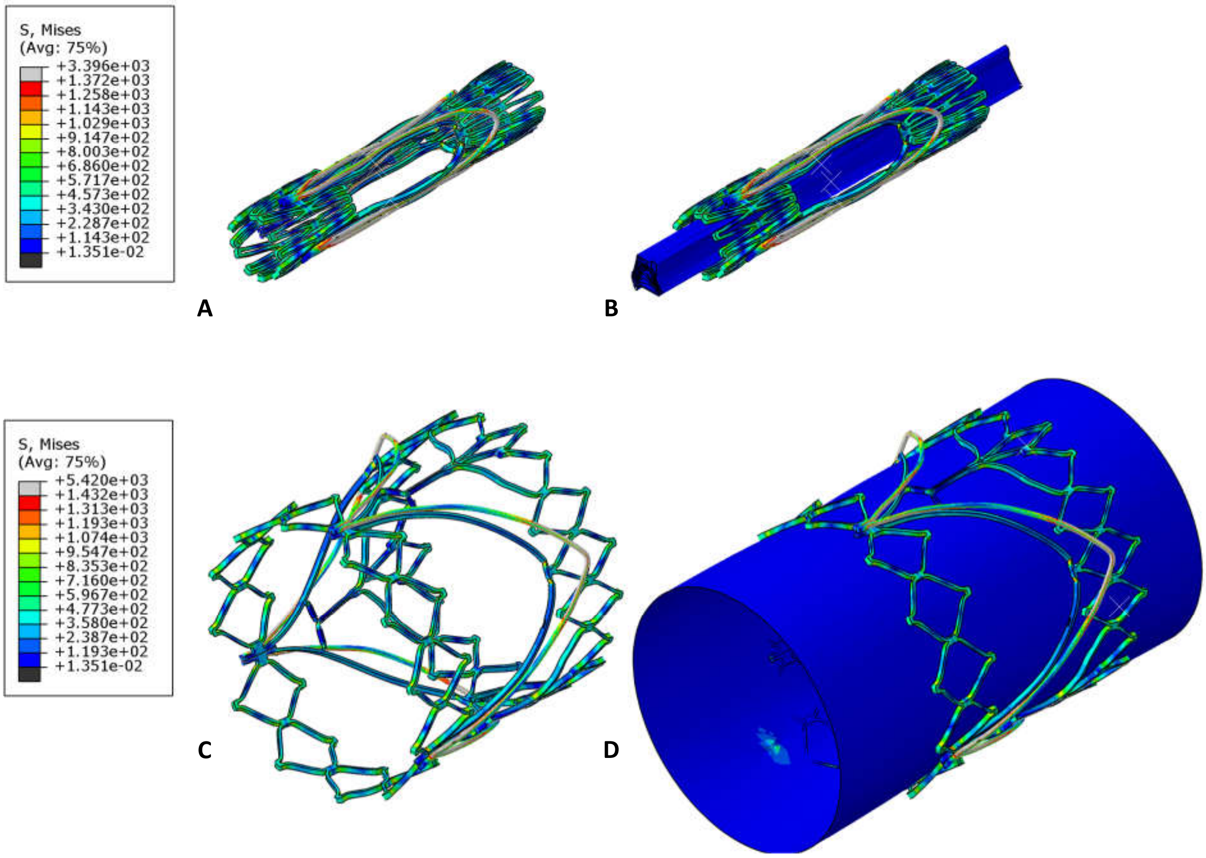

Figure 7-9. Von Mises stress distribution for Design 1 stent in crimped (A&B) and deployed (C&D) conditions. Stents are shown with and without balloons.

During crimping, stent struts did not all compress evenly (see Figure 7-9). Struts closest to the commissure posts tilted towards each other. As the stent compressed further, a more regular stent structure was obtained, as may be seen in the figure of the crimped stent. During deployment, there was tendency for the top row of diamonds to bend slightly up or down. There was also a tendency for the bottom row of struts to open to a greater extent at the longest strut, in the area beneath the commissure posts. The stents also showed distortion of crown geometry near the nadir, particularly in the hinge portions. At one of the hinge points, a single hairpin junction became trapped at the hinge, preventing proper expansion of the stent in this area and resulting in the development of high stresses. These stent irregularities are shown in Figure 7-10.

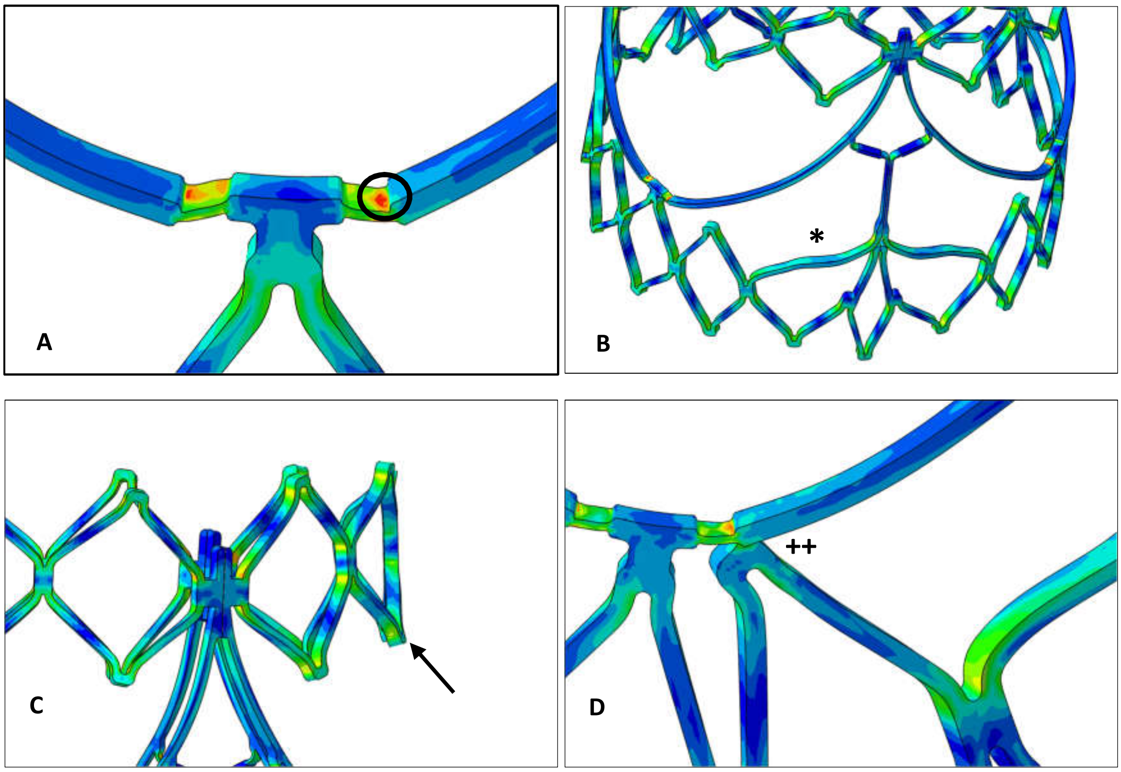

Figure 7-10. Deformed geometry and Von Mises stress distribution associated with Design 1 stent irregularities. A) Distorted crown, showing area of greatest Von Mises stress in the model, B) Preferential stretching of long elements (*), C) Raised top row of diamonds elements (arrow), D) Trapped hairpin junction (++)

7.1.3c Expanding Arm Stent (Design 2)

The expanding arm stent (Design 2) was meshed using 113164 hexahedral elements. The mesh is shown in Figure 7-11. The maximum Von Mises and Maximum Principal stresses in the stent at the end of each modelling step are shown in Table 7-5, as calculated at element integration points. Von Mises Stress reached 1633 MPa at the end of deployment.

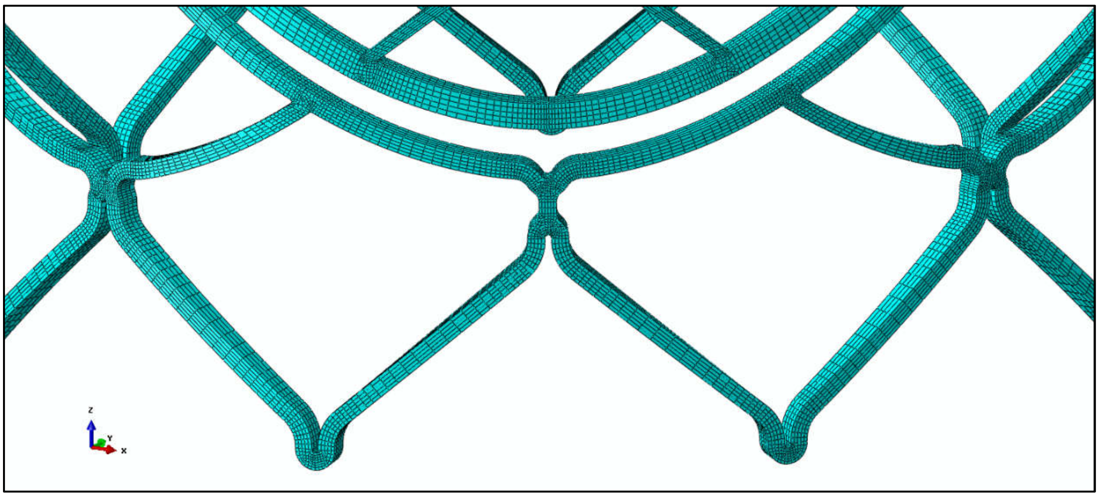

Figure 7-11. Mesh used for Design 2

Table 7-5. Maximum Stress and Strain in expanding arm stent at the end of each step

Step	Von Mises (MPa)	Maximum Principal Stress (MPa)	Equivalent Plastic Strain
Crimp	1434	1914	54%
Relax	1311	927	54%
Deploy	1633	3019	86%
Recoil	1155	962	86%

The Von Mises stress distributions at the end of crimping and deployment steps are shown in Figure 7-12. Crimped and deployed stents showed mildly irregular strut deformation but crimped geometry was compressed in a single layer and arms extended outward during deployment. As shown in the stent shape progression in Table 7-3, the stent reached fully deployed shape at approximately 75% of the deployment step (or 90% of the pressure).

The greatest values of Von Mises Stress occurred during deployment at the inside radii of hairpin junctions in the top row of the expanding arm, as shown in Figure 7-13. The greatest value of Maximum Principle Stress after deployment (3019 MPa) and after subsequent recoil (962 MPa) also occurred in the top row of struts but at the junction between the top row and the support structure of the arm, at an area with a very small radius (with only one element across the width of the radius), therefore representing a stress concentration. When this row of elements was removed from results, the peak Maximum Principle Stresses were 2613 MPa and 949 MPa, respectively, and occurred at the inside radii of hairpins in the bottom row of the stent. As with other stents, lowest stresses occurred near strut midpoints. A distortion of the crown shape occurred near the commissure post, as shown in Figure 7-13B.

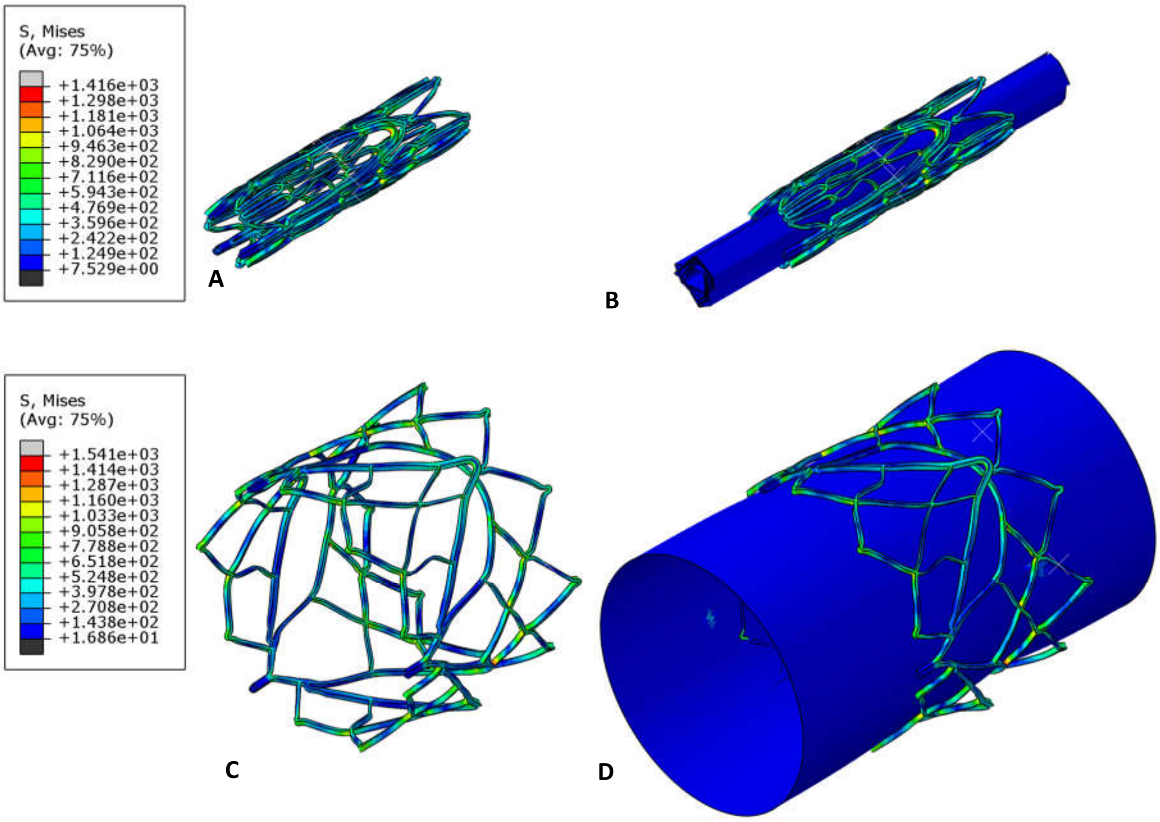

Figure 7-12. Von Mises stress distribution for Design 2 stent in crimped (A&B) and deployed (C&D) conditions. Stents are shown with (B&D) and without (A&C) balloons

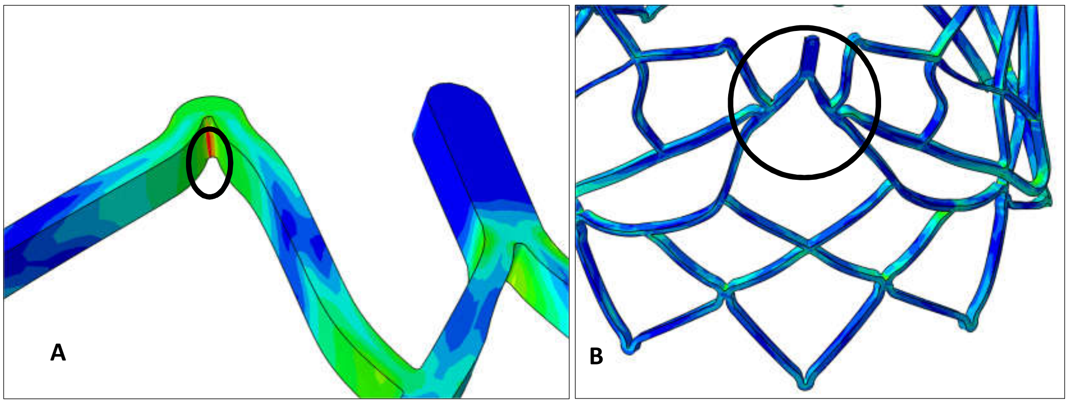

Figure 7-13. Deformed geometry and Von Mises stress distribution associated with Design 2 stent irregularities. A) Area of greatest Von Mises stress in the model, B) Distorted crown element near commissure posts

7.1.4 Foreshortening and recoil

Average deployed outer diameters for the Control stent, Design 1 stent and Design 2 stent, as determined through FEA modelling (and based on orthogonal measurements at three points along the stent length), were 22.3 mm, 23.3 mm and 23.0 mm, respectively. The average predicted percentage recoil values for the stents were 1.9%, 3.4% and 1.9% respectively, as shown in Table 7-6. The measurements did not include arm protrusion.

Table 7-6. Summary of recoil values from FEA and physical measurements

Design	**Position**	**FEA Predictions**			**Physical Measurements**		
		Deployed Diameter (mm)	**Recoiled Diameter (mm)**	**Recoil %**	**Deployed Diameter (mm)**	**Recoiled Diameter (mm)**	**Recoil %**
Control	Top	22.62	22.22	1.8	22.96	22.55	1.8
	Middle	21.23	20.72	2.4	21.17	20.66	2.4
	Bottom	23.08	22.71	1.6	23.01	22.69	1.4
Design 1	Top	23.50	22.71	3.4	23.38	22.67	3.0
	Middle	23.15	22.14	4.4	23.48	22.50	4.2
	Bottom	23.30	22.76	2.3	23.54	22.85	2.9
Design 2	Top	23.25	22.75	2.2	23.39	22.86	2.3
	Middle	22.16	21.74	1.9	22.36	21.92	2.0
	Bottom	23.72	23.32	1.7	24.12	23.74	1.6

Table 7-7. Summary of foreshortening values from FEA and physical measurements

Design	**FEA Predictions**			**Physical Measurements**		
	Relaxed Length (mm)	**Recoiled Length (mm)**	**Fore-shortening %**	**Relaxed Length (mm)**	**Recoiled Length (mm)**	**Fore-shortening %**
Control	24.32	19.53	19.7	24.19	19.45	19.6
Design 1	29.44	24.77	15.9	29.32	24.97	14.8
Design 2	25.51	20.92	18.0	25.39	20.73	18.4

Foreshortening was predicted to be the greatest for the Control stent (19.7%), followed by the Design 2 stent (18.0%) and finally the Design 1 stent (15.9%), as summarised in Table 7-7.

7.1.5 Radial strength and fatigue analysis

Modelling demonstrated that radial strength (radial force at 15% diameter reduction) was much lower for Design 2 stents than Control stents (116 N vs 347 N). The radial force as a function of stent diameter is shown in Figure 7-14.

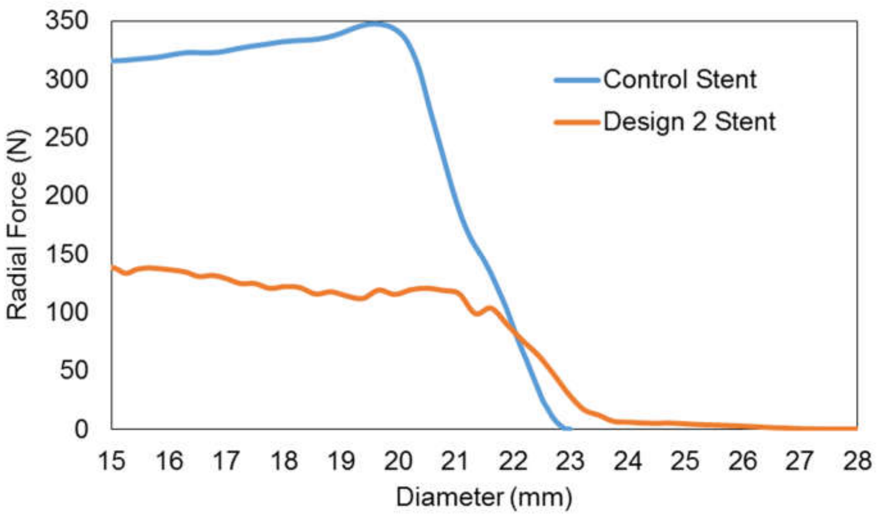

Figure 7-14. Radial strength

Fatigue diagrams (charts of the mean and alternating stresses at each element) are plotted in Figure 7-15 and in Figure 7-17 for the Control stent and Design 2 stent, respectively. Fatigue analysis was not performed for Design 1 due to the fact that mean stresses exceeded the true UTS of the material and therefore necessarily exceed Goodman criteria.

The minimum fatigue safety factor for the Control stent was 2.08, and the location of the element with the worst-case fatigue scenario is shown in Figure 7-16. The mean and alternating stresses at this element were 621 ± 5 MPa, meaning that fatigue risk at this point is mainly influenced by mean stress. An example of an element experiencing greater alternating stresses is shown in Figure 7-16, where mean and alternating stresses were 439 ± 10 MPa, resulting in a fatigue safety factor of 2.7. The minimum fatigue safety factor for the Design 2 stent was 1.00, which narrowly predicts fatigue safety. The location of the two elements with the worst-case fatigue scenarios are shown in Figure 7-18. The highest risk of fatigue occurred in the top row of struts at a small fillet radius, where the mean and alternating stresses were 839 ± 122 MPa. The second highest risk of fatigue occurred at the junction between the crown member and a connecting strut near the nadir, where the mean and alternating stresses were 408 ± 214 MPa.

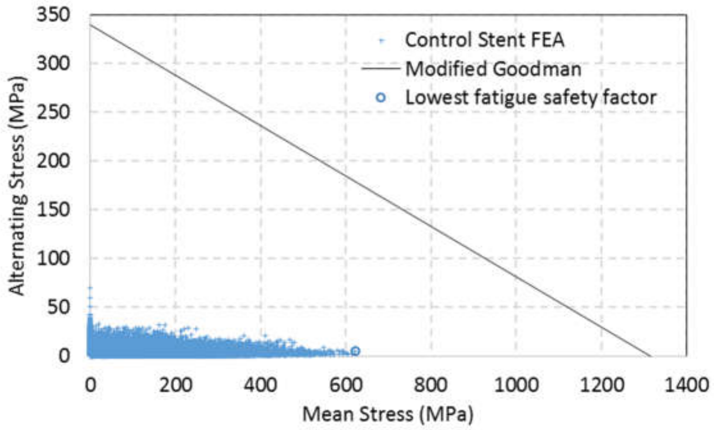

Figure 7-15. Fatigue diagram of inverse fatigue safety factors for Control stent

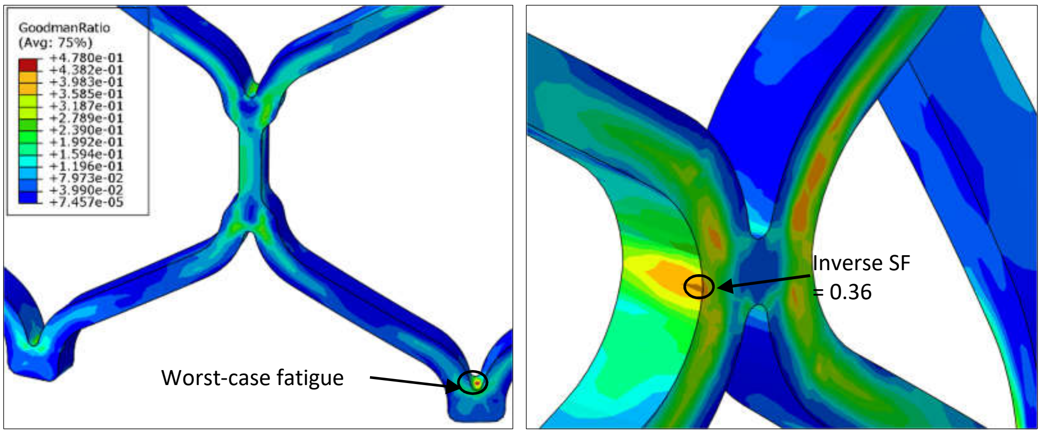

Figure 7-16. Contour plots of nodal inverse fatigue safety factors for Control stent

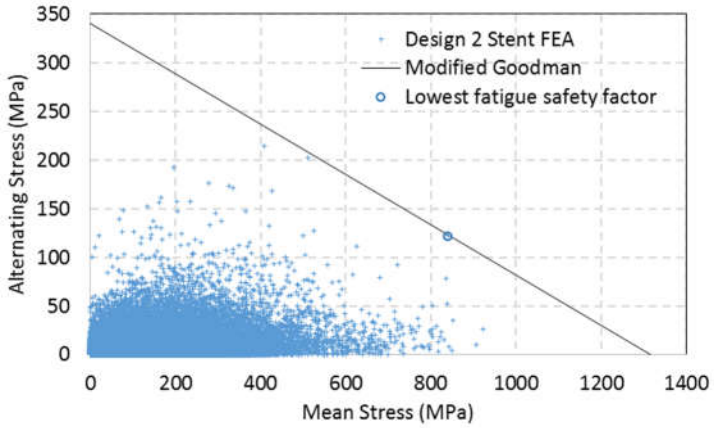

Figure 7-17. Fatigue diagram of inverse fatigue safety factors for Design 2 at the integration points

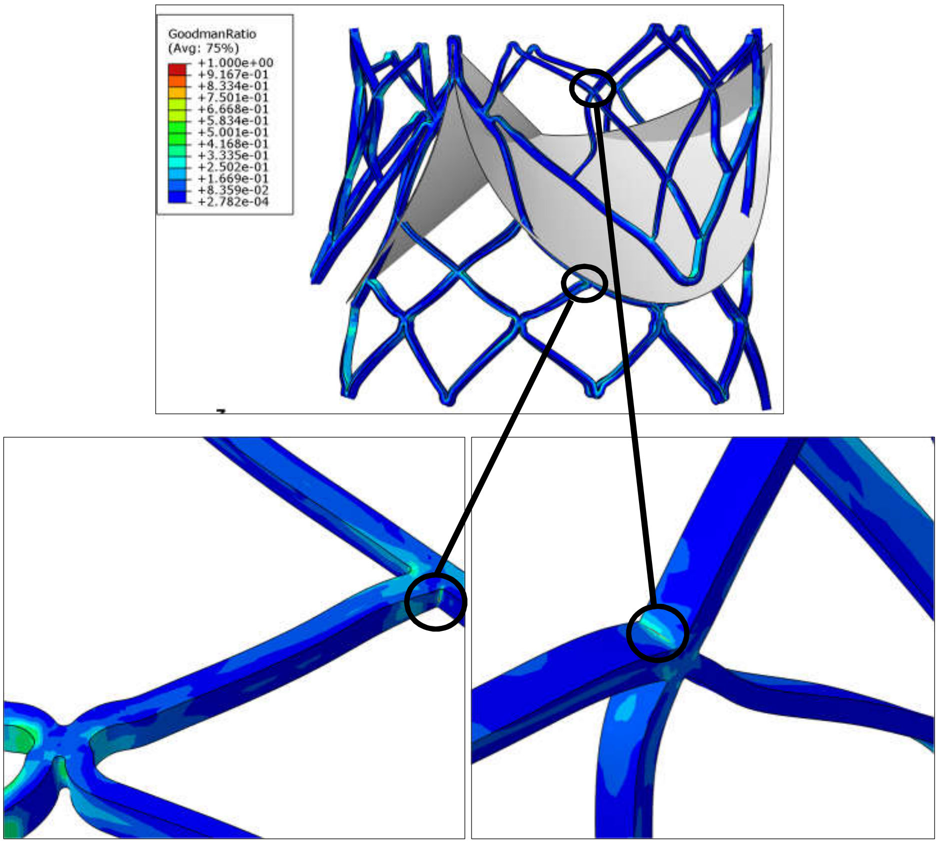

Figure 7-18. Contour plots of inverse fatigue safety factors for Design 2

7.2 *In Vitro* and *Ex Vivo* Results

7.2.1 Material properties

Tubing material properties were similar for all three MP35N samples. Stress-strain curves are shown in Figure 7-19. UTS of the MP35N tubing was determined to be 877 ± 5 MPa, strain to break was 53 ± 0.2 % and the 0.2% proof stress was 424 ± 5 MPa. Plasticity data from Sample 1 were used for FEA (refer to Table 7-8).

Table 7-8 Material Properties for MP35N

Young's Modulus	236 GPa
Poisson's Ratio	0.4
Yield Strength	426 MPa
True stress at start of necking	1315 MPa
True plastic strain at start of necking	41%

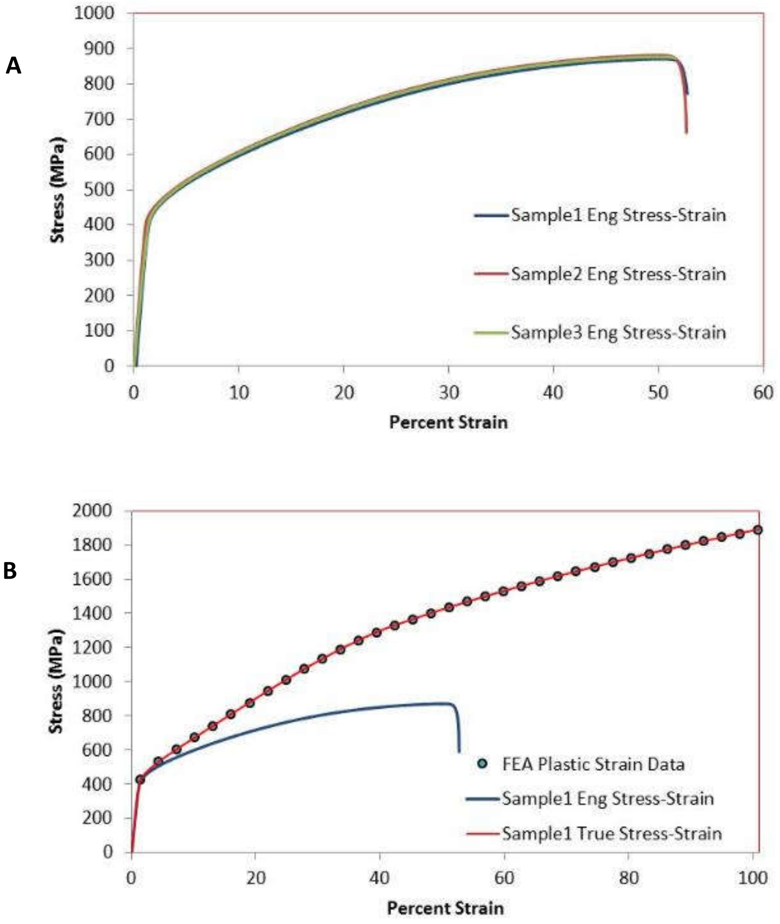

Figure 7-19. Stress-strain curves from uniaxial tensile testing of MP35N dogbones: A) Engineering stress-strain for three samples; B) True stress-strain and extracted plastic stress-strain data for FEA for Sample 1

7.2.2 Stent inspection and measurement

All stent designs could be laser cut, descaled and electropolished as intended. Laser kerf width was measured to be 57 ± 3 µm for slots in the longitudinal direction and 59 ± 2 µm for slots in the circumferential direction. See Appendix D. Approximately one in four cut stents were rejected for obvious cutting errors before three of each design were processed further. These rejects were caused by stent waste material (diamond “windows”) protruding outwards slightly during cutting, causing the stent to briefly bump into the laser cutter nozzle, which rotated the stent tubing in the clamping jaws. The result of these errors is the appearance of very wide struts and very narrow struts in the same stent, which were easily detected by brief stereo microscope inspection. Acid descaling and mechanical scrubbing with a miniature nylon brush were able to remove surface oxides and waste materials from the stent without apparent change in stent structure or attack on the parent metal.

Occasional small oxide particles were considered acceptable, and did not subsequently affect the polished surface.

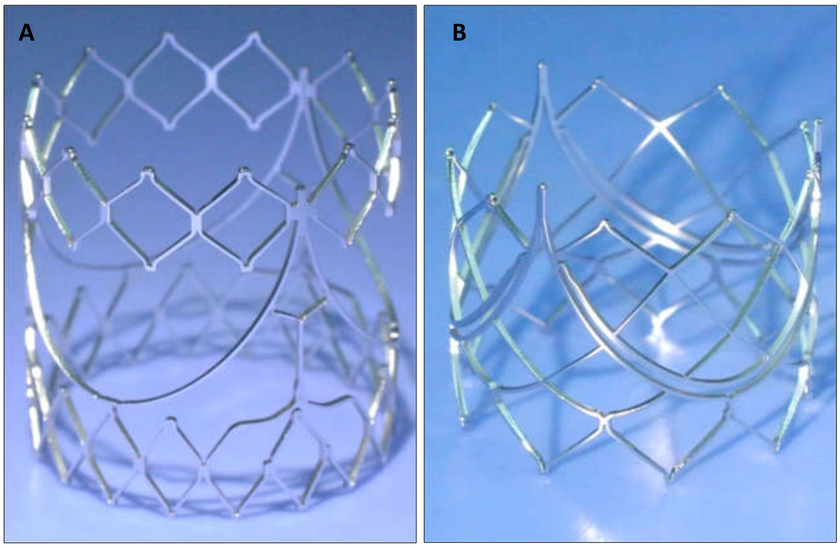

Figure 7-20. Macro photographs of stents. A) Design 1, B) Design 2

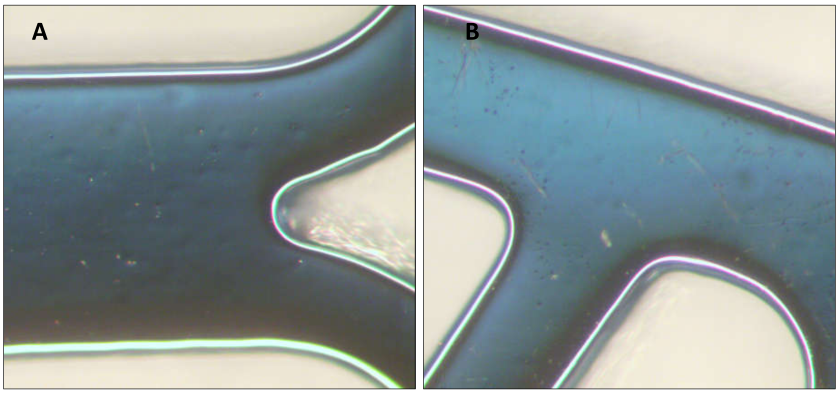

Figure 7-21. Micro photographs of stents. A) Design 1, B) Design 2

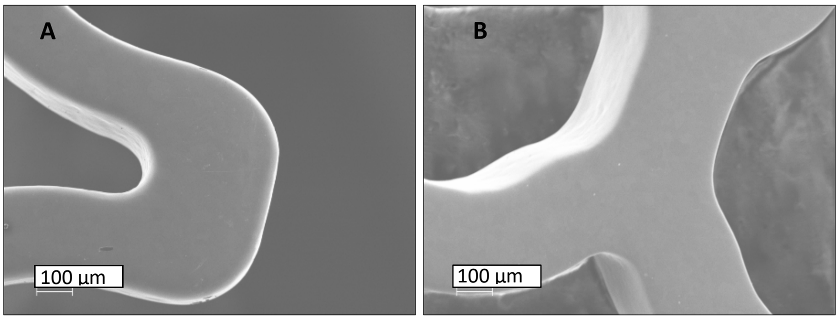

Figure 7-22. SEM images of stents. A) Design 1, B) Design 2

Electropolished stent surfaces were smooth. The outside and inside surfaces were very smooth, while the side (cutting) surfaces were smooth on a micro level but still had a slightly textured topography on a macro level. Macro photographs, microscope images and SEM images of electropolished Design 1 and Design 2 stents are shown in Figure 7-20, Figure 7-21 and Figure 7-22, respectively. Similar images of the cut and pickled stents of both designs are shown in Appendix I. Cut, pickled and polished images of the Control stents are also provided in Appendix I.

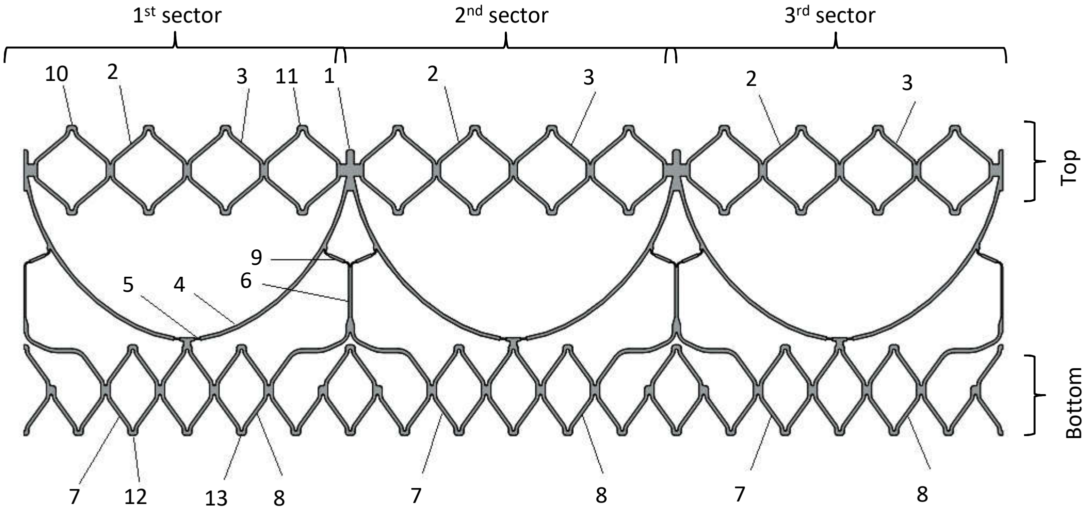

Figure 7-23. Measurement locations for Design 1

Stent measurement locations for Design 1 are shown in Figure 7-23. Mean stent dimensions for Design 1 were all within 4% of target dimensions (Table 7-9). Individual measurements are provided in Appendix E. The greatest deviation from target values occurred for a strut width, which was 29 µm below target for one of the stents. In general strut widths were slightly below target, while hairpin widths were slightly above target. Mean strut widths of the three sectors of the stent were within 1 µm of the stent mean strut width.

Table 7-9. Stent dimensions for Design 1

Region	Specification	Value (µm)	Diff* (µm)	% Diff
Strut	250 µm	247 ± 12	3	1.2
Top strut (2,3)		247 ± 8	3	1.3
Bottom strut (7,8)		247 ± 15	3	1.2
Strut first sector		246 ± 12	4	1.7
Strut second sector		247 ± 11	3	1.0
Strut third sector		248 ± 14	2	1.0
Hairpin	327 µm	330 ± 5	-3	-0.8
Top hairpin (10,11)		330 ± 6	-3	-1.1
Bottom hairpin (12,13)		329 ± 5	-2	-0.6
Commissure post (1)	560 µm	550 ± 5	10	1.7
Crown member (4)	250 µm	252 ± 9	-2	-0.9
Vertical member (6)	260 µm	268 ± 2	-8	-3.0
Branch member (9)	200 µm	207 ± 10	-7	-3.6
Crown hinge (5)	100 µm	101 ± 3	-1	-1.4
Wall thickness	470 µm	466 ± 7	4	0.9

* Diff = specification minus mean

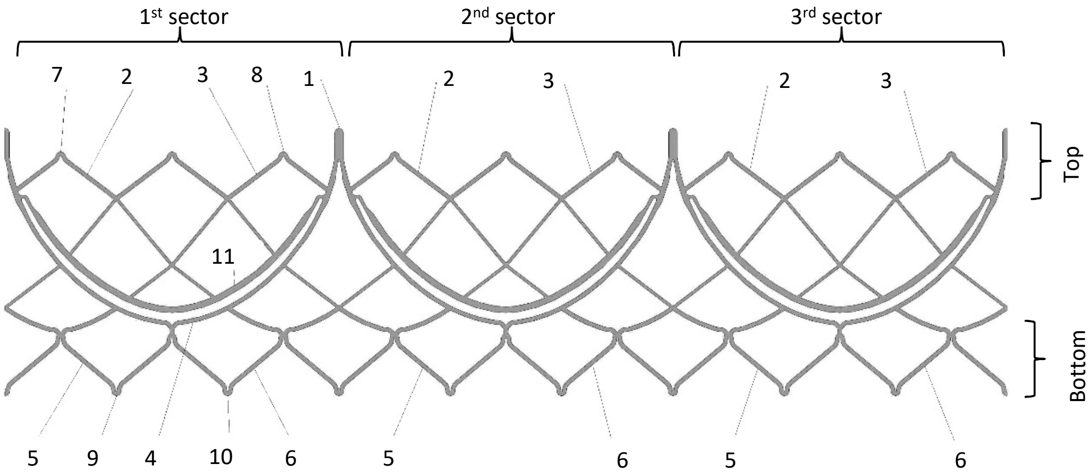

Figure 7-24. Measurement locations for Design 2

Stent measurement locations for Design 2 are shown in Figure 7-24. Mean stent strut dimensions for Design 2 were within 5% of target dimensions (Table 7-9). Individual measurements are provided in Appendix E. The greatest deviation from target values occurred for wall thickness, which was 27 µm below target for one of the stents. In general strut widths were below target, while hairpin widths were slightly above target. Top struts were slightly narrower than bottom struts. Mean strut widths of the three sectors of the stent were within 3 µm of the stent mean strut width.

Table 7-10. Stent dimensions for Design 2

Region	Specification	Value (µm)	Diff (µm)	% Diff
Strut	290 µm	281 ± 9	9	3.1
Top strut (2,3)		278 ± 5	12	4.3
Bottom strut (5,6)		284 ± 11	6	1.9
Strut first sector		279 ± 9	11	3.6
Strut second sector		284 ± 10	10	3.3
Strut third sector		280 ± 9	7	2.3
Hairpin	290 µm	294 ± 6	-4	-1.5
Top hairpin (7,8)		292 ± 6	-2	-0.7
Bottom hairpin (9,10)		297 ± 4	-7	-2.3
Commissure post (1)	600 µm	590 ± 9	-10	-3.4
Crown member (4)	290 µm	300 ± 3	10	2.4
Arm (11)	440 µm	430 ± 4	10	1.7
Wall thickness	470 µm	452 ± 8	18	3.9

Representative photographs and measurements of the Control stent are shown in Appendix E. Individual stent measurements are also provided in Appendix E.

7.2.3 Stent mechanical performance

7.2.3 A) Crimping, deployment, recoil and foreshortening

All stent designs could be crimped to 6mm diameter on a commercial valvuloplasty balloon without fracture and without damaging the balloon. Images of the Control stent and the two favoured designs are shown crimped on a commercial balloon in Figure 7-25. The regular zig-zag pattern of the Control stent allows for a neat crimped stent pattern. This is also largely true for Design 1 at the top and bottom rows of diamonds. Some warping of the scallop hinges near the nadir occur, however, as predicted in FEA. Design 2 shows bending of struts in the bottom row attaching to the nadir, and in struts near the middle of the expanding arm, but the structure is neat and symmetrical as predicted in FEA.

Following crimping to a diameter of 6 mm, stents relaxed to average diameters along the stent length (excluding protruding arms in the case of Design 1) of 6.62 mm, 6.29 mm and 6.34 mm, for the Control, Design 1 and Design 2 stents, respectively; the largest crimped diameters were 6.71 mm, 6.50 mm and 6.49 mm, respectively, which occurred in the centre for the Control stent, but at the ends for the two new designs, as shown in Appendix J. Crimped stent lengths after removal from the crimper were 24.19mm, 29.32 mm and 25.39 mm, respectively. All stent designs could also be deployed on a 23 mm commercial valvuloplasty balloon without fracture or balloon damage. Images of stents deployed on balloons are shown in Figure 7-26. In all cases the proximal end of the balloon filled with water first, followed by filling at the distal end, during which small stent rotations occurred. Obvious stent expansion occurred after this. Control stents deployed at higher pressures than Design 1 and Design 2 stents, requiring almost 4atm to deploy fully. It displayed a clear hourglass shape throughout deployment, and was even slightly hourglass-shaped at 4 atm.

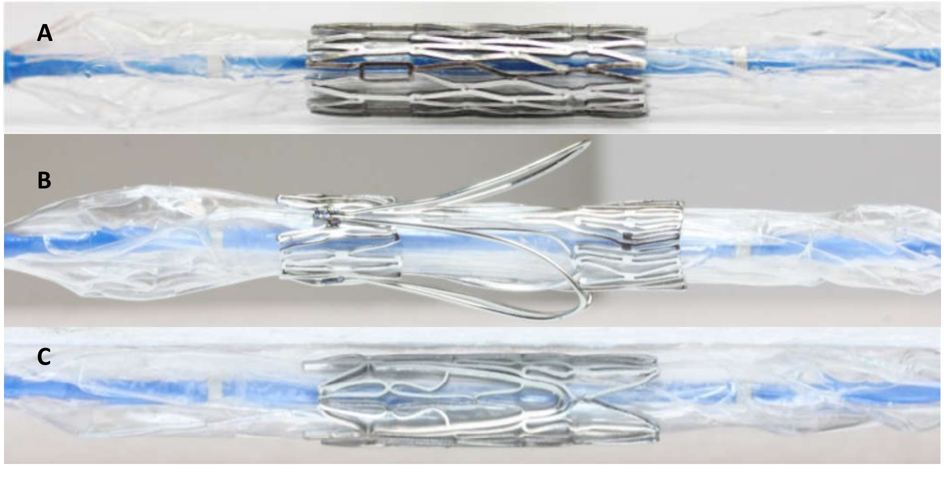

Figure 7-25. Crimped stents on commercial balloon. A) Control stent, B) Design 1, C) Design 2

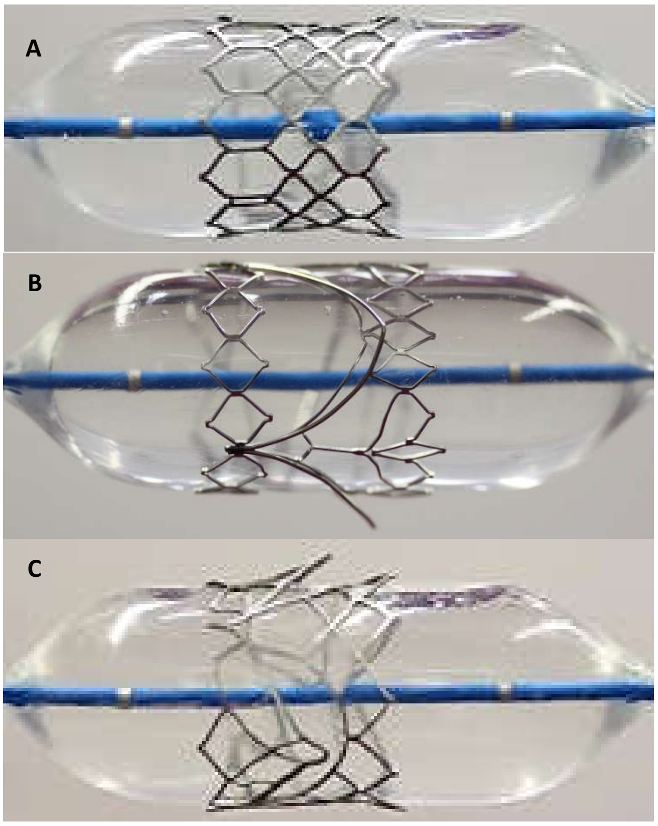

Figure 7-26. Deployed stents on commercial balloon. A) Control stent, B) Design 1, C) Design 2

The Design 1 stent expanded rapidly, opening first at the bottom (proximal) end, followed by the top (distal) end. No true hourglass shape formed. Fully deployed shape occurred at approximately 1 atm, but diameter continued to grow up to 4 atm. The rate of deployment for Design 2 was between the Control and Design 1 stents. The bottom (proximal) end flared initially, follow by relatively even deployment of the rest of the stent, during which time the arms started to protrude. Fully deployed shape occurred at approximately 2 atm, with diameter increasing up to 4 atm. Arms protrusion also increased with increased balloon diameter.

Photographs of undeformed stents and stents after deployment are shown in Figure 7-27, along with deformed and undeformed stents from the FEA modelling. Deformed stent shapes corresponded closely with shapes determined computationally. Average stent diameters (excluding protruding arms) were 22.38 mm, 23.47 mm and 23.29 mm for the Control stent, Design 1 and Design 2, respectively, recoiling to 21.97 mm, 22.67 mm and 22.84 mm, respectively. The experimentally determined average recoil values were therefore 1.9%, 3.4% and 2.0%, for the Control stent, Design 1 stent and Design 2 stent, respectively. The arms protruded to a virtual diameter of 27.26 mm and 27.71 mm for Design 1 and Design 2, respectively, based on average measurements.

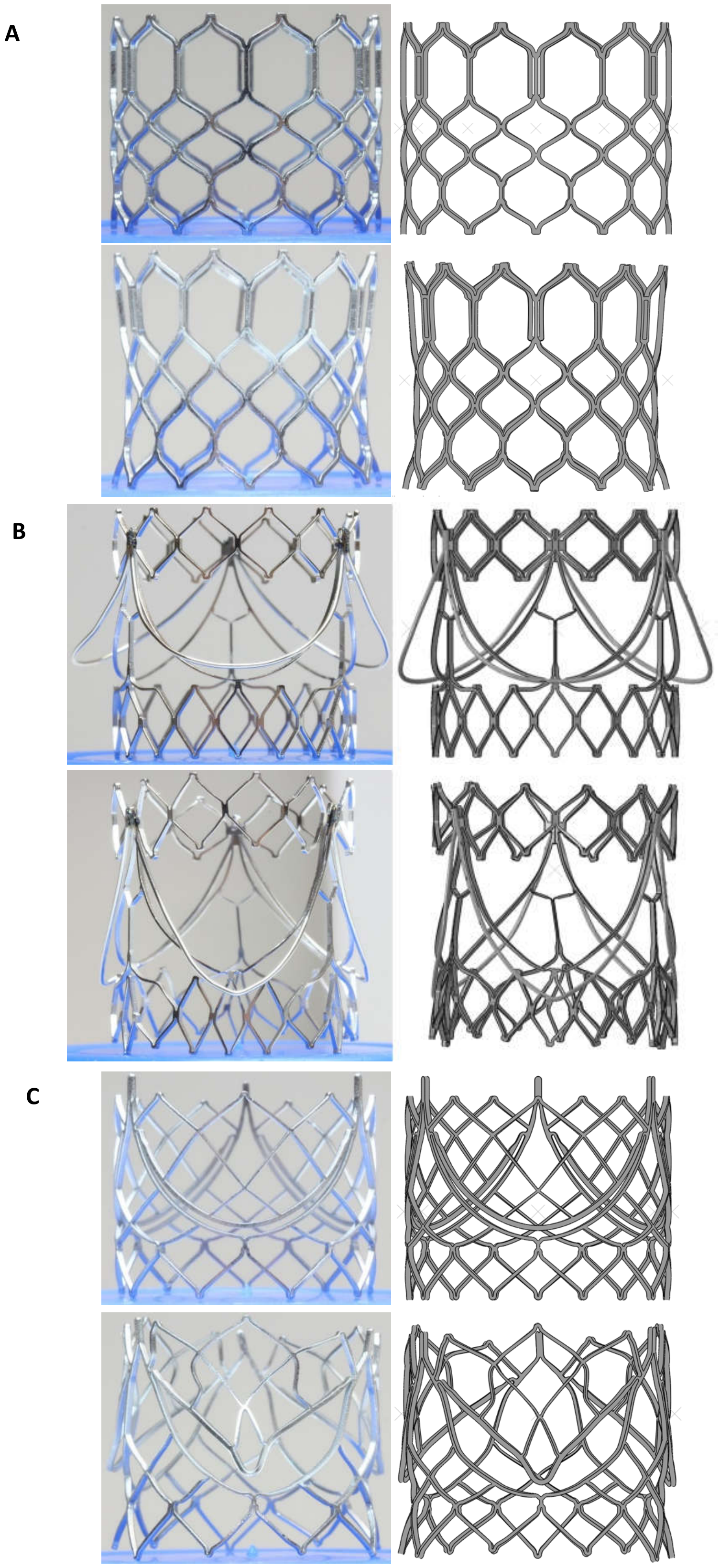

Figure 7-27. Undeformed and deformed stents. A) Control Stent, B) Design 1, C) Design 2. Clockwise from top left for each cluster: photograph of as-manufactured stent, FEA model of original geometry, FEA model of deformed geometry after deployment and recoil, photograph of deformed stent.

.

The stent lengths following deflation of the balloon (recoil phase), were 19.45 mm, 24.97 mm and 20.73 mm for the Control stent, Design 1 stent and Design 2 stent, respectively; therefore physical measurements of foreshortening were 19.6%, 14.8% and 18.4% respectively. Recoil and foreshortening values are provided in Table 7-6 and Table 7-7, respectively, along with FEA predictions of the same values. All stent designs could be inflated to 25.3 mm (10% over-inflation) without fracture. Control and Design 2 stents could be deployed on a 29mm balloon without fracture, but Design 1 fractured at one of the branch members at the attachment to the crown member.

7.2.3 B) Migration resistance

Polymeric valves of Design 1 and Design 2 were deployed under direct sight into a 25 mm Medtronic Freestyle Full Root valve and tested for migration resistance. The inner diameter at the annulus was approximately 21.5 mm, which is within the target native valve size range for a 23mm replacement valve. A stentless replacement valve such as the Freestyle valve offered the advantage that a force could be applied directly to the stent in an axial direction. Images of a Design 2 valve positioned in the xenograft, and tested for migration resistance, are provided in Figure 7-28. Design 1 and Design 2 resisted embolisation up to a force of 22N. At this point it was felt that greater forces would risk damaging the xenograft and the test was stopped.

Figure 7-28. Migration test. A) Design 2 valve deployed into Freestyle xenograft. B) Test setup for migration test, including a force gauge and sutures connecting the base of the stent to the gauge.

7.2.4 Valve performance

7.2.4 A) Valve manufacturability

Stents of both designs were expanded to an inner diameter of 23mm using tapered PTFE rods and positioned over stainless steel spray-coating moulds. In the case of stent Design 2 the arms had to be lifted slightly upwards to prevent the sprayed polyurethane from forming a web or film between the arm and the crown member, and were easily returned to their starting positions.

In the case of Design 1, special care was required during placement on the mould to prevent longitudinal stent compression; the vertical members beneath the commissures could be forced upwards, bending the “branch” elements in the wrong direction. Examples of polymeric valves constructed from Design 1 and Design 2 stents are shown in Figure 7-29. Design 1 valves had polyurethane film sealing skirts while Design 2 valves had electrospun sealing skirts.

Figure 7-29. Polymeric valve constructed from Design 1 stent (left) and Design 2 (right). Design 1 incorporates a polyurethane film skirt and shows marker lines used to indicate free edge of leaflet for cutting. Design 2 incorporates an electrospun polyurethane skirt

7.2.4 B) Valve Deployment behaviour

A polymeric valve constructed from Design 2 was manufactured and crimped onto an SATH mechanical expander and annular balloon and deployed by first expanding the mechanical arms to dilate the valve to approximately 18mm and subsequently to inflate the annular balloon to dilate the valve to 23 mm.

The valve could be crimped onto the deployment device without damage to the valve or device and could be covered by the device protector. Leaflets remained undamaged and the electrospun sealing skirt remained attached to the stent frame.

Although the stent foreshortened as expected, the absolute position of the nadir of the valve moved towards the handle by only approximately 1 mm, as shown in Figure 7-30. The valve deployed fully and the expanding arms protruded as per design.

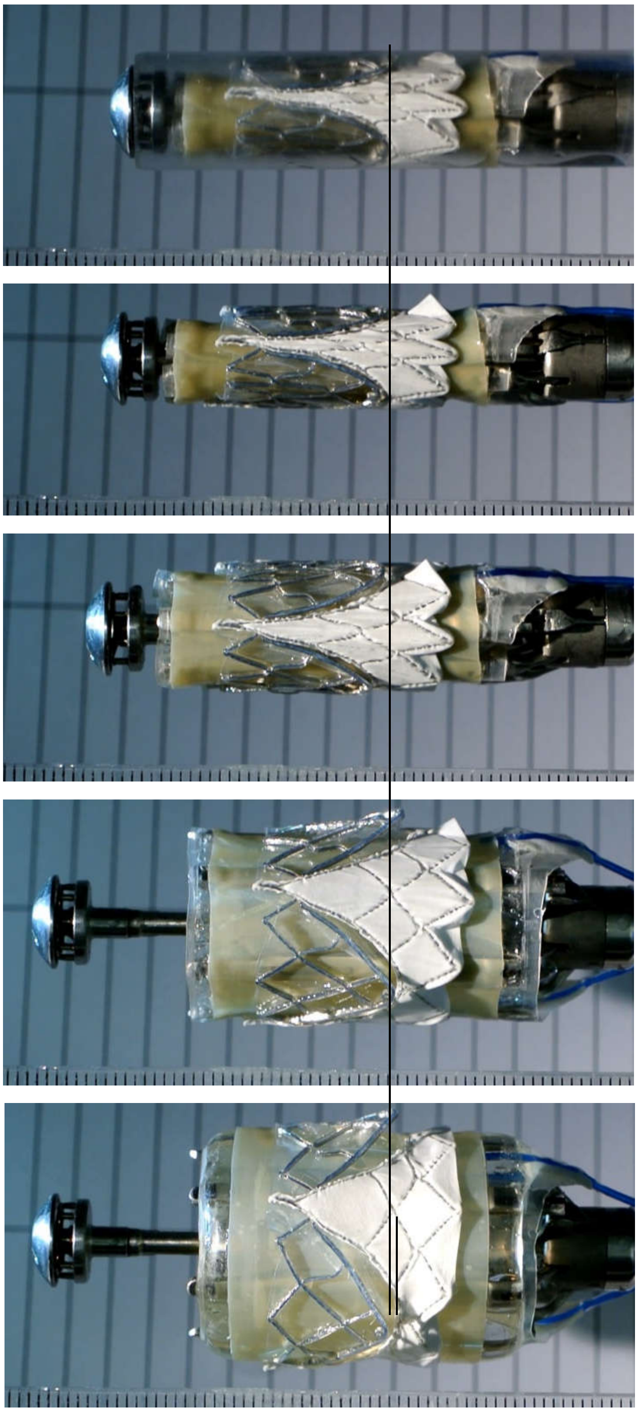

Figure 7-30. Free deployment of Design 2 valve on SATH Mechanical expander and annular balloon. The long black line indicates the location of the nadir of the crown shape in the crimp condition and the short line indicates the location of the nadir in the deployed condition

7.2.4 C) Haemodynamic Behaviour

Ten polymer valves of each stent design were tested for haemodynamic performance. Values for pressure drop, EOA and regurgitation are provided in Table 7-12.

Table 7-11. Frames from high speed photography at different parts of the cardiac cycle

Time (s)	Hancock 2	Design 1	Design 2
0			
0.01			
0.03		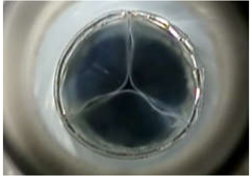	
0.05		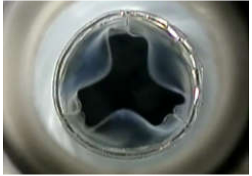	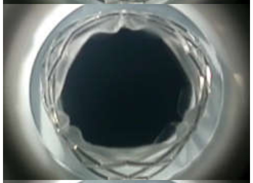
0.11		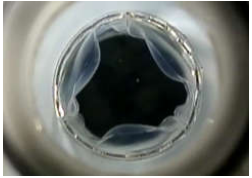	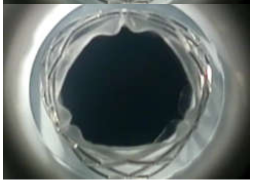
0.33		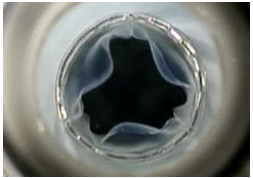	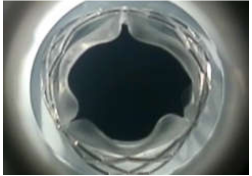
0.40	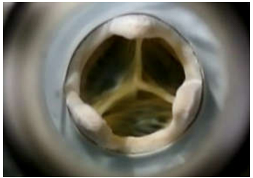		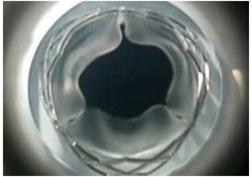
0.43			

Both designs passed the requirements of the relevant ISO standard (ISO-5840-3, 2013). Both stent designs also had lower pressure drop and larger EOA than the Hancock 2 valve, while regurgitation was lowest in the Hancock 2 valve.

Frames from high-speed videos of one of each valve are shown at several moments within the cardiac cycle, from the initial movement of the leaflets at the start of systole to full leaflet closure. The frames show that the polymeric valves open and close slower than the bioprosthetic Hancock 2 valve. The images also illustrate the greater geometric opening area achieved by percutaneous valves, since the outer diameter of each valve is approximately 23mm. Both TAVR stent designs allowed for good hydrodynamic function. EOA was significantly greater for valves constructed from Design 2 compared to Design 1 (2.03 ± 0.12 vs. 2.38 ± 0.19, p<0.001).

Table 7-12. Haemodynamic results

Design	Pressure Drop (mmHg)	Effective Orifice Area (cm^2)	Regurgitation (%)
Design 1	8.56 ± 1.31	2.03 ± 0.12	5.22 ± 1.43
Design 2	6.12 ± 0.93	2.38 ± 0.19	5.14 ± 1.17
Hancock 2	13.50	1.68	3.52

7.2.4 D) Durability

Seven valves constructed using stents of Design 1 (specifically Concept 1A) were subjected to fatigue testing, while 29 valves constructed using stents of Design 2 (Concept 2D) were subjected to fatigue testing. Fatigue testing was performed on valves and not on stents alone, as a stent fatigue tester was not available.

Table 7-13. Durability test results

Design 1	**Numbering of stents without fatigue fracture at various time points (percentage pass)**
0 – 20 million cycles	6 (100%)
21 – 100 million cycles	1 (100%)
Design 2	
0 – 20 million cycles	24 (100%)
21 – 100 million cycles	14 (93%)*
101 – 400 million cycles	2 (100%)
> 400 million cycles	1 (100%)

* A stent failed due to a manufacturing defect from laser cutting

Fatigue fracture was found in only one stent, a stent of Design 2 that had been subjected to 40 million cycles. Stent inspection showed that the stent had a manufacturing defect that had not been identified following laser cutting. In all other cases, valves were removed from the durability testers either to provide space for newer polymer leaflet designs or following failure of the polymer leaflets themselves. As a result, stents were subjected to a wide range of total fatigue cycles. The number of stents surviving valve durability testing free of fatigue fracture is shown in Table 7-13.

The maximum number of cycles tested for Design 1 was 22 million cycles. Seventeen stents of Design 2 survived more than 20 million cycles. This includes a stent that survived more than 400 million cycles, and at the time of writing was still being tested successfully.

7.2.4 E) *Ex Vivo* Explanted Heart

Valves constructed using stents of both designs were delivered and implanted into cadaveric pig hearts in an explanted heart tester. Valves were successfully crimped and could be covered with an introducer sheath, which was used to advance the valves through the port without damage until they were positioned in the left ventricle (in the case of Design 1 the introducer sheath also kept the welded arms down). Valves were delivered and placed under fluoroscopic guidance (and tactile feedback for Design 1), and videos of the implant were captured using endoscopy.

Several attempts were made to locate Design 1 valves within the native valve. Initially the valve passed through the open leaflets during withdrawal without capturing the leaflets, but when stent placement was timed to occur exactly during diastole, the arms of the stent could be placed behind the leaflets, and the correct positioning within the aortic root could be confirmed using fluoroscopy (see Figure 7-32). It was noted from endoscopy that the stent arms had captured the leaflets and prevented the native leaflets from opening fully. During valve deployment the arms remained in position behind the cusps (Figure 7-31). The valve was fully expanded, but it was clear that it was nevertheless undersized for the heart used in the explanted heart tester (the animals available from the abattoir were older than subsequently used for *in vivo* studies). Despite this undersizing, the valve functioned correctly and did not embolise. It is anticipated that some leakage occurred between the replacement valve and the native valve (such leakage may occur at the asterisk shown in Figure 7-31), but the apparatus had no means of determining leaks.

Design 2 valves were crimped onto deployment devices that incorporated location mechanisms. Initially location was performed using these devices, but adjustments were made to valve position based on fluoroscopy alone (see Figure 7-34).

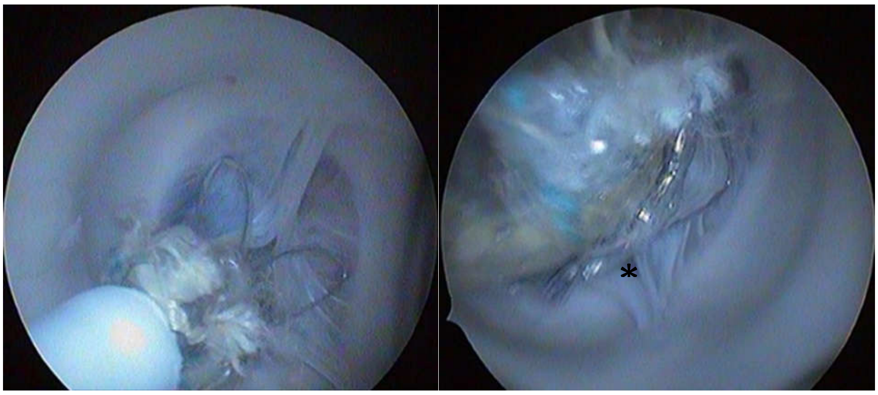

Figure 7-31. Endoscopic images of location and deployment of Design 1 valves, from the aortic view. Asterisk shows area of potential leakage.

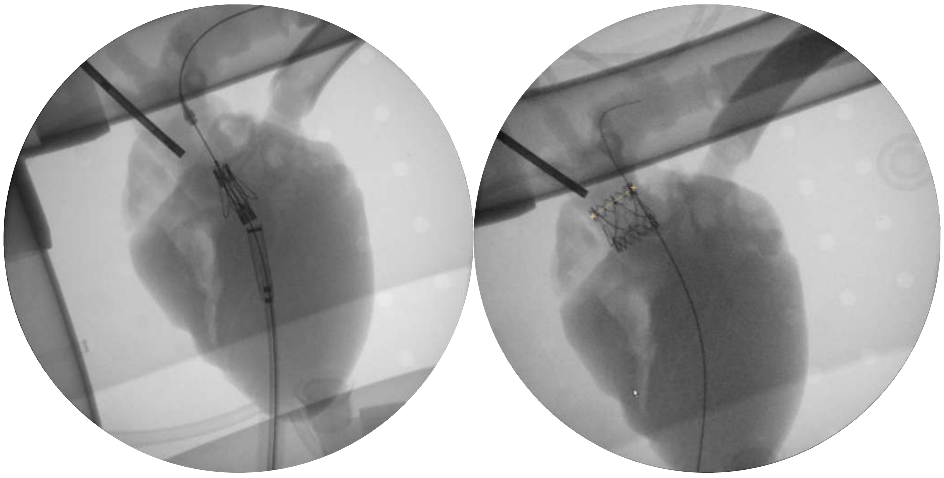

Figure 7-32. Fluoroscopic images of location and deployment of Design 1 valves, deployed using SATH non-occlusive balloon catheter

It was possible to position the valve axially by aligning the nadir of the stent crown-shaped member with a position just above the virtual annulus, and to position the valve circumferentially by aligning the expanding arms with the SoV prior to deployment. When the valve was deployed, two of the arms were positioned as intended, pushing the leaflets into the SoV and resting on the muscular shelf at the VAJ. The third arm, position at the non-coronary cusp was positioned slightly below the virtual annulus. As a result the valve was tilted slightly, and the non-coronary leaflet curved over the top row of struts at the free edge, although this did not interfere with polymer leaflet function. Ventricular and aortic views of the valve are shown in Figure 7-33. The heart used for Design 2 evaluation was also oversized relative to the stent, as had been the case in the evaluation of Design 1. Despite this tilt and relative size difference, Design 2 did not embolise. The replacement leaflets opened and closed over the heart cycle, but a tear was present in one of the leaflets near the commissure post. It was not clear whether this had occurred during crimping or deployment.

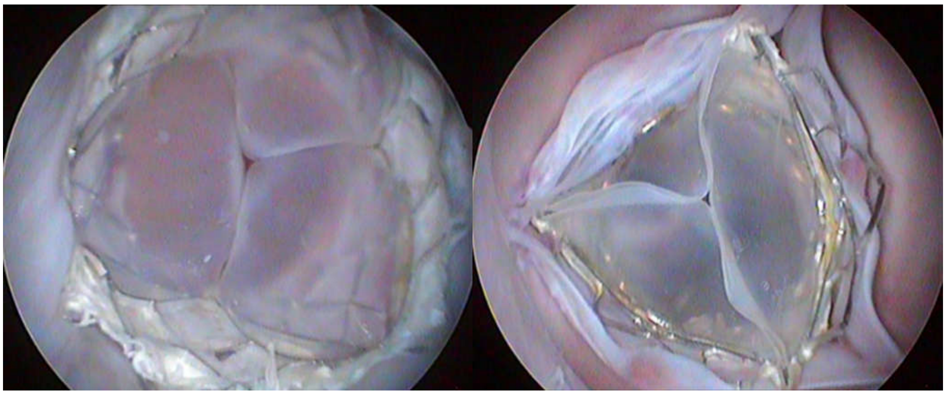

Figure 7-33. Endoscopic images of deployed Design 2 valves, from the ventricular (left) and aortic (right) views

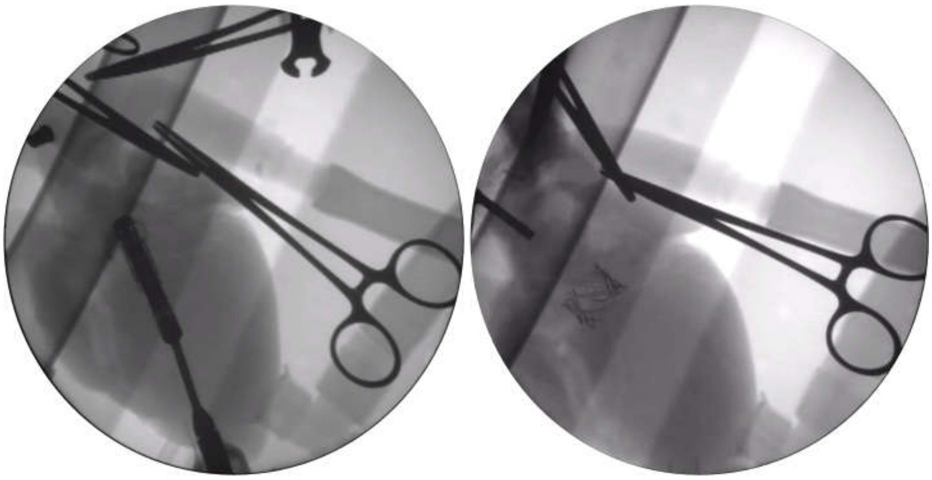

Figure 7-34. Fluoroscopic images of location and deployment of Design 2 valves, deployed using SATH mechanical expander and annular balloon

7.3 *In Vivo* Results

Stents of two different designs were tested in 17 pigs with a mean weight of 47.3 ± 2.8 kg. The mean diameter of the aortic annulus, as determined through (primarily transoesophageal) echocardiography, was 20.6 ± 2.0 mm during systole and 19.7 ± 2.1 mm during diastole (range 17-23 mm for both). Annulus diameter could not be measured reliably in four animals due to difficulties obtaining acceptable TOE images. Animal data, details of devices used and pre-implant comments may be found in Table 7-14.

Implantation of self-locating valves was attempted in the first nine pigs, and implantation of valves with expanding arms was attempted in the last eight pigs. Mean weights of the animals were not statistically different (46.9 ± 2.5 kg and 47.7 ± 3.1 kg, respectively, p=0.5).

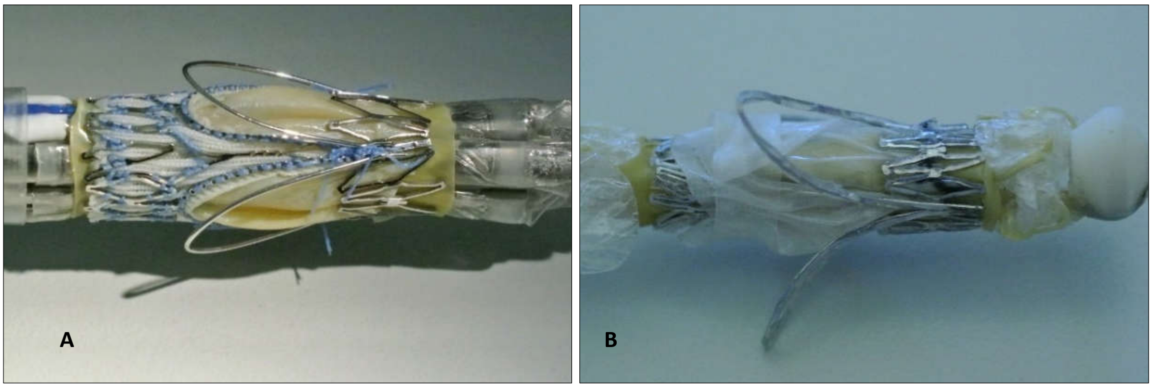

Figure 7-35. Exemplary crimped valves used in the preclinical evaluation of Design 1. A) Bioprosthetic valve on SATH mechanical expander; B) Polymeric valve on SATH self-sustaining balloon catheter

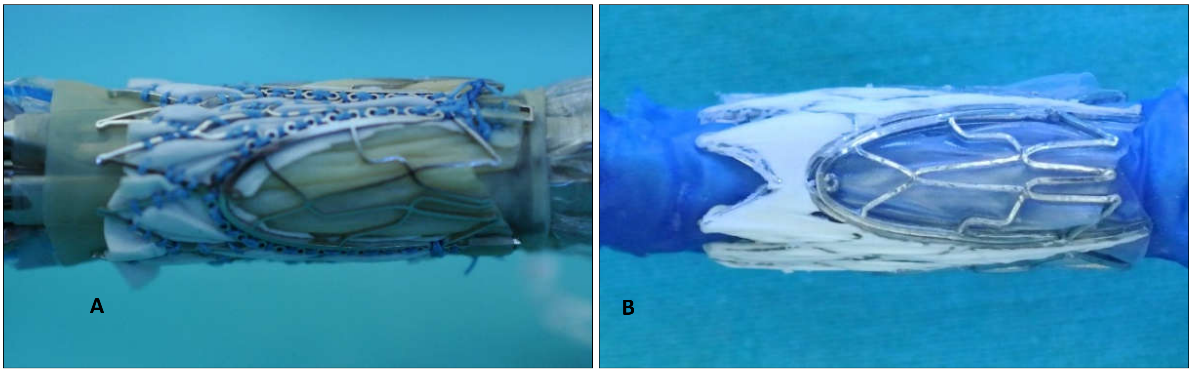

Figure 7-36. Exemplary crimped valves used in the preclinical evaluation of Design 2. A) Bioprosthetic valve on SATH mechanical expander; B) Polymeric valve on SATH self-sustaining balloon catheter

Prior to aortic valve implant, the first nine pigs were also used for the evaluation of mitral valve repair strategies by other investigators; these procedures did not directly appear to influence the ability to deliver and deploy the aortic valve. The mean diameter of the aortic annulus during systole was greater for the first nine animals than for the last eight animals (22.5 ± 0.5 mm versus 19.1 ± 1.2 mm, $p<0.001$), and similarly during diastole (21.7 ± 1.2 versus 18.0 ± 0.8 mm, $p<0.001$). The performance of each valve type is described below.

Table 7-14. Summary of animal data, deployment device and pre-implant conditions for pig study

Pig #	Weight (kg)	AV diam (Sys/Dia)	Stent type	Deployment device type	Valve type	Pre-implant comments/Predilation
1-3	49.0	22/21	D1: Self-locating	SSB	Poly	Mechanical commissurotomy
1-4	48.2	22/20	D1: Self-locating	ME/AB	Bio	Annular balloon predilatation
1-5	47.8	22/21	D1: Self-locating	SSB	Poly	Annular balloon predilatation
1-6	44.7	CNM	D1: Self-locating	ME/AB	Bio	Annular balloon predilatation
1-7	45.8	CNM	D1: Self-locating	SSB	Poly	N/A
1-8	41.4	CNM	D1: Self-locating	ME/AB	Poly	N/A
1-9	49.2	23/23	D1: Self-locating	ME/AB	Poly	N/A
1-10	48.2	23/23	D1: Self-locating	SSB	Bio	Mini-thoracotomy attempt
1-11	47.5	23/22	D1: Self-locating	ME/AB	Bio	N/A
2-5	45.0	17/17	D2: Expanding arms	SSB	Poly	N/A
2-6	47.0	19/18	D2: Expanding arms	SSB	Poly	N/A
2-7	54.9	20/CNM	D2: Expanding arms	ME/AB	Poly	Helical balloon predilation
2-8	49.0	19/17	D2: Expanding arms	ME/AB	Poly	Helical balloon predilation
2-9	46.6	19/18	D2: Expanding arms	SSB	Poly	N/A
2-10	45.9	21/19	D2: Expanding arms	ME/AB	Bio	N/A
2-11	46.0	20/19	D2: Expanding arms	ME/AB	Bio	N/A
2-12	47.5	18/18	D2: Expanding arms	SSB	Bio	N/A

CNM – Could not measure. SSB – Self-sustaining balloon. ME/AB – Mechanical expander with annular balloon. Poly – polymeric. Bio – bioprosthetic.

7.3.1 Design 1: Self-locating valve

The self-locating valve was successfully delivered to the aortic root in all nine pigs in which implant could be attempted. Procedural results are summarised in Table 7-15. Typical images of Design 1 valves crimped onto SATH deployment devices in preparation for implant are shown in Figure 7-35. Successful valve location using locating arms was achieved in eight of the nine cases. In the case of unsuccessful location (Pig 1-3), tactile, echo and fluoroscopic feedback indicated correct placement but with subsequent manipulation one of the arms tore through the native leaflet.

Valves could be successfully deployed without rapid pacing in eight of nine animals (Figure 7-37). Unfortunately prior to attempted deployment, Pig 1-8 experienced fibrillation from which it could not be resuscitated. Valve position was correct (aligned with natural leaflets and positioned within the annulus) in 7 of the 8 valves that were deployed (including Pig 1-3, which had pierced a leaflet cusp). The valve that was deployed in the incorrect position (Pig 1-5) was implanted slightly supra-annularly (thought to be due to slow expansion of the balloon). In one of the cases with correctly deployed valves (Pig 1-6), the pigtail catheter was not pulled back far enough before deployment, causing the stent to crush the pigtail against the wall of the aortic root. The valve nevertheless continued to function.

Table 7-15. Device performance and complications for Design 1 (self-locating) valve

Pig #	Device Success						Complications	
	Delivery	**Location**	**Deployment**	**Anchor/ Function**	**Sealing**	**Withdrawal**	**Device/Procedural complications**	**Stent/Valve complications**
1-3	✓	✗	✓	✗	✗	✗	Catheter leak prevented full inflation, so valve was under-deployed at waist. Balloon caught on stent. Animal experienced cardiac arrest soon after deployment.	Initial tactile feedback obtained but subsequently lost. Valve under-deployed.
	Post-mortem findings: Balloon reinforcing fibres got hooked on stent. One stent arm pierced through native leaflet. Other two arms in correct position.							
1-4	✓	✓	✓	✓	✓	✓	Deployment device inadvertently clamped pigtail catheter. Protective sleeve from balloon appeared to be have been removed after catching on stent. Port complications led to blood loss, reduced cardiac output and subsequent sacrifice. Animal experienced cardiac arrest soon after deployment.	None.
	Post-mortem findings: Valve position was optimal. Stent deployment was cylindrical.							
1-5	✓	✓	✓	✓	✓	✓	Pre-implant air embolization into coronaries; took 90 minutes to stabilise. During inflation balloon not cylindrical. Animal sacrificed after slowly declining physiological conditions.	Valve under-deployed.
	Post-mortem findings: Valve slightly high; thought to be due to slight champagne-cork effect from slow inflation. Polymer skirt separated from bottom row of stent.							
1-6	✓	✓	✓	✓	✓	✓	Extensive pre-implant blood loss due to port leakage; animal stabilised. Pigtail catheter trapped during deployment.	None.
	Post-mortem findings: Stent perfectly positioned with arms in cusps, with full deployment in annulus and at top row. Flushing with syringe on top of leaflets seals without leakage.							
1-7	✓	✓	✓	✓	✓	✓	Throat trauma made TOE difficult. Ventricle cut during sternotomy. Deployment not complete due to balloon leak, despite efforts to maintain 15atm.	Valve under-deployed.
	Post-mortem findings: Valve position correct; all three arms in native cusps. Native leaflets rest on replacement leaflets. Coronaries unobstructed.							
1-8	✓	✓	✗	✗	✗	✗	Air introduced during mitral repair procedures caused rapid blood pressure drop to 60/40 and fibrillation. This required port removal and subsequent port re-entry. When the crimped valve was positioned across the native valve and the sheath was fully retracted, the heart started fibrillating. The heart was defibrillated three times before the procedure was abandoned.	None
	Post-mortem findings: N/A							
1-9	✓	✓	✓	✓	✓	✓	Sheath interfered with the ventricular pressure readings. Animal was sacrificed after gradual drop in aortic pressure.	None
	Post-mortem findings: Stent deployed very well, to correct size. Stent position perfect, with arms in all three cusps. Skirt does not cover bottom row of diamonds fully.							
1-10	✓	✓	✓	✓	✓	✓	Extensive blood loss caused by failure of balloon catheter shaft.	Valve leaflets inadequately cleaned of fatty tissue, causing thickening in vivo.
	Post-mortem findings: Valve in correct place, but leaflets clearly thickened. Outer stent diameters at top and bottom were 23.2mm and 22.5mm. Subsequently tested on pulse duplicator and found to have pressure drop of 8mmHg, EOA of 2.7cm^2 at 5l/min CO.							
1-11	✓	✓	✓	✓	✓	✓	Deployment device leak caused blood to leak through inflation line.	Valve appeared to cause trivial mitral regurgitation to become mild.
	Post-mortem findings: Valve position and size good. Natural leaflets pulled taut. Valve slightly hourglass shaped. Top and bottom outer diameters of stent were 23.0mm and 23.0mm. Deployed length was 25.4mm.							

Successful acute valve function occurred in eight pigs (pigs 1-3, 1-4, 1-5, 1-6, 1-7, 1-9, 1-10, 1-11), with five valves functioning for more than ten minutes (1-5, 1-7, 1-9, 1-10, 1-11), including at least one each of bioprosthetic valve on helical balloon, bioprosthetic valve on mechanical expander, polymer valve on helical balloon and polymer valve on mechanical expander (Figure 7-37). Central leakage and paravalvular leak were absent or insignificant in seven of eight valves; leakage was present in Pig 1-3, as a result of the pierced cusp and under-deployed valve. All valves deployed in the correct position maintained their location, confirmed by echocardiography, fluoroscopy and subsequent autopsy (Figure 7-38).

Two of the deployments resulted in cardiac arrest shortly after deployment (1 to 3 minutes), namely Pigs 1-3 and 1-4. In general, valves deployed using the mechanical expander and annular balloon were fully expanded, while most valves deployed using the self-supporting balloon were under-expanded. All stents were considered sufficiently radiopaque to position the valve in the correct position under fluoroscopy.

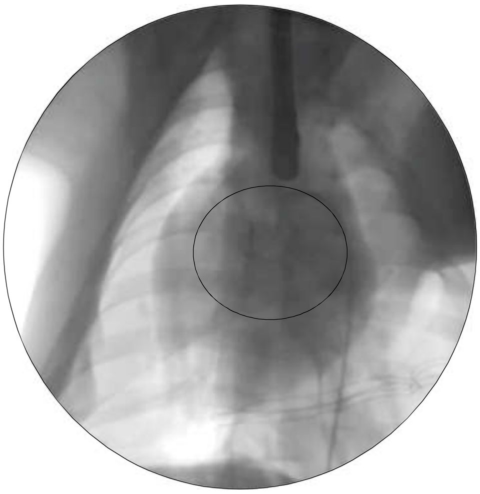

Figure 7-37. Typical fluoroscopic image of an implanted Design 1 valve, from Pig 1-10; the valve is circled

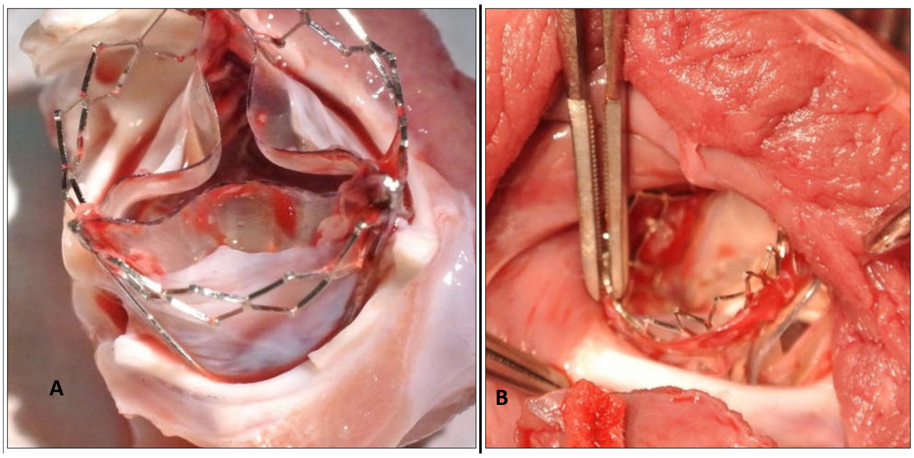

Figure 7-38. Post-mortem images of Design 1 valve in position in a porcine aortic root. A) Typical valve shown with most of the SoV excised; note location of arm behind cusps and proximity of native leaflets to replacement leaflets. B) Ventricular view of valve from Pig 1-3 showing arm pierced through leaflet.

7.3.2 Design 2: Expanding arm valve

Procedural results for Design 2 are summarised in Table 7-16. Typical images of Design 2 valves crimped onto SATH deployment devices in preparation for implant are shown in Figure 7-36. Valves were successfully delivered to the aortic root in seven of the eight pigs in which implant could be attempted. In the case of unsuccessful delivery (Pig 2-10), the valve embolised before deployment could be performed.

Table 7-16. Device performance and complications for Design 2 (expanding arm) valve

<table>
<tr><th rowspan="2">Pig #</th><th colspan="7">Device Success</th><th colspan="2">Complications</th></tr>
<tr><th>Delivery</th><th>Location</th><th>Deployment</th><th>Anchor</th><th>Function</th><th>Sealing</th><th>Withdrawal</th><th>Device/Procedural complications</th><th>Stent/Valve complications</th></tr>
<tr><td rowspan="2">2-5</td><td>✓</td><td>N/A</td><td>✓</td><td>✘</td><td>✘</td><td>✘</td><td>✘</td><td>Balloon leak prevented full inflation. Valve deployed approximately 5mm too low.</td><td>Valve under-deployed. Valve embolised during device withdrawal.</td></tr>
<tr><td colspan="9">Post-mortem findings: The valve could not be properly inspected post-mortem because the stent, which had embolised into the left ventricle, was flattened during explant of the heart. A review of echocardiography showed that the stent was positioned approximately halfway across the native valve.</td></tr>
<tr><td rowspan="2">2-6</td><td>✓</td><td>N/A</td><td>✓</td><td>✓</td><td>✘</td><td>✓</td><td>✓</td><td>Some bleeding from port while placing guidewire across aortic valve.</td><td>Moderate regurgitation at one leaflet.</td></tr>
<tr><td colspan="9">Post-mortem findings: The valve was also orientated correctly, with the replacement valve aligning closely with the native valve. One of the stent arms appeared to be below the native leaflet base. Another appeared to be in the correct position. The third arm was positioned behind one of the native leaflets. One of the replacement valve leaflets was in an open position, which appeared to be due to being positioned against a native leaflet and pressed against the upper wall of the sinotubular junction. The valve was oval at the inflow side, although this may have been caused during explant. The native valve annulus was bruised in the interleaflet triangle areas and just below these.</td></tr>
<tr><td rowspan="2">2-7</td><td>✓</td><td>N/A</td><td>✓</td><td>✓</td><td>✓</td><td>✓</td><td>✓</td><td>Some bleeding from port while placing guidewire across aortic valve.</td><td>N/A. Valve initially pulled back with deployment device and advanced across the valve again. Mild regurgitation.</td></tr>
<tr><td colspan="9">Post-mortem findings: All three valve arms had become secured behind the native leaflets</td></tr>
<tr><td rowspan="2">2-8</td><td>✓</td><td>N/A</td><td>✓</td><td>✓</td><td>✓</td><td>✓</td><td>✓</td><td>Port came out several times. ST Elevation during predilation but resolved. ST changes occurred during valve inflation as well. Balloon leaked.</td><td>Valve under-deployed. Initial moderate regurgitation that resolved.</td></tr>
<tr><td colspan="9">Post-mortem findings: The valve was in the correct position but all three leaflets were behind the native leaflets, and the valve was very secure. Stent internal diameter was under-sized at the distal end (19.5mm).</td></tr>
<tr><td rowspan="2">2-9</td><td>✓</td><td>N/A</td><td>✓</td><td>✓</td><td>✓</td><td>✓</td><td>✓</td><td>Inadvertent cut on left ventricle from sternotomy caused ventricular fibrillation, requiring defibrillation. Port insertion difficult. ST segment elevation after 20 second inflation. Device moved distally during deployment.</td><td>Stent deployed high initially but shifted into correct position. Mild eccentric leakage.</td></tr>
<tr><td colspan="9">Post-mortem findings: At valve explant, valve in correct position in annulus and in correct orientation. Diameter 19.5mm ID. Two location arms were behind native leaflets, while the third was positioned on the luminal side of the native leaflet. Small hole in skirt from damage during manufacturing.</td></tr>
<tr><td rowspan="2">2-10</td><td>✘</td><td>N/A</td><td>✘</td><td>✘</td><td>✘</td><td>✘</td><td>✘</td><td>Animal had to be sacrificed when blood flow to the extremities was obstructed by the embolised valve.</td><td>Valve shifted on device and embolised firstly into left ventricle and then into the aorta</td></tr>
<tr><td colspan="9">Post-mortem findings: The valve was found in the descending aorta, upside down, blocking blood flow to the lower extremities.</td></tr>
<tr><td rowspan="2">2-11</td><td>✓</td><td>N/A</td><td>✓</td><td>✓</td><td>✘</td><td>✘</td><td>✓</td><td>ST elevation developed during deployment and animal never recovered. Blood pressure dropped further. Echocardiography showed anterior mitral leaflet impeded.</td><td>Valve deployed too low. Leakage.</td></tr>
<tr><td colspan="9">Post-mortem findings: Valve was positioned with arms below the level of the basal annulus.</td></tr>
<tr><td rowspan="2">2-12</td><td>✓</td><td>N/A</td><td>✓</td><td>✓</td><td>✘</td><td>✘</td><td>✓</td><td>Blood pressure low after device removal.</td><td>Valve appeared to be regurgitant based on fluoroscopy.</td></tr>
<tr><td colspan="9">Post-mortem findings: Valve damaged during CPR.</td></tr>
</table>

The stent had shifted distally on the balloon during attempts to locate within the valve. An attempt to remove the deployment device and crimped stent (in order to re-crimp) caused the stent to embolise completely firstly into the ventricle and subsequently into the descending aorta. A commercial valvuloplasty balloon was introduced to deploy the stent within the descending arch, but the valve had tilted over, causing it to occlude blood flow to the extremities, and the animal had to be euthanized.

All valves that were successfully delivered to the aortic valve could be deployed. Figure 7-39 presents a fluoroscopic image of a Design 2 valve in position. One of the valves embolised during withdrawal of the deployment device (Pig 2-5). The valve was deployed approximately 5mm too low. This was verified retrospectively from fluoroscopy and echocardiography. The valve had been positioned using a measurement scale on the deployment device, and in all subsequent cases valve position was checked against fluoroscopy and echocardiographic images during the procedure and position was adjusted where necessary. Removal of the balloon before full deflation (slow balloon deflation due to the use of 100% contrast medium) was considered to have contributed to stent embolization.

Valves remained anchored in the remaining six of the eight attempted implants. In four of these valves (Pigs 2-6, 2-7, 2-8 and 2-9), at least one expanding arm was located behind the native leaflet. During removal of the deployment device from the valve implanted in Pig 2-7, part of the deployment device that had failed to deflate fully caught on the valve, causing it to be pulled backwards. The valve was immediately advanced distally into position, and remained in position following withdrawal of the deployment device, and continued to function. At explant, all three arms were found behind the native leaflets. In Pig 2-6, one arm was behind the native leaflet, another was on the luminal side of the leaflet on the muscle shelf and the third was below the level of the annulus. Both of these cases are shown in Figure 7-40. Mild regurgitation was present but the location could not be discerned. In Pig 2-9, fluoroscopy showed that the device had moved substantially distally before deployment (undetected at the time), and that the stent moved under diastolic flow to a secure position at the annulus.

Moderate regurgitation occurred in at least two of the animals. In one of the animals (Pig 2-6), where leakage could be detected on echocardiography and was evidenced through a large pulse pressure, explant showed that one of the leaflets was immobilised due to the fact that it was pressed against the sinotubular junction. In another animal (Pig 2-8), the moderate central regurgitation resolved entirely in the first few minutes. Another two animals also showed signs of regurgitation based on contrast injection (Pigs 2-11 and 2-12), although blood pressure had reduced before and during deployment and animals did not survive long enough to measure flow or regurgitation on echocardiography before euthanasia. In the case of Pig 2-11, ST elevation occurred during deployment, the valve was deployed too low and the anterior mitral valve leaflet motion appeared to be impeded. The location of the regurgitation could not be ascertained for Pig 2-12. Haemodynamics could only be reliably measured in two animals, Pig 2-8 and Pig 2-9, where EOA was measured to be 2.50 cm^2 at a cardiac output of 3.7 L/min and 1.43 cm^2 at 2.8 L/min, respectively.

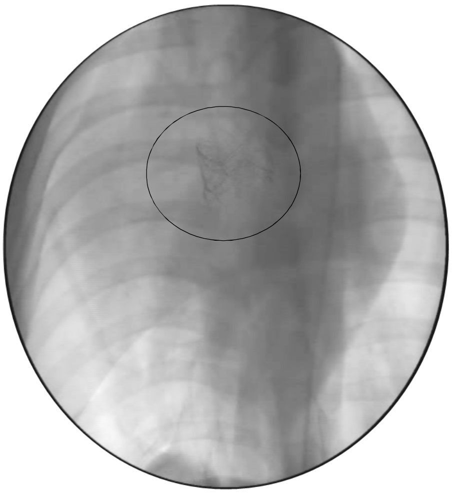

Figure 7-39. Typical fluoroscopic image of an implanted Design 2 valve, from Pig 2-7; the valve is encircled.

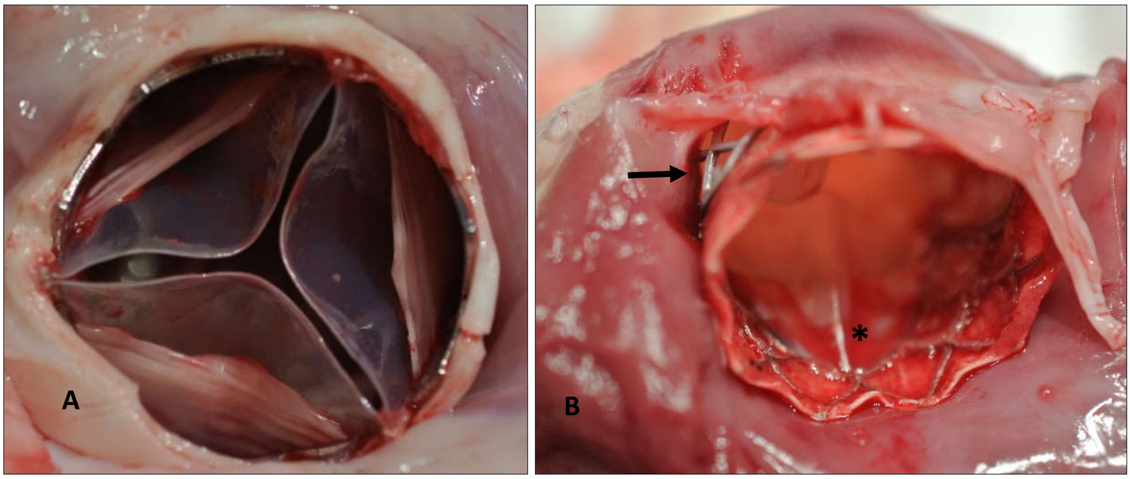

Figure 7-40. Post-mortem images of Design 2 valve in position in a porcine aortic root. A) Valve from Pig 2-7 shown with ascending aorta excised; arms are located behind cusps. B) Ventricular aspect of valve from Pig 2-6 showing arm below the basal plane (arrow); the arm behind the leaflet indicated by the asterisk is on the muscle shelf, while the third arm (not visible) is behind the leaflet

8 Discussion

TAVR has revolutionised the treatment of aortic valve disease. Much current debate centres on the application of this technology to younger patients, who have much lower surgical risk and for whom valve durability will be a more important consideration. Adoption of the technology has been fastest in Europe and the USA due to the advanced facilities required to perform the procedures and the high cost of the devices. Sufferers of rheumatic heart disease have limited access to both traditional surgical valve replacement and TAVR due to the limited resources available in the developing countries affected by the disease.

A report on the design and evaluation of novel balloon-expandable transcatheter valve stents that incorporate a continuous attachment site for polymeric leaflets and mechanisms for anchoring the valves in the absence of calcification is presented. To the best of our knowledge, these are the first balloon-expandable TAVR stents designed to be suitable for implantation in compliant non-calcific aortic roots.

8.1 Stent Design

It was demonstrated that balloon-expandable stents could be constructed with crown-shaped structural members, and still be crimped to 6 mm and deployed to the target diameter of 23 mm. These designs differ appreciably from all other marketed balloon-expandable stents, which have repeating zig-zag, diamond or chevron patterns (Nietlispach, Wijesinghe, Wood, Carere, & Webb, 2010; Ribeiro, Urena, Allende, Amat-Santos, & Rodes-Cabau, 2014).

Two crown support member concepts (either supported at the ends or integrated into the stent structure) combined with four different anchoring mechanisms (relying on friction, bulbous protrusions, welded arms and integrated protruding arms) to produce eight concepts that were subjected to simplified FEA for comparison; some were also prototyped, crimped and deployed. Although FEA suggested all eight concepts were feasible for the construction of polymeric heart valves, they differed substantially in their novelty, ability to anchor effectively, ease of manufacture, ability to return to the correct crown shape and other factors. The two favoured different stent designs reported here as Design 1 and Design 2 were selected from the available concepts for further analysis and testing because they offered two good alternative means of achieving the primary goals of supporting continuous attachment of polymer leaflets and anchoring in a complaint native aortic root. Both stents had axial symmetry to receive a tri-leaflet valve. The two preferred designs also allowed two different support structures and two different anchoring methods to be evaluated further. In addition, Design 1 stents (welded arm anchorage) permitted the stent to be used for locating position within the anatomy during delivery, at a time when such a mechanism had not yet been incorporated into the SATH deployment devices.

Design 1 stents consisted of a triple crown-shaped structure supported by a double row of zig-zags at either end of the stent, a mechanism to join the two ends of the stent to each other between the crowns while allowing the stent to lengthen during crimping, and elastic wire arms welded to the outside of the stent at the commissures. The stent frame was constructed from cobalt chromium in an annealed condition so that it can plastically deform during crimping and expansion, and limit stent recoil. The arms were constructed from the same material as the stent but in a cold-worked form to maximise elasticity so that the arms released following crimping to allow them to be used to locate the native cusps. Since the same material is used for both frame and arms, galvanic corrosion is not a concern (Stoeckel, Pelton, & Duerig, 2004). A few nitinol valves have been manufactured with locating arms, typically formed from the stent tube itself such as in the JenaValve™ (Kempfert et al., 2011) or as an additional layer, such as for the Medtronic Engager valve (Falk et al., 2011) and the JC Medical J-Valve (Zhu, Hu, Meng, & Guo, 2015). No investigators have reported the use of locating arms on a primarily balloon-expandable valve, or indeed a stent that incorporates balloon-expandable and self-expanding elements on the same stent, using either different or identical materials.

Design 2 stents integrated the crown shape into the stent structure, so struts connected to the crown member at the top (commissure), bottom (nadir) and at two regions along the crown with approximately equal spacing around the circumference. The design offered the potential to anchor without the addition of arms on the outside of the stent. Integration of a crown shape within the stent structure has been implemented in some stents constructed from nitinol wire (Cai et al., 2013; Rahmani et al., 2016; Wu et al., 2016) and, in the case of the JenaValve™, included a nearly crown-shaped member in a laser-cut nitinol stent (Rudolph & Baldus, 2013). To our knowledge, no reports on the integration of a crown member into a balloon-expandable stent have been presented. The use of elements that protrude as a result of stent expansion has been reported by M. Young et al. (2012) for a mitral valve stent. Stents were produced at a diameter intermediate between the compressed and expanded diameters, and a “wing anchoring fixation system” was able to remain flush with the stent during crimping, but (due to geometric configuration and indentations) expanded more during deployment. Although the authors report the use of cobalt chromium for the stents, the expansion is caused by a particular geometric shape and would therefore undergo the same shape change even if the stent were constructed from nitinol. In the case of Design 2, however, the expansion of the arms is intended to occur because plastic deformation occurs in the arm. The plastic deformation and work hardening ensure that the arm has higher strength, which means that it requires less energy for the arms to protrude outwards than for the arms to return to their pre-crimped state. The stent can be also be constructed at the functional diameter, which overcomes the deformation that occurs if the stent needs to be expanded from an intermediate geometry first (Kemp et al., 2013). Design 1 arms require a sheath to constrain the arms until ready for release, but Design 2 may be used without a sheath.

The material chosen for both stents was MP35N, for which the properties of high Young's Modulus, high UTS and elongation to failure, and relatively low yield strength make it very suitable for balloon-expandable valve construction. The stent could also have been constructed from L605, which is more frequently used in the construction of coronary stents (Suttorp et al., 2015). These Co-Cr alloys are durable and have history as haemocompatible materials. Valve heights (22.9 mm and 19.3 mm for Design 1 and Design 2, respectively) were slightly higher than an Edwards Sapien 3™ stent (17.9 mm), in part to accommodate higher leaflets and in part to provide sufficient crown support at the inflow and outflow ends of the stent. The heights of the new stents were much shorter than the height of the Medtronic Corevalve Evolut valve (45 mm) (Zavalloni, De Benedictis, Pagnotta, Scrocca, & Presbitero, 2014). Metal-to-artery ratios were 10.3 % and 12.1% for Design 1 and Design 2, respectively, which were lower than the 14.6 % for the Control stent. Although high metal-to-tissue ratios have generally been viewed as harmful due to increased foreign body response (R. Hoffmann & Mintz, 2000), a certain amount of scaffolding support is required to prevent tissue prolapse and therefore reduce cross-sectional lumen area. The surface area ratios for the novel stent designs were below 25% and therefore considered acceptable.

The ideal position for the new valves is with the nadir of the replacement valve at the level of the basal ring or slightly above. Under the former conditions, Design 1 extends 15.7 mm above and 7.2 mm below the basal plane and Design 2 extends 14.1 mm above and 5.2 mm below the basal plane. These dimensions ensure that the stent does not contact the interventricular septum at the level of the LBB, which is approximately 12mm below the basal plane, thereby reducing the risk of conduction disturbances (Atkinson et al., 2016). Valve dimensions also ensure that the outflow end of the replacement valve is at the same level or slightly below the level of the native valve commissures in AS and normal anatomy and therefore will not be contact the wall of the ascending aorta above the SoV. (Akhtar et al., 2009; Calleja et al., 2013). The valves will therefore be unlikely to jail the coronary ostia in most patients and will permit blood flow into the SoV. Calleja et al. (2013) showed that in patients with a mean annulus size of 24.2/24.5 mm (normals/AS), the combined mean free edge lengths were 94.4 mm and 86.2 mm for normals and AS, respectively, corresponding to 30.0 mm and

27.4 mm diameters, respectively. The new replacement valve designs are therefore not expected to stretch the native leaflets taut unless the valves are over-sized in diameter by approximately 24% or 12%, respectively. This may however not hold true for valves affected by RHD as leaflet retraction is a notable feature of this disease (Wallby et al., 2013), but no suitable measurement data is yet available for such valves.

The crown geometry forms a continuous attachment site for leaflets. Crown shapes for valve leaflet attachment are usually defined by conic or cylindrical sections (Bezuidenhout et al., 2015). We chose to define the crown shape using Bézier functions in order to select a shape that provides a compromise between peak stent stress and peak leaflet opening and closing stresses. This approach allows the selection of optimum geometry, rather than using a preselected fixed mathematical relationship. The stent analysis was based on a crown shaped stent member only (without reinforcement), and the leaflet analysis was based on simplified lofted leaflet geometry. It is therefore possible that different leaflet and stent definitions would have led to the selection of different optimum crown-shaped geometry.

Although design was focused on the development of a 23 mm valve (one of the most frequently implanted balloon-expandable valve sizes), the size of the valve may be scaled up or down as appropriate by maintaining the ratio of valve height to diameter and repeating the crown optimisation study (the 23 mm stent accommodates a 14 mm valve). Strut width would have to increase to maintain radial strength at greater diameters if similar wall thickness were used. Since the diameter of the native aortic valve increases by approximately 8 mm from the second to the tenth decade of life, a balloon-expandable valve would however not accommodate this change in diameter and would need subsequent intervention (Kitzman et al., 1988)).

Design 1 and Design 2 stents allow the valve to be positioned for antegrade or retrograde delivery. Both designs satisfy the attribute requirements described in Chapter 3.

8.2 Stent and Valve Manufacture

Stents were produced using techniques that have become standard in the stent industry, but for which the detailed methods are typically protected by companies. A reject rate of approximately 25% at laser cutting (due to material protruding outwards during cutting) suggests that optimisation of cutting parameters, including laser power, process gas pressure, distance of the nozzle from the part, pulse width etc. could result in a more reliable process. All stents that passed inspection after laser cutting were successfully descaled and electropolished, suggesting good reliability of these processes.

Mean stent dimensions after electropolishing differed by less than 4% from specifications for all members, including strut and hairpin widths, and standard deviations were ≤ 15 µm. This was achieved through a two-step electropolishing process whereby the first cycle was used to estimate polishing rate and the time for the second cycle was adjusted accordingly to achieve the weight predicted from the CAD drawings. In general mean strut widths were 3 µm and 9 µm below specification for Design 1 and Design 2, respectively, while mean hairpin widths were 3 µm and 4 µm above specification, respectively. In the absence of cut stent measurements, it is unclear whether these differences were due to cut stent geometry or to differences in electropolishing rate at different stent features, but is thought to be primarily due to electropolishing, since kerf width was very similar in the longitudinal and circumferential directions. It is likely that a small increase in cut strut width and a small decrease in cut hairpin width will therefore allow actual mean dimensions to be closer to specifications. Design 1 stents appeared to have no dimensional variation across the length or around the circumference of the stent. Design 2 showed a slight trend towards thinner struts and hairpins in the top row than in the bottom row; more samples will be required to determine whether these differences are significant.

Stent surface quality for outside and inside surfaces compared favourably with stent surface quality reported in the literature for cobalt chromium coronary stents (Sojitra et al., 2009). The side surfaces created by the cutting path of the laser beam had a waviness that was visible at lower magnifications but showed smooth surface under higher magnifications. It is anticipated that this could be improved through changes in cutting parameters, but more effectively through increased polishing times. Cut stents were intended to have members 30 µm larger than final polished dimensions to allow 15 µm to be removed from either side during electropolishing. A higher than anticipated kerf width however (average 58 µm compared to predicted 50 µm) resulted in cut dimensions that would be expected to be only 22 µm larger than final target dimensions, with only 11 µm removed from each surface. Greater cut stent dimensions should allow greater material removal during polishing and therefore better side surface quality. Although the manufacturing methods developed in this report were sufficient to produce stents of good quality by visual inspection, surface roughness, XPS analysis, corrosion and biocompatibility tests may be required to verify acceptable biocompatibility and enhance the reaction between the cobalt chromium and the tissue (Aihara, 2009).

Both stent designs could be used to manufacture polymeric and bioprosthetic valves. The stents could be expanded to an inner diameter of 23 mm for placing on spray coating mandrels, although some care needed to be taken to avoid longitudinal crushing in Design 1 stents. A slight mismatch between the leaflet attachment line on the mould and the crown shape on the stent sometimes occurred, but this was not sufficient to interfere with leaflet function. Both designs permitted the attachment of a sealing skirt to the outside surface of the stent crown member and to the bottom rows of struts. Early polymer film skirts separated from the bottom of the stent during crimping, but this did not occur for the highly flexible electrospun skirts. Both designs had open structures and allowed for leaflets to be produced using spray coating, although the arms of Design 2 had to be manually separated by a small distance from the crown member to ensure that polymer webs did not form between these members. Both stent designs satisfy the manufacturing criteria listed in Chapter 3.

8.3 Experimental Testing

Both stent designs passed crimping, deployment, recoil and foreshortening requirements. Crimped stent lengths were shorter than the maximum 35 mm length specification (to allow the valve to be crimped on SATH deployment devices) and stents could be deployed to nominal diameter (23 mm) and could be over-expanded by 10% without fracture. Indeed both stents could be dramatically over-expanded without fracture. Stent over-expansion may be considered by clinicians if paravalvular leak is severe or if native valve size is in the zone between to replacement valve sizes (Shivaraju et al., 2015). It is probable that over-expansion limits will be determined by resulting leaflet function changes caused by alterations in crown member geometry and reduced leaflet coaptation rather than due to the risk of stent fracture. All stents could be crimped down to 6 mm diameter on commercial balloons, but such low diameters were not yet possible on SATH devices. Although stent recoil was greater for the two designs than for the Control stent (2.0 to 3.4 % versus 1.9 %), the recoil was lower than the maximum specification of 5%. Recoil is of particular clinical importance because high values of recoil could result in stents being under-deployed (risking paravalvular leak and stent movement), or could necessitate native valve over-expansion, with potential complications such as annular rupture, in order to reduce leakage. This inevitable recoil means that sizing for the current replacement valves should be done based on systolic measurements, as recommended for Edwards valves, rather than diastolic measurements, in order to reduce the risk of migration and leakage.

In order to compare stent performance to a “standard” design, a Control stent was created based on an Edwards Sapien 3^{TM} stent. Stent foreshortening was lower for the new stents than for the Control stent. Although foreshortening was over 14% for both designs, the change in length would not affect stent location within the anatomy: Design 1 is correctly located by the location arms; Design 2 stent deployment demonstrated that the nadir of the replacement valve, which is the most critical landmark, did not move relative to the deployment device handle by more than 1 mm during deployment. Sapien 3^{TM} valves are deployed in the correct positon by positioning the central balloon marker at the level of the basal plane, despite greater foreshortening of the inflow end of the valve (Schymik et al., 2015). In a similar manner, Design 2 would be deployed in the correct position if the nadir of the replacement valve is positioned at the basal plane. The areas of commissure attachment were constructed from straight members that cannot foreshorten during deployment. Foreshortening is therefore considered to be acceptable.

The Control stent crimped length of 24.2 mm was close to the 24.5 mm length reported for the Sapien 3^{TM} valve (Wendt et al., 2015). The deployed (recoiled) length of the Control stent was 19.5 mm (foreshortening 20%), compared to 18 mm expanded length reported for the Sapien 3^{TM}. The difference in deployed stent lengths between the measured Control stent length and the Sapien 3^{TM} expanded length may be partially accounted for by the fact that the mean diameter of the Control stent after deployment and recoil was 22.4 mm. The original 23 mm diameter corresponds to the starting height of 18 mm. Since the valve has five rows of struts, a diameter increase of 0.6 mm results in a length reduction of 0.54 mm (because of a change in strut angle). The remaining difference in height may be accounted for by the presence of leaflets and skirt material that may provide an extra 1 mm to the valve diameter and a resultant additional length reduction of 0.98 mm. The shape of the Control stent after deployment appeared similar to the shape of the Sapien 3^{TM} stent, with slight bottom end flaring and subtle hourglass shape (Schymik et al., 2015).

For correct valve function, it is important that the crown-shape of the valve returns to its intended shape. The deformed shapes of Design 1 and Design 2 were compared to the manufactured shapes and were considered to be acceptable for leaflet function (see Figure 7-27), although Design 2 more closely approximated the starting shape. Design 1 showed distortion of the crown shape near the nadir caused by insufficient ability for struts to extend sufficiently during crimping, which could probably be repaired through tweaks in stent design. Both designs showed the ability to resist migration when positioned correctly in the aortic valve, resisting axial forces four times higher than would be exerted through 100 mmHg diastolic pressure on a 23 mm valve. All stents could be crimped with standard crimping devices to 6 mm diameter. In terms of stent crimpability, Designs 1 and 2 differed appreciably. Design 2 had a wall thickness of 0.47mm, had only one layer of metal in the crimped condition and did not have any protruding elements to snag on the native aortic root. Design 1, on the other hand, had two metal layers, namely a 0.47mm tube-like structure and an additional 0.44mm wire structure that protruded intentionally in the crimped condition. The protruding struts could easily be held down with a removable sheath for delivery.

Valves produced from both stent designs performed well in a left heart simulator, with mean total regurgitant fraction below 6% and mean EOA above 2.0 cm^2; these values are well in excess of the ISO minimum performance requirements of 20% and 1.25 cm^2, respectively (ISO-5840-3, 2013). Mean pressure drop was below 9 mmHg for both valves. This data compares favourably to commercial and experimental valves; using the same commercial pulse duplicator system and identical system parameters (70 beats per minute, 100 mmHg mean pressure and 5 L/min cardac output), the EOA and pressure drop of the Sapien XT valve were 1.7 cm^2 and 18 mmHg, respectively (Rahmani et al., 2017). A possible reason for apparent improved performance for the current valves is that the investigators tested the valves in mock 21 mm aortic roots that included simulated native leaflets, while the current valves were tested in a 23mm mock annulus inside a glass aortic root. EOA was significantly greater for valves constructed from Design 2 compared to Design 1 (2.03 ± 0.12 vs. 2.38 ± 0.19, $p<0.001$), but the differences may be explained by improvements in leaflet design. Design 1 valves were constructed first, using earlier generation leaflet designs while more sophisticated leaflets had been created by the time Design 2 was tested in the pulse duplicator and subsequently in animals. Both stents are considered to be acceptable for producing valves with good haemodynamic function. Stents were demonstrated to be able to function in a high cycle fatigue tester for over 400 million cycles, the target based on ISO 5840 requirements. This is the first reported case of a balloon-expandable polymeric valve having achieved this milestone. With the exception of a stent with a manufacturing defect that had not been detected at spray coating, no stents showed evidence of fatigue fracture. Since durability testing was performed on valves and not directly on stents under appropriate physiological loads, radial loading on the stent was under-estimated. In addition, since valves were routinely removed upon leaflet failure, few valves were subjected to long-term loading. The fatigue testing is encouraging, but can only be viewed as anecdotal until thorough stent fatigue testing can be performed. Although functional valve performance was not evaluated in the pulse duplicator after 400 million cycles, valve performance appeared to be satisfactory based on stroboscopic visualisation of the valve in the high cycle durability tester. Simulated use testing in artificially pressurised cadaveric animal hearts demonstrated proof of concept for both valve designs using intended implant techniques. The ability to deliver and deploy the valves was confirmed using fluoroscopy and endoscopy.

Self-locating stents (Design 1) proved to be an effective method of locating and anchoring valves in the native aortic root of pigs, as demonstrated through successful leaflet capture in all nine animals in which the valves were delivered. The inadvertent piercing of a native leaflet by a location arm in the first animal was ascribed to the “learning curve” associated with tactile location of valve position, and this case provided the only evidence of valve leakage for this group of animals. The protruding arms allowed clear visibility of valve position under fluoroscopy. Although an animal died before deployment could be attempted, the valve was deployed successfully in the remaining eight animals.

Despite the successes in this group, several challenges were experienced. Firstly, aortic valve procedures were typically preceded by experiments with mitral valve intervention by another research group in order to maximise the amount of useful data that could be obtained from live animals. Secondly, the valve was developed alongside early developments in implant technique, apical access ports and balloon catheter technology. The relatively low availability of functional data for the self-locating valves was mostly due to physiological changes in the animals over long procedures, or procedural complications, particularly related to difficulties with the access port such as blood leakage and the introduction of air. Catheter leakage led to valve under-deployment in three animals. Design 1 was constructed with an open crown-shape structure. In *ex vivo* and *in vivo* tests it became apparent that the native leaflets sometimes interacted with the replacement leaflets. Although the healthy leaflets of pigs did not appear to interfere with polymer or bioprosthetic leaflet behaviour, it is possible that the thickened and stiffened leaflets associated with diseased valves would interfere with proper replacement leaflet function.

Expanding arm stents (Design 2) were located within the native valve of pigs using gradations on the deployment devices or using fluoroscopic and/or echocardiographic guidance. Since six of the eight valves in which implant was attempted were able to anchor within the native aorta of the pigs, it appears that self-anchoring using a balloon-expandable stent is feasible. Procedural difficulties meant that the valves were not always deployed in the correct position; two valves were deployed too low, while another was deployed too high. The stents were visible under fluoroscopy, but a prominent radiopaque would be beneficial to indicate more clearly the location of the leaflet nadir. The first of the low deployments embolised but the other remained anchored. Echocardiography showed that the latter interfered with the anterior leaflet of the mitral valve, although no mitral leaflet damage was seen at autopsy. This animal developed ST elevation during deployment that never resolved, and paravalvular leakage also occurred. Two additional animals experienced ST segment changes indicative of myocardial ischaemia that did resolve. In one of these animals the ST elevation occurred during predilatation and during valve deployment. This suggests that the device temporarily occludes coronary blood flow when inflated. The valve that had been deployed high shifted into a secure position with the valve arms behind the leaflets. Interestingly, some valves that were deployed in the correct position also had one or more arms that were positioned behind the native leaflets. This suggests that the flexible leaflets are able to slip under the expanding arms during diastole. Although this leads to secure anchoring, it has the disadvantage that the native leaflets may interfere with the replacement leaflet motion. A design that encourages such leaflet capture while holding the native leaflets away may anchor particularly well.

The single case of stent embolisation during handling (before deployment) is indicative of insufficient stent security. Although stent security is a function of several factors, including the coefficient of friction between the balloon and the valve leaflets, the crimping pressure and the handling of the valve and delivery system, radial strength of the stent directly impacts on this force. Although valves were crimped conservatively with low force to reduce the risk of balloon damage, higher stent radial strength will nevertheless improve security. Regurgitation greater than mild occurred in another three of the valves. In two of these animals the regurgitation was central. In the first of these cases the cause was shown to be due to the entrapment of a leaflet against the roof of the sinus, and this was suspected in the second case because the regurgitation resolved after a few minutes. Although a case of “frozen leaflet” has been reported clinically (Agostoni, Buijsrogge, & Stella, 2012), the occurrence in the current work is associated with the animal model, since the aortic root is shorter in pigs than in humans (Reid, 1970). Some difficulties with the interaction between the valve and the deployment device were also experienced in this group, notably valve under-deployment, catheter leakage, and difficulty in deploying the valve in the correct position. Greater length of the stent below the level of the crown nadir will increase the device “landing zone”, hopefully improving positioning.

The age and weight of pigs in the animal study were chosen to ensure that the native aortic valve diameter was 18 to 21 mm, appropriate for a 23 mm replacement valve. Although TOE measurements placed the animals substantially within these requirements, measurements based on two-dimensional echocardiography are known to under-estimate aortic valve diameter (Tsuneyoshi et al., 2016). Aortic annulus diameters were significantly different between the two groups of pigs. This is assumed to be due to inter-operator measurement variability, as pigs were sourced from the same supplier and weights were similar. In the absence of three-dimensional TOE or CT imaging, fluoroscopy measurements prior to implant could help ensure appropriate valve sizing. The selection of slightly smaller animals may also be prudent for the evaluation of future stent generations, since pig aortic valves are much more compliant than human valves (Li, Wang, Pham, & Sun, 2014).

8.4 Finite Element Modelling

In order to most efficiently model stent behaviour in this report, two different levels of complexity were used in model construction. Simple models based on the use of one-sixth symmetry and an expanding cylinder for stent deployment allowed the comparison of eight design alternatives in approximately 10 hours per simulation on an 8 core AMD Opteron computer. Complex models based on full 360° geometry and balloon simulation for stent deployment ran for up to 14 days. The complex modelling process was demonstrated to be accurate, and therefore a validated model, through comparison of predicted and physical geometry (see Figure 8-1), predicted and measured radial crushing force (less than 10% difference for all stents), and predicted and measured recoil and foreshortening. Absolute predicted recoil percentage differed by ≤ 0.1% and absolute predicted foreshortening differed by ≤ 1.1% from experimental values, with the greatest difference occurring for the relatively less stable Design 1.

A nonlinear Ogden material model was used to describe the balloon material for complex modelling, based on uniaxial tensile test data. Since rubberlike materials exposed to biaxial stress (such as experienced in a thin-walled pressure vessel such as the balloon) often have behaviour that cannot be modelled accurately using uniaxial data alone, biaxial test data may have produced a more accurate model of balloon behaviour. The close correlation between the experimental and predicted balloon diameters, however, suggests that errors introduced through the use of uniaxial data are negligible in the present investigation.

A Hollomon necking model was used to predict stresses beyond the UTS (i.e. during necking), and is a method frequently used in metal forming simulation such as for drop-forming (Joun et al., 2007). This model provides a more conservative estimate of stent stresses than when perfect plasticity is assumed to occur after the UTS. This is the first reported use of a power law in stent FEA. As shown in Appendix K, the Hollomon model predicts higher Von Mises and Maximum Principle Stresses while reaction forces are unaffected by the model. No validation of necking stress predictions against experimental calculations were however attempted in the current work. Unfortunately this model cannot currently be used to predict the onset of acute fracture. It would be beneficial to model the stent over-expansion described above in order to calculate the predicted true fracture strains and stresses.

Maximum Von Mises stresses predicted from the simple model were similar to the complex model for Design 1 (≤ 3.0% difference), while the simple model over-predicted maximum stresses by 13.0% at deployment for Design 2, and the location of peak stresses differed between the two models as well. The discrepancies are considered to be as a result of differences in deformation behaviour between stents deployed using a balloon and using an expanding cylinder. Stents deployed using the balloon simulation had a notably more hour-glassed shape than stents deployed using a rigid cylinder, and transient behaviour was very different. Balloon configuration has also been found to affect stent stresses and the impact on the anatomy (Martin & Boyle, 2013).

Although the complex model provided more accurate stent performance predictions (including stress, fatigue and deformation), the long run times make it unsuitable for rapid evaluation of design alternatives, for which the simple model is well suited. The simple model is limited in its ability to predict such behaviour as stent extremity flaring, or buckling across the symmetry planes. Since it was typically possible to produce physical prototypes and test crimping and deployment behaviour within in a few days, certain design behaviours may be better tested through agile rapid prototype manufacture.

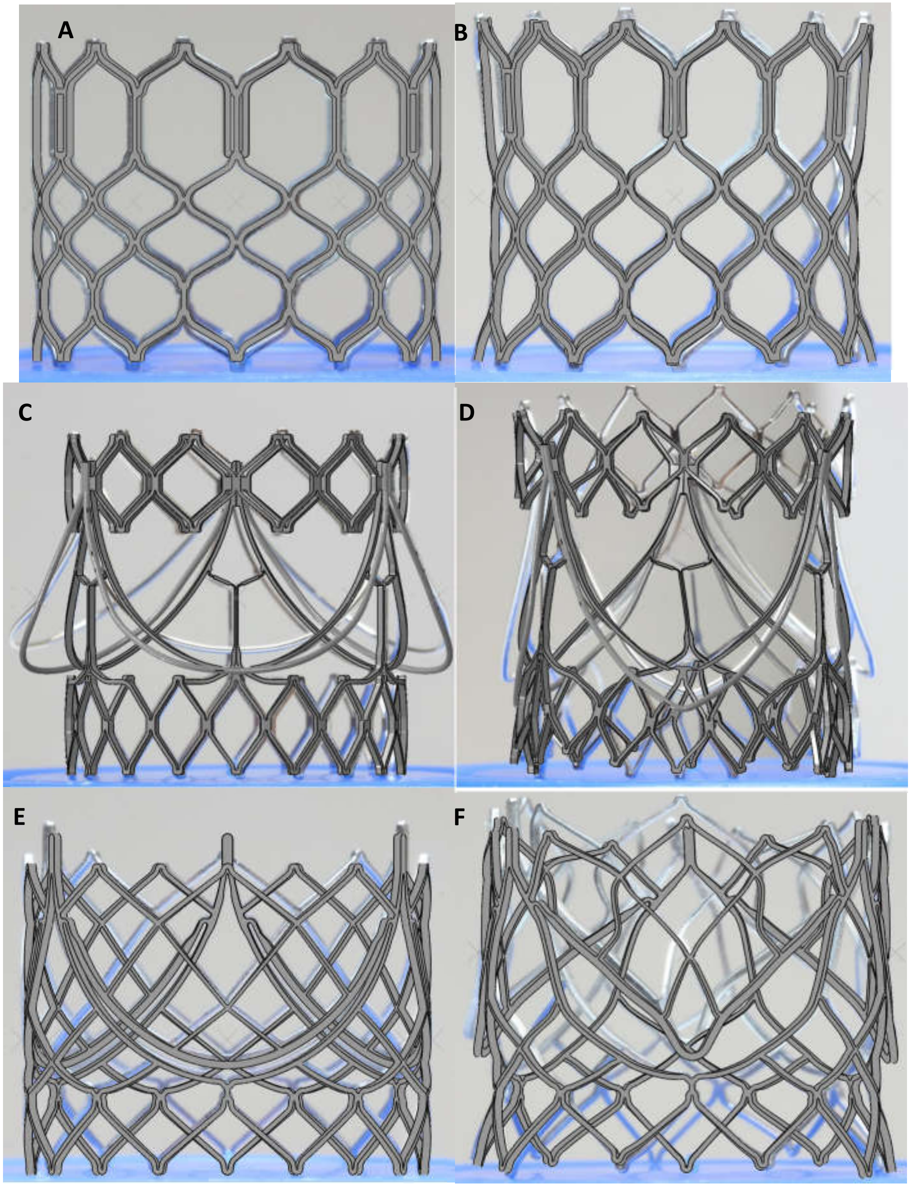

Figure 8-1. Comparison between *In Vitro* test geometry and FEA geometry for Control (A,B), Design 1 (C,D) and Design 2 (E,F). The images on the left (A,C,E) show FEA original geometry superimposed over photograph of as-manufactured stent. The images on the right (B,D,F) show FEA deformed geometry superimposed over photograph of deployed stent

Leaflets are sometimes modelled in TAVR simulations, either indirectly through the application of forces on the stent frame (Esterhuyse et al., 2012), or directly through the inclusion of leaflets in the original geometry (J. Bailey et al., 2015) or applied after stent deployment (Auricchio, Conti, Morganti, et al., 2014). In the latter study the leaflet attachment edge was altered to map onto the stent surface prior to the application of pressure loads. The inclusion of leaflets after stent deployment were successfully modelled in the current study by attaching the leaflet to the deformed stent geometry using tie constraints and appropriate position tolerances.

The radial strength predicted for Design 2 under free loading conditions (116 N) was higher than the radial strength predicted for the Sapien^{TM} stent (88 N) by Tzamtzis et al. (2013), but it was lower than the radial strength predicted for the Control stent (347 N). No comparative radial strength measurements or predictions could be found for the Sapien 3^{TM}. A Stress/Life method of fatigue analysis suggested that Design 2 stents were safe from fatigue failure, although no safety factor could be applied. A safety factor of 2 on the control stent suggests that Design 2 is twice as likely to fail in fatigue as the Control stent under the same loading conditions. This is due in part to the high residual stresses in the stent following recoil and to the lower radial strength of Design 2 compared to the Control stent, which would reduce the alternating stresses. An increase in radial strength is proposed for the stent, together with fatigue-focused geometric optimisation. Design 1 was particularly vulnerable to fatigue failure because mean stresses exceeded the true UTS of the material and therefore necessarily exceeded Goodman criteria, although no formal analysis was done on Design 2 due to time constraints.

In this report stent designs were evaluated through free crimping and deployment, without simulation of the aortic root. This was done in order to effectively compare the performance of competing designs. Patient-specific models of a preferred stent will be required to more accurately predict the behaviour of stents in relevant anatomy (Bosi et al., 2015; Morganti et al., 2015; Ovcharenko et al., 2016; Schultz et al., 2016). An early version of Design 1 (specifically Concept 1A) has been subjected to patient-specific modelling (Shirzadi, 2016), where the susceptibility to stent migration was demonstrated, but for which fatigue analysis was not performed.

9 Conclusions and Recommendations

Novel compressible stents were developed for the manufacture of a polymeric balloon-expandable polymeric TAVR, capable of anchoring in an aortic root in the absence of calcification. Designs successfully incorporated a crown shape into the balloon-expandable frame to allow for continuous attachment of polymeric leaflets. Two different novel mechanisms were developed, and proof of concept obtained, for anchoring the valve into a compliant aortic root. The first of these involved the use of annealed cobalt chromium stent frame to which a cold-worked wire member of the same material was welded. This combination allowed a stent to be constructed from a single material but nevertheless incorporated balloon-expandable and self-expanding elements. It further provided a location mechanism to ensure correct positioning within the anatomy. The second concept involved the use of elements in the stent frame that deform plastically during crimping, to cause an outward protrusion of anchoring arms during stent expansion, in order to secure the stent above the base of the native leaflets.

It was shown that the stents could be manufactured through laser cutting, descaling and electropolishing and had good surface quality and dimensions were within specifications. The stents also facilitated manufacture of polymeric valves through spray coating.

Satisfaction of engineering requirements was demonstrated through *in vitro*, *ex vivo* and *in vivo* testing. Stent mechanical properties such as recoil, foreshortening and the ability to crimp and deploy as required were shown to be acceptable, and valves manufactured from the stents exceeded the haemodynamic requirements of international standards. Stents were shown to be able to anchor securely in explanted aortic root xenografts and in explanted hearts through simulated use testing. Implantation of valves in an acute termination porcine model demonstrated proof of concept for both stent designs.

FEA proved to be a powerful technique to aid in concept selection, characterise deformed geometry and quantify stresses. Simulations matched experimental results closely, and provided a tool to estimate fatigue resistance. Despite the demonstration that stent requirements were satisfied in general, physical testing and numerical simulation highlighted aspects of stent design that could be further improved.

While self-locating stents performed well in experiments, further valve development will align with the goal to deliver and deploy valves on deployment devices that employ location members. Expanding arm (self-anchoring) stents promise to provide the basis for this strategy. Further animal studies will need to be performed once design changes have been made to demonstrate consistently reliable device performance.

9.1 Limitations

The lack of sufficiently powered numbers of animals in preclinical studies is a significant limitation in terms of device safety and efficacy. For this project, however, the goal of initial preclinical trials was to demonstrate proof of concept, which has been done. Furthermore, the valves described in this paper were being developed simultaneously with the development of the delivery system, meaning that failures in the delivery system and difficulties deploying the valves in the correct position interfered with the ability to judge valve performance. No dedicated stent fatigue testing was performed. Such testing needs to be performed in a compliant tube to adequately simulate physiological loading. Several aspects of stent and valve performance were tested on one or only a few samples. True verification of stent performance will require greater numbers of samples.

Simulation results should be interpreted within the context of possible limitations of the modelling in this thesis. Concepts were compared to each other during free deployment of the stents. This means that the effects of aortic root geometry and physiology, including the effects of fibrous thickening and calcification, are not considered. It is possible that such conditions may have favoured one of the concepts over another or led to specific design changes.

A sensitivity study was used to select a stent crown shape that would minimise stent and leaflet stresses. This study was however performed using simple stent crown and leaflet geometry. Results may differ for more complex stent geometries and the complex interaction between the leaflet and the stent. An extensive stent and leaflet combination study may yield different optimum geometry but will require considerable computing resources and are anticipated to yield similar geometry.

9.2 Recommendations

Based on the experimental and numerical results in this report, the following design improvements are recommended for Design 2:

- An additional row of struts below the nadir is recommended to provide a larger “landing zone”. *In vivo* animal testing demonstrated that the area below the nadir of the stent was too short to provide reliable coverage.
- The stent should be also be provided with a radiopaque marker at the crown. Tantalum wire was purchased for this purpose. While animal studies showed that the stent crown was basically

visible, orientation of the valve was time-consuming and valves were occasionally deployed in the wrong position.

- Stent struts should be made wider to increase radial strength. Higher radial strength is expected to reduce the susceptibility of stents to slip off balloons, and is expected to improve fatigue resistance. The crown should also be made wider to more reliably align the polymer valve manufacturing mandrels with the crown of the stent. It is also anticipated that this would allow the crown to more closely form the correct shape upon deployment.
- Linkage elements that attach near the bottom of the crown should be curved slightly and should attach to the crown at a shallower angle to reduce the extensive deformation that occurs during crimping and expansion and hence high stresses. Larger radii are also recommended to reduce stress concentrations.
- A mechanism to increase the distance by which the stent arms protrude is also recommended. This may be achieved by moving the point at which the attachment arms attach to the stent from the crown member itself to the centre of the first strut connected to the commissure post. It is also proposed that more than one set of arms should be included above the crowns, to allow the uppermost arms to latch over the native leaflet free edge while the bottommost arm rests on the VAJ.

For stent manufacturing, it is recommended that that cut stent geometry be made larger such that more material may be removed during electropolishing and a better surface quality on the side of stent struts may be achieved. To ensure all stent elements are as close as possible to their intended dimensions, material should preferentially be added to the cut stent in the straight portion of struts.

Several procedural and species-specific challenges were faced during animal trials. Porcine aortic roots are far more compliant than aged human aortic roots (Li et al., 2014), so it is recommended to over-inflate substantially more than has been done in animal studies by using younger animals. Echocardiographic measurements of aortic annulus size should be supplemented using fluoroscopic measurements to ensure correct valve sizing. While deployment device performance is being refined, it may be prudent to consider using commercial valvuloplasty balloons in animal trials to ensure full deployment of replacement valves.

Once design refinements have been made and analysed using the simple and complex approaches developed in this thesis, it is recommended that valve deployment should be simulated in various patient-specific models that include detailed fatigue analysis.

9.3 List of Outputs

9.3.1 Patents

The following patent applications have been submitted based on the work presented in this thesis:

WO 2014/170870 US 2016/0067038	"A Prosthetic Heart Valve"
GB 2513195 A	"A Stent for a Prosthetic Heart Valve"
GB 2513194 A	"A Valve"

9.3.2 Congresses and Presentations

Park, K., Appa, H., Scherman, J., Conradie, D., Coetzee, J., de Villiers, J., Geldenhuys, G., Williams, D., Zilla, P., Bezuidenhout, D. (2014). Transcatheter aortic heart valves for rheumatic heart valve disease. Surgical Research Day, University of Cape Town, Cape Town, 28 November 2014.

9.3.3 Proposed Publications

The following manuscripts are being prepared for publication:

1. Review of experimental and commercial transcatheter valves – *Journal of Surgical Technology* (invited)
2. Research paper with working title "New stents for transcatheter aortic valve implantation" (in progress)

10 References

Abad, E. M. K., Pasini, D., & Cecere, R. (2012). Shape optimization of stress concentration-free lattice for self-expandable Nitinol stent-grafts. *Journal of Biomechanics, 45*(6), 1028-1035. doi:10.1016/j.jbiomech.2012.01.002

Abu-Omar, Y., & Ratnatunga, C. P. (2007). Prosthetic heart valves. *Surgery (Oxford), 25*(5), 224-227. doi:10.1016/j.mpsur.2007.04.014

Agostoni, P., Buijsrogge, M. P., & Stella, P. R. (2012). "Frozen" leaflet: a dreadful complication of transcatheter aortic valve implantation. *Circulation: Cardiovascular Interventions, 5*(2), 321-323. doi:10.1161/CIRCINTERVENTIONS.112.968396

Agreli, G. (2017). *Vienna Mitral Valve.* Paper presented at the EuroPCR 2017, Paris.

Aihara, H. (2009). *Surface and biocompatibility study of electropolished Co-Cr Alloy L605.* (Master's Thesis), San Jose State University. (3699)

AISI. (1988). *Cleaning and Descaling Stainless Steels*. Toronto: Nickel Development Institute.

Akhtar, M., Tuzcu, E. M., Kapadia, S. R., Svensson, L. G., Greenberg, R. K., Roselli, E. E., . . . Sola, S. (2009). Aortic root morphology in patients undergoing percutaneous aortic valve replacement: Evidence of aortic root remodeling. *The Journal of Thoracic and Cardiovascular Surgery, 137*(4), 950-956. doi:10.1016/j.jtcvs.2008.07.062

Akujuo, A. C., Dellis, S. L., Britton, L. W., & Bennett, E. V. (2015). Transcatheter aortic and mitral valve implantation (TAMVI) in native rheumatic valves. *Journal of Cardiac Surgery, 30*, 813–816. doi:10.1111/jocs.12612

Alfieri, O. R. (2015). *Cardiac surgery: where are we going?* Paper presented at the Swiss Society of Cardiology Meeting, Lausanne.

Ali, M. N., Amin, F., Ansari, U., Minhas, M. A., & Shahid, W. (2015). Anisotropic coronary stent device: fabrication and structural analysis. In T. Wang (Ed.), *Computational intelligence and industrial engineering* (pp. 161-173). Ashurst: Wit Press.

Altman, P. A., Meagher, J. M., Walsh, D., W., & Hoffmann, D., A. (1998). Rotary bending fatigue of coils and wires used in cardiac lead design. *Journal of Biomedical Materials Research (Applied Biomaterials), 43*, 21-37.

Amirjani, A., Yousefi, M., & Cheshmaroo, M. (2014). Parametrical optimization of stent design; a numerical-based approach. *Computational Materials Science, 90*, 210-220. doi:10.1016/j.commatsci.2014.04.002

Andersen, H. R., Knudsen, L. L., & Hasenkam, J. M. (1992). Transluminal implantation of artificial heart valves. Description of a new expandable aortic valve and initial results with implantation by catheter technique in closed chest pigs. *European Heart Journal, 13*(5), 704-708.

Anderson, R. H. (1991). The myth of the aortic annulus: the anatomy of the subaortic outflow tract. *The Annals of Thoracic Surgery, 52*(3), 640-646.

Anderson, R. H. (2000). Clinical anatomy of the aortic root. *Heart, 84*(6), 670-673. doi:10.1136/heart.84.6.670

Anderson, R. H., Becker, A., & Piazza, N. (2009). The anatomy of the aortic valvar complex. In P. W. Serruys, N. Piazza, A. Cribier, J. G. Webb, J.-C. Laborde, & P. de Jaegere (Eds.), *Transcatheter aortic valve implantation: Tips and tricks to avoid failure* (1st ed., pp. 1-17). New York, NY: Informa Healthcare.

Anderson, R. H., Yanni, J., Boyett, M. R., Chandler, N. J., & Dobrzynski, H. (2009). The anatomy of the cardiac conduction system. *Clinical Anatomy, 22*(1), 99-113. doi:10.1002/ca.20700

Arsalan, M., & Walther, T. (2016). Durability of prostheses for transcatheter aortic valve implantation. *Nature Reviews Cardiology, 13*(6), 360-367. doi:10.1038/nrcardio.2016.43

Ashby, M. F. (2005). *Materials selection in mechanical design* (3rd Edition ed.). Oxford: Butterworth-Heinemann.

ASTM. (2014). F2514 08 (2014) Standard Guide for Finite Element Analysis (FEA) of Metallic Vascular Stents Subjected to Uniform Radial Loading.

Atkinson, A. J., Kharche, S. R., Bateman, M. G., Iaizzo, P. A., & Dobrzynski, H. (2016, 16-20 Aug. 2016). *3D anatomical reconstruction of human cardiac conduction system and simulation of bundle branch block after TAVI procedure.* Paper presented at the 2016 38th Annual International Conference of the IEEE Engineering in Medicine and Biology Society (EMBC).

Attmann, T., Steinseifer, U., Cremer, J., & Lutter, G. (2006). Percutaneous valve replacement: a novel low-profile polyurethane valved stent. *European Journal of Cardio-Thoracic Surgery, 30*(2), 379-379. doi:10.1016/j.ejcts.2006.04.035

Atwood, A., Bougie, L., Carneiro, H., Pico, A., & Wnek, K. (2007). *Insertion of heart valves by catheterization.* Northeastern University. (MIME 1501-1502, http://hdl.handle.net/2047/d10011444)

Auricchio, F., Conti, M., & Morganti, S. (2014). Aortic biological prosthetic valve for open-surgery and percutaneous implant: procedure simulation and performance assessment. *Cardiovascular and cardiac therapeutic devices: studies in mechanobiology, tissue engineering and biomaterials* (Vol. 15, pp. 131-168).

Auricchio, F., Conti, M., Morganti, S., & Reali, A. (2014). Simulation of transcatheter aortic valve implantation: a patient-specific finite element approach. *Computer Methods in Biomechanics and Biomedical Engineering, 17*(12), 1347-1357. doi:10.1080/10255842.2012.746676

Azadani, A. N., Jaussaud, N., Matthews, P. B., Ge, L., Guy, T. S., Chuter, T. A., & Tseng, E. E. (2009). Valve-in-valve implantation using a novel supravalvular transcatheter aortic valve: proof of concept. *Annals of Thoracic Surgery, 88*(6), 1864-1869. doi:10.1016/j.athoracsur.2009.08.004

Bai, Y., Zong, G. J., Wang, H. R., Jiang, H. B., Wang, H., Wu, H., . . . Qin, Y. W. (2010). An integrated pericardial valved stent special for percutaneous tricuspid implantation: an animal feasibility study. *Journal of Surgical Research, 160*(2), 215-221. doi:10.1016/j.jss.2008.10.029

Bailey, C. P. (1949). The surgical treatment of mitral stenosis (mitral commissurotomy). *Diseases of the Chest, XV*(4), 377-393.

Bailey, C. P., Bolton, H. E., Jamison, W. L., & Nichols, H. T. (1954). Commissurotomy for Rheumatic Aortic Stenosis I. Surgery. *Circulation, 9*(1), 22-31. doi:10.1161/01.CIR.9.1.22

Bailey, J., Curzen, N., & Bressloff, N. W. (2015). Assessing the impact of including leaflets in the simulation of TAVI deployment into a patient-specific aortic root. *Computer Methods in Biomechanics and Biomedical Engineering*, 1-12. doi:10.1080/10255842.2015.1058928

Balachandran, K., Sucosky, P., & Yoganathan, A. P. (2011). Hemodynamics and mechanobiology of aortic valve inflammation and calcification. *International Journal of Inflammation, 2011*, 263870. doi:10.4061/2011/263870

Banbury, M. K., Cosgrove, D. M., White, J. A., Blackstone, E. H., Frater, R. W. M., & Okies, J. E. (2001). Age and valve size effect on the long-term durability of the Carpentier-Edwards aortic pericardial bioprosthesis. *Annals of Thoracic Surgery, 72*, 753-787.

Barbanti, M., Webb, J. G., Tamburino, C., Van Mieghem, N. M., Makkar, R. R., Piazza, N., . . . Tamburino, C. (2016). Outcomes of redo transcatheter aortic valve replacement for the treatment of postprocedural and late occurrence of paravalvular regurgitation and transcatheter valve failure. *Circulation: Cardiovascular Interventions, 9*(9), e003930. doi:10.1161/circinterventions.116.003930

Barbanti, M., Ye, J., Pasupati, S., El-Gamel, A., & Webb, J. G. (2013). The Helio transcatheter aortic dock for patients with aortic regurgitation. *EuroIntervention, 9 Suppl*, S91-94. doi:10.4244/EIJV9SSA17

Basquin, A., Pineau, E., Galmiche, L., Bonnet, D., Sidi, D., & Boudjemline, Y. (2010). Transcatheter valve insertion in a model of enlarged right ventricular outflow tracts. *Journal of Thoracic and Cardiovascular Surgery, 139*(1), 198-208. doi:10.1016/j.jtcvs.2009.07.025

Bateman, M. G., Quill, J. L., Hill, A. J., & Iaizzo, P. A. (2013). The anatomy and function of the semilunar valves. In P. A. Iaizzo, R. W. Bianco, A. J. Hill, & J. D. St. Louis (Eds.), *Heart valves: From design to clinical implantation* (pp. 27-43). New York: Springer.

Berdajs, D., Lajos, P., & Turina, M. (2002). The anatomy of the aortic root. *Cardiovascular Surgery, 10*(4), 320-327.

Bezuidenhout, D., Williams, D. F., & Zilla, P. (2015). Polymeric heart valves for surgical implantation, catheter-based technologies and heart assist devices. *Biomaterials, 36*, 6-25. doi:10.1016/j.biomaterials.2014.09.013

Bianchi, M., Ghosh, R. P., Das, D., Marom, G., Claiborne, T. E., Slepian, M. J., & Bluestein, D. (2015). *Transcatheter aortic valve replacement model: Crimping and deploying in patient-pathology specific roots*. Paper presented at the SB3C2015 Summer Biomechanics, Bioengineering and Biotransport Conference June 17-20, 2015,, Snowbird Resort, Utah, USA.

Bilge, M., Saatci Yasar, A., Alemdar, R., & Ali, S. (2014). Transcatheter aortic valve implantation with the CoreValve for the treatment of rheumatic aortic stenosis. *Anadolu kardiyoloji dergisi, 14*(3), 296-297. doi:10.5152/akd.2014.5226

BioWin. AVATAR2. Retrieved from http://www.biowin.org/Biowin/AVATAR%C2%B2.pdf, retrieved 23 May 2017.

Bland, E. F. (1952). Surgery for mitral stenosis: a review of progress. *Circulation, 5*, 290-299.

Blanke, P., Russe, M., Leipsic, J., Reinöhl, J., Ebersberger, U., Suranyi, P., . . . Schoepf, U. J. (2012). Conformational pulsatile changes of the aortic annulus. *JACC: Cardiovascular Interventions, 5*(9), 984-994. doi:10.1016/j.jcin.2012.05.014

Bonhoeffer, P., Boudjemline, Y., Saliba, Z., Merckx, J., Aggoun, Y., Bonnet, D., . . . Kachaner, J. (2000). Percutaneous replacement of pulmonary valve in a right-ventricle to pulmonary-artery prosthetic conduit with valve dysfunction. *The Lancet, 356*(9239), 1403-1405. doi:10.1016/S0140-6736(00)02844-0

Bosi, G. M., Capelli, C., Khambadkone, S., Taylor, A. M., & Schievano, S. (2015). Patient-specific finite element models to support clinical decisions: A lesson learnt from a case study of percutaneous pulmonary valve implantation. *Catheterization and Cardiovascular Interventions, 86*(6), 1120-1130. doi:10.1002/ccd.25944

Bosmans, B., Famaey, N., Verhoelst, E., Bosmans, J., & Vander Sloten, J. (2016). A validated methodology for patient specific computational modeling of self-expandable transcatheter aortic valve implantation. *Journal of Biomechanics, 49*(13), 2824-2830. doi:10.1016/j.jbiomech.2016.06.024

Bouleti, C., Iung, B., Laouenan, C., Himbert, D., Brochet, E., Messika-Zeitoun, D., . . . Vahanian, A. (2012). Late results of percutaneous mitral commissurotomy up to 20 years: development and validation of a risk score predicting late functional results from a series of 912 patients. *Circulation, 125*(17), 2119-2127. doi:10.1161/CIRCULATIONAHA.111.055905

Bourantas, C. V., Farooq, V., Onuma, Y., Piazza, N., Van Mieghem, N. M., & Serruys, P. W. (2012). Transcatheter aortic valve implantation: new developments and upcoming clinical trials. *EuroIntervention, 8*(5), 617-627. doi:10.4244/EIJV8I5A94

Bourantas, C. V., & Serruys, P. W. (2014). Evolution of transcatheter aortic valve replacement. *Circulation Research, 114*(6), 1037-1051. doi:10.1161/CIRCRESAHA.114.302292

Bozkurt, S., Preston-Maher, G. L., Torii, R., & Burriesci, G. (2017). Design, analysis and testing of a novel mitral alve for transcatheter implantation. *Annals of Biomedical Engineering*. doi:10.1007/s10439-017-1828-2

Braile. (2011). Inovare Transcatheter Valve. Catalogue code 604510. Rev. 01. In B. Biomedica (Ed.): Agência Prospecta. (Reprinted from: Rev 01).

Braunwald, N. S. (1989). It will work: The first successful mitral valve replacement. *The Annals of Thoracic Surgery, 48*(3), S1-S3. doi:http://dx.doi.org/10.1016/0003-4975(89)90615-2

Buellesfeld, L., Stortecky, S., Kalesan, B., Gloekler, S., Khattab, A. A., Nietlispach, F., . . . Windecker, S. (2013). Aortic root dimensions among patients with severe aortic stenosis undergoing transcatheter aortic valve replacement. *JACC: Cardiovascular Interventions, 6*(1), 72-83. doi:10.1016/j.jcin.2012.09.007

Butany, J., Ahluwaliaa, M. S., Fayet, C., Munroe, C., Blit, P., & Ahn, C. (2002). Hufnagel valve: The first prosthetic mechanical valve. *Cardiovascular Pathology, 11*, 351-353.

Buzzatti, N., Maisano, F., Latib, A., Cioni, M., Taramasso, M., Mussardo, M., . . . Alfieri, O. (2013). Computed tomography-based evaluation of aortic annulus, prosthesis size and impact on early residual aortic regurgitation after transcatheter aortic valve implantation. *European Journal of Cardio-Thoracic Surgery, 43*(1), 43-50; discussion 50-41. doi:10.1093/ejcts/ezs155

Cai, J., Huang, H., Zhou, Y., Mei, Y., Shao, J., & Wang, Y. (2013). A new type of aortic valved stent with good stability and no influence on coronary artery. *Journal of Cardiothoracic Surgery, 8*, 210. doi:10.1186/1749-8090-8-210

Calderan, J., Mao, W., Sirois, E., & Sun, W. (2016). Development of an in vitro model to characterize the effects of transcatheter aortic valve on coronary artery flow. *Artificial Organs, 40*(6), 612-619. doi:10.1111/aor.12589

Calleja, A., Thavendiranathan, P., Ionasec, R. I., Houle, H., Liu, S., Voigt, I., . . . Vannan, M. A. (2013). Automated quantitative 3-dimensional modeling of the aortic valve and root by 3-dimensional transesophageal echocardiography in normals, aortic regurgitation, and aortic stenosis: comparison to computed tomography in normals and clinical implications. *Circulation: Cardiovascular Imaging, 6*(1), 99-108. doi:10.1161/CIRCIMAGING.112.976993

Cannon, J., Roberts, K., Milne, C., & Carapetis, J. R. (2017). Rheumatic Heart Disease severity, progression and outcomes: A multi-state model. *Journal of the American Heart Association, 6*(3). doi:10.1161/JAHA.116.003498

Capelli, C., Biglino, G., Petrini, L., Migliavacca, F., Cosentino, D., Bonhoeffer, P., . . . Schievano, S. (2012). Finite element strategies to satisfy clinical and engineering requirements in the field of percutaneous valves. *Annals of Biomedical Engineering, 40*(12), 2663-2673. doi:10.1007/s10439-012-0617-1

Capelli, C., Bosi, G. M., Cerri, E., Nordmeyer, J., Odenwald, T., Bonhoeffer, P., . . . Schievano, S. (2012). Patient-specific simulations of transcatheter aortic valve stent implantation. *Medical and Biological Engineering and Computing, 50*(2), 183-192. doi:10.1007/s11517-012-0864-1

Capelli, C., Taylor, A. M., Migliavacca, F., Bonhoeffer, P., & Schievano, S. (2010). Patient-specific reconstructed anatomies and computer simulations are fundamental for selecting medical device treatment: application to a new percutaneous pulmonary valve. *Philosophical Transactions of the Royal Society A Mathematical, Physical and Engineering Sciences, 368*(1921), 3027-3038. doi:10.1098/rsta.2010.0088

Carapetis, J. R. (2007). Rheumatic heart disease in developing countries. *New England Journal of Medicine, 357*(5), 439-441. doi:doi:10.1056/NEJMp078039

Chiam, P. T. L., & Chao, V. T. T. (2013). Percutaneous transcatheter aortic valve implantation — the evolution, current status and the future. *Proceedings of Singapore Healthcare, 22*(2), 146-150.

Chiang, Y. P., Chikwe, J., Moskowitz, A. J., Itagaki, S., Adams, D. H., & Egorova, N. N. (2014). Survival and long-term outcomes following bioprosthetic vs mechanical aortic valve replacement in patients aged 50 to 69 years. *Journal of the American Medical Association, 312*(13), 1323-1329. doi:10.1001/jama.2014.12679

Cholteesupachai, J., Franzen, O., & Sondergaard, L. (2014). Transcatheter aortic valve implantation in a patient with severe native aortic regurgitation after infective endocarditis. *International Journal of Cardiology, 172*(1), e187-189. doi:10.1016/j.ijcard.2013.12.138

Choudhary, S. K., Talwar, S., & Airan, B. (2016). Choice of prosthetic heart valve in a developing country. *Heart Asia, 8*(1), 65-72. doi:10.1136/heartasia-2015-010650

Claiborne, T. E., Bluestein, D., & Schoephoerster, R. T. (2009). Development and evaluation of a novel artificial catheter-deliverable prosthetic heart valve and method for in vitro testing. *The International Journal of Artificial Organs, 32*(5), 262-272.

Cohn, L. H. (2003). Fifty years of open-heart surgery. *Circulation, 107*(17), 2168-2170. doi:10.1161/01.CIR.0000071746.50876.E2

Cosentino, D., Quail, M. A., Pennati, G., Capelli, C., Bonhoeffer, P., Diaz-Zuccarini, V., . . . Schievano, S. (2014). Geometrical and stress analysis of factors associated with stent fracture after melody percutaneous pulmonary valve implantation. *Circulation: Cardiovascular Interventions, 7*(4), 510-517. doi:10.1161/CIRCINTERVENTIONS.113.000631

Cribier, A. (2012). Development of transcatheter aortic valve implantation (TAVI): A 20-year odyssey. *Archives of Cardiovascular Diseases, 105*(3), 146-152. doi:10.1016/j.acvd.2012.01.005

Cribier, A., Eltchaninoff, H., Bash, A., Borenstein, N., Tron, C., Bauer, F., . . . Leon, M. B. (2002). Percutaneous transcatheter implantation of an aortic valve prosthesis for calcific aortic stenosis: first human case description. *Circulation, 106*, 3006-3008. doi:10.1161/01.CIR.0000047200.36165.B8

Daly, M. J., Blair, P. H., Modine, T., Donnelly, P. M., Jeganathan, R., Manoharan, G., & Spence, M. S. (2015). Carotid-Access transcatheter aortic valve replacement in a patient with a previous mitral valve replacement. *Journal of Cardiac Surgery, 30*(3), 256-259. doi:10.1111/jocs.12324

Dassault-Systèmes. (2014). *Abaqus Theory Guide Version 6.14*. Providence, RI: Dassault Systèmes.

Davies, H. (1965). Catheter-mounted valve for temporary relief of aortic insufficiency. *The Lancet, 285*(7379), 250.

De Backer, O., Piazza, N., Banai, S., Lutter, G., Maisano, F., Herrmann, H. C., . . . Sondergaard, L. (2014). Percutaneous transcatheter mitral valve replacement: an overview of devices in preclinical and early clinical evaluation. *Circulation: Cardiovascular Imaging, 7*(3), 400-409. doi:10.1161/CIRCINTERVENTIONS.114.001607

De Beule, M., Mortier, P., Carlier, S. G., Verhegghe, B., Van Impe, R., & Verdonck, P. (2008). Realistic finite element-based stent design: the impact of balloon folding. *Journal of Biomechanics, 41*(2), 383-389. doi:10.1016/j.jbiomech.2007.08.014

De Gaetano, F., Serrani, M., Bagnoli, P., Brubert, J., Stasiak, J., Moggridge, G. D., & Costantino, M. L. (2015). Fluid dynamic characterization of a polymeric heart valve prototype (Poli-Valve) tested under continuous and pulsatile flow conditions. *International Journal of Artificial Organs, 38*(11), 600-606. doi:doi:10.5301/ijao.5000452

de Heer, L. M., Budde, R. P. J., Mali, W. P. T. M., de Vos, A. M., van Herwerden, L. A., & Kluin, J. (2011). Aortic root dimension changes during systole and diastole: evaluation with ECG-gated multidetector row computed tomography. *The International Journal of Cardiovascular Imaging, 27*(8), 1195-1204. doi:10.1007/s10554-011-9838-x

de Jaegere, P., De Santis, G., Rodriguez-Olivares, R., Bosmans, J., Bruining, N., Dezutter, T., . . . Mortier, P. (2016). Patient-Specific Computer Modeling to Predict Aortic Regurgitation After Transcatheter Aortic Valve Replacement. *JACC Cardiovascular Interventions, 9*(5), 508-512. doi:10.1016/j.jcin.2016.01.003

De Kerchove, L., Jashari, R., Boodhwani, M., Duy, K. T., Lengelé, B., Gianello, P., . . . El Khoury, G. (2015). Surgical anatomy of the aortic root: Implication for valve-sparing reimplantation and aortic valve annuloplasty. *The Journal of Thoracic and Cardiovascular Surgery, 149*(2), 425-433. doi:10.1016/j.jtcvs.2014.09.042

Dee, R. (2003). Who assisted whom. *Texas Heart Institute Journal, 30*(1), 90.

Dewey, T. M., Walther, T., Doss, M., Brown, D., Ryan, W. H., Svensson, L., . . . Mack, M. J. (2006). Transapical aortic valve implantation: an animal feasibility study. *Annals of Thoracic and Cardiovascular Surgery, 82*(1), 110-116. doi:10.1016/j.athoracsur.2006.02.035

Dhaval, N. (2010). Vascular surgery: What's old? What's new? What's in the future? *Gujarat Medical Journal, 65*(2), 88-93.

Dimasi, A., Stevanella, M., Votta, E., Sturla, F., Burriesci, G., & Redaelli, A. (2015). Finite element analysis of transcatheter aortic valve implantation in the presence of aortic leaflet calcifications. In T. Lenarz & P. Wrtiggers (Eds.), *Biomedical Technology* (Vol. Volume 74, pp. 101-115): Springer.

Douglas, G. R., Phani, A. S., & Gagnon, J. (2014). Analyses and design of expansion mechanisms of balloon expandable vascular stents. *Journal of Biomechanics, 47*(6), 1438-1446. doi:10.1016/j.jbiomech.2014.01.039

Du Plessis, L. A., & Marchand, P. (1964). The anatomy of the mitral valve and its associated structures. *Thorax, 19*(3), 221-227.

Ducrocq, G., Himbert, D., Hvass, U., & Vahanian, A. (2010). Compassionate aortic valve implantation for severe aortic regurgitation. *Journal of Thoracic and Cardiovascular Surgery, 140*(4), 930-932. doi:10.1016/j.jtcvs.2010.02.003

Dumonteil, N., Marcheix, B., Lairez, O., & Laborde, J. C. (2013). Transcatheter aortic valve implantation for severe, non-calcified aortic regurgitation and narrow aortic root: description from a case report of a new approach to potentially avoid coronary artery obstruction. *Catheterization and Cardiovascular Interventions, 82*(2), E124-127. doi:10.1002/ccd.24541

Edwards. (2015). *P140031b: Edwards Sapien 3: Summary of Safety and Effectiveness.* Retrieved from https://www.accessdata.fda.gov/cdrh_docs/pdf14/P140031B.pdf

Esterhuyse, A., Van Der Westhuizen, K., Doubell, A., Weich, H., Scheffer, C., & Dellimore, K. (2012). Application of the Finite Element Method in the fatigue life prediction of a stent for a percutaneous heart valve. *Journal of Mechanics in Medicine and Biology, 12*(01), 1250007. doi:10.1142/s021951941200448x

Ewert, P., Riesenkampff, E., Neuss, M., Kretschmar, O., Nagdyman, N., & Lange, P. E. (2004). Novel growth stent for the permanent treatment of vessel stenosis in growing children: an experimental study. *Catheterization and Cardiovascular Interventions, 62*(4), 506-510. doi:10.1002/ccd.20136

Falk, V., Walther, T., Schwammenthal, E., Strauch, J., Aicher, D., Wahlers, T., . . . Mohr, F. W. (2011). Transapical aortic valve implantation with a self-expanding anatomically oriented valve. *European Heart Journal, 32*(7), 878-887. doi:10.1093/eurheartj/ehq445

Fanning, J. P., Platts, D. G., Walters, D. L., & Fraser, J. F. (2013). Transcatheter aortic valve implantation (TAVI): valve design and evolution. *International Journal of Cardiology, 168*(3), 1822-1831. doi:10.1016/j.ijcard.2013.07.117

FDA. (1997). Design control guidance for medical device manufacturers: FDA Center for Devices and Radiological Health.

FDA. (2010). 1545 Guidance for industry and FDA staff: Non-clinical engineering tests and recommended labeling for intravascular stents and associated delivery systems.

FDA. (2011). CDRH innovation initiative: FDA Center for Devices and Radiological Health.

Figini, F., Bijuklic, K., Schofer, J., Ruparelia, N., Davidson, C., Colombo, A., & Latib, A. (2015). *Impact of systole and diastole on prosthesis sizing in transcatheter aortic valve (Abstract)*. Paper presented at the EuroPCR 2015.

Fischione-Instruments. MODEL 110 Twin-Jet Electropolisher General Instructions.

Fish, R. D., Paniagua, D., Urena, P., & Chevalier, B. (2013). The Colibri heart valve: theory and practice in the achievement of a low-profile, pre-mounted, pre-packaged TAVI valve. *EuroIntervention, 9 Suppl*, S111-114. doi:10.4244/EIJV9SSA23

Franzone, A., Piccolo, R., Siontis, G. C., Lanz, J., Stortecky, S., Praz, F., . . . Pilgrim, T. (2016). Transcatheter aortic valve replacement for the treatment of pure native aortic valve regurgitation: A systematic review. *JACC Cardiovascular Interventions, 9*(22), 2308-2317. doi:10.1016/j.jcin.2016.08.049

Funayama, M., Sumikura, H., Takewa, Y., Tatsumi, E., & Nakayama, Y. (2015). Development of self-expanding valved stents with autologous tubular leaflet tissues for transcatheter valve implantation. *Journal of Artificial Organs, 18*(3), 228-235. doi:10.1007/s10047-015-0820-6

Fuster, V., O'Rourke, R. A., & Walsh, R. A. E. (2007). *Hurst's the Heart* (12th Edition ed.): McGraw-Hill Companies.

Gerber, M. A., Baltimore, R. S., Eaton, C. B., Gewitz, M., Rowley, A. H., Shulman, S. T., & Taubert, K. A. (2009). Prevention of rheumatic fever and diagnosis and treatment of acute Streptococcal pharyngitis: a scientific statement from the American Heart Association Rheumatic Fever, Endocarditis, and Kawasaki Disease Committee of the Council on Cardiovascular Disease in the Young, the Interdisciplinary Council on Functional Genomics and Translational Biology, and the Interdisciplinary Council on Quality of Care and Outcomes Research: endorsed by the American Academy of Pediatrics. *Circulation, 119*(11), 1541-1551. doi:10.1161/CIRCULATIONAHA.109.191959

Gessat, M., Hopf, R., Pollok, T., Russ, C., Frauenfelder, T., Sundermann, S. H., . . . Falk, V. (2014). Image-based mechanical analysis of stent deformation: concept and exemplary implementation for aortic valve stents. *IEEE Transactions in Biomedical Engineering, 61*(1), 4-15. doi:10.1109/TBME.2013.2273496

Guilhen, J. C. S., Palma, J. H., Gaia, D. F., de Araujo, A. T. V., Teles, C. A., Branco, J. N., & Buffolo, E. (2011). Transcatheter implantation of self-expandable valved prosthesis in outlet right ventricle an experimental study in pigs. *Revista Brasileira de Cirurgia Cardiovascular, 26*(3), 348-354. doi:10.5935/1678-9741.20110008

Gunning, P. S., Vaughan, T. J., & McNamara, L. M. (2014). Simulation of self expanding transcatheter aortic valve in a realistic aortic root: implications of deployment geometry on leaflet deformation. *Annals of Biomedical Engineering, 42*(9), 1989-2001. doi:10.1007/s10439-014-1051-3

Haïdopoulos, M., Turgeon, S., Sarra-Bournet, C., Laroche, G., & Mantovani, D. (2006). Development of an optimized electrochemical process for subsequent coating of 316 stainless steel for stent applications. *Journal of Materials Science: Materials in Medicine, 17*(7), 647-657.

Hall, G. J., & Kasper, E. P. (2006). Comparison of element technologies for modeling stent expansion. *Journal of Biomechanical Engineering, 128*, 751-756. doi:10.1115/1.2264382

Hamdan, A., Guetta, V., Konen, E., Goitein, O., Segev, A., Raanani, E., . . . Schwammenthal, E. (2012). Deformation dynamics and mechanical properties of the aortic annulus by 4-dimensional Computed Tomography: Insights into the functional anatomy of the aortic valve complex and implications for transcatheter aortic valve therapy. *Journal of the American College of Cardiology, 59*(2), 119-127. doi:10.1016/j.jacc.2011.09.045

Hammermeister, K., Sethi, G. K., Henderson, W. G., Grover, F. L., Oprian, C., & Rahimtoola, S. H. (2000). Outcomes 15 years after valve replacement with a mechanical versus a bioprosthetic valve: final report of the Veterans Affairs randomized trial. *Journal of the American College of Cardiology, 36*(4), 1152-1158. doi:10.1016/s0735-1097(00)00834-2

Harewood, F., Thornton, R., & Sharp, P. (2011). Step change in design: exploring sixty stent design variations overnight. Leamington Spa, UK: Altair Product Design.

Harken, D. E., Soroff, H. S., W.J., T., Lefemine, A. A., Gupta, S. K., & Lunzer, S. (1960). Partial and complete prostheses in aortic insufficiency. *Journal of Thoracic and Cardiovascular Surgery, 40*, 744-762.

Hashimoto, M., Kaminou, T., Ohuchi, Y., Nakamura, K., Sugiura, K., Adachi, A., . . . Ogawa, T. (2008). Development of a re-positionable aortic stent-valve: a preliminary study in swine. *Journal of Interventional Cardiology, 21*(5), 432-440. doi:10.1111/j.1540-8183.2008.00393.x

Hengstenberg, C., Condado, J., Garcia, D., Martinez, M. M., La Forgia, G., Ebner, A., . . . Hilker, M. (2015). TRINITY heart valve prosthesis: a novel repositionable and retrievable transapical transcatheter aortic valve system. *EuroIntervention, 10*(11), 1332-1335. doi:10.4244/EIJY14M07_08

Hildebrandt, H. A., Erbel, R., & Kahlert, P. (2013). Compassionate use of the self-expandable medtronic CoreValve prosthesis for the treatment of pure aortic regurgitation in a patient at prohibitive risk for surgical valve replacement. *Catheterization and Cardiovascular Interventions, 82*(7), E939-943. doi:10.1002/ccd.24763

Ho, S. Y. (2009). Structure and anatomy of the aortic root. *European Heart Journal Cardiovascular Imaging, 10*(1), i3-i10.

Ho, S. Y., & Nihoyannopoulos, P. (2006). Anatomy, echocardiography, and normal right ventricular dimensions. *Heart, 92 Suppl 1*, i2-13. doi:10.1136/hrt.2005.077875

Hoffmann, G., Lutter, G., & Cremer, J. (2008). Durability of bioprosthetic cardiac valves. *Deutsches Ärzteblatt International, 105*(8), 143-148. doi:10.3238/arztebl.2008.0143

Hoffmann, R., & Mintz, G. S. (2000). Coronary in-stent restenosis - predictors, treatment and prevention. *European Heart Journal, 21*(21), 1739-1749. doi:10.1053/euhj.2000.2153

Homjabok, W., Permpoon, S., & Lothongkum, G. (2010). Pickling behavior of AISI 304 stainless steel in sulfuric and hydrochloric acid solutions. *Journal of Metals, Materials and Minerals, 20*(2), 1-6.

Hopf, R., Gessat, M., Falk, V., & Mazza, E. (2012). *Stent induced loading of the aortic valve complex.* Paper presented at the International Conference on Medical Image Computing and Computer Assisted Intervention (MICCAI), Nice, 1 October 2012 - 5 October 2012.

Hopf, R., Gessat, M., Russ, C., Sundermann, S. H., Falk, V., & Mazza, E. (2017). Finite element stent modeling for the postoperative analysis of Transcatheter Aortic Valve Implantation. *Journal of Medical Devices, 11*, 021002-021001-021007. doi:10.1115/1.4036334]

Hopf, R., Sundermann, S. H., Born, S., Ruiz, C. E., Van Mieghem, N. M., de Jaegere, P. P., . . . Mazza, E. (2017). Postoperative analysis of the mechanical interaction between stent and host tissue in patients after transcatheter aortic valve implantation. *Journal of Biomechanics, 53*, 15-21. doi:10.1016/j.jbiomech.2016.12.038

Hsiao, H.-M., Wu, L.-W., Yin, M.-T., Lin, C.-H., & Chen, H. (2014). Quintupling fatigue resistance of intravascular stents via a simple design concept. *Computational Materials Science, 86*, 57-63. doi:10.1016/j.commatsci.2014.01.023

Huber, C. H., & von Segesser, L. K. (2006). Direct access valve replacement (DAVR) - are we entering a new era in cardiac surgery? *European Journal of Cardio-Thoracic Surgery, 29*(3), 380-385. doi:10.1016/j.ejcts.2005.12.014

Ionescu, M. I., Pakrashi, B. C., Holden, M. P., Mary, D. A., & Wooler, G. H. (1972). Results of aortic replacement with frame-supported fascia lata and pericardial grafts. *Journal of Thoracic and Cardiovascular Surgery, 64*, 340-355.

Ishmaku, A., & Han, K. (2004). Deformation induced nanostructure and texture in MP35N alloys. *Journal of Materials Science, 39*, 5417-5420.

Ismail, M., Hon, J. K. F., Chan, Z. W., & Leo, H. L. (2012). Recent advances in transcatheter heart valve replacement: a review on aortic and mitral implantation. *Recent Patents on Biomedical Engineering, 5*(3), 235-252.

ISO-5840-3. (2013). Cardiovascular implants — Cardiac valve prostheses - Part 3 Heart valve substitutes implanted by transcatheter techniques.

James, K. A., & Waisman, H. (2016). Layout design of a bi-stable cardiovascular stent using topology optimization. *Computer Methods in Applied Mechanics and Engineering*. doi:http://dx.doi.org/10.1016/j.cma.2016.02.036

Jamieson, W. R. E., Zhang, J., & Quijano, R. (2006). Antegrade placement of the aortic valve stent: transventricular delivery with the ENTRATA™ system. *EuroIntervention, Supplement A*, A14-A18.

Jilaihawi, H., Bonan, R., Asgar, A., Ibrahim, R., Spyt, T., Chin, D., & Kovac, J. (2010). Anatomic suitability for present and next generation transcatheter aortic valve prostheses. *JACC: Cardiovascular Interventions, 3*(8), 859-866. doi:10.1016/j.jcin.2010.05.015

Jilaihawi, H., Kashif, M., Fontana, G., Furugen, A., Shiota, T., Friede, G., . . . Makkar, R. R. (2012). Cross-sectional computed tomographic assessment improves accuracy of aortic annular sizing for transcatheter aortic valve replacement and reduces the incidence of paravalvular aortic regurgitation. *Journal of the American College of Cardiology, 59*(14), 1275-1286. doi:10.1016/j.jacc.2011.11.045

Joun, M., Choi, I., Eom, J., & Lee, M. (2007). Finite element analysis of tensile testing with emphasis on necking. *Computational Materials Science, 41*(1), 63-69. doi:10.1016/j.commatsci.2007.03.002

Judkins, M. P. (1967). Selective coronary arteriography. *Radiology, 89*(5), 815-824. doi:doi:10.1148/89.5.815

Karnessis, N., & Burriesci, G. (2013). Uniaxial and buckling mechanical response of auxetic cellular tubes. *Smart Materials and Structures, 22*(8), 084008. doi:10.1088/0964-1726/22/8/084008

Katayama, S., Umetani, N., Sugiura, S., & Hisada, T. (2008). The sinus of Valsalva relieves abnormal stress on aortic valve leaflets by facilitating smooth closure. *Journal of Thoracic and Cardiovascular Surgery, 136*(6), 1528-1535, 1535 e1521. doi:10.1016/j.jtcvs.2008.05.054

Katz, A. M. (2010). *Physiology of the heart* (Fifth Edition ed.). Philadelphia: Lippincott Williams & Wilkins.

Keevy, P.-A. (2004). *Finite element tool for modelling stent deployment to aid stent design.* (MSc(Med)), University of Cape Town, Cape Town.

Kemp, I., Dellimore, K., Rodriguez, R., Scheffer, C., Blaine, D., Weich, H., & Doubell, A. (2013). Experimental validation of the fluid-structure interaction simulation of a bioprosthetic aortic heart valve. *Australasian Physical and Engineering Science in Medicine, 36*(3), 363-373. doi:10.1007/s13246-013-0213-1

Kempfert, J., Rastan, A. J., Beyersdorf, F., Schonburg, M., Schuler, G., Sorg, S., . . . Walther, T. (2011). Trans-apical aortic valve implantation using a new self-expandable bioprosthesis: initial outcomes. *European Journal of Cardio-Thoracic Surgery, 40*(5), 1114-1119. doi:10.1016/j.ejcts.2011.01.078

Kheradvar, A., Groves, E. M., Dasi, L. P., Alavi, S. H., Tranquillo, R., Grande-Allen, K. J., . . . Canic, S. (2015). Emerging trends in heart valve engineering: Part I. Solutions for future. *Annals of Biomedical Engineering, 43*(4), 833-843. doi:10.1007/s10439-014-1209-z

Kheradvar, A., Groves, E. M., & Tseng, E. (2015). Proof of concept of FOLDAVALVE, a novel 14 Fr totally repositionable and retrievable transcatheter aortic valve. *EuroIntervention, 11*(5), 591-596. doi:10.4244/EIJY15M03_04

Kitzman, D. W., Scholz, D. G., Hagen, P. T., Ilstrup, D. M., & Edwards, W. D. (1988). Age-related changes in normal human hearts during the first 10 decades of life. Part II (maturity): A quantitative anatomic study of 765 specimens from subjects 20 to 99 years old. *Mayo Clinic Proceedings, 63*(2), 137-146. doi:10.1016/s0025-6196(12)64946-5

Knight, J., Kurtcuoglu, V., Muffly, K., Marshall, W., Jr., Stolzmann, P., Desbiolles, L., . . . Alkadhi, H. (2009). Ex vivo and in vivo coronary ostial locations in humans. *Surgical and Radiologic Anatomy, 31*(8), 597-604. doi:10.1007/s00276-009-0488-9

Kocher, A. A., Laufer, G., Haverich, A., Shrestha, M., Walther, T., Misfeld, M., . . . Borger, M. A. (2013). One-year outcomes of the Surgical Treatment of Aortic Stenosis With a Next Generation Surgical Aortic Valve (TRITON) trial: a prospective multicenter study of rapid-deployment aortic valve replacement with the EDWARDS INTUITY Valve System. *Journal of Thoracic and Cardiovascular Surgery, 145*(1), 110-115; discussion 115-116. doi:10.1016/j.jtcvs.2012.07.108

Kosmac, A. (2010). *Electropolishing stainless steels*: Euro Inox.

Kovac, J., Baron, J. H., Al-Jilaihawi, H., & Chin, D. T. (2017). Novel TAVI designs. *Cor et Vasa, 59*(1), e42-e50. doi:10.1016/j.crvasa.2017.01.014

Kumar, G. V. P., Cui, F., Danpinid, A., Su, B., Hon, J. K. F., & Leo, H. L. (2013). Design and finite element-based fatigue prediction of a new self-expandable percutaneous mitral valve stent. *Computer-Aided Design, 45*(10), 1153-1158. doi:10.1016/j.cad.2013.05.003

Kumar, G. V. P., Cui, F., Phang, H. Q., Su, B., Leo, H. L., & Hon, J. K. (2014). Design considerations and quantitative assessment for the development of percutaneous mitral valve stent. *Medical Engineering and Physics, 36*(7), 882-888. doi:10.1016/j.medengphy.2014.03.010

Kumar, G. V. P., Jafary-Zadeh, M., Tavakoli, R., & Cui, F. (2016). Feasibility of using bulk metallic glass for self-expandable stent applications. *Journal of Biomedical Materials Research B Applied Biomaterials*. doi:10.1002/jbm.b.33718

Kumar, G. V. P., & Mathew, L. (2008). Novel stent design for percutaneous aortic valve replacement. *IFMBE Proceedings, 21*, 446-448.

Kumar, G. V. P., & Mathew, L. (2009). Biomaterial optimization in a percutaneous aortic valve stent using finite element analysis. *Cardiovascular Revascularization Medicine, 10*(4), 247-251. doi:10.1016/j.carrev.2008.12.003

Kumar, P., Dalvi, B., Chikkatur, R., Kandhachar, P., Parida, R., Ahuja, V., . . . Tendolkar, A. (2004). TTK Chitra tilting disc valve: Hemodynamic evaluation. *Indian Journal of Thoracic and Cardiovascular Surgery, 20*, 117-121.

Kumar, V. (2012). Crocheted cellulose-based heart valve and small diameter vascular graft prostheses. Retrieved from http://www.flintbox.com/public/project/22055 on 21 May 2017

Kunzelman, K. S., Grande, K. J., David, T. E., Cochran, R. P., & Verrier, E. D. (1994). Aortic root and valve relationships: Impact on surgical repair. *The Journal of Thoracic and Cardiovascular Surgery, 107*(1), 162-170. doi:null

Labrosse, M. R., Beller, C. J., Robicsek, F., & Thubrikar, M. J. (2006). Geometric modeling of functional trileaflet aortic valves: development and clinical applications. *Journal of Biomechanics, 39*(14), 2665-2672. doi:10.1016/j.jbiomech.2005.08.012

Lansac, E., Lim, H. S., Shomura, Y., Lim, K. H., Goetz, W. A., Rice, N. T., . . . Duran, C. M. G. (2002). Aortic and pulmonary root: are their dynamics similar? *European Journal of Cardio-Thoracic Surgery, 21*(2), 268-275.

Lee, S.-J., & Li, J.-J. (2003). The effects of electropolishing (EP) process parameters on corrosion resistance of 316L stainless steel. *Journal of Materials Processing Technology, 140*, 206-210.

Leon, M. B. (2013). *New and novel TAVR devices.* Paper presented at the ICI 2013, Tel Aviv, Israel.

Li, K., Wang, Q., Pham, T., & Sun, W. (2014). Quantification of structural compliance of aged human and porcine aortic root tissues. *Journal of Biomedical Materials Research Part A, 102*(7), 2365-2374. doi:10.1002/jbm.a.34884

Litmanovich, D. E., Ghersin, E., Burke, D. A., Popma, J., Shahrzad, M., & Bankier, A. A. (2014). Imaging in Transcatheter Aortic Valve Replacement (TAVR): role of the radiologist. *Insights into Imaging, 5*(1), 123-145. doi:10.1007/s13244-013-0301-5

Loukas, M., Bilinsky, E., Bilinsky, S., Blaak, C., Tubbs, R. S., & Anderson, R. H. (2014). The anatomy of the aortic root. *Clinical Anatomy, 27*(5), 748-756. doi:10.1002/ca.22295

Lutter, G., Metzner, A., Jahnke, T., Bombien, R., Boldt, J., Iino, K., . . . Stock, U. A. (2010). Percutaneous tissue-engineered pulmonary valved stent implantation. *Annals of Thoracic Surgery, 89*(1), 259-263. doi:10.1016/j.athoracsur.2009.06.048

Manoharan, G., Spence, M. S., Rodes-Cabau, J., & Webb, J. G. (2012). St Jude Medical Portico valve. *EuroIntervention, 8 Suppl Q*, Q97-101. doi:10.4244/EIJV8SQA18

Marchand, C., Heim, F., & Durand, B. (2010a). Heart valve stent for percutaneous implantation: design optimization. *Journal of Biomedical Materials Research B Applied Biomaterials, 92*(1), 138-148. doi:10.1002/jbm.b.31499

Marchand, C., Heim, F., & Durand, B. (2010b). A novel stent for percutaneous heart valve implantation: first in vitro results. *Journal of Biomechanical Engineering, 132*(5), 054502. doi:10.1115/1.4001026

Marijon, E., Mirabel, M., Celermajer, D. S., & Jouven, X. (2012). Rheumatic heart disease. *The Lancet, 379*(9819), 953-964. doi:10.1016/s0140-6736(11)61171-9

Marrey, R. V., Burgermeister, R., Grishaber, R. B., & Ritchie, R. O. (2006). Fatigue and life prediction for cobalt-chromium stents: A fracture mechanics analysis. *Biomaterials, 27*(9), 1988-2000. doi:http://dx.doi.org/10.1016/j.biomaterials.2005.10.012

Martens, S., Sadowski, J., Eckstein, F. S., Bartus, K., Kapelak, B., Sievers, H. H., . . . Carrel, T. (2011). Clinical experience with the ATS 3f Enable(R) Sutureless Bioprosthesis. *European Journal of Cardio-Thoracic Surgery, 40*(3), 749-755. doi:10.1016/j.ejcts.2010.12.068

Martin, D., & Boyle, F. (2013). Finite element analysis of balloon-expandable coronary stent deployment: influence of angioplasty balloon configuration. *International Journal of Numerical Methods in Biomedical Engineering, 29*(11), 1161-1175. doi:10.1002/cnm.2557

Martinez-Clarke, P. (2014). *Syntheon Cardiology TAVR: Precise Control and Constant Force*. Paper presented at the TCT2014.

Masson, J. B., & Webb, J. G. (2009). Percutaneous treatment of mitral regurgitation. *Circulation: Cardiovascular Interventions, 2*(2), 140-146. doi:10.1161/CIRCINTERVENTIONS.108.837781

Matsumura, T., Ohtaki, E., Misu, K., Tohbaru, T., Asano, R., Nagayama, M., . . . Hosoda, S. (2002). Etiology of aortic valve disease and recent changes in Japan:a study of 600 valve replacement cases. *International Journal of Cardiology, 86*(2–3), 217-223. doi:http://dx.doi.org/10.1016/S0167-5273(02)00199-7

Matweb. (2016). Retrieved from http://www.matweb.com/search/datasheet.aspx?matguid=bf5886b231ca4f63ac78e0149552bbaf&ckck=1

Mazilu, D., Li, M., Kocaturk, O., & Horvath, K. A. (2012). Self-expanding stent and delivery system for aortic valve replacement. *Journal of Medical Devices, 6*(4), 410061-410069. doi:10.1115/1.4007750

Mercer, J. L., Benedicty, M., & Bahnson, H. T. (1973). The geometry and construction of the aortic leaflet. *Journal of Thoracic and Cardiovascular Surgery, 65*(4), 511-518.

Metzner, A., Iino, K., Steinseifer, U., Uebing, A., de Buhr, W., Cremer, J., & Lutter, G. (2010). Percutaneous pulmonary polyurethane valved stent implantation. *Journal of Thoracic and Cardiovascular Surgery, 139*(3), 748-752. doi:10.1016/j.jtcvs.2009.08.013

Mohammadi, H., & Mequanint, K. (2011). Prosthetic aortic heart valves: modeling and design. *Medical Engineering and Physics, 33*(2), 131-147. doi:10.1016/j.medengphy.2010.09.017

Mollmann, H., Diemert, P., Grube, E., Baldus, S., Kempfert, J., & Abizaid, A. (2013). Symetis ACURATE TF aortic bioprosthesis. *EuroIntervention, 9 Suppl*, S107-110. doi:10.4244/EIJV9SSA22

Morganti, S., Brambilla, N., Petronio, A. S., Reali, A., Bedogni, F., & Auricchio, F. (2015). Prediction of patient-specific post-operative outcomes of TAVI procedure: The impact of the positioning strategy on valve performance. *Journal of Biomechanics*. doi:10.1016/j.jbiomech.2015.10.048

Morganti, S., Conti, M., Aiello, M., Valentini, A., Mazzola, A., Reali, A., & Auricchio, F. (2014). Simulation of transcatheter aortic valve implantation through patient-specific finite element analysis: two clinical cases. *Journal of Biomechanics, 47*(11), 2547-2555. doi:10.1016/j.jbiomech.2014.06.007

Mueller, R. L., & Sanborn, T. A. (1995). The history of interventional cardiology: Cardiac catheterization, angioplasty, and related interventions. *American Heart Journal, 129*(1), 146-172. doi:http://dx.doi.org/10.1016/0002-8703(95)90055-1

Myers, P. O., Tissot, C., Christenson, J. T., Cikirikcioglu, M., Aggoun, Y., & Kalangos, A. (2010). Aortic valve repair by cusp extension for rheumatic aortic insufficiency in children: Long-term results and impact of extension material. *Journal of Thoracic and Cardiovascular Surgery, 140*(4), 836-844. doi:10.1016/j.jtcvs.2010.06.036

Mylotte, D., & Piazza, N. (2015). Transcatheter mitral valve implantation: a brief review. *EuroIntervention, 11 Suppl W*, W67-70. doi:10.4244/EIJV11SWA19

Neyt, M., Van Brabandt, H., Devriese, S., & Van De Sande, S. (2012). A cost-utility analysis of transcatheter aortic valve implantation in Belgium: focusing on a well-defined and identifiable population. *BMJ Open, 2*(3). doi:10.1136/bmjopen-2012-001032

Nietlispach, F., Wijesinghe, N., Wood, D., Carere, R. G., & Webb, J. G. (2010). Current balloon-expandable transcatheter heart valve and delivery systems. *Catheterization and Cardiovascular Interventions, 75*(2), 295-300. doi:10.1002/ccd.22279

Nishimura, R. A., Otto, C. M., Bonow, R. O., Carabello, B. A., Erwin, J. P., 3rd, Guyton, R. A., . . . American College of Cardiology/American Heart Association Task Force on Practice, G. (2014). 2014 AHA/ACC guideline for the management of patients with valvular heart disease: a report of the American College of Cardiology/American Heart Association Task Force on Practice Guidelines. *Journal of the American College of Cardiology, 63*(22), e57-185. doi:10.1016/j.jacc.2014.02.536

Nkoke, C., Lekoubou, A., Dzudie, A., Jingi, A. M., Kingue, S., Menanga, A., & Kengne, A. P. (2016). Echocardiographic pattern of rheumatic valvular disease in a contemporary sub-Saharan African pediatric population: an audit of a major cardiac ultrasound unit in Yaounde, Cameroon. *BMC Pediatrics, 16*, 43. doi:10.1186/s12887-016-0584-z

O'Brien, B., & Carroll, W. (2009). The evolution of cardiovascular stent materials and surfaces in response to clinical drivers: a review. *Acta Biomaterialia, 5*(4), 945-958. doi:10.1016/j.actbio.2008.11.012

Ovcharenko, E. A., Klyshnikov, K. U., Savrasov, G. V., Nyshtaev, D. V., & Glushkova, T. V. (2014). The choosing of optimal cell parameters of transcatheter aortic valve prosthesis (Russian). *Computer Research and Modeling, 6*(6), 943-954.

Ovcharenko, E. A., Klyshnikov, K. U., Savrasov, G. V., Nyshtaev, D. V., & Kudryavtseva, Y. A. (2015). Choice of design of transcatheter aortic valve prosthesis frame based on finite element analysis (Russian). *Computer Research and Modeling, 7*(4), 909-922.

Ovcharenko, E. A., Klyshnikov, K. U., Yuzhalin, A. E., Savrasov, G. V., Kokov, A. N., Batranin, A. V., . . . Kudryavtseva, Y. A. (2016). Modeling of transcatheter aortic valve replacement: Patient specific vs general approaches based on finite element analysis. *Computers in Biology and Medicine, 69*, 29-36. doi:10.1016/j.compbiomed.2015.12.001

Paar, J. A., Berrios, N. M., Rose, J. D., Caceres, M., Pena, R., Perez, W., . . . Dale, J. B. (2010). Prevalence of rheumatic heart disease in children and young adults in Nicaragua. *American Journal of Cardiology, 105*(12), 1809-1814. doi:10.1016/j.amjcard.2010.01.364

Padala, M., & Sarin, E. L. MitraCath: A transcatheter heart valve replacement device. Retrieved from http://atlanticpediatricdeviceconsortium.org/mitracath-transcatheter-heart-valve-replacement-device

Padala, M., Sarin, E. L., Willis, P., Babaliaros, V., Block, P., Guyton, R. A., & Thourani, V. H. (2010). An engineering review of transcatheter aortic valve technologies. *Cardiovascular Engineering and Technology, 1*(1), 77-87. doi:10.1007/s13239-010-0008-4

Panayiotides, I. M., & Nikolaides, E. (2014). Transcatheter Aortic Valve Implantation (TAVI): Is it Time for This Intervention to be Applied in a Lower Risk Population? *Clinical Medicine Insights: Cardiology, 8*, 93-102. doi:10.4137/CMC.S19217

Paniagua, D., Condado, J. A., Mejia, C., Induni, E., & Fish, R. D. (2006). Paniagua heart valve preclinical testing and transcatheter implantation of an aortic valve prosthesis. *EuroIntervention Supplements, 1*(Supplement A), A9-A13.

Patil, Y. B., & Dulange, S. R. (2014). A review on electropolishing process and its affecting parameters. *International Journal of Advanced Research in Science and Engineering, 3*(12), 246-252.

Perlman, G. Y., Loncar, S., Pollak, A., Gilon, D., Alcalai, R., Planer, D., . . . Danenberg, H. D. (2013). Post-procedural hypertension following transcatheter aortic valve implantation: incidence and clinical significance. *JACC Cardiovascular Interventions, 6*(5), 472-478. doi:10.1016/j.jcin.2012.12.124

Perme, H., Sharma, A. K., Kumar, N., Singh, H., Dewangan, R., & Maiti, S. K. (2009). In-vitro biocompatibility evaluation of crosslinked cellular and acellular bovine pericardium. *Trends in Biomaterials and Artificial Organs, 23*(2), 65-75.

Phan, K., Tsai, Y. C., Niranjan, N., Bouchard, D., Carrel, T. P., Dapunt, O. E., . . . Di Eusanio, M. (2015). Sutureless aortic valve replacement: a systematic review and meta-analysis. *Annals of Cardiothoracic Surgery, 4*(2), 100-111. doi:10.3978/j.issn.2225-319X.2014.06.01

Piazza, N. (2016). *Percutaneous mitral valve replacement in 2016: Unmet needs and future perspectives?* Paper presented at the PCR London Valves 2016.

Piazza, N., de Jaegere, P., Schultz, C., Becker, A. E., Serruys, P. W., & Anderson, R. H. (2008). Anatomy of the aortic valvar complex and its implications for transcatheter implantation of the aortic valve. *Circulation: Cardiovascular Imaging, 1*(1), 74-81. doi:10.1161/CIRCINTERVENTIONS.108.780858

Pibarot, P., & Dumesnil, J. G. (2009). Prosthetic heart valves: selection of the optimal prosthesis and long-term management. *Circulation, 119*(7), 1034-1048. doi:10.1161/CIRCULATIONAHA.108.778886

Piehler, H. R. (2005). Metallic Biomaterials. In S. A. Guelcher & J. O. Hollinger (Eds.), *An Introduction to Biomaterials* (pp. 300): CRC Press.

Piesslinger-Schweiger, S., & Bohme, O. (2011). US 8,080,148 B2 Electropolishing process for cobalt and cobalt alloys. U. S. P. Office.

Pietzsch, J. B., Shluzas, L. A., Paté-Cornell, M. E., Yock, P. G., & Linehan, J. H. (2009). Stage-Gate Process for the Development of Medical Devices. *Journal of Medical Devices, 3*(2), 021004. doi:10.1115/1.3148836

Pilliar, R. M. (2009). Metallic biomaterials. In R. Narayan (Ed.), *Biomedical Materials* (pp. 41-81). New York: Springer.

Poncin, P., & Proft, J. L. (2003). *Stent tubing: Understanding the desired attributes*. Paper presented at the Materials & Processes for Medical Devices Conference, 8-10 September 2003.

Pontes, J. C., Duarte, J. J., Silva, A. D., Gardenal, N., Dias, A. M., Benfatti, R. A., . . . Benfatti, A. F. (2013). Initial and pioneer experience of transcatheter aortic valve implantation (Inovare) through femoral or iliac artery. *Revista Brasileira de Cirurgia Cardiovascular, 28*(2), 208-216. doi:10.5935/1678-9741.20130030

Pott, D., Kutting, M., Zhong, Z., Amerini, A., Spillner, J., Autschbach, R., & Steinseifer, U. (2015). Development of a transcatheter tricuspid valve prosthesis through steps of iterative optimization and Finite Element Analysis. *Artificial Organs, 39*(10), 903-915. doi:10.1111/aor.12605

Prasad, M. J. N. V., Reiterer, M. W., & Kumar, K. S. (2014). Microstructure and mechanical behavior of an as-drawn MP35N alloy wire. *Materials Science and Engineering: A, 610*, 326-337. doi:10.1016/j.msea.2014.05.046

Preston-Maher, G. L., Torii, R., & Burriesci, G. (2015). A technical review of minimally invasive mitral valve replacements. *Cardiovascular Engineering and Technology, 6*(2), 174-184. doi:10.1007/s13239-014-0203-9

Rahmani, B., Tzamtzis, S., Sheridan, R., Mullen, M. J., Yap, J., Seifalian, A. M., & Burriesci, G. (2016). A new transcatheter heart valve concept (the TRISKELE): feasibility in an acute preclinical model. *EuroIntervention, 12*(7), 901-908. doi:10.4244/EIJV12I7A148

Rahmani, B., Tzamtzis, S., Sheridan, R., Mullen, M. J., Yap, J., Seifalian, A. M., & Burriesci, G. (2017). In vitro hydrodynamic assessment of a new transcatheter heart valve concept (the TRISKELE). *Journal of Cardiovascular Translational Research, 10*(2), 104-115. doi:10.1007/s12265-016-9722-0

Reardon, M. J., Van Mieghem, N. M., Popma, J. J., Kleiman, N. S., Søndergaard, L., Mumtaz, M., . . . Kappetein, A. P. (2017). Surgical or transcatheter aortic-valve replacement in intermediate-risk patients. *New England Journal of Medicine*. doi:10.1056/NEJMoa1700456

Regueiro, A., Granada, J. F., Dagenais, F., & Rodés-Cabau, J. (2017). Transcatheter mitral valve replacement. *Journal of the American College of Cardiology, 69*(17), 2175-2192. doi:10.1016/j.jacc.2017.02.045

Reid, K. (1970). The anatomy of the sinus of Valsalva. *Thorax, 25*(1), 79-85. doi:10.1136/thx.25.1.79

Remenyi, B., ElGuindy, A., Smith, S. C., Yacoub, M., & Holmes, D. R. (2016). Valvular aspects of rheumatic heart disease. *The Lancet, 387*(10025), 1335-1346. doi:10.1016/s0140-6736(16)00547-x

Ribeiro, H. B., Urena, M., Allende, R., Amat-Santos, I. J., & Rodes-Cabau, J. (2014). Balloon-expandable prostheses for transcatheter aortic valve replacement. *Progress in Cardiovascular Diseases, 56*(6), 583-595. doi:10.1016/j.pcad.2014.02.001

Ribeiro, H. B., Urena, M., Kuck, K. H., Webb, J. G., & Rodes-Cabau, J. (2012). Edwards CENTERA valve. *EuroIntervention, 8 Suppl Q*, Q79-82. doi:10.4244/EIJV8SQA14

Righini, G. (2017). EP 2986255 B1 Implant, intended to be placed in a blood circulating passage, comprising a system for separating the proximal arms. E. P. Office.

Roberts, W. C. (1970). Anatomically isolated aortic valvular disease. The case against its being of rheumatic etiology. *American Journal of Medicine, 49*(2), 151-159.

Roberts, W. C., & Ko, J. M. (2008). Some observations on mitral and aortic valve disease. *Baylor University Medical Center Proceedings, 21*(3), 282-299.

Root-Bernstein, R. (2014). Rethinking molecular mimicry in Rheumatic Heart Disease and autoimmune myocarditis: Laminin, collagen IV, CAR, and B1AR as initial targets of disease. *Frontiers in Pediatrics, 2*, 85. doi:10.3389/fped.2014.00085

Rosato, S., Santini, F., Barbanti, M., Biancari, F., D'Errigo, P., Onorati, F., . . . Seccareccia, F. (2016). Transcatheter aortic valve implantation compared with surgical aortic valve replacement in low-risk patients. *Circulation: Cardiovascular Interventions, 9*(5), e003326. doi:10.1161/CIRCINTERVENTIONS.115.003326

Ross, D. N. (1962). Homograft replacement of the aortic valve. *The Lancet, 2*, 487.

Rowe, S., & Bash, A. (2012). *Edwards in Israel-How it all began*. Paper presented at the ICI2012, Tel Aviv.

Rozeik, M. M., Wheatley, D. J., & Gourlay, T. (2014). Percutaneous heart valves; past, present and future. *Perfusion, 29*(5), 397-410. doi:10.1177/0267659114523464

Rudolph, T. K., & Baldus, S. (2013). JenaValve--transfemoral technology. *EuroIntervention, 9 Suppl*, S101-102. doi:10.4244/EIJV9SSA20

Russ, C., Hopf, R., Hirsch, S., Sundermann, S., Falk, V., Szekely, G., & Gessat, M. (2013). *Simulation of transcatheter aortic valve implantation under consideration of leaflet calcification.* Paper presented at the Engineering in Medicine and Biology Society (EMBC), 35th Annual International Conference of the IEEE, 3-7 July 2013, Osaka.

Russ, C., Hopf, R., Sundermann, S. H., Born, S., Hirsch, S., Falk, V., . . . Gessat, M. (2014). Computational stent placement in Transcatheter Aortic Valve Implantation. In F. Bello & S. Cotin (Eds.), *Biomedical Simulation. ISBMS 2014.* (Vol. 8789, pp. 95-105): Springer, Cham.

Sangiorgi, G., Melzi, G., Agostoni, P., Cola, C., Clementi, F., Romitelli, P., . . . Colombo, A. (2007). Engineering aspects of stents design and their translation into clinical practice. *Annali dell'Istituto Superiore di Sanità, 43*(1), 89-100.

Schievano, S., Capelli, C., Cosentino, D., Bosi, G., & Taylor, A. M. (2012). Finite element analysis to study percutaneous heart valves. In D. Moratal (Ed.), *Finite Element Analysis* (pp. 167-174): InTech.

Schievano, S., Petrini, L., Migliavacca, F., Coats, L., Nordmeyer, J., Lurz, P., . . . Bonhoeffer, P. (2007). Finite element analysis of stent deployment: understanding stent fracture in percutaneous pulmonary valve implantation. *Journal of Interventional Cardiology, 20*(6), 546-554. doi:10.1111/j.1540-8183.2007.00294.x

Schievano, S., Taylor, A. M., Capelli, C., Lurz, P., Nordmeyer, J., Migliavacca, F., & Bonhoeffer, P. (2010). Patient specific finite element analysis results in more accurate prediction of stent fractures: application to percutaneous pulmonary valve implantation. *Journal of Biomechanics, 43*(4), 687-693. doi:10.1016/j.jbiomech.2009.10.024

Schmidt, D., Dijkman, P. E., Driessen-Mol, A., Stenger, R., Mariani, C., Puolakka, A., . . . Hoerstrup, S. P. (2010). Minimally-invasive implantation of living tissue engineered heart valves: a comprehensive approach from autologous vascular cells to stem cells. *Journal of the American College of Cardiology, 56*(6), 510-520. doi:10.1016/j.jacc.2010.04.024

Scholz, D. G., Kitzman, D. W., Hagen, P. T., Ilstrup, D. M., & Edwards, W. D. (1988). Age-related changes in normal human hearts during the first 10 decades of life. Part I (growth): A quantitative anatomic study of 200 specimens from subjects from birth to 19 years old. *Mayo Clinic Proceedings, 63*(2), 126-136. doi:10.1016/s0025-6196(12)64945-3

Schrijnemakers, L. ImaValve: Intelligent materials for in-situ heart valve tissue engineering. Retrieved from https://www.tue.nl/en/university/departments/biomedical-engineering/research/research-groups/soft-tissue-biomechanics-engineering/imavalve/#top on 21 May 2017

Schubert, S. A., & Ghanta, R. K. (2016). Aortic valve anatomy: Implications for transcatheter aortic valve replacement. In G. Ailawadi & I. L. Kron (Eds.), *Catheter based valve and aortic surgery* (pp. 1-10). New York: Springer-Verlag.

Schultz, C., Rodriguez-Olivares, R., Bosmans, J., Lefevre, T., De Santis, G., Bruining, N., . . . de Jaegere, P. (2016). Patient-specific image-based computer simulation for the prediction of valve morphology and calcium displacement after TAVI with the Medtronic CoreValve and the Edwards SAPIEN valve. *EuroIntervention, 11*(9), 1044-1052. doi:10.4244/EIJV11I9A212

Schymik, G., Schrofel, H., Heimeshoff, M., Luik, A., Thoenes, M., & Mandinov, L. (2015). How to adapt the implantation technique for the new SAPIEN 3 transcatheter heart valve design. *Journal of Interventional Cardiology, 28*(1), 82-89. doi:10.1111/joic.12165

Seldinger, S. I. (1953). Catheter replacement of the needle in percutaneous arteriography: A new technique. *Acta Radiologica [Old Series], 39*(5), 368-376. doi:10.3109/00016925309136722

Shahzad, M., Kamran, A., Siddiqui, M. Z., & Farhan, M. (2015). Mechanical characterization and FE modelling of a hyperelastic material. *Materials Research, 18*(5), 918-924. doi:10.1590/1516-1439.320414

Shibayama, K., Harada, K., Berdejo, J., Tanaka, J., Mihara, H., Itabashi, Y., & Shiota, T. (2014). Comparison of aortic root geometry with bicuspid versus tricuspid aortic valve: real-time three-dimensional transesophageal echocardiographic study. *Journal of the American Society of Echocardiography, 27*(11), 1143-1152. doi:10.1016/j.echo.2014.07.008

Shih, C.-C., Shih, C.-M., Chou, K.-Y., Lin, S.-J., & Su, Y.-Y. (2006). Electrochemical behavior of MP35N implant alloy in simulated physiological media. *Journal of The Electrochemical Society, 153*(10), B403. doi:10.1149/1.2221854

Shirzadi, M. M. (2016). *Development of a patient-specific finite element model of the Transcatheter Aortic Valve Implantation (TAVI) procedure.* (MSc Mechanical Engineering), University of Cape Town, Cape Town.

Shivaraju, A., Kodali, S., Thilo, C., Ott, I., Schunkert, H., von Scheidt, W., . . . Kasel, A. M. (2015). Overexpansion of the SAPIEN 3 Transcatheter Heart Valve: A feasibility study. *JACC Cardiovascular Interventions, 8*(15), 2041-2043. doi:10.1016/j.jcin.2015.10.006

Shumacker, H. B. (1992). Valve replacement and valve reconstruction. *The evolution of cardiac surgery* (pp. 303-315). Bloomington: Indiana University Press.

Sliwa, K., & Zilla, P. (2012). Rheumatic heart disease: The tip of the iceberg. *Circulation, 125*(25), 3060-3062. doi:10.1161/CIRCULATIONAHA.112.114199

Sochman, J., Peregrin, J. H., Pavcnik, D., Timmermans, H., & Rosch, J. (2000). Percutaneous transcatheter aortic disc valve prosthesis implantation: a feasibility study. *Cardiovascular and Interventional Radiology, 23*(5), 384-348.

Sojitra, P., Kotadia, H., Engineer, C., Raval, A., Kothwala, D., Jariwala, A., . . . Mehta, G. (2009). Surface enhancement and characterization of L-605 cobalt alloy cardiovascular stent by novel electrochemical treatment. *Trends in Biomaterials and Artificial Organs, 23*(2), 55-64.

Sorensen, D., Li, B. Q., Gerberich, W. W., & Mkhoyan, K. A. (2014). Investigation of secondary hardening in Co–35Ni–20Cr–10Mo alloy using analytical scanning transmission electron microscopy. *Acta Materialia, 63*, 63-72. doi:10.1016/j.actamat.2013.10.005

Spranger, K., Capelli, C., Bosi, G. M., Schievano, S., & Ventikos, Y. (2015). Comparison and calibration of a real-time virtual stenting algorithm using Finite Element Analysis and Genetic Algorithms. *Computer Methods in Applied Mechanics and Engineering, 293*, 462-480. doi:10.1016/j.cma.2015.03.022

Srimahachota, S., Buddhari, W., & Sondergaard, L. (2016). *First-in-man study of transcatheter aortic valve implantations in aortic stenosis using the Hydra self-expanding valve*. Paper presented at the EuroPCR2016, Paris.

Stalder, M., Suri, R. M., Kraehenbuehl, E. S., Hellige, G., Wenaweser, P., Zobrist, C., . . . Carrel, T. P. (2010). Transapical implantation of a novel self-expanding sutureless aortic valve prosthesis. *Mayo Clinic Proceedings, 19*, 182-188.

Stoeckel, D., Bonsignore, C., & Duda, S. (2002). A survey of stent designs. *Minimally Invasive Therapies & Allied Technologies, 11*(4), 137–147.

Stoeckel, D., Pelton, A., & Duerig, T. (2004). Self-expanding nitinol stents - material and design considerations. *European Radiology, 14*(2), 292-301.

Sturla, F., Ronzoni, M., Vitali, M., Dimasi, A., Vismara, R., Preston-Maher, G., . . . Redaelli, A. (2016). Impact of different aortic valve calcification patterns on the outcome of transcatheter aortic valve implantation: A finite element study. *Journal of Biomechanics, 49*(12), 2520-2530. doi:10.1016/j.jbiomech.2016.03.036

Surmann, H., & Huser, J. (1998). Automatic electropolishing of cobalt chromium dental cast alloys with a fuzzy logic controller. *Journal of Computers and Chemical Engineering, 22*(7-8), 1099-1111.

Sussman, T., & Bathe, K.-J. (2014). Spurious modes in geometrically nonlinear small displacement finite elements with incompatible modes. *Computers & Structures, 140*, 14-22. doi:10.1016/j.compstruc.2014.04.004

Sutton, J. P., Ho, S. Y., & Anderson, R. H. (1995). The forgotten interleaflet triangles: A review of the surgical anatomy of the aortic valve. *Annals of Thoracic Surgery, 59*, 419-427.

Suttorp, M. J., Stella, P. R., Dens, J., McKenzie, J. M., Park, K. S., & Frambach, P. (2015). Ultra-thin strut cobalt chromium bare metal stent usage in a complex real-world setting. (SOLSTICE registry). *Netherlands Heart Journal, 23*(2), 124-129. doi:10.1007/s12471-014-0629-6

Swanson, W. M., & Clark, R. E. (1974). Dimensions and geometric relationships of the human aortic value as a function of pressure. *Circulation Research, 35*(6), 871-882. doi:10.1161/01.RES.35.6.871

Taramasso, M., Pozzoli, A., Latib, A., La Canna, G., Colombo, A., Maisano, F., & Alfieri, O. (2014). New devices for TAVI: technologies and initial clinical experiences. *Nature Reviews: Cardiology, 11*(3), 157-167. doi:10.1038/nrcardio.2013.221

Tedder, M. E., Liao, J., Weed, B., Stabler, C., Zhang, H., Simionescu, A., & Simionescu, D. T. (2009). Stabilized collagen scaffolds for heart valve tissue engineering. *Tissue Engineering Part A, 15*(6), 1257-1268.

Tilea, I., Suciu, H., Tilea, B., Tatar, C. M., Ispas, M., & Serban, R. C. (2013). Anatomy and function of normal aortic valvular complex. In E. Aikawa (Ed.), *Anatomy and function of normal aortic valvular complex, calcific aortic valve disease*: Intech.

Tops, L. F., Wood, D. A., Delgado, V., Schuijf, J. D., Mayo, J. R., Pasupati, S., . . . Bax, J. J. (2008). Noninvasive evaluation of the aortic root with multislice computed tomography implications for transcatheter aortic valve replacement. *JACC: Cardiovascular Imaging, 1*(3), 321-330. doi:10.1016/j.jcmg.2007.12.006

Treede, H., Lubos, E., Conradi, L., Deuschl, F., Asch, F. M., Weissman, N. J., . . . Schaefer, U. (2015). Thirty-day VARC-2 and performance data of a new self-expanding transcatheter aortic heart valve. *EuroIntervention, 11*(8), 785-792. doi:10.4244/eijy15m05_05

Treede, H., Mohr, F.-W., Baldus, S., Rastan, A., Ensminger, S., Arnold, M., . . . Figulla, H.-R. (2012). Transapical transcatheter aortic valve implantation using the JenaValve™ system: acute and 30-day results of the multicentre CE-mark study. *European Journal of Cardio-Thoracic Surgery, 41*(6), e131-e138. doi:10.1093/ejcts/ezs129

Tsuneyoshi, H., Komiya, T., & Shimamoto, a. (2016). Accuracy of aortic annulus diameter measurement: Comparison of multi-detector CT, two- and three-dimensional echocardiography. *Journal of Cardiac Surgery, 31*, 18-22. doi:10.1111/

Tzamtzis, S., Viquerat, J., Yap, J., Mullen, M. J., & Burriesci, G. (2013). Numerical analysis of the radial force produced by the Medtronic-CoreValve and Edwards-SAPIEN after transcatheter aortic valve implantation (TAVI). *Medical Engineering and Physics, 35*(1), 125-130. doi:10.1016/j.medengphy.2012.04.009

Vaizasatya, A. (2013). *A methodology for coronary stent product development: design, simulation and optimization.* (PhD), North Carolina A&T State University, Greensboro, North Carolina.

Van der Merwe, H., Reddy, D. B., Zilla, P., Bezuidenhout, D., & Franz, T. (2008). A computational study of knitted Nitinol meshes for their prospective use as external vein reinforcement. *Journal of Biomechanics, 41*(6), 1302-1309. doi:10.1016/j.jbiomech.2008.01.016

Vesely, I. (2003). The evolution of bioprosthetic heart valve design and its impact on durability. *Cardiovascular Pathology, 12*(5), 277-286. doi:10.1016/s1054-8807(03)00075-9

Vesely, I. (2010). Transcatheter valves: A brave new world. *The Journal of Heart Valve Disease, 19*, 543-558.

Vizient. (2017). Heart valves, structural heart and endograft technologies. *Vizient Technology Watch, Vol. 1,* 28 pages.

von Aspern, K., Foldyna, B., Etz, C. D., Hoyer, A., Girrbach, F., Holzhey, D., . . . Lehmkuhl, L. (2015). Effective diameter of the aortic annulus prior to transcatheter aortic valve implantation: influence of area-based versus perimeter-based calculation. *International Journal of Cardiovascular Imaging, 31*(1), 163-169. doi:10.1007/s10554-014-0527-4

Vongpatanasin, W., Hillis, L., & Lange, R. A. (1996). Prosthetic heart valves. *New England Journal of Medicine, 335*(6), 407-416.

Vy, P., Auffret, V., Badel, P., Rochette, M., Le Breton, H., Haigron, P., & Avril, S. (2015). Review of patient-specific simulations of transcatheter aortic valve implantation. *International Journal of Advances in Engineering Sciences and Applied Mathematics, 8*(1), 2-24. doi:10.1007/s12572-015-0139-9

Wallby, L., Steffensen, T., Jonasson, L., & Broqvist, M. (2013). Inflammatory characteristics of stenotic aortic valves: A comparison between rheumatic and nonrheumatic aortic stenosis. *Cardiology Research and Practice, 2013*, 895215. doi:10.1155/2013/895215

Waller, B. F., McKay, C., Vantassel, J. W., Taliercio, C., Howard, J., & Green, F. (1991). Catheter balloon valvuloplasty of stenotic aortic valve Part 1: Anatomic basis and mechanisms of balloon dilation. *Clinical Cardiology, 14*, 836-846.

Walters, A. (2015). The TTK Chitra Heart Valve: A high quality prosthesis for $350. Retrieved from http://www.globalhealth.care/2015/03/the-chitra-heart-valve-high-quality.html

Walther, T., Falk, V., Borger, M. A., Dewey, T., Wimmer-Greinecker, G., Schuler, G., . . . Mohr, F. W. (2007). Minimally invasive transapical beating heart aortic valve implantation — proof of concept. *European Journal of Cardio-Thoracic Surgery, 31*(1), 9-15. doi:10.1016/j.ejcts.2006.10.034

Wang, Q., Kodali, S., Primiano, C., & Sun, W. (2015). Simulations of transcatheter aortic valve implantation: implications for aortic root rupture. *Biomechanics and Modeling in Mechanobiology, 14*(1), 29-38. doi:10.1007/s10237-014-0583-7

Wang, Q., Sirois, E., & Sun, W. (2012). Patient-specific modeling of biomechanical interaction in transcatheter aortic valve deployment. *Journal of Biomechanics, 45*(11), 1965-1971. doi:10.1016/j.jbiomech.2012.05.008

Wei, L., Liu, H., Zhu, L., Yang, Y., Zheng, J., Guo, K., . . . Wang, C. (2015). A new transcatheter aortic valve replacement system for predominant aortic regurgitation: Implantation of the J-Valve and early outcome. *JACC Cardiovascular Interventions, 8*(14), 1831-1841. doi:10.1016/j.jcin.2015.08.021

Weir, W. (2014). Tiny heart valve has big potential for UConn startup. *UConn Today.* Retrieved from http://today.uconn.edu/2014/09/tiny-heart-valve-has-big-potential-for-uconn-startup/

Weiss, D., Ruiz, C. E., Pirelli, L., Jelnin, V., Fontana, G. P., & Kliger, C. (2015). Available transcatheter aortic valve replacement technology. *Current Atherosclerosis Reports, 17*(3), 488. doi:10.1007/s11883-015-0488-7

Wendt, D., Al-Rashid, F., Kahlert, P., Eissmann, M., El-Chilali, K., Janosi, R. A., . . . Thielmann, M. (2015). Low incidence of paravalvular leakage with the balloon-expandable Sapien 3 Transcatheter Heart Valve. *Annals of Thoracic Surgery, 100*(3), 819-825;discussion 825-816. doi:10.1016/j.athoracsur.2015.03.079

WHO. (2004). *Rheumatic fever and rheumatic heart disease: Report of a WHO expert consultation, Geneva, 29 October–1 November 2001*. Geneva: World Health Organisation.

Wiegerinck, E. M., Van Kesteren, F., Van Mourik, M. S., Vis, M. M., & Baan, J., Jr. (2016). An up-to-date overview of the most recent transcatheter implantable aortic valve prostheses. *Expert Review of Medical Devices, 13*(1), 31-45. doi:10.1586/17434440.2016.1120665

Wu, W., Pott, D., Mazza, B., Sironi, T., Dordoni, E., Chiastra, C., . . . Migliavacca, F. (2016). Fluid-structure interaction model of a percutaneous aortic valve: Comparison with an in vitro test and feasibility study in a patient-specific case. *Annals of Biomedical Engineering, 44*(2), 590-603. doi:10.1007/s10439-015-1429-x

Yano, M., Nakamura, K., Nagahama, H., Matsuyama, M., Nishimura, M., & Onitsuka, T. (2012). Aortic annulus diameter measurement: What Is the best modality? *Annals of Thoracic and Cardiovascular Surgery, 18*(2), 115-120. doi:10.5761/atcs.oa.11.01727

Yoganathan, A. P., Lemmon, J. D., & Ellis, J. T. (2000). Heart valve dynamics. In J. D. Bronzino (Ed.), *The Biomedical Engineering Handbook* (2nd Edition ed.): CRC Press LLC in cooperation with IEEE Press.

Young, E., Chen, J. F., Dong, O., Gao, S., Massiello, A., & Fukamachi, K. (2011). Transcatheter heart valve with variable geometric configuration: in vitro evaluation. *Artificial Organs, 35*(12), 1151-1159. doi:10.1111/j.1525-1594.2011.01331.x

Young, M., Erdemir, A., Stucke, S., Klatte, R., Davis, B., & Navia, J. L. (2012). Simulation based design and evaluation of a transcatheter mitral heart valve frame. *Journal of Medical Devices, 6*(3), 31005-31012. doi:10.1115/1.4007182

Zahn, E. M., Hellenbrand, W. E., Lock, J. E., & McElhinney, D. B. (2009). Implantation of the melody transcatheter pulmonary valve in patients with a dysfunctional right ventricular outflow tract conduit early results from the U.S. clinical trial. *Journal of the American College of Cardiology, 54*(18), 1722-1729. doi:10.1016/j.jacc.2009.06.034

Zavalloni, D., De Benedictis, M., Pagnotta, P., Scrocca, I., & Presbitero, P. (2014). New CoreValve Evolut 23 mm: Technology for treatment of degenerated bioprosthesis. *Heart, Lung and Circulation, 23*(2), 183-185. doi:https://doi.org/10.1016/j.hlc.2013.08.002

Zegdi, R., Ciobotaru, V., Noghin, M., Sleilaty, G., Lafont, A., Latremouille, C., . . . Fabiani, J. N. (2008). Is it reasonable to treat all calcified stenotic aortic valves with a valved stent? Results from a human anatomic study in adults. *Journal of the American College of Cardiology, 51*(5), 579-584. doi:10.1016/j.jacc.2007.10.023

Zegdi, R., Khabbaz, Z., Borenstein, N., & Fabiani, J. N. (2006). A repositionable valved stent for endovascular treatment of deteriorated bioprostheses. *Journal of the American College of Cardiology, 48*(7), 1365-1368. doi:10.1016/j.jacc.2006.07.017

Zhang, B., Chen, X., Xu, T. Y., Zhang, Z. G., Li, X., Han, L., & Xu, Z. Y. (2014). Transcatheter pulmonary valve replacement by hybrid approach using a novel polymeric prosthetic heart valve: proof of concept in sheep. *PLoS One, 9*(6), e100065. doi:10.1371/journal.pone.0100065

Zhao, Z.-G., Feng, Y., Baccarob, J. A., & Chen, M. (2017). *First-in-human experience with a next-generation pre-packaged self-expandable dry-tissue TAVI device.* Paper presented at the EuroPCR 2017, Paris.

Zhu, D., Hu, J., Meng, W., & Guo, Y. (2015). Successful transcatheter aortic valve implantation for pure aortic regurgitation using a new second generation self-expanding J-Valve(TM) system - the first in-man implantation. *Heart, Lung and Circulation, 24*(4), 411-414. doi:10.1016/j.hlc.2014.10.007

Zienkiewicz, O. C., & Taylor, R. L. (2000). *The Finite Element Method* (Vol. 1. The Basis). Oxford: Butterworth-Heinemann.

Zilla, P., Brink, J., Human, P., & Bezuidenhout, D. (2008). Prosthetic heart valves: Catering for the few. *Biomaterials, 29*(4), 385-406. doi:http://dx.doi.org/10.1016/j.biomaterials.2007.09.033

Zühlke, L. J., Engel, M. E., Karthikeyan, G., Rangarajan, S., Mackie, P., Cupido, B., . . . Mayosi, B. M. (2015). Characteristics, complications, and gaps in evidence-based interventions in rheumatic heart disease: the Global Rheumatic Heart Disease Registry (the REMEDY study). *European Heart Journal, 36*(18), 1115-1122. doi:10.1093/eurheartj/ehu449

Zühlke, L. J., Engel, M. E., Remenyi, B., Wyber, R., & Carapetis, J. (2013). The second rheumatic heart disease forum report. *Global Heart, 8*(3), 253-261. doi:10.1016/j.gheart.2013.08.006

Zühlke, L. J., Mirabel, M., & Marijon, E. (2013). Congenital heart disease and rheumatic heart disease in Africa: recent advances and current priorities. *Heart, 99*(21), 1554-1561. doi:10.1136/heartjnl-2013-303896

Appendix A. Comprehensive list of transcatheter valves

Appendix Table A-1. Balloon Expandable Valves

	Device name	Stent	Leaflet/ (skirt) material	Access Routes	Valve diam. (mm)	Aortic ann. diam. (mm)	Catheter size (Fr)	Status
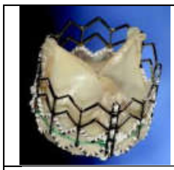	Cribier-Edwards THV™ (Edwards Lifesciences) (Walther et al., 2007)	Stainless steel	Equine pericardium/(PET)	TA	23, 26	TBD	33	Clinical trial
	Edwards SAPIEN THV™ (Edwards Lifesciences) (Jilaihawi et al., 2010) (Bourantas et al., 2012)	Stainless steel	Bovine pericardium/(PET)	TF, TA	23	18-22	22-24	FDA approved, CE marked
					26	21-25		
	Edwards SAPIEN XT™ (Edwards Lifesciences) (Bourantas et al., 2012)	Co-Cr (MP35N)	Bovine pericardium/(PET)	TF, TA, TAo, SC	20	TBD	TBD	CE Marked
					23	18-22	16/18	
					26	21-25	18/19	
					29	TBD	20/22	
	Edwards SAPIEN 3™ (Edwards Lifesciences) (Bourantas et al., 2012; Wiegerinck et al., 2016)	Co-Cr (MP35N)	Bovine pericardium/(PET)	TF, TA, TAo, SC	23, 26	TBD	14 (18TA)	CE Mark (Wiegerinck et al., 2016)
	Colibri (Colibri Heart Valve LLC, formerly Endolumix Technology, formally Endoluminal Technology Research) (Fish, Paniagua, Urena, & Chevalier, 2013; Ismail et al., 2012; Ribeiro et al., 2014; Wiegerinck et al., 2016)	Platinum-Iridium, Stainless Steel	Porcine pericardium	TF	N/A	N/A	11-16 (Bourantas & Serruys, 2014)	Clinical case (Paniagua, Condado, Mejia, Induni, & Fish, 2006)
		Stainless steel	Porcine pericardium	TBD	24, 21, 27	TBD	14/16	CE Mark (Wiegerinck et al., 2016)
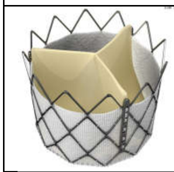	Inovare™ (Braille Biomedica) (Bourantas et al., 2012; Braile, 2011)	Co-Cr	Bovine Pericardium/ (PET)	TA (Braile, 2011) /TF	20, 22, 24, 26, 28 (Braile, 2011)	TBD	24 (Braile, 2011)	CE Mark (Wiegerinck et al., 2016)
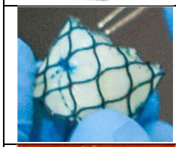	Dura LowPro Valve (Dura Biotech) (Calderan, Mao, Sirois, & Sun, 2016; Weir, 2014)	Co-Cr	Pericardium	TBD	TBD	TBD	14	Develop-ment
	Stellenbosch University (Kemp et al., 2013)	Co-Cr	Kangaroo pericardium	TBD	TBD	TBD	TBD	Animal

	MyVal™ (Meril Cardio-vascular) (Leon, 2013)	Co-Cr	Bovine pericardium (Pericardial/ PET)	TBD	TBD	TBD	TBD	Animal
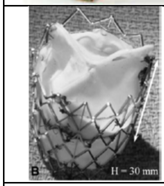	University of California (Azadani et al., 2009)	Stainless steel	Bovine pericardium (Pericardial/ PET)	TBD	TBD	TBD	TBD	TBD
	Vienna Aortic Valve Balloon Expandable (Products and Features) (Agreli, 2017)	TBD	TBD	TBD	TBD	TBD	TBD	TBD

Appendix Table A-2. Self-expanding bioprosthetic valves without orientation

	Device name	Stent	Leaflet/ (skirt) material	Access Routes	Valve diam. (mm)	Aortic ann. diam. (mm)	Catheter size (Fr)	Status
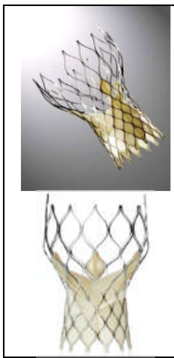	CoreValve™ and CoreValve Evolut™ (Medtronic) (Wiegerinck et al., 2016)	Nitinol	Porcine pericardium/ (porcine pericard)	TF, SC,TAo	23	TBD	18-22	FDA and CE Mark Approval
					26	20-23		
					29	23-27		
					31	TBD		
	Edwards Centera™ (Edwards Lifesciences) (Ribeiro, Urena, Kuck, Webb, & Rodes-Cabau, 2012)	Nitinol	Bovine/PET	TF, SC (retro-grade)	23,26,29	TBD	14 (eSheath)	CE Mark
	Portico™ (St Jude) (Manoharan, Spence, Rodes-Cabau, & Webb, 2012; Wiegerinck et al., 2016)	Nitinol	Bovine pericardium/ (porcine pericard)	TF, TA	23, 25, 27, 29	19-21	18	CE Mark
	Valve Medical (Leon, 2013)	Nitinol, SE, two-part	Bovine pericardium/ (polymer coating)	TF	TBD	TBD	12	TBD
	HLT Transcatheter Valve System (Heart Leaflet Technologies/ Bracco) (Wiegerinck et al., 2016)	Nitinol	Porcine pericardium (braided polyester)	TF	19,21,23, 25	TBD	16,17	Clinical

	Trinity Flexx™ (Transcatheter Technologies, formerly EndoCor) (Hengstenberg et al., 2015)	Nitinol	Bovine pericardium	TA	TBD	TBD	TBD	CE Mark (Wiegerinck et al., 2016)
	Lotus™ (Boston Scientific) (Wiegerinck et al., 2016)	Nitinol	Bovine pericardium/ (poly urethane)	TF	23, 27	19-26	18,20	CE Mark
	Foldavalve (Kheradvar University of California Irvine/ Foldavalve) (Kheradvar, Groves, & Tseng, 2015)	Nitinol	TBD	TA,TF, SC	TBD	TBD	12	Animal
	(Braile/University of Sao Paulo) (Guilhen et al., 2011)	Nitinol	Bovine	TBD	TBD	TBD	TBD	Animal
	CHUV valve (Huber & von Segesser, 2006)	Nitinol	Pericardial	TBD	TBD	TBD	TBD	TBD
	W-model valved stent (Yuan et al.) (Bai et al., 2010)	Nitinol	Porcine pericardium	TF	20-25	TBD	14	TBD
	Venus A-valve™ (Venus MedTec) (Zhao, Feng, Baccarob, & Chen, 2017)	Nitinol	Porcine pericardium	TBD	23, 26, 29, 32	TBD	16-18	Animal
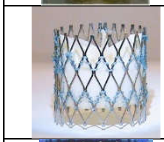	Optimum TAV (Thubrikar Aortic Valve) (Wiegerinck et al., 2016)	Nitinol	Bovine pericardium	TF, TA, TAo	25	23	22	Animal
	Xeltis AG, University of Zurich (Schmidt et al., 2010)	Nitinol	Tissue engineered valve	TBD	TBD	30	TBD	TBD
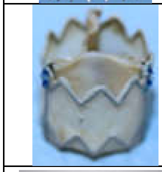	Biovalve (Funayama, Sumikura, Takewa, Tatsumi, & Nakayama, 2015)	Nitinol	Tissue engineered valve	TBD	TBD	TBD	TBD	Animal
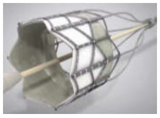	Syntheon Cardiology TAVR device (Martinez-Clarke, 2014)	TBD	TBD	TBD	TBD	TBD	TBD	TBD
	Imavalve (European Union project) (Schrijnemakers)	Nitinol	Tissue engineered valve	TBD	TBD	TBD	TBD	TBD

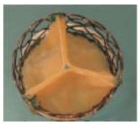	Cormove/ Perouse Medical (Zegdi et al., 2008; Zegdi, Khabbaz, Borenstein, & Fabiani, 2006)	Nitinol	Initially Porcine root (Toronto PAV), later bovine pericardium	TBD (Experi-mental TA)	25	20	39	Animal
	Biovalve™ (Biotronik) (Treede et al., 2015)	Nitinol	Porcine pericardium	TF	29	23-26	18	Clinical
	Hydra (Vascular Innovations) (Srimahachota, Buddhari, & Sondergaard, 2016)	Nitinol	Bovine pericardium	TF	22, 26, 30	18-20, 20-24, 24-26	18	FIM
	NIH/National Heart Lung and Blood Institute (Mazilu, Li, Kocaturk, & Horvath, 2012)	Nitinol	Various commercial/PET	TA	26	TBD	TBD	Animal
	Cleveland Clinic (E. Young et al., 2011)	Nitinol	Bovine pericardium	TA	26	TBD	TBD	TBD
	Vienna Aortic Valve Self-Expanding (Products and Features) (Agreli, 2017)	TBD	TBD	TBD	TBD	TBD	TBD	TBD

Appendix Table A-3. Self-expanding bioprosthetic valves with orientation

	Device name	**Stent**	**Leaflet/ (skirt) material**	**Access Routes**	**Valve diam. (mm)**	**Aortic ann. diam. (mm)**	**Catheter size (Fr)**	**Status**
	ACURATE™ (Symetis) (Kempfert et al., 2011)	Nitinol	Porcine root/ (TBD)	TA /TF	23	21-23	18	CE Mark
			Porcine pericardium/ (porcine pericard) (Mollmann et al., 2013)		25	23-25		
					27	25-27		
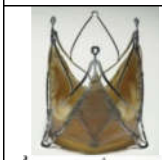 	JenaValve™ (JenaValve Technologies) (Kempfert et al., 2011; Rudolph & Baldus, 2013)	Nitinol	Porcine root/(porcine pericard) (TA)	TA,TF	19	19-21	27/18	CE Mark (Treede et al., 2012)
					23	21-23		
			Porcine pericardium (TF) / (Porcine pericard)		25	23-25		
					27	25-27		

	Engager™ (Medtronic) (Falk et al., 2011)	Nitinol	Bovine Pericardium/ (polyester)	TA	23,26	TBD	26	CE Mark
	J-Valve (Jiecheng Medical Technology; possibly linked to Cardiovantage or Causper)	Nitinol	Porcine root/(?PET skirt)	TA	23	TBD	TBD	Clinical (Zhu et al., 2015)
	Tongji University Valve (Cai et al., 2013)	Nitinol	Decell porcine pericard/ (N/A)	TBD	TBD	TBD	TBD	Animal

Appendix Table A-4. Alternative valve technologies

	Device name	Stent	Leaflet/ (skirt) material	Access Routes	Valve diam. (mm)	Aortic ann. diam. (mm)	Catheter size (Fr)	Status
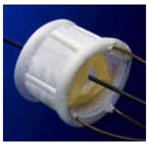	Direct Flow™ (Direct Flow Medical, Santa Rosa) (Kovac, Baron, Al-Jilaihawi, & Chin, 2017)	PET, inflatable	Bovine pericardium/ (Polyester)	TF	23, 25, 27	19-36	18	CE Mark
	PercValve (Advanced Bioprosthetic Surfaces) (Wiegerinck et al., 2016)	e-nitinol	e-nitinol	TA,TF	NR	NR	10	TBD
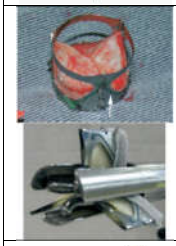	Aortx (Hansen Medical Inc, formerly Aortx Inc, formerly CardiacMD, perhaps incl. REVA Medical) (Wiegerinck et al., 2016)	Nitinol	Pericardial	TA,TF	N/A	N/A	18	CE Mark
	Vanguard II (ValveX change) (Bourantas et al., 2012; Bourantas & Serruys, 2014)	Nitinol	Bovine pericardium	TA, surgical	TBD	TBD	TBD	CE Mark (Wiegerinck et al., 2016)

Appendix Table A-5. Adjunct Devices

	Device name	Stent	Leaflet/ (skirt) material	Access Routes	Valve diam. (mm)	Aortic ann. diam. (mm)	Catheter size (Fr)	Status
	Edwards Helio™ aortic dock (Barbanti, Ye, Pasupati, El-Gamel, & Webb, 2013)	Nitinol	N/A	TF	25 (for 29mm Sapien)	TBD	16	Clinical

	M-Valve mitral dock (Boston Scientific) (Piazza, 2016; Regueiro, Granada, Dagenais, & Rodés-Cabau, 2017)	Nitinol	N/A	TA	TBD	TBD	TBD	Clinical
	Endoluminal Sciences (Fanning, Platts, Walters, & Fraser, 2013)	N/A	Expandable skirt with hydrogels	TBD	TBD	TBD	TBD	TBD

Appendix Table A-6. Polymer transcatheter valves

	Device name	**Stent**	**Leaflet/ (skirt) material**	**Access Routes**	**Valve diam. (mm)**	**Aortic ann. diam. (mm)**	**Catheter size (Fr)**	**Status**
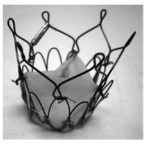	PHV (Stony Brook) (Claiborne, Bluestein, & Schoephoerster, 2009)	Nitinol	Dacron-reinforced SIBS	TBD	19	TBD	<24	Develop-ment
	Polynova™ (Cardio-vascular, Inc.) (Bianchi et al., 2015)	Nitonol	xSIBS	TBD	TBD	TBD	TBD	Develop-ment
 	Triskele™ UCL (Bezuidenhout et al., 2015; Rahmani et al., 2016)	Nitinol	POSS-PCU, (POSS-PCU)	TF	23, 26, 29	TBD	TBD	Develop-ment
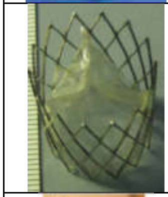	Lutter (Attmann, Steinseifer, Cremer, & Lutter, 2006; Metzner et al., 2010)	Nitinol	Poly-urethane	TF	TBD	TBD	14F	TBD
	University of Iowa (V. Kumar, 2012)	Nitinol	Cellulose and cellulose-silicone composite	TBD	TBD	TBD	TBD	TBD
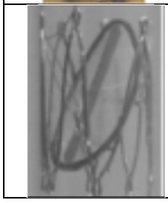	Sochman (Sochman, Peregrin, Pavcnik, Timmermans, & Rosch, 2000)	Nitinol	Poly-urethane tilting disc	TBD	TBD	TBD	TBD	TBD

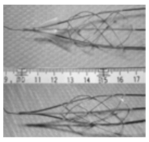	Hashimoto (Tottori University) (Hashimoto et al., 2008)	Nitinol	Desmorac 4125 (Poly-urethane)	TF	16	TBD	TBD	TBD
	Zhang et al. (Changhai Hospital) (Zhang et al., 2014)	Co-Cr	PC-coated ePTFE	Right ventricle	20, 23	TBD	22F	Animal
	Colorado State University (Kheradvar, Groves, Dasi, et al., 2015)	Nitinol	HA/LLDPE	TBD	TBD	TBD	TBD	TBD
	Politecnico di Milano/ Helmholtz Instuitute (Wu et al., 2016)	Nitinol	Poly-urethane	TBD	TBD	TBD	TBD	Develo-pment
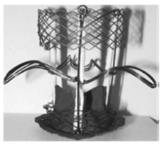	Universite de Haute Alsace (Marchand, Heim, & Durand, 2010b)	Nitinol	Fabric	TBD	TBD	TBD	TBD	Develop-ment

Appendix Table A-7. Nitinol valves for minimally invasive surgery

	Device name	Stent	Leaflet/ (skirt) material	Access Routes	Valve diam. (mm)	Aortic ann. diam. (mm)	Catheter size (Fr)	Status
	ATS 3F Enable 6000™ (ATS Medical) (Martens et al., 2011)	Nitinol, surgical	Equine, (PET)	Mini-mally invasive	TBD	TBD	TBD	Clinical
	Entrata ATS 3F™ (ATS Medical) (Jamieson et al., 2006)	Stainless steel	Equine (Pericardial)	TA	19-29	TBD	TBD	TBD
	Edwards Intuity™ (Edwards Lifesciences) (Kocher et al., 2013)	Nitinol	Bovine pericardium, (PET)	Mini-mally invasive	19, 21, 23, 25, 27	TBD	TBD	CE marked
	Perceval™ S (Sorin group) (Stalder et al., 2010)	Nitinol	Bovine pericardium	TA/ Open Surgical	21,23	18-20,21-22	TBD (on 12mm sheath)	TBD

Appendix Table A-8. Self-expanding pulmonary, tricuspid, caval and mitral valves

	Device name	Stent	Leaflet/ (skirt) material	Access Routes	Valve diam. (mm)	Ann. diam. (mm)	Catheter size (Fr)	Status
	Changhai valve (Bai et al., 2010)	Nitinol	Porcine	TBD	TBD	TBD	TBD	TBD

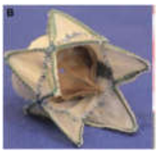	"Double-crown" self-expanding stent (Masson & Webb, 2009)	Nitinol	Porcine root	TBD	TBD	TBD	TBD	TBD
	Melody™ (Medtronic) (Zahn, Hellenbrand, Lock, & McElhinney, 2009)	Platinum/Gold	Bovine jugular vein	Trans-venous	18, 20, 22	TBD	22	CE Mark
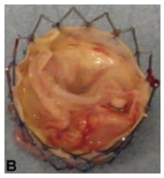	Tissue-engineered pulmonary valve (Lutter et al., 2010)	Nitinol	Porcine pulmonary valve/ (small intestinal submucosa), tissue engineered	Trans-venous	TBD	TBD	20	Animal studies
	CardiAQ™ (CardiAQ Valve Technologies) (De Backer et al., 2014; Mylotte & Piazza, 2015)	Nitinol	Bovine pericardium	Trans-femoral/ Trans-apical	30	TBD	32F	Clinical
	Tiara™ (Neovasc/ Boston Scientific) (De Backer et al., 2014)	Nitinol	Bovine pericardium/(PET)	Trans-apical	35,40	TBD	32F	Clinical Trials
	Tendyne (Tendyne Inc/Abbott Vascular) (De Backer et al., 2014; Piazza, 2016)	Nitinol	Porcine pericardium/(PET)	Trans-apical	30-43/ 34-50	TBD	30F	Clinical
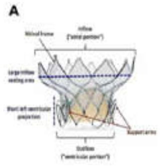	Medtronic TMVR™ (Medtronic)	Nitinol	TBD	Tran-atrial/TF	TBD	TBD	TBD	Preclinical
	FORTIS™ (Edwards) (De Backer et al., 2014)	Nitinol	Bovine pericardium/ (PET)	TA/TF	TBD	TBD	TBD	Clinical
	Cardiovalve (Valtech Cardio) (De Backer et al., 2014)	Nitinol	TBD	Trans-femoral	TBD	TBD	26F	Preclinical
	HighLife (Highlife/Sorin) (De Backer et al., 2014; Piazza, 2016)	Nitinol	Pericardium	Trans-atrial	TBD	TBD	TBD	Clinical (Regueiro et al., 2017)

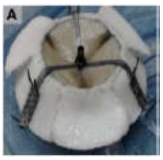	Endovalve (Micro Interventional Devices) (De Backer et al., 2014)	Nitinol	TBD	Trans-apical	TBD	TBD	TBD	Preclinical
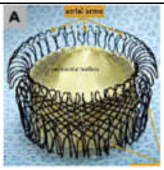	Gorman (De Backer et al., 2014)	Nitinol	TBD	Trans-atrial	TBD	TBD	30F	Preclinical
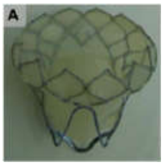	MitrAssist (MitrAssist Medical) (De Backer et al., 2014)	Nitinol	Pericardium	Trans-aortic	TBD	TBD	18F	Preclinical
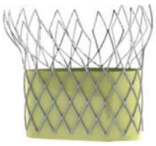	MiVar (Trinity College Dublin) (Preston-Maher, Torii, & Burriesci, 2015)	Nitinol	Pericardium	TBD	TBD	TBD	TBD	Preclinical
	NaviGate (Navigate Cardiac Structures) (Preston-Maher et al., 2015)	Co-Cr (?TBD)	Pericardium	TA/ Trans-septal/ Trans-atrial	TBD	TBD	TBD	Clinical
	Intrepid (Twelve Inc/Foundry TMVR/ Medtronic) (Regueiro et al., 2017)	Nitinol	Bovine pericardium/(PET)	TA	43, 46, 50 outer	TBD	TBD	Clinical
	MitraSeal (Avalon) Canine MVRD (Preston-Maher et al., 2015)	Nitinol	TBD	Trans-apical	TBD	TBD	TBD	Preclinical
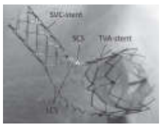	Tricuspid Valve (Pott et al., 2015)	Nitinol	Porcine pericardium	TBD	TBD	TBD	TBD	Preclinical
	UCL Mitral Valve (Bozkurt, Preston-Maher, Torii, & Burriesci, 2017)	Nitinol	Bovine Pericardium (polyester)	TBD	TBD	TBD	TBD	Preclinical
	Vienna Pulmonary Valve (Products and Features) (Agreli, 2017)	TBD	TBD	TBD	TBD	TBD	TBD	TBD
	Tricvalve (Products and Features) (Agreli, 2017)	TBD	TBD	TBD	TBD	TBD	TBD	TBD

	Vienna Mitral Valve (Products and Features) (Agreli, 2017)	TBD	TBD	TBD	30x40, 33x45 mm	TBD	TBD	TBD
	Braille Biomedica (Piazza, 2016)	TBD	TBD	TBD	TBD	TBD	TBD	TBD
	Cephea Valve Technologies (Piazza, 2016)	TBD	TBD	TBD	TBD	TBD	TBD	TBD
	Direct Flow (Piazza, 2016)	TBD	TBD	TBD	TBD	TBD	TBD	TBD
	PermaValve MID (Piazza, 2016)	TBD	TBD	TBD	TBD	TBD	TBD	TBD
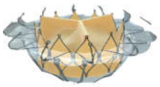	Sinomed (Piazza, 2016)	TBD	TBD	TBD	TBD	TBD	TBD	TBD
	Saturn TMVR (HT Consultant) (Piazza, 2016)	TBD	TBD	TBD	TBD	TBD	TBD	TBD
	Daidalos (Piazza, 2016)	TBD	TBD	TBD	TBD	TBD	TBD	TBD
	Caisson TMVR (Piazza, 2016; Regueiro et al., 2017)	Nitinol	Porcine pericardium	TF	TBD	TBD	31F	Clinical
	MitraCath (Emory) MVRD (Padala & Sarin)	TBD	TBD	TBD	TBD	TBD	TBD	Develop-ment

Appendix Table A-9. Valves with minimal information

	Device name	Stent	Leaflet/ (skirt) material	Access Routes	Valve diam. (mm)	Aortic ann. diam. (mm)	Catheter size (Fr)	Status
TBD	Padala et al. (MedShape/ Emory)	TBD	PEEK-based	TBD	TBD	TBD	TBD	TBD
TBD	Tresillo (Transcatheter Technologies)	Nitinol	Bovine pericardium	Trans-septal	TBD	TBD	TBD	TBD
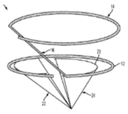	Maestro (Mitralix) MVRD (Alfieri, 2015; Piazza, 2016)	TBD	TBD	TBD	TBD	TBD	TBD	Preclinical

TBD	Medi-Line aortic valve S.A (BioWin)	TBD	TBD	TA	TBD	TBD	TBD	TBD
TBD	Mitricares (Vizient, 2017)	TBD	TBD	TBD	TBD	TBD	TBD	Develop-ment
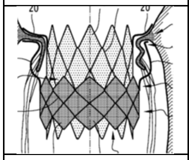	Laboratoirs Invalv (Alfieri, 2015; Righini, 2017)	TBD	TBD	TBD	TBD	TBD	TBD	Develop-ment
TBD	VueKlar MR-Enhancing Valve	TBD	TBD	TBD	TBD	TBD	TBD	TBD
TBD	UMC Utrecht Holding BV/DSM	TBD	TBD	TBD	TBD	TBD	TBD	TBD
TBD	MitraHeal (Piazza, 2016)	TBD	TBD	TBD	TBD	TBD	TBD	TBD
TBD	Mitrassist (Piazza, 2016)	TBD	TBD	TBD	TBD	TBD	TBD	Preclinical
TBD	Mitraltech (Piazza, 2016)	TBD	TBD	TBD	TBD	TBD	TBD	TBD
TBD	Mehr Medical (Piazza, 2016)	TBD	TBD	TBD	TBD	TBD	TBD	TBD
TBD	Nakostech (Piazza, 2016)	TBD	TBD	TBD	TBD	TBD	TBD	TBD
TBD	St George Atlas (Piazza, 2016)	TBD	TBD	TBD	TBD	TBD	TBD	TBD

Appendix B. Characterisation of stents

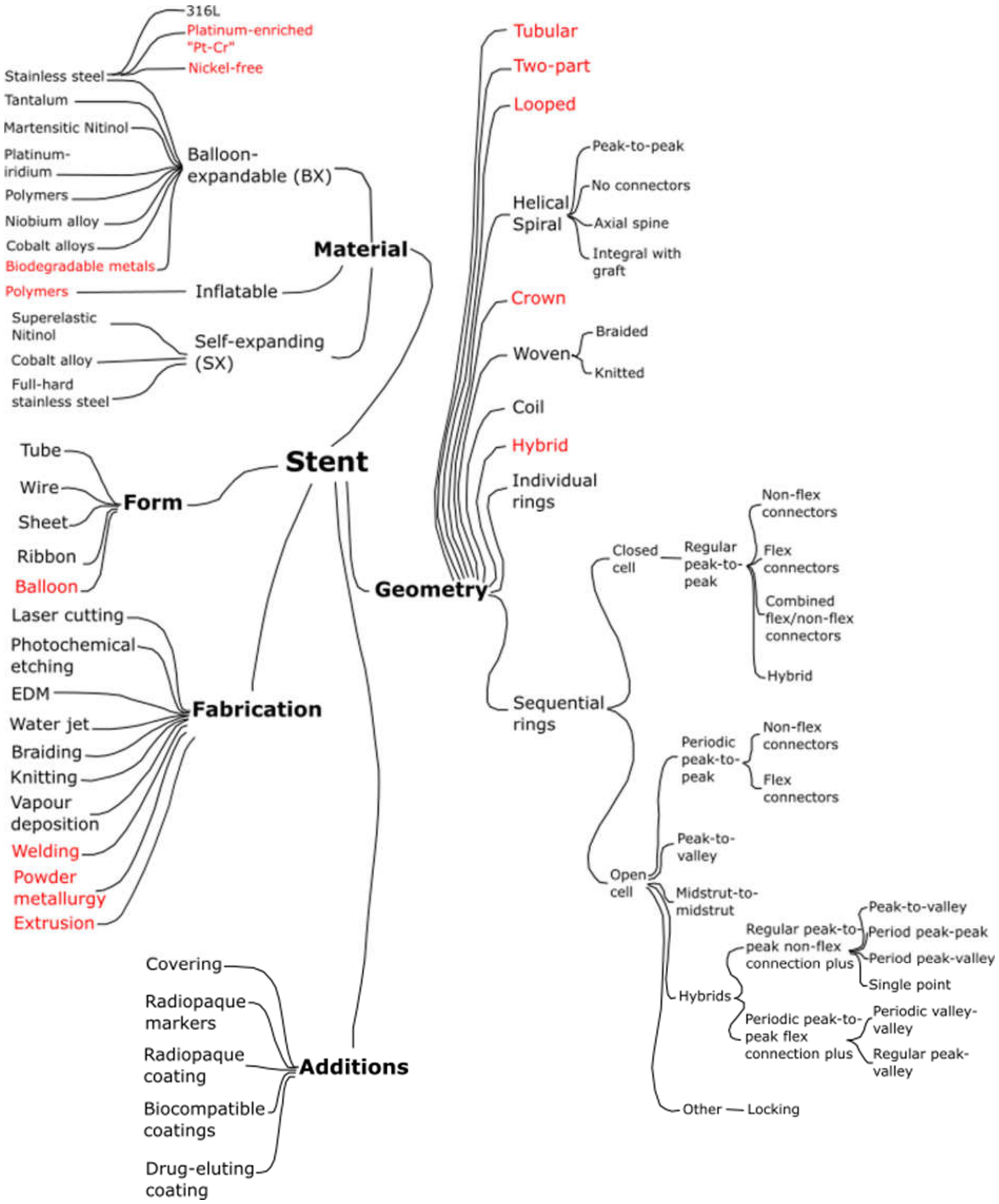

Appendix Figure B-1. Categorisation of stents based on form, material, geometry and method of fabrication

Adapted from Stoeckel et al. (2002)

Appendix C. Mesh refinement

Introduction

The accuracy of a finite element solution is linked to the size of the mesh used. As the element size approaches zero, the accuracy of the solution to the finite element equations approaches the exact solution. Finer meshes require additional computational cost, so a mesh refinement study is required to establish the trade-off between the accuracy of the approximation and the computational resources. Mesh refinement studies were therefore performed to determine the level of refinement required to accurately represent stress, strains and displacements in a typical valve stent at reasonable computational cost. Studies were performed on a portion of a Control stent.

Methods

Two struts were used to model a representative portion of the Control stent. Although axial and longitudinal symmetry were used to simplify the model, two struts were included to ensure there were no erroneous edge effects associated with the symmetry assumptions. An image of the struts is provided in Appendix Figure C-1, which illustrates where symmetry boundary conditions were applied, defines major parts of the stent, and shows where the geometry was typically partitioned. Semi-rigid cylinders, shown in Appendix Figure C-2, were used to crimp and expand the stent. The expansion cylinder was meshed using 63 linear quadrilateral (S4R) shell elements, while the crimping cylinder was compressed using 364 elements.

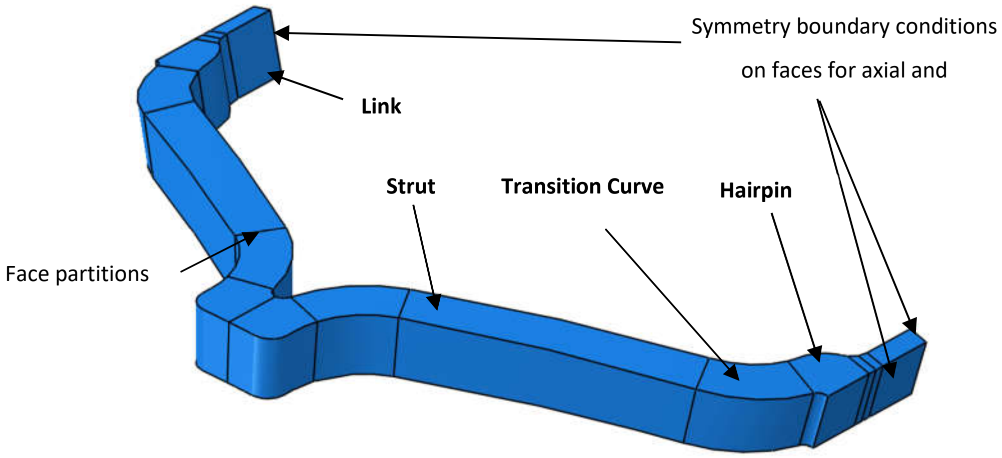

Appendix Figure C-1. Control stent struts used for mesh refinement study

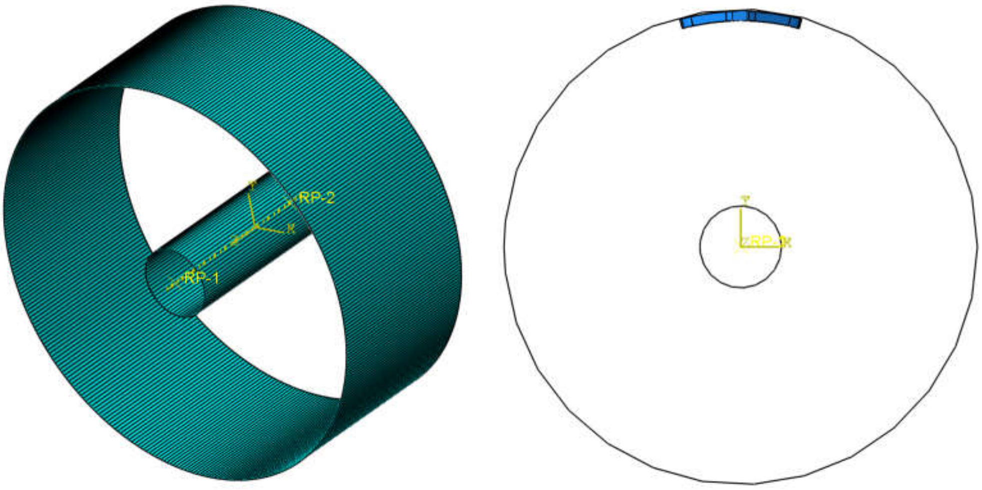

Appendix Figure C-2. Crimping and expansion cylinders

Stents were subjected to crimping, relaxation, expansion, relaxation and pressurisation steps similar to those described in Chapter 4; similarly contact definitions and material definitions have been described and are not repeated here. Stent geometry was partitioned to demarcate distinct parts of the stent, defined here as the *strut*, which is the straight or near-straight portion of the stent, the *hairpin*, which arch-shaped end of the struts, the *transition curve*, which is the curved area joining the strut to the hairpin, and the *link*, which joins two rings of struts to each other. *Thickness* corresponds to tubing wall thickness, while *width* and *length* refer to measurements on the outer surface of the stent.

Four different levels of mesh refinement were modelled, labelled Coarse, Medium, Fine and Superfine. Stents were meshed using 8-noded linear brick elements with reduced integration and hourglass control (C3D8R). Each level of refinement used different numbers of elements along the strut thickness, strut width, strut length, transition curve length, hairpin inside radius length, hairpin outside radius length, hairpin depth and link width. These are illustrated in Appendix Table C-1. For all parameters elements were evenly distributed, except for strut length, which was given a double bias of 4 to ensure areas with most bending had a more refined mesh. Strut width typically had more elements than strut thickness since bending in a circumferential direction dominates.

Appendix Table C-1. Number of elements used in mesh refinement studies

	Strut			**Hairpin**			**Curve length**	**Link width**	**# Elements**
Mesh	**Thick**	**Width**	**Length***	**Inside**	**Outside**	**Depth**			
Coarse	2	2	6	2	4	2	4	1	184
Medium	4	5	12	4	8	7	8	2	1888
Fine	8	10	24	8	16	14	16	4	15160
Superfine	16	20	48	16	32	28	32	8	118784

* Elements along strut length were given a double bias of 4 so that mesh was finer at each end.

The mesh for each level of mesh refinement is shown in Appendix Figure C-3.

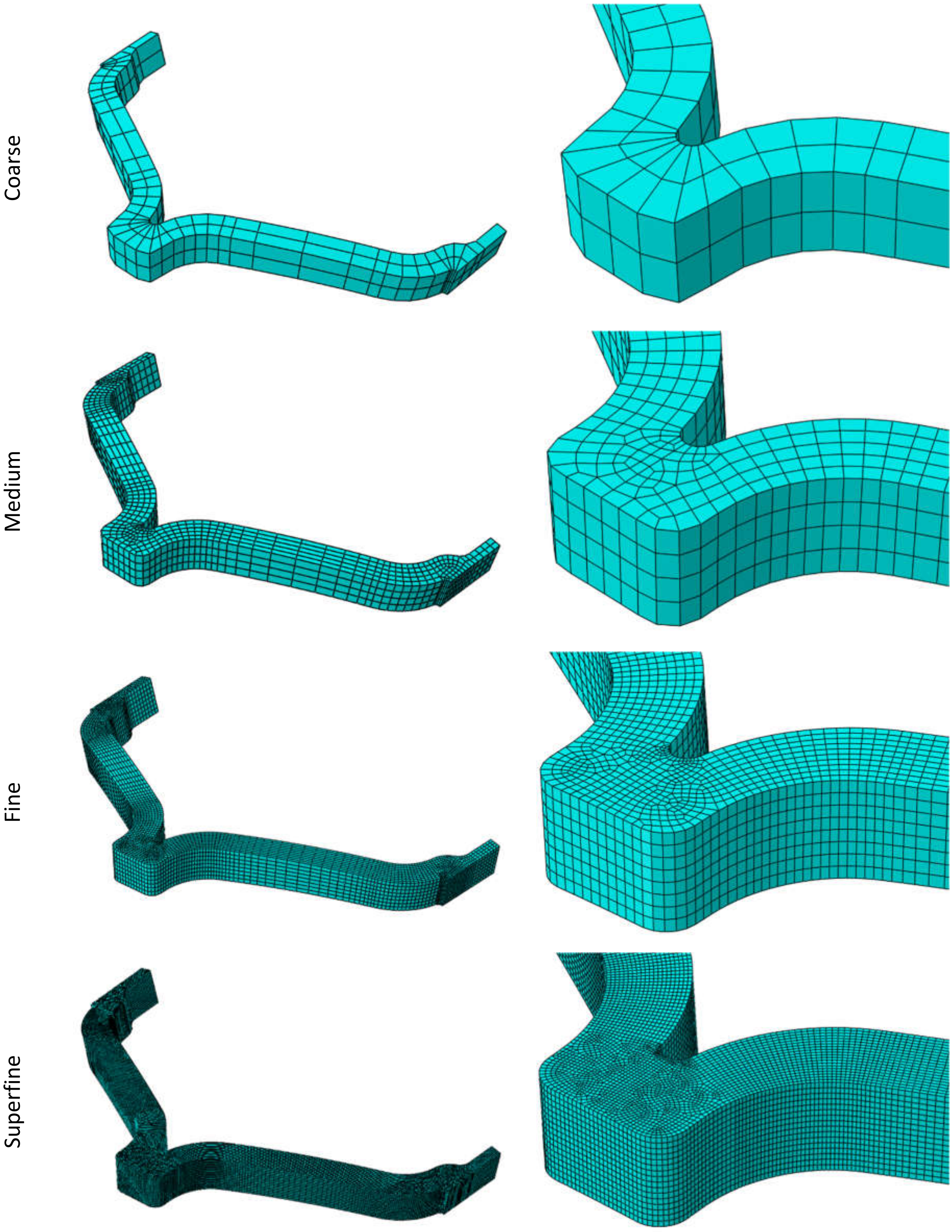

Appendix Figure C-3. Four levels of mesh refinement

Results

The critical Von Mises Stress at the end of the expansion step, the critical Maximum Principle Stress at the end of the expansion step and at the end of the relaxation step, and the maximum magnitude of displacement and the end of expansion are shown in Appendix Figure C-4, normalised with respect to the values of the Superfine model for each parameter. The computational cost is reflected in the total number of variables for each model, shown in Appendix Figure C-5.

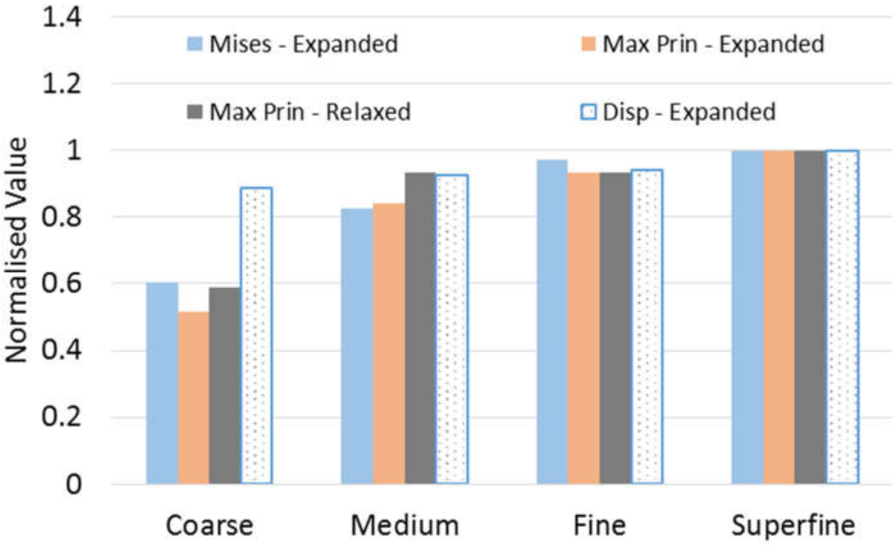

Appendix Figure C-4. Critical nodal Von Mises Stress, Critical Maximum Principle Stress and Displacement Magnitude for each level of mesh refinement, normalised by the Superfine value

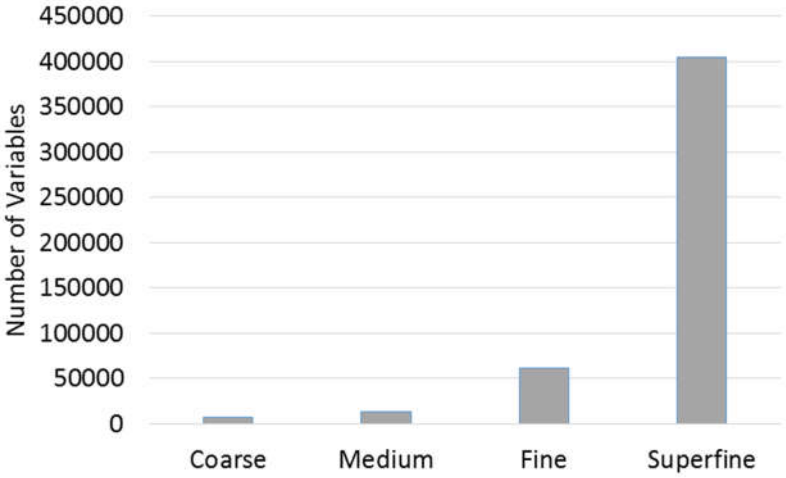

Appendix Figure C-5. Total number of variables for each level of mesh refinement

The Von Mises Stress in the stent, as determined with a Medium mesh and a Superfine mesh are compared in the contour plot in Appendix Figure C-6. The magnitude of Von Mises Stress are higher in the Superfine mesh model, but stress distribution is similar for both levels of meshing.

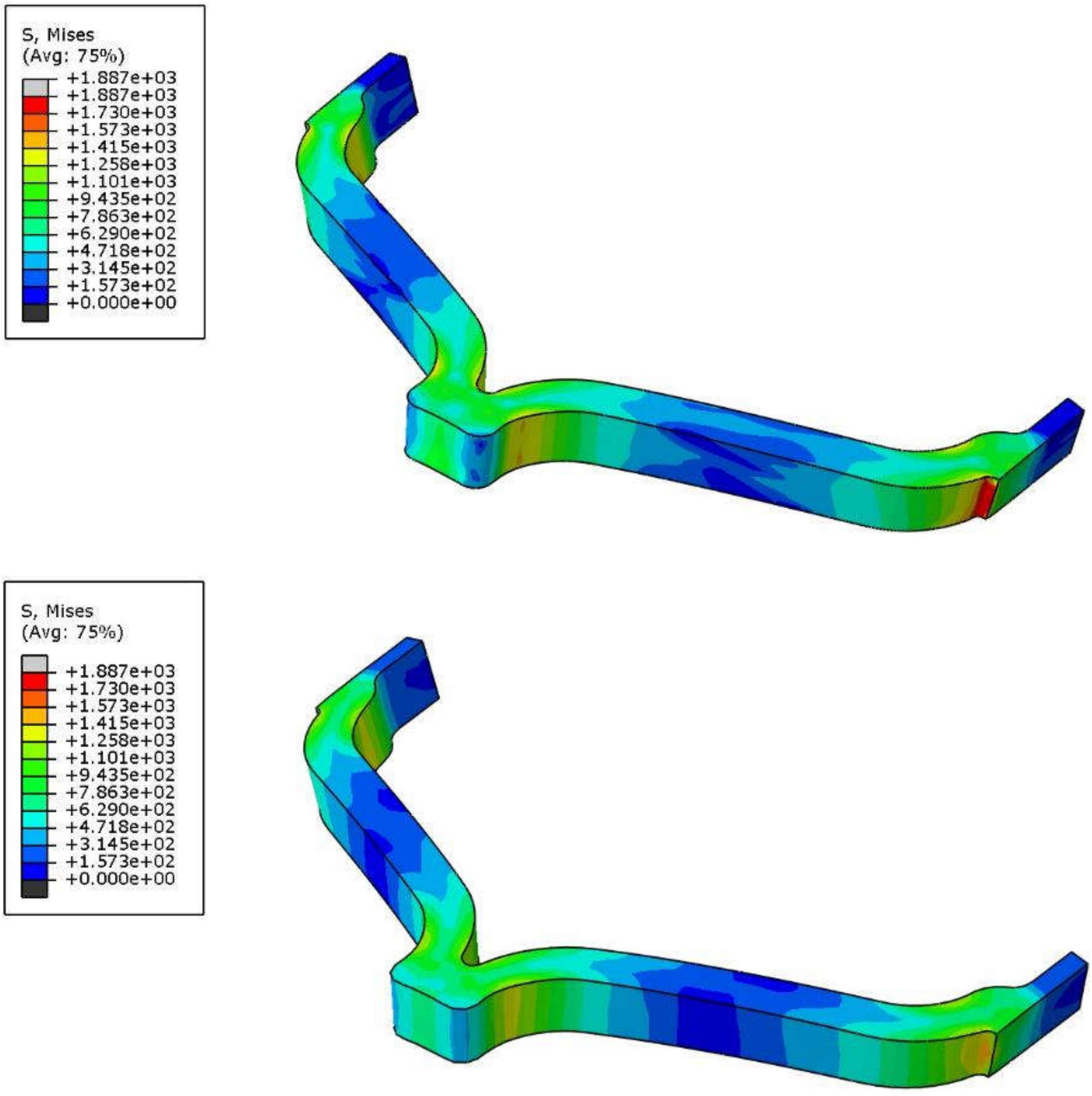

Appendix Figure C-6. Contour plots of Von Mises stress for Superfine (top) and Medium (bottom) meshes

Discussion

Stresses and displacements are under-estimated for coarse, medium and fine meshes.

A coarse mesh predicts maximum displacement to within 89% of the value for the Superfine mesh, but stresses are less than 60% of the Superfine values.

A medium mesh offered an acceptable compromise. The maximum displacement was 93% of the accurate displacement, which is an error of only 43 µm. Although the crucial Von Mises and Maximum Principle Stresses at the end of expansion were 83% and 84% of the accurate values, respectively, the residual Maximum Principle Stress after relaxation was 93% of the accurate value. This is considered more important because of the implications for fatigue analysis.

A fine mesh offered a small improvement in accuracy for Von Mises and Maximum Principle Stresses at the end of expansion, but offered no significant advantage for residual (relaxed) Maximum Principle Stress or peak displacement, despite a five-fold increase in the number of variables compared to the Medium mesh (and ten-fold compared to the coarse mesh). For the superfine mesh the cost is extremely high, with 63 times the number of variables compared to the coarse mesh. Incompatible mode elements are frequently used for FEA modelling of stents. An attempt was made to include incompatible mode elements (C3D8I) in the mesh refinement study, but numerical instabilities were seen consistently across all levels of refinement. This is illustrated in Appendix Figure C-7, which shows a singularity in the Maximum Principle Stress at the end of the crimping step. The instability is also evident (see Appendix Figure C-8) when plotting the stress at the node in the bottom right corner of Appendix Figure C-7. This is discussed further in the body of this report.

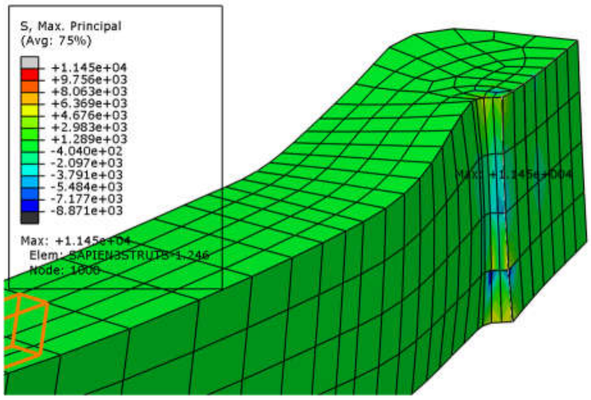

Appendix Figure C-7. Contour plot (sectioned) of Maximum Principle Stress at the end of the crimping step, showing singularities with stress up to 11450 MPa for incompatible mode elements

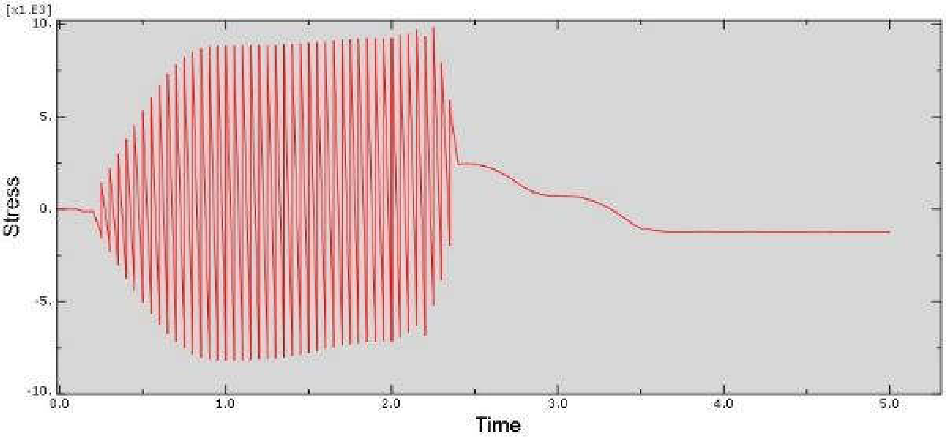

Appendix Figure C-8. Plot of nodal Maximum Principle Stress versus time (1s per step), showing instability in incompatible mode elements

Appendix D. Additional manufacturing information

Laser Cutting

Stent tube rotation eccentricity was reduced by measuring using a dial gauge, as shown in Appendix Figure D-1) and adjusting tube position accordingly.

Appendix Figure D-1. Method of measuring eccentricity in tube rotation

Kerf width was measured by making axial and circumferential cuts in the tubing (Appendix Figure D-2), photographing under a calibrated metallurgical microscope and measuring digitally (kerf width measurements are shown in Appendix Table D-1).

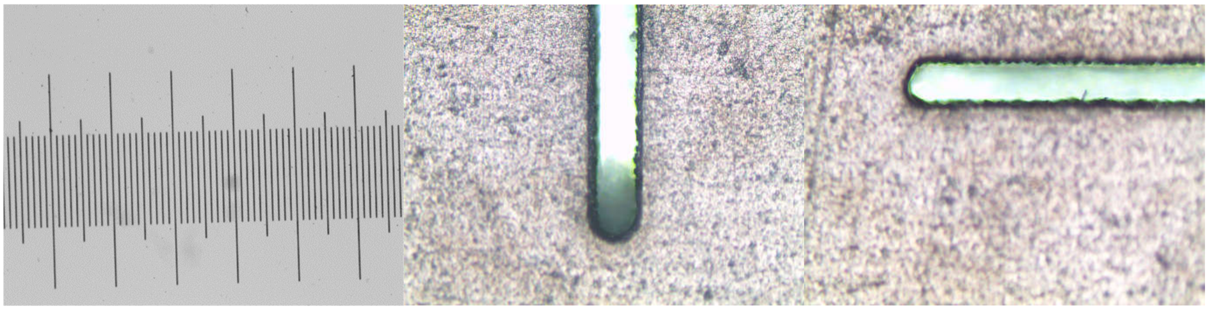

Appendix Figure D-2. Kerf width measurement – example images

Appendix Table D-1. Kerf Width (in µm)

Slot Direction	Cut Number					Mean
	1	2	3	4	5	
Longitudinal	60.0	60.6	56.9	54.7	53.8	57 ± 3
Circumferential	56.4	58.5	60.6			59 ± 2

Acid Descaling

Acid descaling of stainless steels, nickel-cobalt or cobalt-chromium alloys is frequently performed using mixtures of nitric (5-25%) and hydrofluoric (1-3%) acids (Sojitra et al., 2009). Hydrofluoric acid

(HF) is a strong reducing agent that reduces the oxide scale present, but also reduces the protective oxide layer on the base material of the stent. Nitric acid on the other hand is an oxidising agent and serves to preserve the protective oxide layer and therefore effectively inhibits the attack by the hydrofluoric acid on the base metal (AISI, 1988). An ideal pickling process removes oxide scale while preserving the base metal.

Stents were observed to have light oxide scale on the outside surfaces, heavy oxide scale on the laser-cut surfaces, and a build-up of oxide-rich scale and dross on the inside surface, even after removing burrs mechanically. Initial attempts to perform pickling using different concentrations of hydrofluoric acid (0.5% to 3%) and nitric acid (5% to 20%) were not considered optimal. High concentrations of hydrofluoric acid (up to 3%) tended to attack the base material aggressively, while lower concentrations tended to be ineffective at removing oxides even after several hours of pickling. Two changes were made to the HF/Nitric acid mixtures to improve pickling. Firstly the HF was replaced by an aqueous ammonium bifluoride solution (a common alternative to HF in pickling solutions) in order to allow safer storage and mixing of chemicals. Secondly, since sulphuric acid has been shown to be an effective first step in multi-step pickling processes (Homjabok, Permpoon, & Lothongkum, 2010), sulphuric acid was also added to the solution.

A mixture of sulphuric acid, nitric acid, ammonium bifluoride and deionised water was therefore used for pickling, in the mass ratio 22:7:15:55. This solution proved to be effective at removing oxides without aggressive base metal attack.

Polishing

Several different electrolytes were identified from academic and commercial literature for cobalt chromium and chromium-rich alloys; these are shown in Appendix Table D-2. Informal exploratory tests were conducted on short diamond-mesh rings[7] (to simulate a stent) using the electrolytes and parameters described in the table, except for electrolytes consisting of perchloric acid (due to safety concerns) or those requiring active cooling (to simplify the process). Although all electrolytes polished the rings to some degree, the electrolyte used by Surmann and Huser (1998) gave the best surface appearance by visual estimation and was therefore used for stent polishing; this electrolyte consisted of 10% Sulphuric Acid, 5% Hydrochloric acid and 85% Glycol by volume.

---

[7] Initial electropolishing experiments were not exhaustive as electrolyte comparison was not a goal of this thesis project; they were merely used to select an effective electrolyte to produce stents with good surface quality. Unless specifically stated otherwise in the references provided, temperatures of 70°C and currents of 3A were used.

Appendix Table D-2. Electrolytes used by other investigators

Investigators	**Material**	**Electrolyte**	**Temperature, parameters**
Aihara (2009)	L605	Phosphoric acid (85%, 50% or 15%)	0°C to 45°C
Surmann and Huser (1998)	Co-Cr-Mn	10% sulphuric acid, 5% hydrochloric acid and 85% ethylene glycol	48°C
Fischione-Instruments	Cobalt-Nickel alloys	25% perchloric acid and 75% acetic acid	30°C, 25V
Piesslinger-Schweiger and Bohme (2011)	Cobalt and Cobalt Alloys	55% methanesulfonic acid and 45% glycolic acid	40°C to 70°C
Ishmaku and Han (2004)	MP35N discs	19% sulphuric acid, 76% methanol and 5% phosphoric acid	3°C to 5°C, 28-32mA
Shih, Shih, Chou, Lin, and Su (2006)	MP35N wire	80% phosphoric acid and 20% glycerine	65°C, 10Acm^{-2}, 30s
Lee and Li (2003)	316L	Sulphuric acid, phosphoric acid, glycerine and deionised water.	60°C
Kosmac (2010)	Stainless steels	50% sulphuric acid and 50% orthophosphoric acid	40°C to 75°C, 5Adm^{-2} to 5Adm^{-2}
Kang and Lee [17]	316L	34% phosphoric acid, 47% glycerol and 19% water (by weight)	3 min. at 1 Acm^{-2}
Haïdopoulos, Turgeon, Sarra-Bournet, Laroche, and Mantovani (2006)	316	35% phosphoric acid, 50% glycerol, and 15% water (v/v)	0.75 A.cm ^{1}, 20°C to 90°C

Appendix E. Stent measurements – additional information

Measurement of Control Stent

Stent measurement locations for the Control stent are provided in Appendix Figure E-1, and mean (± standard deviations) of measurements for this stent are provided in Appendix Table E-1.

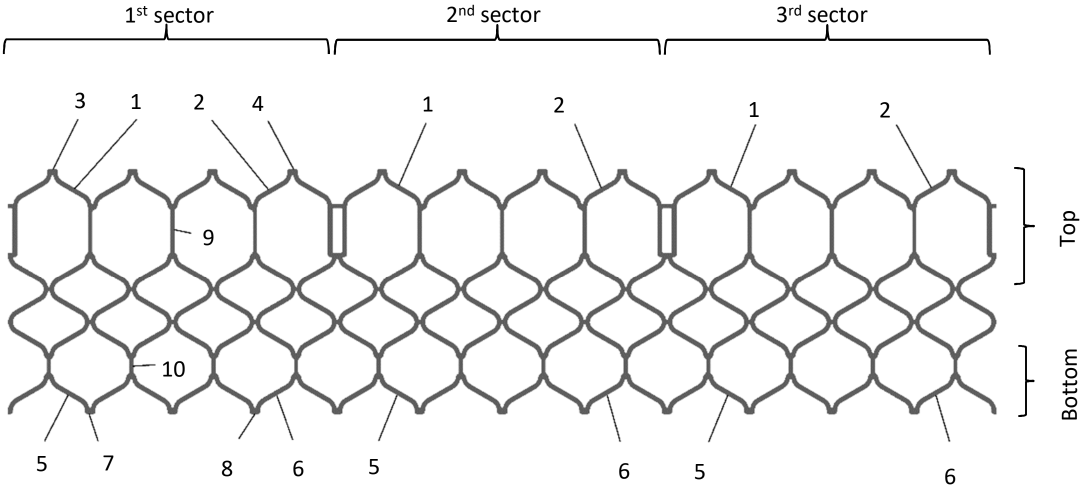

Appendix Figure E-1. Control stent measurement points

Appendix Table E-1. Mean Control stent measurements

Region	Specification	Value (µm)	Diff (µm)	% Diff
Strut	350 µm	350 ± 10	0	0.0
Top strut (1,2)		349 ± 9	1	0.2
Bottom strut (5,6)		351 ± 11	-1	-0.2
Strut first sector		352 ± 11	-2	-0.7
Strut second sector		349 ± 12	1	0.3
Strut third sector		348 ± 7	2	0.5
Hairpin	450 µm	462 ± 11	-12	-2.6
Top hairpin (3,4)		459 ± 13	-9	-2.0
Bottom hairpin (7,8)		465 ± 9	-15	-3.3
Vertical long member (9)	300 µm	298 ± 6	2	0.7
Vertical short member (10)	300 µm	304 ± 4	-4	-1.3
Wall thickness	470 µm	465 ± 5	5	1.0

Individual Stent Measurements for All Designs

Individual measurements performed on three of each design, including the Control stent, are shown in Appendix Table E-2. Each measurement is given a sector number and a member number, e.g. #2-1 refers to the second sector and the strut numbered “1” within the sector. Location of these member numbers may be found in Figure 7-23, Figure 7-24 and Appendix Table E-1.

Appendix Table E-2. Individual stent measurements (in µm)

Control			
Stent	**1**	**2**	**3**
#1-1	354	358	351
#1-2	332	365	340
#1-3	464	467	457
#1-4	434	471	461
#1-5	361	363	344
#1-6	352	366	344
#1-7	467	467	452
#1-8	467	477	458
#1-9	292	304	298
#1-10	307	299	305
#2-1	352	358	359
#2-2	333	360	343
#2-5	336	359	346
#2-6	349	364	328
#3-1	339	348	352
#3-2	352	348	342
#3-5	361	348	343
#3-6	354	353	339
Thick	466	460	470

Design 1			
Stent	**1**	**2**	**3**
#1-1	555	547	549
#1-2	232	244	250
#1-3	247	243	260
#1-4	252	244	261
#1-5	100	100	105
#1-6	268	266	269
#1-7	267	251	255
#1-8	227	240	233
#1-9	215	195	212
#1-10	323	323	334
#1-11	334	330	339
#1-12	328	324	333
#1-13	329	323	336
#2-2	244	247	254
#2-3	236	252	244
#2-7	263	263	262
#2-8	231	239	236
#3-2	252	235	250
#3-3	259	242	249
#3-7	266	256	265
#3-8	221	233	241
Thick	469	457	471

Design 2			
Stent	**1**	**2**	**3**
#1-1	580	597	593
#1-2	280	272	275
#1-3	283	266	276
#1-4	302	297	301
#1-5	272	296	281
#1-6	287	274	293
#1-7	284	293	285
#1-8	296	294	300
#1-9	300	289	298
#1-10	300	294	299
#1-11	430	425	434
#2-2	275	277	284
#2-3	276	274	275
#2-5	276	269	280
#2-6	294	287	298
#3-2	282	-	283
#3-3	284	279	281
#3-5	273	266	288
#3-6	300	289	298
Thick	454	458	443

Measurement Definitions

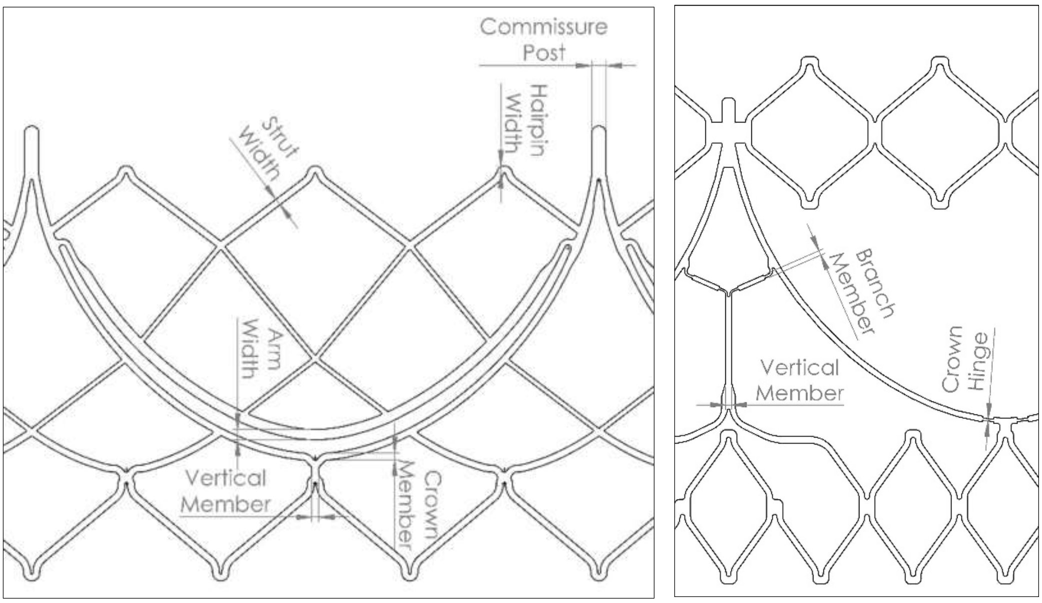

Appendix Figure E-2. Measurement Definitions

Measurement definitions are shown in Appendix Figure E-2. Typical microscopy images used for the measurement of stent members is shown in Appendix Figure E-3.

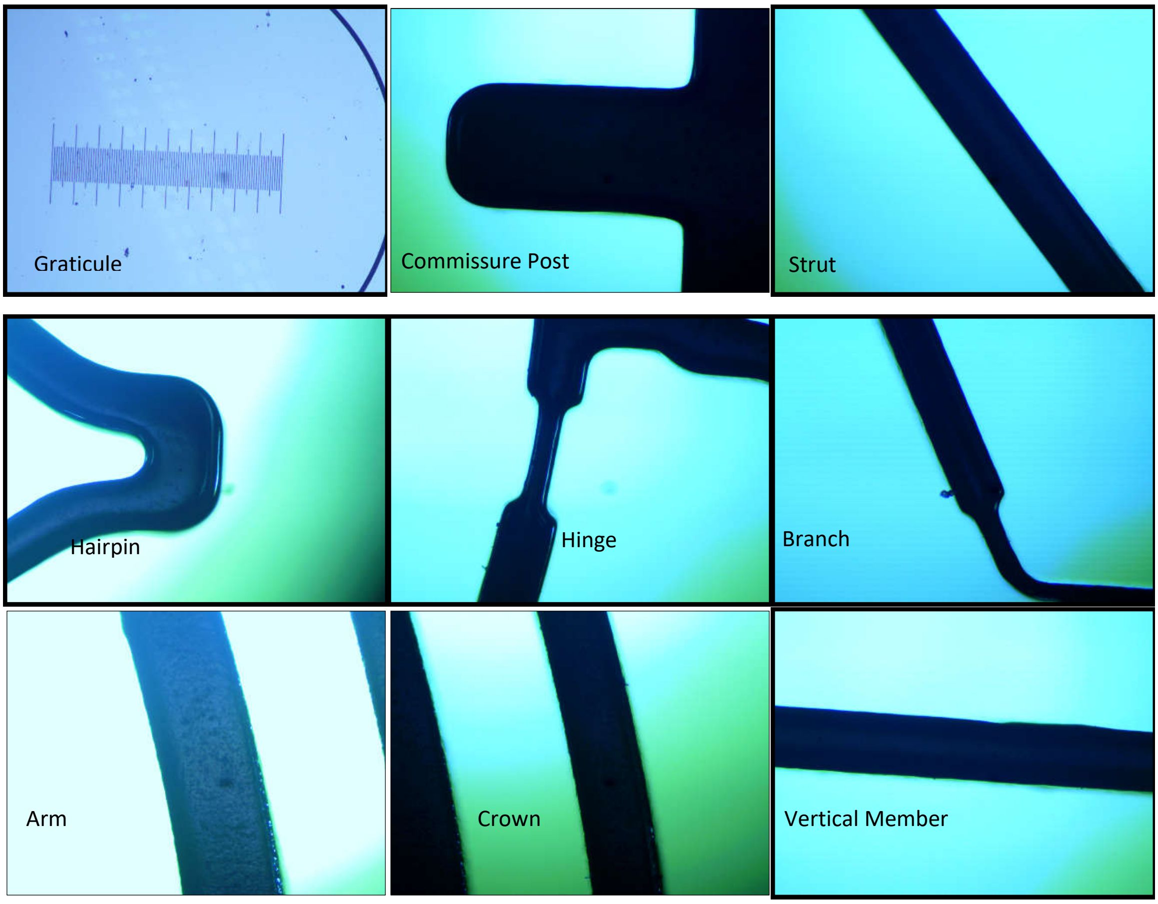

Appendix Figure E-3. Typical images used for measurements of stent members

Appendix F. Dogbone for materials testing

To determine the material properties of MP35N, tensile dogbone (dumbbell) specimens were laser cut from the stent tubing with the following dimensions.

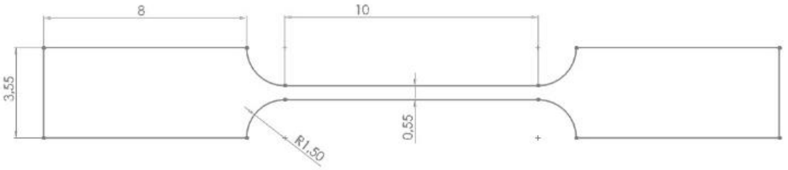

Appendix Figure F-1. Dogbone drawing

Multiple dogbones were cut (cutting geometry shown below) and three random samples were taken for tensile testing.

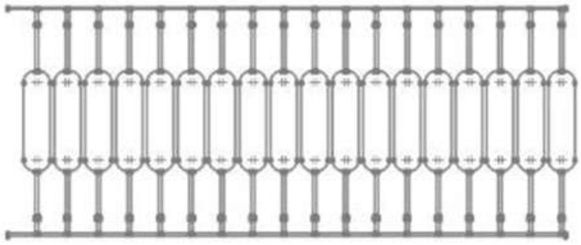

Appendix Figure F-2. Dogbone laser cutting geometry

One of the dogbones was sectioned for cross-sectional area measurement, as shown below. The cross-sectional strut area was 0.277 mm^2.

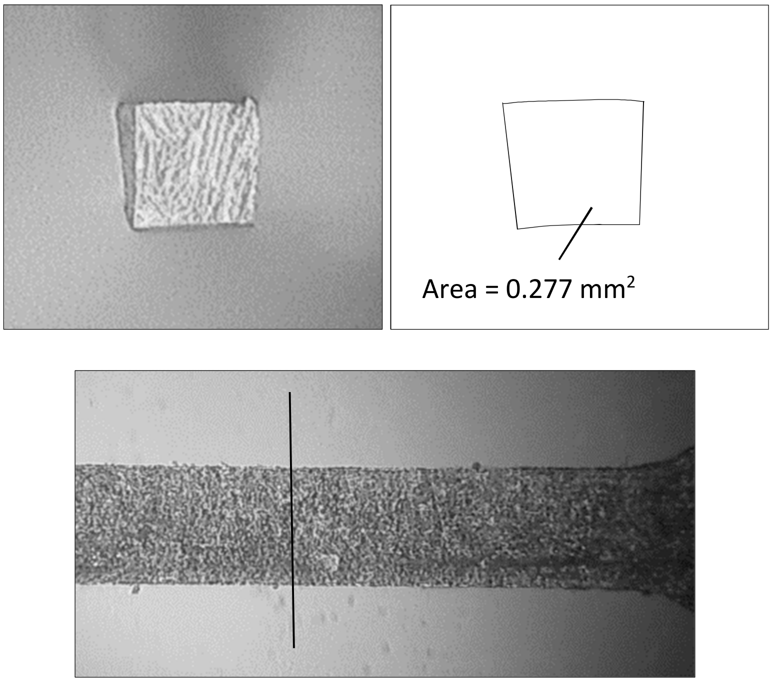

Appendix Figure F-3. Images used to measure dogbone cross-sectional area

Appendix G. Stent origins, concepts and structures: the fuzzy front end

Stent concepts evolved from simple cylindrical designs to the more complex designs summarised in this thesis. In order to make rapid design changes as part of an agile design process, several manufacturing methods were used during early stent concept development. This appendix presents some of the original concepts and some concepts that did not progress to the prototyping stage. These early prototypes were handled, used to make valves, shown to surgeons and the sponsor and served as a base for the development described in the body of this report.

Sheet metal stent The first stent prototypes were constructed from laser-cut 316 stainless steel and had very simple diamond mesh designs. Stents were laser cut by a nearby sheet metal company and cost approximately US$5 for 20 stents. The stents were curved into a cylindrical shape and the ends were brazed together. These prototypes only helped determine some of the parameters important for polymer valve manufacture.	
First additive manufacturing stent The next stent prototypes were constructed from titanium by selective laser melting ("lasercusing"). These stents were more reliable and accurate than sheet metal stents but still could not be used to construct a stent that could be crimped from 23mm to 6mm without breaking, even after annealing. Surface roughness was also a problem when attaching polymer leaflets.	
First laser cut full-size stents The first prototype stents to be laser cut and electropolished were constructed with a structure similar to traditional balloon-expandable stents. Radial strength was designed to be similar to the Edwards Sapien XT valve. Valve height was 16.5mm to accommodate a 14mm polymeric valve of 14mm height and allow space below the leaflets for a skirt. Three posts also allowed the stent to be used for early bioprosthetic valve manufacture. For these prototypes the laser cutting and electropolishing was outsourced to MeKo (Sarstedt, Germany) as a laser cutting machine had not yet been procured and electropolishing methods had not yet been developed.	
Miniature prototypes The limitations of diamond mesh "chicken fence" designs became clear during early valve manufacture and testing, so various concepts were generated based on the incorporation of a crown shape. A local coronary stent manufacturer, DISA Vascular (Pty) Ltd., kindly manufactured miniature versions of stent crown support members out of 1.8mm outer diameter L605 tubing.	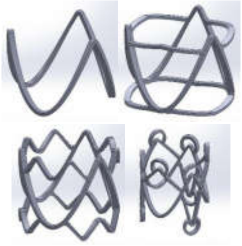
Crown-shaped stents - Lasercusing The first crown-based stents of appropriate size were created for testing. These designs, including those shown here, were prototyped using additive manufacturing techniques. A) The first design consisted of a crown shape with zig-zag struts at inflow and outflow ends. B) Various shapes of the crown were developed to improve crimping and expansion behaviour, including changes in crown width. C) Crown shapes with different angles at the commissure posts were developed in an attempt to lower leaflet stresses at this point. Crown-shaped stents without structures connecting the top row to the bottom row were susceptible to longitudinal shortening during valve loading, so designs such as D) were created to provide longitudinal support. E) Instability in a single row of zig-zags was solved by incorporating a double row at the outflow end. D) was also laser cut by MeKo and used to evaluate the ability to spray coat polymeric valves.	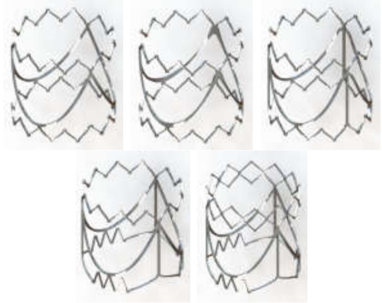
Alternative Connector Mechanisms Several alternatives to connect the top row of struts to the bottom row were attempted.	

	
<u>Different starting diameter</u> An attempt was made to produce 23mm valves from 20mm tubing. Although this was successful, it was difficult to match stent crown shape to spray coating mandrel shape.	

-

Appendix H. FEA results of stent crimping and deployment

The figures below show the Control stent, Design 1 and Design 2 at various stages of simulation.

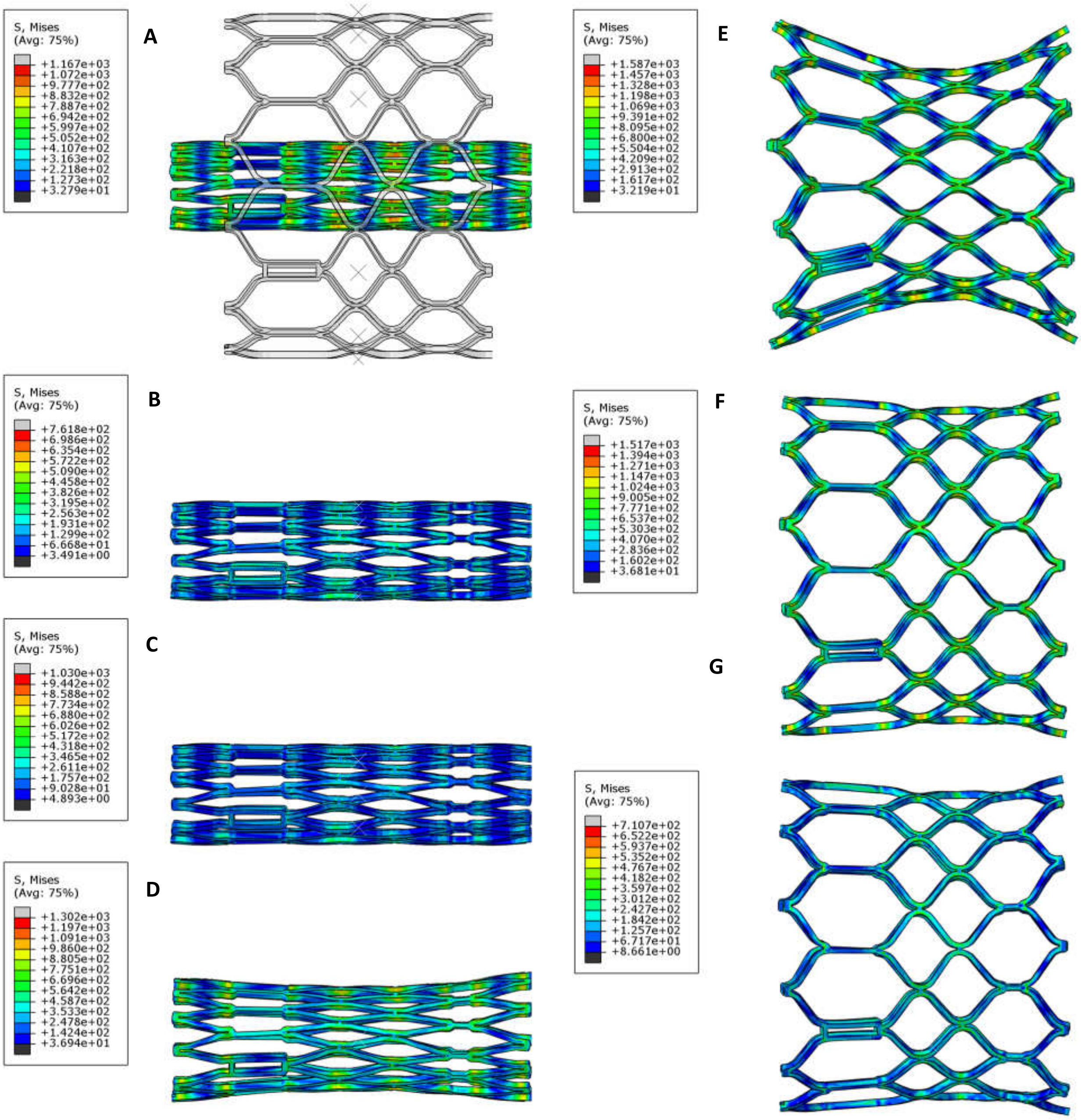

Appendix Figure H-1. Stent shape changes over the analysis for Control stent. A) Crimped (original & deformed), B) Relaxed, C) 25% deployed, corresponding to approx. 0.4 atm, D) 50% deployed, E) 75% deployed, corresponding to approx. 3.6 atm, F) 100% deployed, G) Recoil

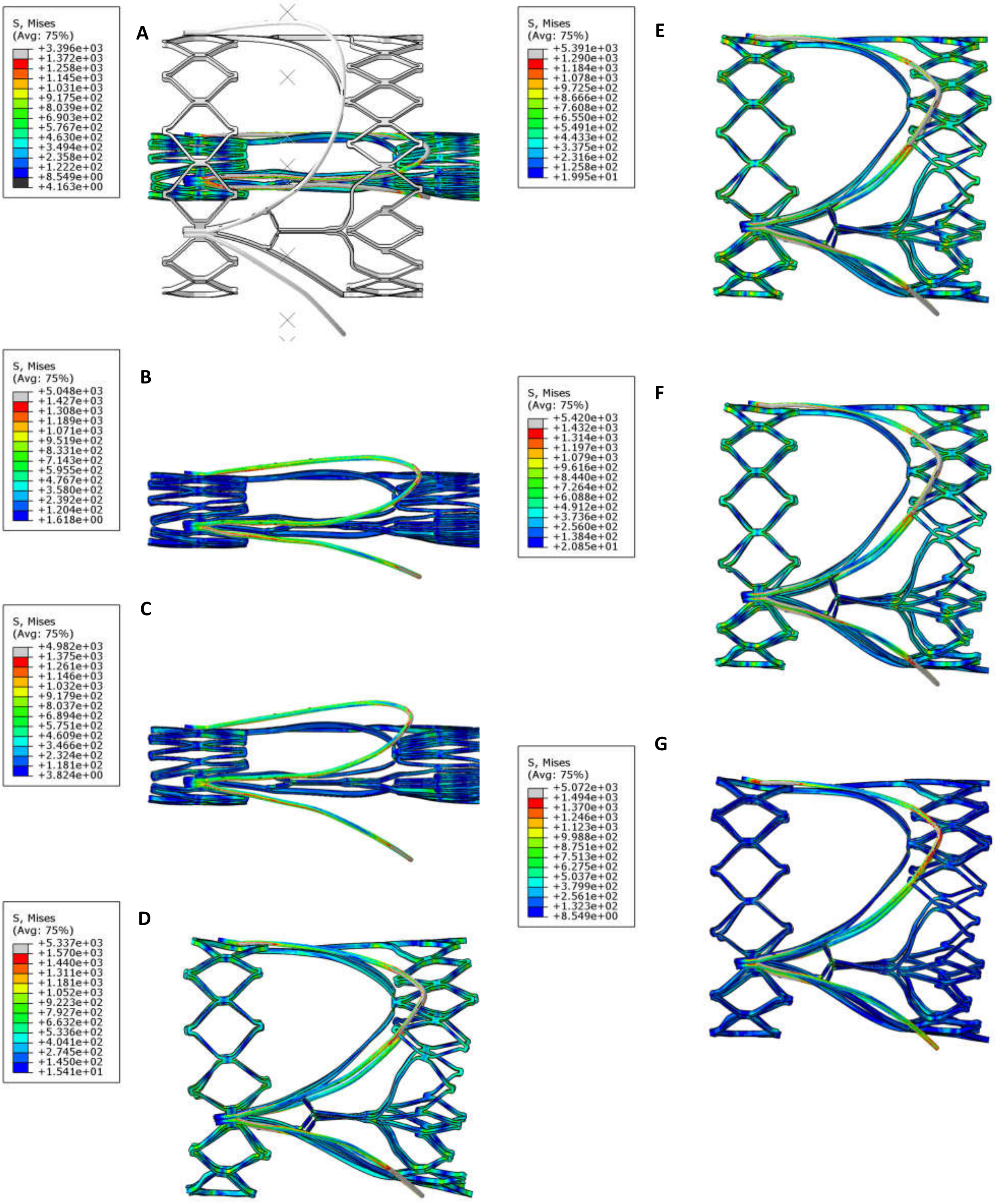

Appendix Figure H-2. Stent shape changes over the analysis for Design 1 stent. A) Crimped (original & deformed), B) Relaxed, C) 25% deployed, corresponding to approx. 0.4 atm, D) 50% deployed, E) 75% deployed, corresponding to approx. 3.6 atm, F) 100% deployed, G) Recoil

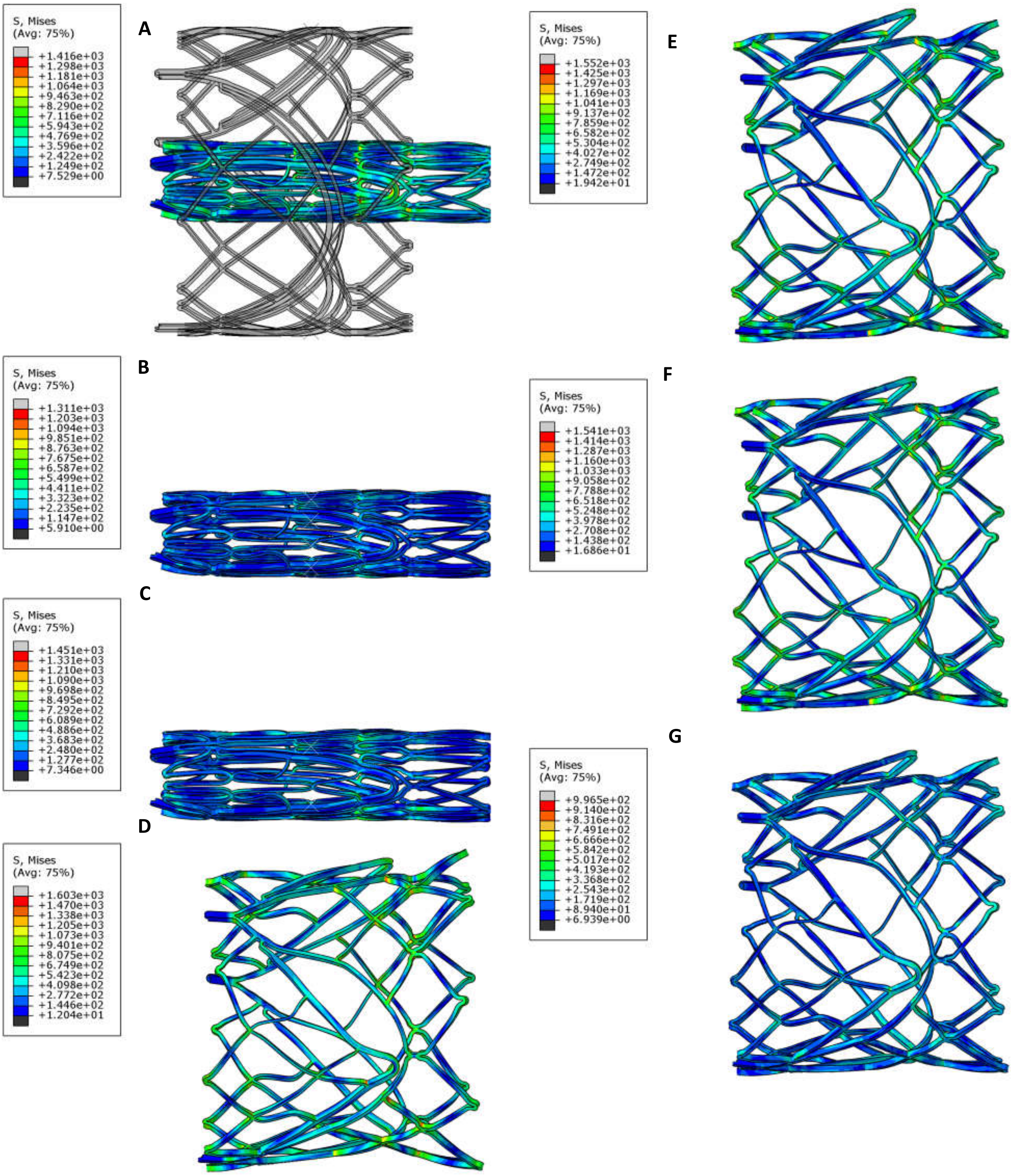

Appendix Figure H-3. Stent shape changes over the analysis for Design 2 stent. A) Crimped (original & deformed), B) Relaxed, C) 25% deployed, corresponding to approx. 0.4 atm, D) 50% deployed, E) 75% deployed, corresponding to approx. 3.6 atm, F) 100% deployed, G) Recoil

Appendix I. Additional stent images

Microscopic, microscopic and SEM images of cut, descaled and electropolished stents for Control, Design 1 and Design 2 stents are shown in the figures below.

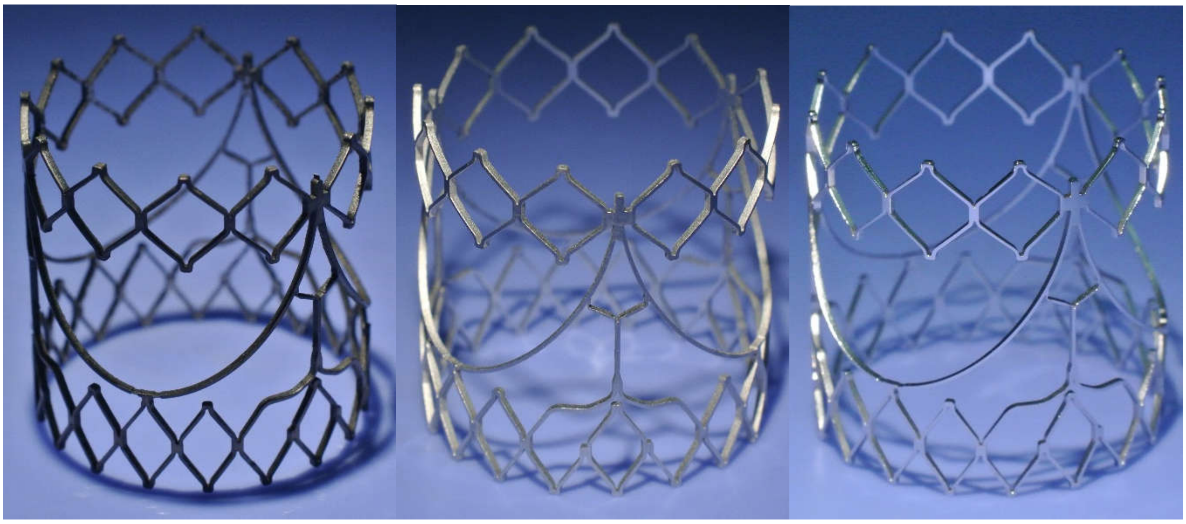

Appendix Figure I-1. Macro photographs of Design 1 after a) laser cutting, b) descaling and c) electropolishing

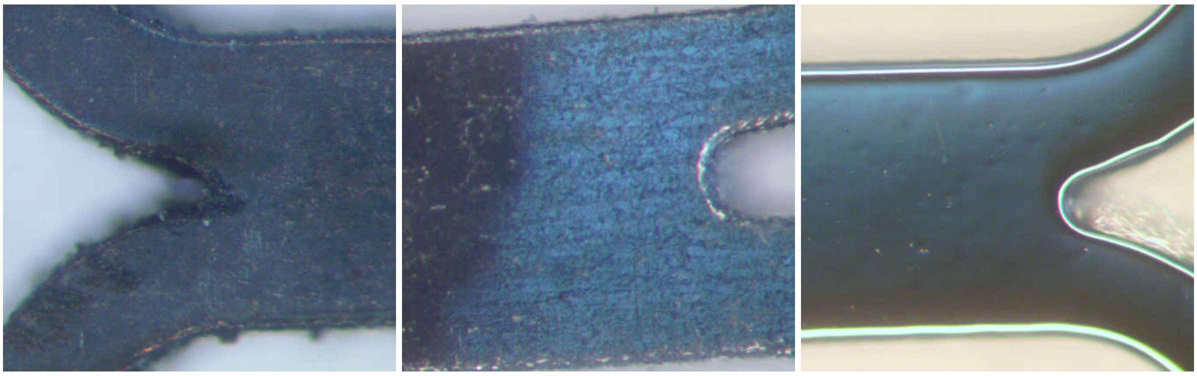

Appendix Figure I-2. Microscopic images of Design 1 after a) laser cutting, b) descaling and c) electropolishing

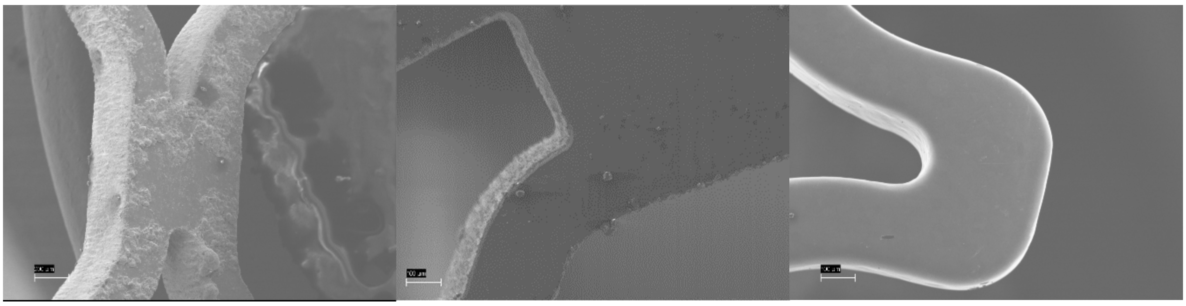

Appendix Figure I-3. SEM images of Design 1 after a) laser cutting, b) descaling and c) electropolishing

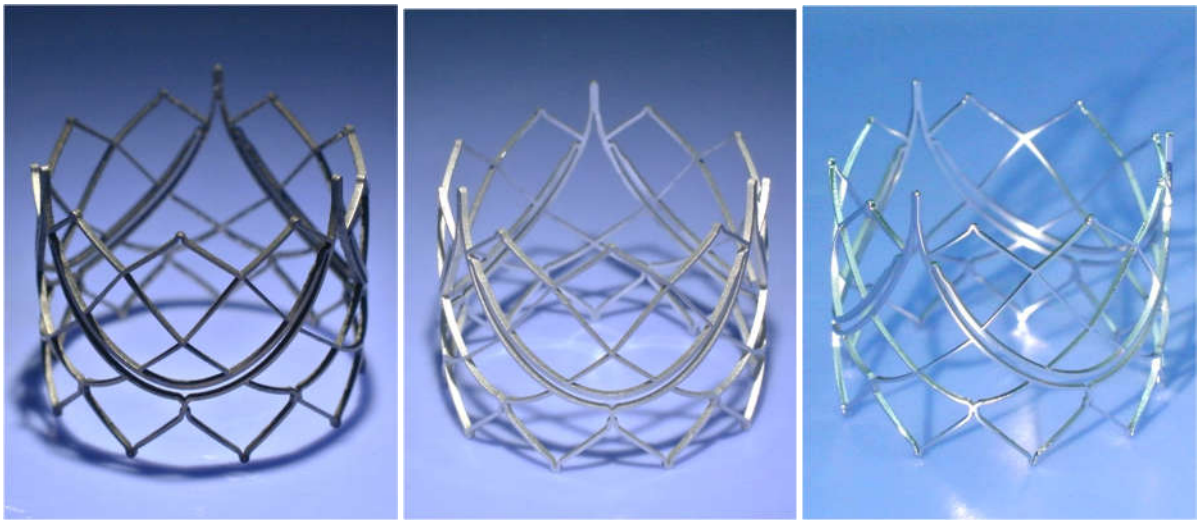

Appendix Figure I-4. Macro photographs of Design 2 after a) laser cutting, b) descaling and c) electropolishing

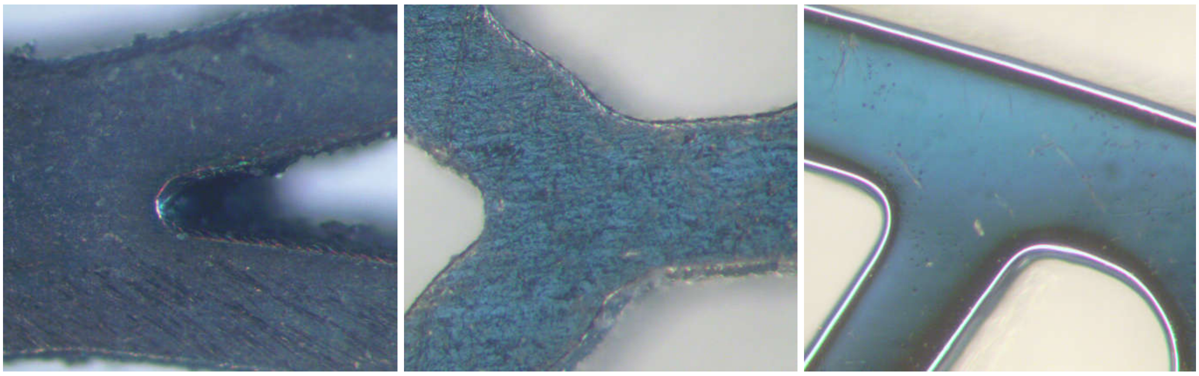

Appendix Figure I-5. Microscopic images of Design 2 after a) laser cutting, b) descaling and c) electropolishing

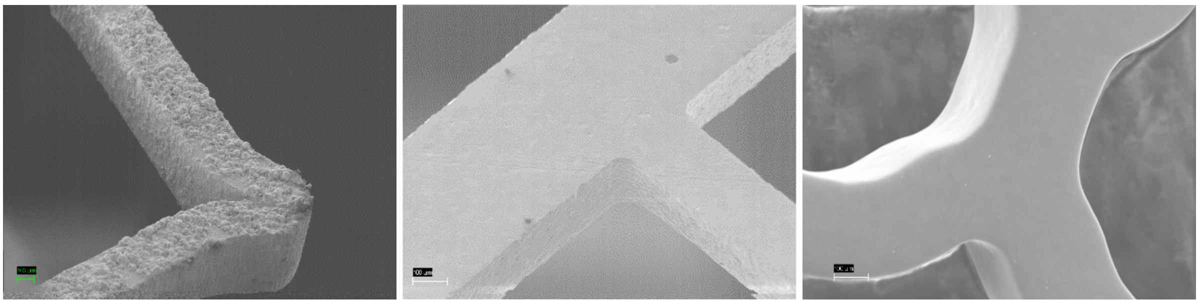

Appendix Figure I-6. SEM images of Design 2 after a) laser cutting, b) descaling and c) electropolishing

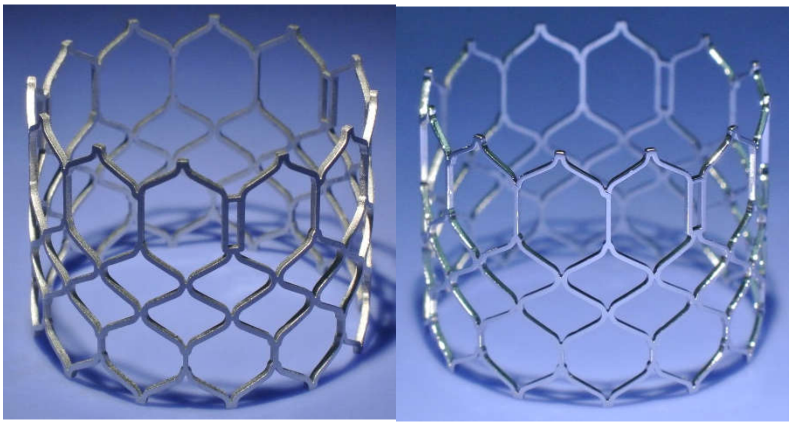

Appendix Figure I-7. Macro photographs of Control stent after a) descaling and b) electropolishing

Appendix Figure I-8. Microscopic images of Control after a) laser cutting, b) descaling and c) electropolishing

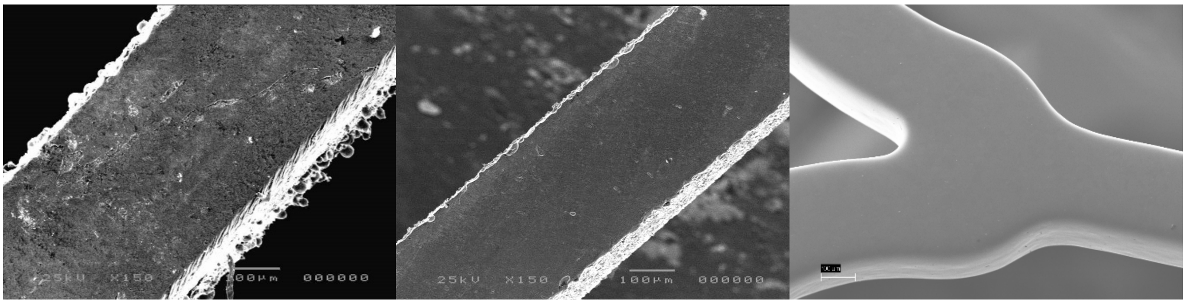

Appendix Figure I-9. SEM images of Control after a) laser cutting, b) descaling and c) electropolishing

Appendix J. Detailed predictions and measurements of stent recoil and foreshortening

Recoil

Detailed stent diameter and recoil predictions from FEA are shown in Appendix Table J-1. Detailed experimental measurements of diameter and recoil are shown in Appendix Table J-2.

Appendix Table J-1. Stent diameter and recoil predictions from FEA

Design	Position	Crimped Diameter	Relaxed		Deployed Diameter	Recoiled	
			Diameter	Crimped Recoil %		Diameter	Deployed Recoil %
Control	Top	6.00	6.65	10.8	22.62	22.22	1.8
	Middle	6.00	6.66	11.0	21.23	20.72	2.4
	Bottom	6.00	6.65	10.8	23.08	22.71	1.6
Design 1	Top	6.00	6.77	12.8	23.50	22.71	3.4
	Middle	6.00	6.28	4.7	23.15	22.14	4.4
	Bottom	6.00	6.65	10.8	23.30	22.76	2.3
Design 2	Top	5.75	6.13	6.2	23.25	22.75	2.2
	Middle	6.00	6.41	6.8	22.16	21.74	1.9
	Bottom	5.87	6.33	7.8	23.72	23.32	1.7

Appendix Table J-2. Stent diameter and recoil experimental measurements

Design	Position	Crimped Diameter	Relaxed		Deployed Diameter	Recoiled	
			Diameter	Crimped Recoil %		Diameter	Deployed Recoil %
Control	Top	Could not measure	6.55	Could not calculate	22.96	22.55	1.8
	Middle		6.71		21.17	20.66	2.4
	Bottom		6.59		23.01	22.69	1.4
Design 1	Top	Could not measure	6.50	Could not calculate	23.38	22.67	3.0
	Middle		5.87		23.48	22.50	4.2
	Bottom		6.50		23.54	22.85	2.9
Design 2	Top	Could not measure	6.19	Could not calculate	23.39	22.86	2.3
	Middle		6.49		22.36	21.92	2.0
	Bottom		6.35		24.12	23.74	1.6

The amount of arm protrusion following deployment as also measured physically for each arm as the distance from the arm extremity to the opposite outside wall of the stent. These arm protrusions were measured to be 24.63 mm, 25.02 mm and 24.99 mm for Design 1, and 25.00 mm, 24.73 mm and 24.72 mm for Design 2.

Foreshortening

Detailed stent length and foreshortening predictions from FEA are shown in Appendix Table J-3. Detailed experimental measurements of length and foreshortening are shown in Appendix Table J-4.

Appendix Table J-3. Stent length and foreshortening predictions from FEA

Design	Crimped Length	Relaxed Length	Deployed Length	Recoiled Length	Fore-shortening %
Control	24.36	24.32	19.24	19.53	19.7
Design 1	29.43	29.44	24.18	24.77	15.9
Design 2	25.54	25.51	20.58	20.92	18.0

Appendix Table J-4. Stent length and foreshortening measurements

Design	Relaxed Length	Deployed Length	Recoiled Length	Foreshortening %
Control	24.19	19.16	19.45	19.6
Design 1	29.32	24.28	24.97	14.8
Design 2	25.39	20.46	20.73	18.4

Appendix K. Hollomon material model

A Hollomon power law was used to model stress-strain behaviour beyond the point of necking. In order to determine whether stent stress and radial strength were affected by the use of this model, a Design 2 stent was subjected to modelling using the simple FEA described in Section 4.2, followed by crushing described in Section 4.3.

Two material models were used. The first material model used stress-strain behaviour up to 1330 MPa, near the true stress value of UTS. In this model the stress is assumed to stay constant after necking. The second material model used stress-strain behaviour extrapolated to 200% strain (2508 MPa stress) using the power law.

The Hollomon material model predicted higher stresses than the UTS model, for Von Mises Stress and Maximum Principal Stress (see Appendix Table K-1). Radial strength did not differ between the two material models, as shown in Appendix Figure K-1.

Appendix Table K-1. Stress stresses for different material models

Material model	**Highest Stress (MPa)**	
	Von Mises	**Max Principal**
UTS	1330	1936
Hollomon	1954	2527

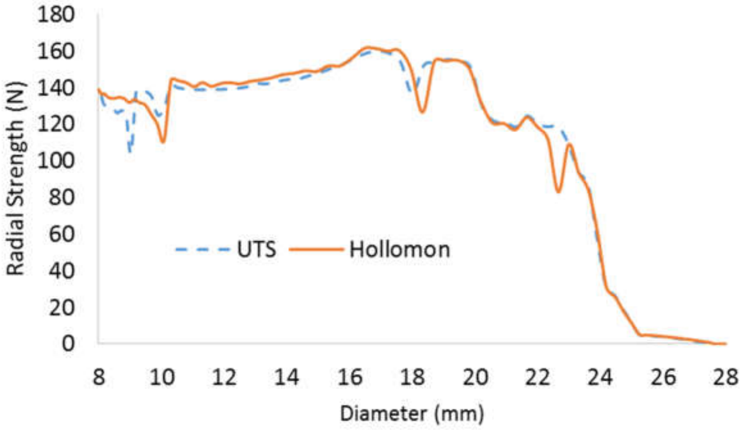

Appendix Figure K-1. Radial strength of Design 2 stents as predicted using simple FEA modelling, for two material models, firstly using stress-strain behaviour up to true UTS, 1330 MPa ("UTS") and secondly using stress-strain behaviour projected to 2508 MPa based on the Hollomon power law ("Hollomon")